TUM School of Engineering and Design

From imaging to numerical characterization: a simulation workflow for additively manufactured products

Nina Korshunova, M.Sc.(hons)

Vollständiger Abdruck der von der TUM School of Engineering and Design der Technischen Universität München zur Erlangung des akademischen Grades einer

Doktorin der Ingenieurwissenschaften, Dr.-Ing.

genehmigten Dissertation.

Vorsitzender:		Prof. Dr.-Ing. habil. Fabian Duddeck
Prüfender der Dissertation:	1.	Prof. Dr. rer. nat. Ernst Rank
	2.	Prof. Dr. sc. techn. Daniel Straub
	3.	Prof. Ferdinando Auricchio, Ph.D.

Die Dissertation wurde am 12.05.2021 bei der Technischen Universität München eingereicht und durch die TUM School of Engineering and Design am 24.11.2021 angenommen.

Zusammenfassung

Die Palette der Strukturen, die mit additiver Fertigung (AM) hergestellt werden können, ist extrem breit. Im letzten Jahrzehnt hat diese Technologie ein beträchtliches Wachstum erlebt. Ein bemerkenswerter Aspekt der AM ist die Möglichkeit, hochkomplexe Mikrostrukturen herzustellen, die auf traditionelle Weise nur schwer zu erzeugen wären. Trotz des großen Potenzials müssen vor einem breiten produktiven Einsatz von AM noch zahlreiche Fragen gelöst werden. Einer dieser Aspekte ist das Entstehen von prozessinduzierten Defekten. Da die Prozessparameter aufgrund der zugrundeliegenden Physik nur schwer präzise zu kontrollieren sind, kann die Mikrostruktur signifikante Abweichungen der gefertigten geometrischen Form im Vergleich zum Entwurf aufweisen. Diese Unterschiede können die Qualität und Leistung des Endprodukts erheblich beeinträchtigen, was mögliche Anwendungsbereiche von AM-Strukturen in Frage stellt.

Numerische Simulation bietet eine einzigartige Möglichkeit, die Auswirkungen von prozessbedingten Defekten zu bewerten, das strukturelle Verhalten von gefertigten und entworfenen Produkten zu vergleichen, einen Einblick in die mögliche Optimierung von Prozessparametern zu erhalten und die durch diese Imperfektionen verursachte Unsicherheit abzuschätzen. Allerdings wird es oft als undurchführbar angesehen, die aus Computertomogrammen erhaltenen *as-manufactured*-Geometrien in die traditionelle rechnerische Finite-Element-Analyse zu integrieren, da die Vernetzungsprozedur für solche hochauflösenden geometrischen Modelle zu komplex ist und die numerischen Kosten zu hoch sind. Daher zielt diese Arbeit darauf ab, ein numerisches Framework vorzuschlagen, das für die Analyse von *as-manufactured* AM-Produkten geeignet ist. Es wird die Möglichkeit untersucht, die Auswirkungen von prozessinduzierten Defekten auf das endgültige Bauteilverhalten zu bewerten und eine Unsicherheitsquantifizierung der mikrostrukturellen Variabilität durchzuführen. Im Rahmen dieser Kriterien wird der Verifizierung und Validierung der vorgeschlagenen Techniken große Aufmerksamkeit gegeben.

Abstract

The range of structures that can be produced with additive manufacturing (AM) is exceptionally vast. The last decade witnessed a considerable growth of this technology. A remarkable feature of AM is the possibility to produce highly complex microarchitectured structures that are difficult to manufacture traditionally. Despite its potential, AM still faces challenges that have to be addressed before it can be widely used in production lines. One of these aspects is the occurrence of process-induced defects. As process parameters are difficult to precisely control due to the underlying physics, the microstructure can exhibit significant deviations of as-manufactured shapes from as-designed ones. These discrepancies can seriously alter the final part quality and performance, putting uncertainty on possible application areas of AM structures.

Numerical simulation provides a unique possibility to evaluate the effects of process-induced defects, compare the structural behavior of as-manufactured and as-designed products, gain an insight into possible optimization of process parameters and estimate uncertainty introduced by these imperfections. However, it is often considered infeasible to integrate the as-manufactured geometries into the traditional computational Finite Element analysis due to the complexity of the meshing procedure for such high-resolution geometrical models and the prohibitive numerical costs. Thus, this thesis aims at establishing a numerical framework suitable for the analysis of as-manufactured AM products. The present work's objective is to investigate the possible way to evaluate the effects of process-induced defects on the final part performance and perform uncertainty quantification of microstructural variability. Within the framework of these criteria, significant attention is given to the verification and validation of the proposed techniques.

Acknowledgements

This work has been conducted during my time at the Chair for Computation in Engineering (currently, Computational Modeling and Simulation) at the Technical University of Munich from 2016 to 2021. Many people and institutions have supported me on this path. I could only imagine that I would be working together with Siemens AG, the University of Pavia, Aalto University, and the TUM ERA Group. This unique international and very diverse experience of scientific collaboration shaped not only this thesis but also my personality. This research's success would not have been possible without the support and guidance of each and every person I met in this way, which I am incredibly grateful for.

First and foremost, I would like to express my deepest gratitude to my doctoral supervisor, Prof. Ernst Rank, for his excellent guidance and support. He believed in me and my scientific progress from day one. I knew that every time I needed any advice or help, he would always be open to find a possible solution. And even when I came to his office feeling like I did not know how to move forward, I always walked out feeling confident that this research will turn out in the best possible way. Without his knowledge, advice, and patience, this thesis would have never been completed. The incredible working atmosphere that he has provided to me made my time at the chair really special. He has offered me a lot of freedom and numerous opportunities to grow both scientifically and personally.

I am also deeply indebted to Dr. Stefan Kollmannsberger. He has guided me in both the best and the most challenging moments of this research. He was always ready to listen and shape this work. Stefan has inspired me with his original ideas, showed new research directions, and constantly supported new beginnings. His door was always open for me, and his incredible character has provided the best possible environment I could only imagine.

This thesis's topic has originated from the initial project with Siemens AG, which partially financed this research. This financial support is gratefully acknowledged. In this project's framework, I had the pleasure to be advised by Dr. Daniel Reznik from Siemens AG. I would like to thank him for providing me this opportunity to dive into the topic of additive manufacturing. His guidance and support with both the scientific and experimental side of this work opened up new research possibilities and made this thesis complete. I gratefully acknowledge the opportunities to visit his working group and the testing facilities, get familiar with the technology, and his constant help on the way to completing this research.

Special thanks go to Prof. Ferdinando Auricchio and Prof. Alessandro Reali from the University of Pavia. They have made possible a huge part of this work. I had an invaluable experience of staying abroad at their department, where I had always felt welcome. Prof. Auricchio and Prof. Reali have provided me with access to 3D printing and experimental facilities. They have also guided me on the way to completing our joint project and have constantly contributed with new ideas and directions. Their expertise in the field of additive manufacturing showed me aspects I had not seen before. For this reason, I am really grateful that Prof. Auricchio is part of my PhD committee as well.

Furthermore, I would like to thank Massimo Carraturo, PhD, and Gianluca Alaimo,

PhD, from the University of Pavia. They made my stay in Pavia really memorable. I appreciate all your scientific support in our joint project. But most of all, I thank them for all their personal motivation and their inner drive in life. I will definitely remember the atmosphere they have created for me during my stay in Pavia. Massimo and Gianluca have made me feel like a part of the CompMech group, even in such a short time. And I really thank each and every one of them for the incredible experience I had there.

I would like to extend my sincere thanks to Prof. Jarkko Niiranen. Although my stay in Helsinki and Aalto University was not as long as planned, I will definitely remember it. The ideas that we all dreamed about in the office in Munich turned out to be much more than we all expected. He was always open for discussions, generated new insights, and contributed with his unparalleled knowledge. Whether I was asking him the most basic questions or the most tricky ones, he has always managed to clarify everything in the best possible way. Prof. Niiranen provided me with a chance to see Finland and meet his working group, with whom I am still in contact.

I would like to express my most profound appreciation to Prof. Daniel Straub and Dr. Iason Papaioannou. This collaboration started with a simple discussion at the office of Prof. Rank. I could not even imagine that I would go in the direction of uncertainty quantification. But I must say that this was the steepest learning curve I ever had. And this project, with all its challenges, was fascinating for me. I would really like to express my deepest gratitude to Dr. Papaioannou for his patience and his knowledge. At the moment, when he had to explain to me that "one plus one is two" in an absolutely unknown field for me, he provided me with such encouragement and motivation that I wanted only to move forward. Weekly meetings, numerous questions, even debugging my code - I could not even imagine how dedicated this person can be. With the invaluable advice and experience from Prof. Straub, we have created an impressive outcome of our joint work. For this reason, I greatly appreciate Prof. Straub being a reviewer of this work.

I also would like to thank Prof. Alexander Düster for discussions about homogenization techniques and invaluable guidance on the way of their investigations. Furthermore, I thank Prof. Fabian Duddeck for chairing this examination and providing me with opportunities to learn more during my PhD time. I greatly appreciate the opportunity to have participated in the MMiFEM seminar, where I also met his working group. These contacts became long-lasting support in this research work.

I further would like to acknowledge all institutions and collaborators who made a contribution to this work. I thank all organizations, who performed CT scans, did experimental testings, provided me with data. Without all of you, this thesis would not have been possible.

Furthermore, I want to thank all the colleagues from both the Chair for Computation in Engineering and Chair of Computational Modeling and Simulation. I enjoyed working with each of you, and you have enormously contributed to this thesis. Our endless coffee pauses and discussions shaped the way this thesis looks now. But most importantly, the atmosphere at the chair was my biggest motivation to come every day. I enjoyed all the moments: the hikes, trips, discussions, meetings. I will never forget this fantastic group. Special thanks go to Philipp Kopp, John Jomo, Alexander Paolini, Davide D'Angella, László Kudela, Benjamin Wassermann, Mohamed Elhaddad, Lisa Hug, and Oguz Ozto-

prak. I have shared the office with Philipp for about four years. I enjoyed all discussions, coffees, and a "jungle-office" we had during my stay at the chair. I had the pleasure of having joint projects with John, Alex, and Benjamin. Working with you was really easy and very enjoyable. And what can I say more – one project, one publication! Lisa had shared with me my time at IGSSE. I had a lot of fun in the IGSSE Forum, preparing the posters and presenting our project together. I still remember that László helped me design my first pre-processor GUI when I just started my PhD. And from Davide, Mohamed and Oguz, I have always learned more about coding and enjoyed having a coffee in the morning. I thank each and every one of you for all experiences we had together.

I cannot begin to express my thanks to my friends. They became a second family for me: from Forum to Master's to PhD to working life – always together. Every single one of them deserves a medal. They went through working and writing this thesis with me: they were unconditionally there for me sharing ups and downs. Thank you for your positivity, your belief in me, and your constant help. I would never manage to finish this thesis without you.

I am deeply indebted to my family. I know that my PhD was like a roller coaster for them. They have listened to everything I had to say and encouraged me in whatever I began. Although I can only see you once per year, I feel your presence every day. Without your support and your motivation, this work would have never been completed.

Last but definitely not least, I would like to thank Iñigo Lopez. He was the one who listened to my ideas, saw me drawing schemes after dinner, and discussed with me my code and work. His loving understanding and unconditional everyday support have allowed me to complete this research. I thank you for reading this thesis chapter by chapter in the evenings and on the weekends. Without you, I would not be able to finish this thesis.

Contents

Chapter 1

Introduction

1.1 Motivation

Additive manufacturing (AM) has drawn significant interest both in industry and research due to the unique possibility to produce complex structures for a wide range of applications (see, e.g., [18, 114, 139]). The term "additive manufacturing" refers to multiple techniques [72], in which a structure is produced by successively adding material in a layerwise fashion. These techniques can be classified according to the process and used materials. An example of an AM method suitable to manufacture metal structures is Laser Powder Bed Fusion (LPBF), which is the main focus of this thesis.

In the LPBF process, a high-power density laser melts a material powder layer by layer to form the final product. In this manner, highly complex metal structures with sophisticated microstructural architecture can be produced. Lattice structures (see, e.g., Figure 1.1) are a classic example of such components that are difficult to manufacture by traditional methods [103] . These regular, usually periodic designs are attractive for many industries due to the possibility of largely decoupling their effective stiffness and strength from their relative density [32, 124, 152, 187]. Lattices are also very important for industrial applications due to their lightweight design, their exceptional mechanical, acoustic, and dielectric properties (e.g. [11, 23, 45, 153, 188]), and the possibility to relate their mechanical properties to the truss topology and geometry (see e.g. [32, 92, 124, 162]).

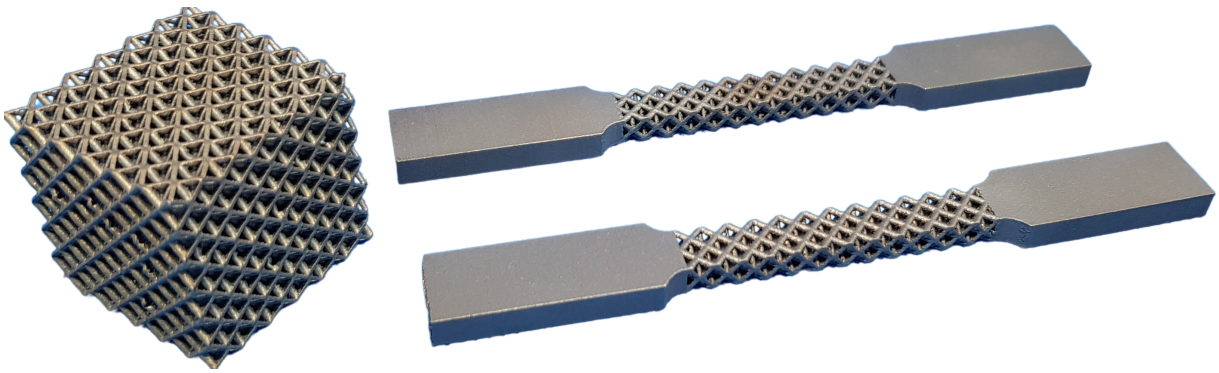

Figure 1.1: An example of lattice structures produced using Laser Powder Bed Fusion.

Although the LPBF allows the production of such challenging lattice shapes, this design freedom comes with the difficulty of controlling the underlying physics. In particular, process-induced features, even defects, often occur in the produced structures. Some of the most common imperfections are the change in the lattice strut thickness, its shape, or its connectivity, which arise from the size of the melt pool [7, 26]. Another process-induced defect that typically occurs in the manufactured parts is the surface roughness caused by the attachment of the unmelted powder to the struts [31, 34, 47, 179]. Due to the lack of fusion, internal porosity can also occur in the final specimens (e.g. [52, 77, 186]). Finally, material can accumulate on the inclined and overhanging parts of the lattice, as the size of the melt pool strongly depends on the fraction of solid and powder parts in the layer [106]. To indicate the presence of these process-induced defects, the printed geometries are often referred to as *as-manufactured* shapes, while the original models as *as-designed*. Surely, such changes in the structure have a certain effect on their quality, applicability, and performance. Thus, the field of these defects' characterizations has received significant attention in the past years (see, e.g., [103, 98, 107, 106, 138, 7]).

Overall, the process-induced defects can considerably alter the mechanical behavior of final parts (e.g., [26, 37, 40, 62, 101, 103]). Therefore, a reliable evaluation of the mechanical behavior of printed LPBF lattice components is crucial for determining their field of application. This has motivated many experimental investigations to evaluate AM final parts' mechanical properties (see, e.g., [56, 163, 103]). However, since the defects are specific for different designs, materials, and process parameters, a strong interest in incorporating as-manufactured geometries into the numerical analysis has emerged. There is a considerable amount of research directed to the characterization of the mechanical behavior of additively manufactured lattice structures (e.g., [26, 35, 98, 130, 132, 162]). Such investigations aim to compare the behavior of as-manufactured and as-designed components and characterize the influence of the process-induced defects on the final parts' behavior. Yet, efficient incorporation of as-manufactured shapes into the computational simulation remains a challenge.

Another level of complexity is added by the fact that such predictive evaluations of the as-manufactured geometries do not take into account the effects of the geometrical variability introduced by the LPBF process. This, however, is an important research question to improve the quality of the as-manufactured products, establish a relation between the process parameters and the final result of a printing, and predict the possible spread of the obtained mechanical characteristics. At present, the most common approach to performing such characterization is to use statistical models. To this end, a set of considered defects, such as, e.g., strut waviness, diameter, or a cross-sectional shape change, is usually defined. Commonly, the effects of one group of defects or a combination of a few are considered in the numerical analysis. However, efficient analysis of the possible variation of lattice's mechanical behavior due to the combination of all geometrical process-induced defects remains an open research question.

1.2 Objectives and contributions

In light of the above motivation, this thesis aims to establish an efficient and reliable computational workflow to characterize as-manufactured AM products' mechanical be-

havior. To achieve this, a basic understanding of the manufacturing challenges and the as-manufactured shape acquisition should be gained. These insights will also help to identify the challenges in AM product simulation and to define the requirements to the mathematical models and numerical approaches, which can incorporate the as-manufactured geometries into the analysis.

Having identified the significant demands on the path of AM product simulation, the first main objective of this work is to propose an image-to-material-characterization workflow. As the utmost goal is to establish a technique helping to assess the quality of the produced parts, the proposed methods' reliability is a central part of this research. Thus, the verification and experimental validation of the investigated techniques are of crucial importance for this work. Furthermore, to apply this workflow to industrial applications, the proposed methods' efficiency and flexibility are critical. Hence, three main techniques with increasing levels of complexity are investigated. In particular, beam theories, numerical homogenization, and direct numerical simulation are analyzed and compared on two examples of manufactured lattices with different microstructural scales.

Although such a predictive workflow can be employed to analyze and compare the mechanical behaviour of designed and printed parts, the essential question of how the arising manufacturing defects can affect the printed structures' overall behaviour remains unanswered. It is crucial to understand whether such shape deviations can also be modelled and incorporated into the established workflow. Thus, the second main objective here is to propose a stochastic model to mimic the process-induced defects and assess their influence on the variability of the mechanical behaviour of as-manufactured AM products.

Even though the primary focus of this thesis is to investigate the linear elastic mechanical behavior of lattices structures, the proposed approach is neither limited to the linear regime, nor to the type of used structures. Therefore, the range of applicability and possible limitations of the proposed methods will be thoroughly discussed in the manuscript.

The contributions presented in this work have been published and submitted to publishing in several scientific journals. The first idea of the image-to-material-characterization workflow was introduced in [85]. In this article, verification and validation of the numerical homogenization and the direct numerical simulation on the microarchitectured lattices were presented. Next, the proposed idea was applied to compare as-designed and as-manufactured octet-truss lattice structures produced at a larger scale in [84]. Then, the applicability of the beam models and the validation of the proposed workflow was investigated on an example of AM lattice beams in bending in [83]. Finally, a stochastic model for investigating the influence of microstructural variability on the mechanical behavior of AM lattice structures was introduced in [86]. Thus, throughout the thesis, the following footnotes are used to reference the original publications, literal transposition and adjusted text version[abcdefg].

[a]The following chapter/section/paragraph is based on [85]. The main scientific research and the textual elaboration of the publication were performed by the author of this work.

[b]The following chapter/section/paragraph is based on [84]. The main scientific research and the textual elaboration of the publication were performed by the author of this work.

[c]The following chapter/section/paragraph is based on [83]. The main scientific research and the textual elaboration of the publication were performed by the author of this work.

[d]The following chapter/section/paragraph is based on [86]. The main scientific research and the textual elaboration of the publication were performed by the author of this work.

1.3 Outline

This work is organized into eight chapters, which are outlined as follows. Chapter 2 starts with describing the basic idea of additive manufacturing of lattice structures. In this section, the main challenges of the AM product simulation are defined. Then, the image-based numerical workflow proposed in this thesis is presented.

In chapter 3 the basic fundamentals needed to perform the direct numerical simulation of AM products is presented. In particular, classical and strain gradient continuum foundations are introduced. Then, the assumptions of the classical and strain-gradient beam theories are discussed. This chapter recaps the theory needed for a direct numerical simulation of AM products and the evaluation of bending quantities by using the simplified beam theories. Then, the Finite Cell Method for material characterization of as-manufactured structures is presented in Chapter 4. Due to the nature of the considered problems, special attention is given to an efficient integration technique of discontinuous integrands in the scope of the image-to-material characterization workflow and to parallel linear system solutions.

Chapter 5 discusses another possible technique to characterize the mechanical behavior of AM products. The first-order mean-field computational homogenization technique allows to reduce the required computational costs to evaluate the overall structural response. First, the fundamental homogenization concepts are introduced. Then, the necessary approximations and relations are thoroughly discussed. As the structures considered in this thesis are lattices, the implications of having voids in the geometry are introduced. To this extent, the window method, a specific technique aiming to treat the problematic void inclusions in the considered structures, is described. Finally, this section is concluded with numerical investigations. The considered examples help to identify the applicability area and the boundaries of the numerical homogenization approach demonstrated in this chapter. In chapter 6 the validation and verification of the presented numerical workflow is performed. In particular, two manufactured lattices at two different printing scales are shown.

Chapter 7 presents the proposed binary random field model used to assess the effects of AM product microstructural variability. This chapter starts with the formulation of the random binary field model, followed by a description of the design parameter identification procedure. Then, the random field generation concepts and the method to perform uncertainty quantification are discussed. Finally, this chapter is concluded with the impact assessment of the process-induced geometrical defects on the mechanical behavior of the structures presented in chapter 6. Lastly, the summary of this thesis and the outlook are presented in chapter 8.

[e] According to Elsevier publishing agreement [43], the text/part in the following chapter/section/paragraph is taken in an adjusted form from [85]. The main scientific research and the textual elaboration of the publication were performed by the author of this work.

[f] According to Elsevier publishing agreement [43], the text/part in the following chapter/section/paragraph is taken in an adjusted form from [84]. The main scientific research and the textual elaboration of the publication were performed by the author of this work.

[g] According to Elsevier publishing agreement [43], the text/part in the following chapter/section/paragraph is taken in an adjusted form from [83]. The main scientific research and the textual elaboration of the publication were performed by the author of this work.

Chapter 2

Numerical characterization of additively manufactured products

As briefly outlined in section 1.1, products produced by Laser Powder Bed Fusion can suffer from multiple process-induced defects, which strongly affect the quality and performance of manufactured structures. Relating these imperfections to the final mechanical behaviour of AM products is a challenging task. This chapter aims to identify the challenges in performing a versatile mechanical analysis of imperfect manufactured products. The first part focuses on a general description of Laser Powder Bed Fusion and outlines possible process-induced defects. Thereby, a particular focus is provided to lattice structures. In the following part, the main challenges of as-manufactured shape acquisition are discussed. Special attention is given to computed tomography (CT) and related CT imaging problems. In this context, a deep learning segmentation technique to address these issues is proposed. Then, the possible methods for mechanical analysis of the as-manufactured structures are elaborated. Finally, considering all defined challenges, an image-to-material-characterization workflow is presented.

2.1 Metal Laser Powder Bed Fusion for lattices

Powder Bed Fusion (PBF) was initially established at the Univesity of Texas at Austin [51]. This process, among other AM processes, was the first to attract the interest of the industry. The general idea of PBF is schematically depicted in Figure 2.1 and can be described as follows. A layer of chosen powder, e.g., stainless steel or nickel alloy, is deposited on the powder bed from the feed region with the help of a rolling (recoating) mechanism. A high-energy power source, in Figure 2.1 a laser beam, is directed to the powder bed to partially fuse the powder with the layer below. The laser follows a pre-defined pattern to form a designed part. This pattern is usually defined based on the computer-aided design (CAD) model of the final product. Finally, the build platform is lowered opposite to the printing direction, and a new powder layer is deposited. This procedure is repeated until the part is completed.

Multiple specific techniques share the PBF operating scheme. However, the three most commonly used ones are Selective Laser Sintering (SLS), Electron Beam Melting (EBM)

and Selective Laser Melting (SLM). These methods are different by the powder which is used for manufacturing, by the origin and the intensity of the energy source, and by the manufacturing atmosphere. SLS process employs a lower laser power and operates in chambers filled with nitrogen to maximize oxidation. As in this technique the powder is not fully melted, it is often applied to produce polymer structures. By contrast, EBM and SLM allow to manufacture metal parts by fully melting the powder with a much stronger energy source. The difference between them is that the EBM process employs an electron beam, whereas the SLM process uses a laser beam. In this manner, much higher temperatures are reached, requiring a longer cooling time of the finished parts. As opposed to the SLM process, where the manufacturing happens in a chamber with an inert atmosphere, EBM occurs in a vacuum environment. One additional aspect of the EBM and SLM techniques is the need to introduce support structures. As the high energy source causes high thermal gradients, a structural distortion can arise due to residual stresses. Furthermore, the overhanging features often change their shape under gravity, which requires additional supports to preserve the designed geometry. Overall, SLM is cheaper than EBM and has fewer limitations on the produced parts. In the following, the primary focus is placed on SLM, or also called Laser Powder Bed Fusion (LPBF).

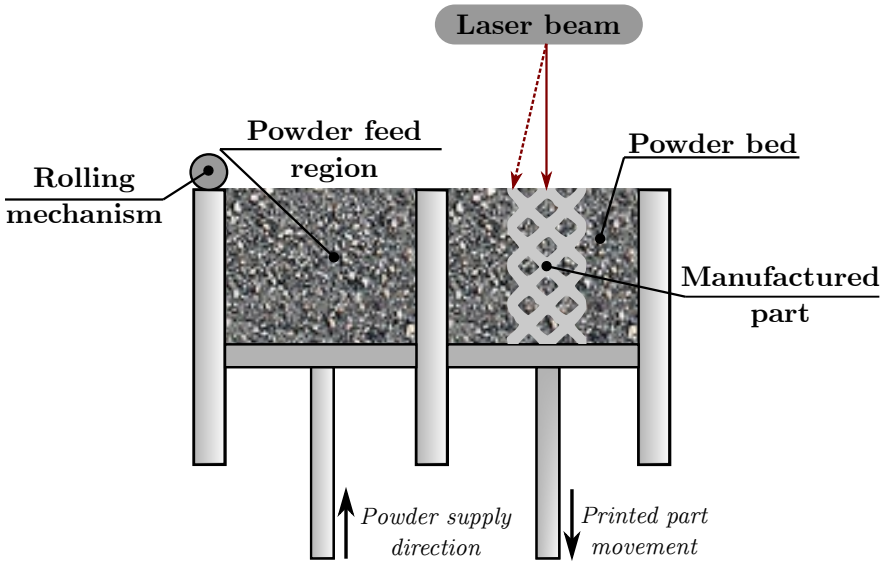

Figure 2.1: A scheme of Laser Powder Bed Fusion process.

The LPBF manufacturing technique has a few advantages and disadvantages. The main benefit, which makes this process so attractive to industry, is its material versatility and relatively low costs. With the SLM process, many Al-based, Ti-based, Cu-based or other alloys and their composites can be manufactured (see, e.g., [133, 102, 178]). Furthermore, this manufacturing process allows the production of high-quality complex structures [182]. On the downside, LPBF is a slow process primarily governed by the laser speed needed to produce a specific geometry. The limitations in the manufacturable part size and geometries are also rather specific for LPBF and are essential to consider. For example, the enclosed volumes or microarchitectured lattices at a microscopic scale are nearly impossible to produce with SLM due to the presence of trapped powder and other

physical phenomena [151]. Besides constraints on printable sizes of geometrical features and shapes, one further major limitation of this technique is the presence of geometrical and topological defects, often called *process-induced defects*. These defects are especially critical as the deviations in shape can significantly affect the final part quality.

There is a large variety of known process-induced defects in AM products. As the name indicates, they are caused by a combination of a few process parameters. Gibson et al. [51] propose to classify these process parameters in four groups:

- Laser parameters, such as e.g., laser power
- Parameters related to scanning technique (e.g., scan speed, hatch distances)
- Powder parameters (e.g., grain size, layer thickness)
- Temperature parameters (e.g., powder bed temperature)

Due to the nature of the underlying physics, all process parameters interact with each other and significantly impact the final shape. Thus, the optimization of these parameters is critical for improving the printing outcome. However, the process parameters are very sensitive to the used printer, material powder, printed parts and other conditions. Although a deeper understanding of these relations could allow to improve the quality of manufactured components significantly, process-induced defects would still not be negligible [103].

Process-induced defects are not only formed by diverse physical mechanisms and are different for particular materials and types of printed structures, but they also occur at different scales. For instance, the local material microstructure is strongly affected by the printing direction and the speed of the solidification process [176]. This can change the grain structure of the printed material and affect the mechanical behaviour of AM products. However, as mentioned in [176], a heat treatment procedure after manufacturing can alter the achieved properties at the cost of other mechanical characteristics. This defect can be especially significant for solid parts. Yet, for structures with complex microarchitectures, such as lattices, the geometrical process-induced imperfections have a more substantial effect on the manufacturing quality [41]. These are surface, internal porosity, lack of fusion, dimensional inaccuracies and manufacturability defects.

Surface defects occur in AM parts due to two main reasons: the unstable behaviour of the melt pool caused by the source energy density, and the general orientation of geometrical details with respect to the build platform. The former usually leads to balling and splatter of the material. The melt pool dynamics can also produce discontinuities between the layers, i.e., stair stepping [40]. The latter requires to distinguish between the down-skin (normal towards the build platform) and up-skin surfaces. The down-skin surfaces are in contact with the unmelted powder bed (see Figure 2.1). As often they experience overheating, the unmelted powder particles fuse with the surface and remain attached after completing the printing process [103]. When lattice structures are printed, the increase of the inclination angle can hinder this effect [148].

Internal porosity and *lack of fusion defects* can occur in the final structures because of an inadequate choice of power density, cooling rates or printing strategies, as well as gas entrapment in the powder. For example, to improve the speed of the LPBF process, machines are set to operate at very high power densities and deposition rates. This, in turn, causes collapses of keyholes or insufficient melting of subsequent layers,

leading to internal porosity formation [30]. The pores can also be formed due to the gas entrapment caused by high cooling rates or gaps in the powder bed [40]. Such defects, especially insufficient melting, can propagate through the layers causing large pores or even breakages.

Dimensional inaccuracies are often observed at the same scale as microstructural geometries. They are usually driven by the residual stresses causing warping or shrinkage [54], attachment of the unmelted powder or material collection at specific locations. These effects cause geometrical discrepancies between design and printing outcome, influencing the quality of manufactured structures (e.g., [171, 98]). The most common dimensional inaccuracies in lattices are strut waviness, changes in shape and size of the strut cross-section, and node material accumulation [40]. The size and the magnitude of these defects can largely deviate and is utterly hard to control. Especially when the microstructure of the printed parts is complex, these geometric defects can impact the mechanical behaviour of these parts, e.g., resulting in a significant reduction of stiffness [103].

Finally, the *manufacturability* of the designed shapes is a crucial point to remark. Not all possible dimensions of geometrical parts can be printed without a significant loss of quality. Although a particular choice of process parameters can allow considerable design freedom, the minimum printable strut size has been reported to be 300μm [131]. Moreover, when structures have an inclination angle to the printing bed, there is a limit on the maximum possible angle, until which the parts can be printed without additional structural supports. However, lattices are usually not manufacturable with supports. This is since the support removal on the post-processing stage becomes practically infeasible from the internal microstructure.

Undoubtedly, the defects mentioned above affect the result of a printing, putting a significant uncertainty on the final product confidence levels. To be applicable and standardized for many industrial applications [151], AM parts should be evaluated on the presence of such defects and assessed for possible application areas. To achieve this, the first question to be answered is how to detect these defects. Traditional approaches do not suffice to provide comprehensive information about the internal structure of AM parts, thus, bringing up the first significant challenge on finding an appropriate technique to acquire the manufactured geometries.

2.2 As-manufactured geometries acquisition via computed tomography

Destructive and non-destructive methods can be applied to assess process-induced geometrical defects. As the AM imperfections are specific for different structural designs, process parameters and post-treatment techniques, the destructive approach is rather unfavourable. In this way, many possible combinations of influencing factors would have to be investigated. Thus, non-destructive methods to analyze the as-manufactured AM shapes have become especially popular (e.g., [37, 41, 137]).

An overall classification of the existing methods is shown in Figure 2.2. A more thorough overview of non-destructive testing techniques can be found in [10]. From this classification, a very attractive approach could be optical or scanning microscopy, which was also

extensively applied to the analysis of AM structures (see, e.g., [3, 137, 146, 155]). These techniques provide a high resolution allowing to detect even the smallest process-induced defects. However, they only provide observable surface information, thus, requiring to destroy the products with internal microstructure. For lattices it is crucial to assess all effects, especially the ones arising in the areas inaccessible to surface measurements. Thus, the most attractive approach is X-ray computed tomography (CT) (see Figure 2.2).

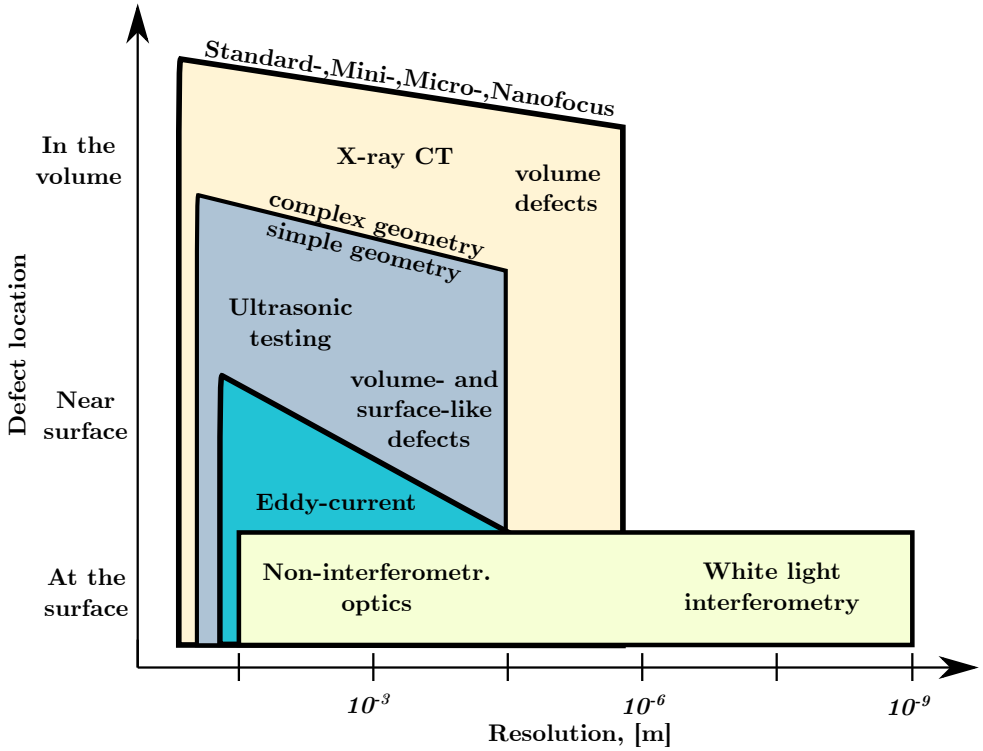

Figure 2.2: Methods for defect detection in manufactured geometries (adapted by permission from Springer Nature Customer Service Centre GmbH: Springer Nature, The Journal of The Minerals, Metals & Materials Society [151]).

CT scans are known initially from medical applications but have also been extensively applied in metrology and in the field of additive manufacturing [36, 37, 40, 179]. In this approach, two-dimensional cross-sectional images with a predefined resolution are acquired by measuring attenuation coefficients of a scanned body [109]. These attenuation coefficients are then converted to so-called *Hounsfield Units (HU)*. The result of this procedure is a set of grey-scale two-dimensional images approximating the boundaries of a scanned object. An example of such 2D image is shown in Figure 2.3. The resolution of acquired images is entirely defined by a *scan resolution*, or a *voxel size*, a three dimensional smallest spatial block over which the acquired data is averaged. The main advantage of this technology is the possibility to capture all geometrical defects discussed in section 2.1. The only limiting factor is the possible CT scan resolution, as features smaller than the voxel size cannot be detected. However, the provided span of possible scan resolutions is rather large and is sufficient for most industrial applications. This aspect makes computed tomography a preferable choice for the acquisition of the as-manufactured geometry.

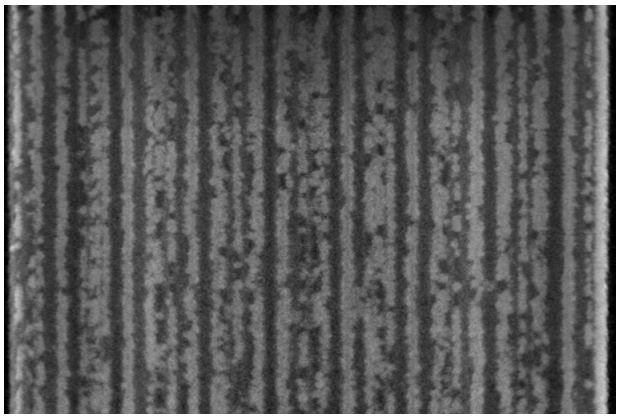

Figure 2.3: An example of a two-dimensional slice of CT scan of a metal lattice structure.

Nonetheless, there is a major challenge arising when CT methods are applied to assess the process-induced defects of AM products. As shown in Figure 2.3, the image slices do not provide exact information about the object's geometrical boundary. Instead, a grey-scale distribution is achieved. Thus, to reliably identify the location of the geometrical boundaries, an *image segmentation* technique is required.

The process of image segmentation is well-established in the field of medical imaging. Although the main application area of this work is metal CTs, algorithms similar to those established for medical imaging can be applied. One of the most straightforward techniques to detect the geometrical boundary is the *single threshold technique* (see, e.g., [122] and the literature cited therein). When CT scans of metal materials or other one-material objects are obtained, the contrast of the acquired images is very high, i.e., there is a large difference between the HU in the material and non-material areas. This is also true for multiple materials when their attenuation properties are further apart from each other. For one-material objects, the CT images have a bimodal histogram of the HU values. Thus, the object's geometrical boundary can be obtained by setting a single threshold HU_{thres}. All other HU values above (or below) correspond to the material, while the rest represent voids. To simplify the identification technique of HU_{thres}, multiple mathematical approaches can be employed. For bimodal histograms, *Otsu's global thresholding technique* is recommended [122]. This provides a reasonable estimate of the necessary value relying on the fact that the CT image histogram has two large HU units clusters. Of course, there is a particular transition area that justifies a slightly varying HU_{thres}. However, the determined threshold values can be used "as is" without any necessary modification.

Still, it is well known that different artefacts can be encountered in the CT images [15]. Ring artefacts, noise, beam hardening, etc., can obscure geometrical boundaries and make the single threshold technique inapplicable. Another critical obstacle is the presence of trapped powder in the enclosed volumes, as mentioned in section 2.1. The attenuation properties of the melted metal and its powder are similar. Consequently, they result in very close HU values in the CT scan challenging the single thresholding technique. Furthermore, the CT image acquisition of metal objects can lead to the presence of severe metal artefacts. They arise due to the high attenuating material properties of the metal itself and the metal edges [14, 105]. The question of artefacts reduction for a better reflection of the real objects is a separate research area. Many different methods, e.g.,

projection completion strategies, multidimensional adaptive filtering, or the metal deletion technique, were introduced ([15, 76, 134] and the literature cited therein). However, to overcome these challenges in the scope of this work, an alternative *deep learning segmentation* technique is proposed. This approach allows preparing the CT images to the single thresholding technique, such that no geometrical boundaries are obscured. In the following, the proposed method is briefly explained.

2.3 CT image segmentation using Convolutional Neural Networks[e]

Artificial Neural Network (ANN) is today's best-known tools of artificial intelligence and machine learning. ANNs are widely used in a variety of ways when a task is needed to be learnt. A Convolutional Neural Network (CNN) [88] is different from the structure of other neural networks since CNN's include mainly image processing functions and can also handle different types of input (e.g., image, video, voice). A typical use case of CNNs is to provide image data to the network as input and, based on this information, to perform the necessary classification.

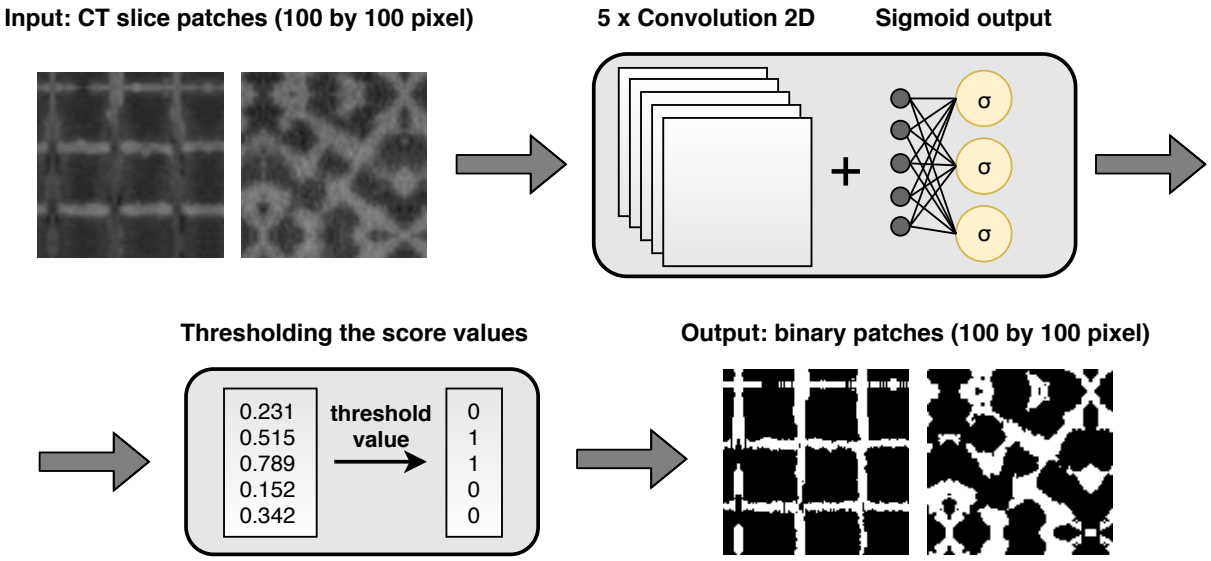

Figure 2.4: Segmentation pipeline of CT scans of microarchitectured metal structures.

For the segmentation of CT image slices which inhibit the imaging artefacts, a U-Net-based [143] deep convolutional network is adopted. Figure 2.4 summarizes the main stages of the proposed segmentation approach. The proposed network consists of 6 blocks containing convolutional, max-pooling, dropout and merge layers. An overview of these convolutional layers (depicted in Figure 2.4) can be seen in Figure 2.5. The type of operation and the number of convolutional kernels are noted above the boxes. The height, width and depth of the boxes are representative of the convolutional layers' output shape. Such architecture is implemented in Keras [22]. To activate the layers, the Rectified Linear Unit (ReLU) activations are utilized, except for the last layer where a sigmoid

function is used. For optimization, an adaptive moment estimation (Adam) [82] with a binary cross-entropy loss function is employed. Depending on the task, three or four original two-dimensional CT slices are required. They usually contribute to less than 1% of the overall CT scan size. To this extent, these slices have to be manually segmented to provide labeled data, so called gold standards, for the CNN. The training data is then formed by these few original grey-scale CT slices and the corresponding gold standard binary masks. The test dataset consists of the remaining non-segmented slices of the CT scan.

To further increase the number of training images, the input data is cut into pixel patches of size $n \times n$, where n is chosen from a certain interval such that the remainder of the integer division $image\_width/n$ is minimum. After the classification, the CT slices are reassembled from the patches. Since some false negatives and false positives may appear on the patches outer parts, they are padded on all sides to have a result of 100×100 pixel size. The specimen may contain some powder in it, which has a very similar intensity to the foreground pixels, so that it might cause wrong classification results on a pixel level. Thus, some patches – in which powder is present – are shown twice to the neural network to overcome this problem.

The network output is a probability distribution, where the resulting values are expected to be very close to 0 or 1, so they can be interpreted as binary pixel values. As a post-processing step, a single thresholding technique is applied.

Finally, either the single threshold or the deep learning segmentation technique can be applied to determine the scanned object's geometrical boundary. To this extent, the CT images provide comprehensive information about a large variety of geometrical process-induced defects discussed in section 2.1. Although CT images do not give information on features smaller than the scan resolution or about the effects of the change in the material grain microstructure, they help to identify the manufacturing imperfections and compare the as-manufactured geometries to the as-designed ones.

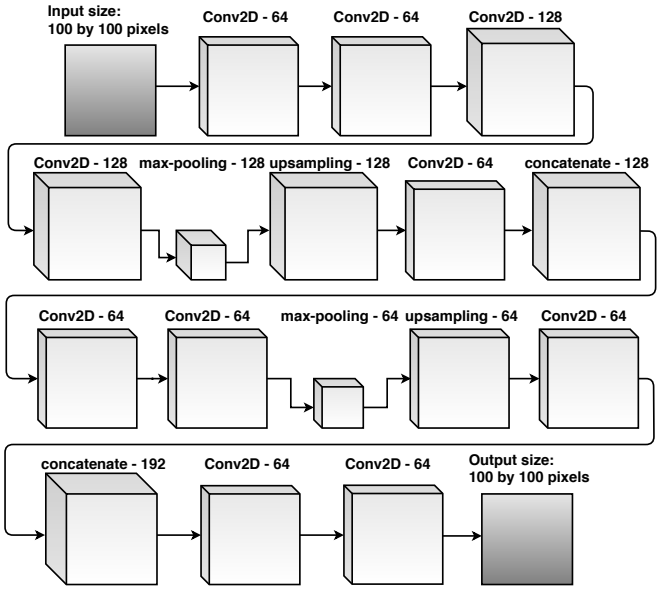

Figure 2.5: An overview of the convolutional layers of the U-Net network.

2.4 Numerical characterization of AM products

The assessment of the process-induced defects with the help of the techniques described in the previous sections can help to understand how the process parameters affect the printing result and imperfections. But this information is not sufficient to describe the *effects of defects* on the performance of the final products. A traditional approach would be to collect this data through many experimental tests on manufactured sample products. However, the process-induced defects differ significantly from one structure to another. Thus, a large number of all possible combinations of these parameters would be required to characterize the effects of occurring imperfections altogether. Furthermore, some defects can be critical for one application while well-accepted in another. For example, surface roughness is typically not desirable in engineering, but can be advantageous in biomedical applications [136]. Also, the pores' criticality or dimensional inaccuracies could be potentially more significant when structures are loaded in shear rather than in tension. For these reasons, the numerical analysis of the AM products became especially attractive.

The key in numerical AM products characterization is to define the overall properties of final products establishing the possible application areas. For example, typical required mechanical quantities are Young's modulus, bending rigidity, yield strength, fatigue limits, or other specific properties for different applications, such as e.g., thermal conductivity or permeability. Apart from these fundamental characteristics, the overall behaviour under various loading conditions is often required. Undoubtedly, the incorporation of imperfect AM geometries into numerical analysis delivers a better prediction of these properties (e.g., [26, 50, 95, 98, 101, 175]).

There are two main approaches to incorporate geometrical information from CT scans into the numerical analysis[f]: a full 3D model reconstruction from the obtained CT data (e.g., [26, 65, 50, 175]) and a statistically equivalent CAD model generation based on the detected imperfections (e.g., [95, 98, 101]). Both methods encounter three main challenges. First, the reconstruction of a 3D model from a CT scan is quite demanding since it requires a lot of manual effort before the analysis [26]. Second, a boundary conforming mesh, needed for the numerical analysis, is not trivial to generate. Finally, due to lattices' complex geometrical features, a numerical study of these structures is generally computationally expensive. Hence, most of the research focuses on incorporating a specific set of geometrical defects, limiting it to, e.g., strut waviness and strut diameter variation, or reducing the computational domain to a smaller size.

The next challenging task is to choose an appropriate numerical analysis type. The most versatile and complex technique to analyze the imperfect AM structures is to perform three-dimensional (3D) Finite Element Analysis (FEA). In the following, it will be referred to as *Direct Numerical Simulation (DNS)*. A full structure is analyzed with this method numerically under predefined loading. For example, experimental tensile testing can be repeated numerically to obtain an overall Young's modulus of the structure. This approach can provide the most realistic approximation of the AM product behaviour. Furthermore, DNS can be theoretically applied to any kind of physics, e.g., to analyze lattices' thermal behaviour. This technique is currently considered highly computationally demanding for numerical analysis of lattices with small-scale details. To address these issues, beam elements are often used (e.g [26, 95, 98]) even though the 3D solid models remain the

most accurate.

Thus, for these kinds of structures, *numerical homogenization* methods are often preferred to the DNS of the considered experimental setup. This approach evaluates the macroscopic behaviour of the structure by considering a Representative Volume Element (RVE). In general, this method is especially efficient when highly complex geometries need to be analyzed. It can be applied to cheaply determine the linear elastic characteristics, thermal or permeability quantities of a full structure. However, when the imperfections are highly irregular, or the structures become non-periodic with a high voids content, this approach faces multiple challenges on the boundary conditions applications. In particular, the question of a RVE existence, which represents the behaviour of the whole structure, arises.

To reduce the computational costs even further[c], one-dimensional (1D) beam theories can be employed. This technique represents an engineering extreme, as it provides a quick approximation to the structure's mechanical behaviour. However, the conventional continuum beam theories are not necessarily applicable to evaluating imperfect lattice components' effective behaviour. They strongly rely on the assumption of the separation of scales, i.e., the microstructural characteristic length should be much smaller than the representative volume element's size. Nevertheless, it has been determined experimentally and numerically that conventional continuum models cannot describe these components, such as e.g. by using Euler-Bernoulli or Timoshenko beam theories. They are mostly inapplicable when the periodic cell size approaches the typical wavelength of the macroscopic mechanical fields' variation. Such deviations are typically referred to as size effects. These effects can arise at different scales. When lattice or foam-like structures are considered, size effects can occur at the scale of millimetres [125]. If this scale is comparable to the component dimension, size effects are crucial for evaluating the part's behaviour. In metamaterials, size effects become especially pronounced when the corresponding structures are loaded in shear or bending [181]. For example, when lattice beams are considered, the relative bending rigidity increases significantly when the size of the lattice's representative cell approaches the thickness of the beam structure. This occurs when the beam structure is composed of very few layers of lattice cells in the thickness direction [79, 80].

Having these characterization methods at hand, a predictive assessment of final AM parts' behaviour can be performed. Although this is already a crucial step towards understanding the effects of the process-induced defects in manufactured components, it is also essential to evaluate the variability they can cause in the final properties. For example, when a lattice structure is printed multiple times with fixed process parameters and the same machine, should a variability in the final Young's modulus be expected? Or how does this variability change with the scale of the produced lattice?

There is a wide amount of research also going towards this direction (e.g., [20, 21, 95, 98])[d]. A general focus is placed on a statistical analysis of the process-induced defects and their consequent incorporation into a CAD model for facilitating the subsequent numerical analysis. The former is typically achieved by statistical modelling of certain defects. Yet, only single imperfections or a combination of a few is commonly incorporated. A flexible description of many of the occurring geometrical and topological variations can be very challenging within this approach.

2.5 Proposed workflow

The challenges mentioned in sections 2.1, 2.3 and 2.4 are addressed in this thesis by proposing an image-to-numerical-characterization workflow. In this scheme, as-designed and as-manufactured traditional numerical characterization approaches are marked with black arrows, while the proposed workflow is visualized with green lines in Figure 2.6.

First of all, to overcome tedious steps of traditional boundary conforming FEA on CT scans, an immersed boundary method, the Finite Cell Method (FCM) [39], is employed. This approach separates the geometrical representation from the applied discretization, thus, eliminating the necessity of 3D geometry reconstruction from CT images and simplifying the mesh generation process. It allows performing the numerical analysis directly on CT images of imperfect geometries without further additional steps. The only essential requirement is the availability of CT segmentation. The proposed deep learning segmentation or a simple thresholding technique described in section 2.3 provide a solid basis for this method.

Although the Finite Cell Method in its core provides an effective solution to the numerical analysis on non-standard geometries, such as CT scans, one more challenge needs to be considered. Process-induced defects, especially on AM lattices, can have a significantly smaller size than the overall structural size. The numerical models of these geometries are still very large. Thus, in this thesis, a parallel version of the Finite Cell Method with an efficient integration technique is introduced. This approach is specifically tuned for analyzing CT-based microarchitectured geometries allowing for fast and efficient evaluation of mechanical effects of process-induced defects.

In this image-to-numerical-characterization workflow, both the direct numerical simulation of full AM structure and numerical homogenization is feasible. Special treatment of the manufactured microstructure's occurring randomness is further introduced in a particular CT-based computational homogenization approach of this thesis.

The proposed workflow also allows incorporating beam models for fast estimation of the required mechanical behavior[c]. To this extent, the strain gradient extensions of the classical continuum models are introduced [4, 169, 168, 119, 79, 80]. They are proven to be accurate in predicting the mechanical behaviour of size-dependent lattice structures. These beam theories are especially relevant when additively manufactured lattices are analyzed as the produced scales are relatively small.

Finally, the image-to-numerical-characterization workflow includes[d] a CT-based approach to incorporate process-induced defects in lattice structures into an uncertainty analysis of the final product's mechanical behaviour. The presented method does not require an ideal CAD model of the considered lattice. It employs a non-homogeneous binary random field model to efficiently generate three-dimensional CT-based statistically equivalent realizations of the imperfect AM products without limitations on the occurring type of geometrical imperfections.

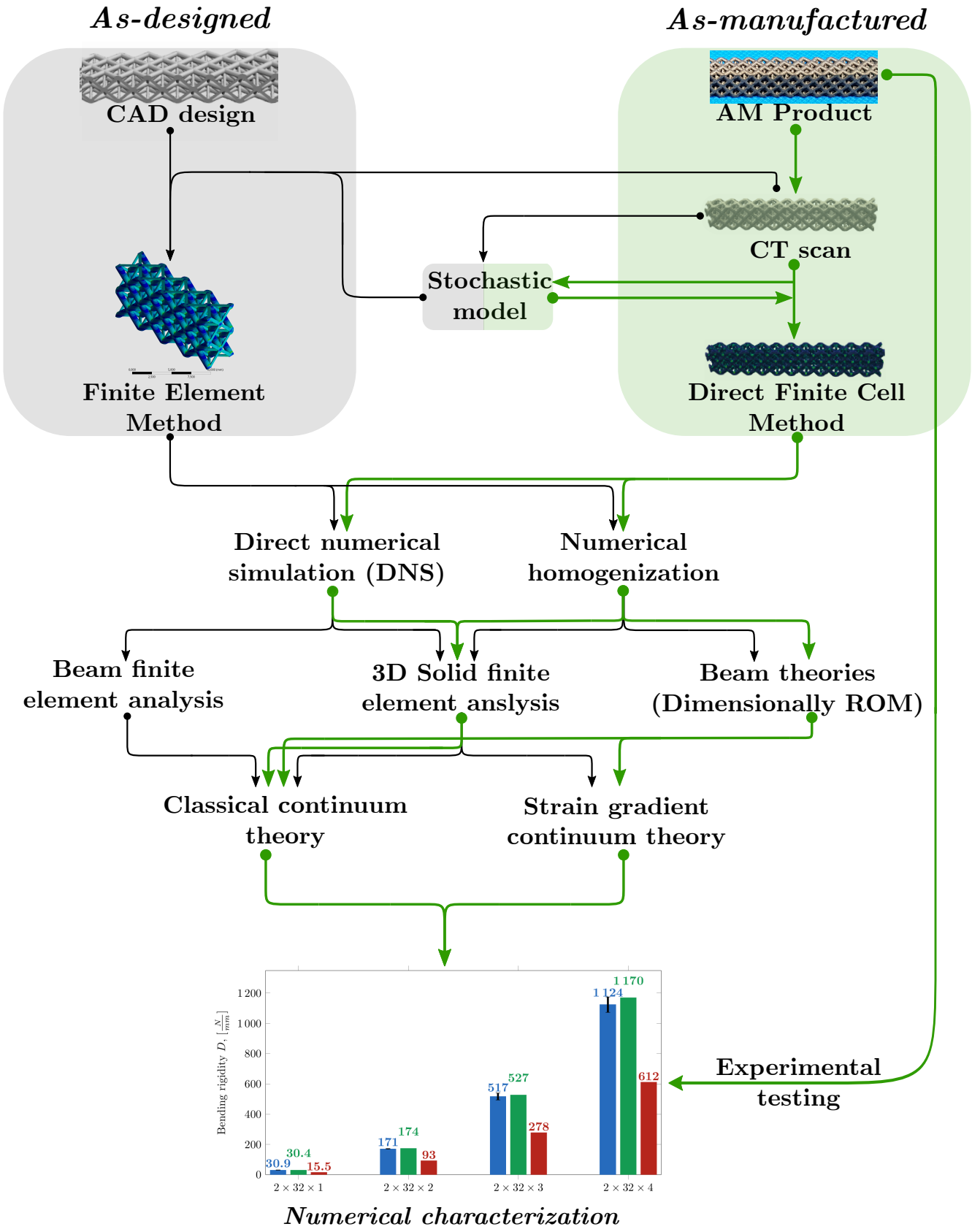

Figure 2.6: Image-to-numerical-characterization workflow of imperfect additively manufactured structures[f].

Chapter 3

Two engineering extremes: direct numerical simulation and beam theories

The most basic and the most common test to characterize the behavior of newly produced materials or parts is to determine their Young's modulus. To achieve this, a tensile experiment is usually performed.

Figure 3.1: Example of a tensile experiment on manufactured AM lattice structure [86].

However, these conditions can also be simulated numerically on a geometrical representation of the same structure as shown in Figure 3.2. A field of continuum mechanics provides fundamental means to create a mathematical model of this physical phenomena. To this extent, all bodies are assumed to be composed of a continuous medium without

any gaps or empty spaces. This assumption disregards molecular structure of matter and is, thus, valid for length scales greater than inter-atomic distances [104]. Then, by applying the loads similar to the experimental setting, a comprehensive mathematical description can be established. In the following, only the key steps to achieve this are recapitulated. A more thorough explanation and necessary derivations can be found in a large amount of literature (e.g., [16, 69, 100, 104]).

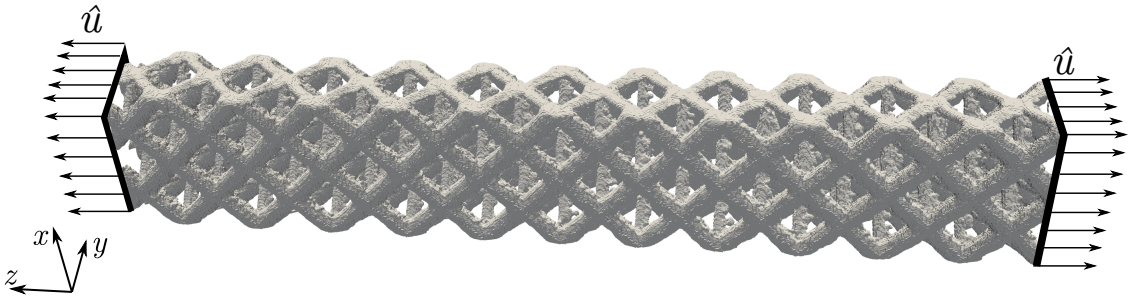

Figure 3.2: Numerical setup of a tensile experiment on manufactured AM lattice structures.

Although such a mathematical model provides an extensive description of a bodies' physical behavior under certain conditions, the solutions to these problems usually cannot be established in a closed-form. A standard approach to obtain these solutions is by using the Finite Element Method (FEM). As this approach is well-established, only the fundamental points are mentioned in this chapter to prepare for a discussion on an immersed method to solve these equations in the next chapter.

All things considered, a virtual experiment based on classic continuum theory provides accurate results for most engineering examples. However, when the structures possess microarchitecture such as considered lattices, their mechanical response under specific loading can differ for small and large specimens. These so-called size effects bring the classical continuum theory to its boundaries, as the mathematical models became inaccurate. To represent such effects, a strain gradient continuum theory can be introduced [9, 79, 119, 70]. In section 3.2, the most significant differences with classical continuum theory are briefly discussed.

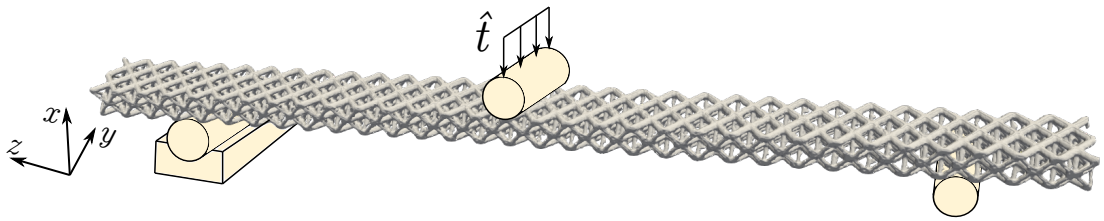

Figure 3.3: Numerical setup of a bending experiment on manufactured AM lattice structures.

These size effects are especially pronounced when the bending characteristics of lattice structures are determined. In particular, for a three-point bending experiment as depicted

in Figure 3.3, the lattices can exhibit much larger bending rigidities when the height of the specimen approaches the characteristic size of the geometrical details. Although one can expect that a full direct numerical simulation of this setup can provide an accurate and realistic solution of the complex mechanical behavior often, a fast prediction is essential for an early analysis stage. One of the approaches to obtain this quick solution is to use beam theories. On that account, the fundamental simplifications of both classical and strain gradient continuum theories are discussed.

3.1 Direct numerical simulation using classical continuum theory

Kinematics

Suppose an elastic body with volume Ω and boundary Γ moves from its original configuration to a deformed state $\chi(\Omega)$ with boundary $\chi(\Gamma)$ as depicted in Figure 3.4. Then, the difference between an initial and current position of a material point of this body is expressed by a *displacement vector* $\boldsymbol{u}$ as

$$\boldsymbol{u} \equiv \boldsymbol{x} - \boldsymbol{X} \tag{3.1}$$

with $\boldsymbol{x} = (x, y, z)$ being a cartesian coordinate vector of a spatial point in deformed configuration and $\boldsymbol{X}$ a coordinate vector in initial configuration.

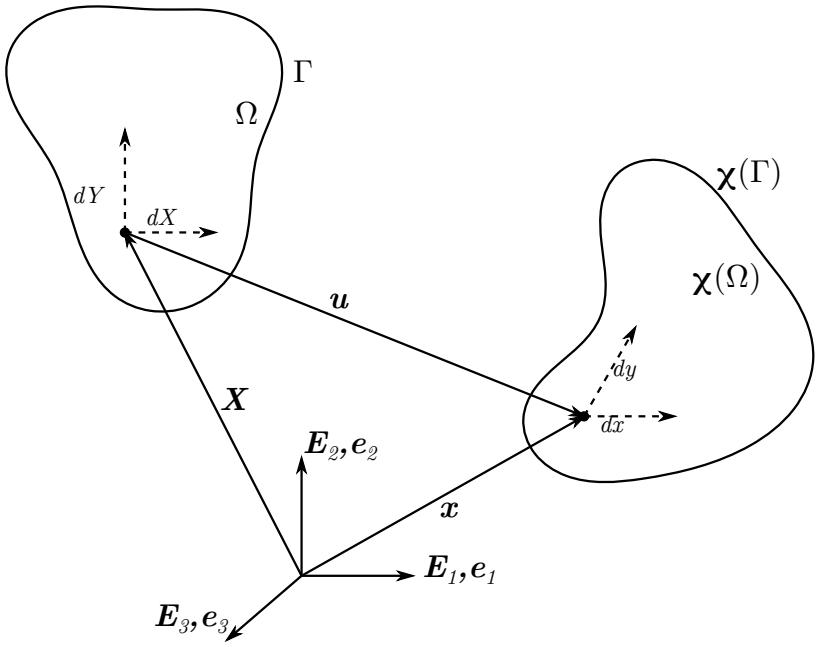

Figure 3.4: Motion of material point in classic continuum: $\boldsymbol{E}$ and $\boldsymbol{e}$ indicate the Cartesian unit vectors in initial and deformed configurations respectively.

To indicate an instantaneous direction of this motion and establish the mapping between

the initial and reference configurations, a *deformation gradient tensor* $\boldsymbol{F}$ is defined:

$$\boldsymbol{F} \equiv 1 + \nabla_X \boldsymbol{u} \tag{3.2}$$

where ∇ denotes the vector differential operator with respect to initial or current configuration as

$$\nabla_{\boldsymbol{X}}(\cdot) \equiv \frac{\partial(\cdot)}{\partial \boldsymbol{X}} \quad \text{and} \quad \nabla_{\boldsymbol{x}}(\cdot) \equiv \frac{\partial(\cdot)}{\partial \boldsymbol{x}} \tag{3.3}$$

In this work, the small deformation theory is employed, as the displacement of every material point of body Ω is assumed to be much smaller than its representative dimensions. Thus, the distinction between the reference and current configuration is not necessary and $\nabla_{\boldsymbol{X}}(\cdot) \approx \nabla_{\boldsymbol{x}}(\cdot) \equiv \nabla(\cdot)$.

However, for engineering applications, a different measure of deformation is often preferred. The *Green-Lagrange strain* $\boldsymbol{\varepsilon}$ is a common choice, as a rigid body motion imposed on the body would not lead to any non-zero strain components. Following the same assumption of the small deformation theory, i.e., $|\nabla \boldsymbol{u}| << 1$, the strain tensor can be defined as follows:

$$\boldsymbol{\varepsilon} \equiv \frac{1}{2}\left(\nabla \boldsymbol{u} + \nabla^T \boldsymbol{u}\right) \tag{3.4}$$

Constitutive relations

In response towards an action of surface forces $\boldsymbol{t}$ or body forces $\boldsymbol{b}$, an internal force distribution, or *stresses*, arise. The relation between stress and strain in the body can be defined through a *strain energy density function* $\mathcal{W}$ [53]. Assuming linear elastic material this quadratic function is only the function of strain [55]:

$$\mathcal{W}(\boldsymbol{\varepsilon}) = \frac{1}{2}\boldsymbol{\varepsilon} : \boldsymbol{C} : \boldsymbol{\varepsilon} \tag{3.5}$$

where $\boldsymbol{C}$ is the fourth-order elasticity tensor. Then, the Cauchy stress tensor $\boldsymbol{\sigma}$ is defined as work conjugate to the strain tensor as

$$\boldsymbol{\sigma} = \frac{\partial \mathcal{W}(\boldsymbol{\varepsilon})}{\partial \boldsymbol{\varepsilon}} = \boldsymbol{C} : \boldsymbol{\varepsilon} \tag{3.6}$$

The elasticity tensor $\boldsymbol{C}$ can represent various degrees of material symmetry, i.e., the variation of the material's properties with respect to a direction at a fixed point in the structure. In a fully *anisotropic* case, this tensor has 21 independent characteristics. When the body possesses similar material properties in all directions, the behavior is called *isotropic*, and the tensor has only two independent coefficients. In this work, all structures are considered to be linear elastic with isotropic material symmetry. However, when the homogenized properties are analyzed, the effective material symmetry can change, which will be further discussed in chapter 5.

Boundary value problem

In the following, inertia effects are neglected. Thus, applying the law of conservation of linear momentum, the Cauchy's equations of equilibrium for elastostatics read:

$$\nabla \cdot \boldsymbol{\sigma} + \boldsymbol{b} = 0 \qquad \text{on} \quad \Omega \tag{3.7}$$

However, these equilibrium equations are incomplete without *Boundary Conditions (BCs)* to model a physical problem drafted in Figures 3.2 and 3.3. Usually the primary unknowns are displacements $\boldsymbol{u}$ that occur in the body under specific loading. Thus, the following boundary conditions are additionally formulated:

$$\begin{aligned} \boldsymbol{\sigma} \cdot \boldsymbol{n} &= \hat{\boldsymbol{t}} \qquad \text{on } \Gamma_N \\ \boldsymbol{u} &= \hat{\boldsymbol{u}} \qquad \text{on } \Gamma_D \end{aligned} \tag{3.8}$$

where $\boldsymbol{n}$ is the outward unit normal vector on Γ, $\hat{\boldsymbol{u}}$ and $\hat{\boldsymbol{t}}$ are prescribed displacement and tractions, Γ_D indicates a part of the domain boundary where Dirichlet conditions are applied, while Γ_N refers to Neumann domain boundary such that $\Gamma = \Gamma_D \cup \Gamma_N$ and $\Gamma_D \cap \Gamma_N = \emptyset$.

The Finite Element Method

Equations 3.7 and 3.8 can be solved numerically using the Finite Element Method [71]. This method requires to transform the strong formulation of the elastostatic problem into a *weak form*. The most commonly used weak form reads as follows:

$$\text{Find } \boldsymbol{u} \in \mathcal{S} \text{ such that } \mathcal{B}(\boldsymbol{v}, \boldsymbol{u}) = \mathcal{F}(\boldsymbol{v}) \;\; \forall\, \boldsymbol{v} \in \mathcal{V} \tag{3.9}$$

where $\boldsymbol{v}$ is the test function. The bilinear form $\mathcal{B}(\cdot,\cdot)$ and the linear form $\mathcal{F}(\cdot,\cdot)$ are defined as:

$$\begin{aligned} \mathcal{B}(\boldsymbol{v}, \boldsymbol{u}) &= \int_\Omega \boldsymbol{\varepsilon}(\boldsymbol{v}) : \boldsymbol{C}(\boldsymbol{x}) : \boldsymbol{\varepsilon}(\boldsymbol{u})\, d\Omega \\ \mathcal{F}(\boldsymbol{v}) &= \int_\Omega \boldsymbol{v} \cdot \boldsymbol{b}\, d\Omega + \int_{\Gamma_N} \boldsymbol{v} \cdot \hat{\boldsymbol{t}}\, d\Gamma_N \end{aligned}$$

The function spaces $\mathcal{S}$ and $\mathcal{V}$ are defined as follows:

$$\begin{aligned} \mathcal{S} &= \{u_i \in H^1(\Omega) : u_i = \hat{u}_i \;\; \forall \boldsymbol{x} \in \Gamma_D\} \\ \mathcal{V} &= \{v_i \in H^1(\Omega) : v_i = 0 \quad \forall \boldsymbol{x} \in \Gamma_D\} \end{aligned} \tag{3.10}$$

where $H^1(\cdot)$ denotes the Sobolev space of degree one [71].

The probably most well-known approach to approximate these equations numerically is the Galerkin approach [71]. In this approach, the function spaces $\mathcal{S}$ and $\mathcal{V}$ are approximated by finite dimensional subspaces $\mathcal{S}^h \subset \mathcal{S}$ and $\mathcal{V}^h \subset \mathcal{V}$ respectively. These subspaces are characterized by a finite element mesh, the elements' polynomial degrees, and the

mapping functions [160]. Then, an approximated solution to Equation 3.9 can be determined by solving the following finite dimensional problem:

$$\text{Find } \boldsymbol{u}_{FE} \in \mathcal{S}^h \text{ such that } \mathcal{B}(\boldsymbol{v}^h, \boldsymbol{u}_{FE}) = \mathcal{F}(\boldsymbol{v}^h) \;\forall\, \boldsymbol{v}^h \in \mathcal{V}^h \tag{3.11}$$

where $\boldsymbol{u}_{FE}$ is an approximation to $\boldsymbol{u}$ and $\boldsymbol{v}^h$ are the finite dimensional trial functions [159].

The quality of the finite element approximation is determined by the finite element space, the elements' polynomial degree p and the mapping functions. The finite element space can be defined by different sets of basis functions, also called *shape functions*. They should be hierarchic, have a minimum number of shape functions vanishing at vertices, edges and faces, and should be constructed such that the underlying polynomial functions fulfill certain orthogonality properties [160]. In this thesis, the integrated Legendre polynomials are used [39, 159]. Compared to the classical shape functions defined by the set of Lagrange polynomials, the integrated Legendre polynomials do not lead to a drastic increase of stiffness matrix condition number when the polynomial degree p is elevated. Furthermore, the set of basis functions of polynomial degree $(p+1)$ includes the set of shape functions of polynomial degree p [160].

To improve the finite element approximation of the solution, the finite elements spaces can be enlarged using multiple strategies. In this work, the following three methods are considered [39, 160]:

- $h-$refinement: the polynomial degree of the elements p is kept constant while reducing the size of the used elements.
- $p-$refinement: the polynomial degree of the elements p is progressively increased while keeping the element size constant.
- $hp-$refinement: the polynomial degree of the elements p is progressively increased while reducing the element size.

The choice of these methods depends on the nature of the solution to be approximated. Although the $h-$refinement is probably the most commonly used method, the numerical approximation converges to the analytical solution at a comparably slow rate. The $p-$refinement can lead to a faster convergence especially for smooth problems. However, when non-smooth problems are considered, such as, e.g., in the presence of singularities, the convergence of the latter method decays and is only slightly better than the convergence of the $h-$refinement. In this case, the $hp-$refinement provides a significantly higher accuracy for the same number of unknowns [184].

Summary

All in all, these aspects complete the necessary fundamental formulation of a direct numerical simulation. Equation 3.9 can be solved numerically by applying a different set of boundary conditions. For example, in the case of a virtual tensile experiment as shown in Figure 3.2 Dirichlet boundary conditions are employed on both sides of the specimen, whereas no traction is prescribed. In the case of a bending experiment as depicted in Figure 3.3 both Dirichlet conditions at the supports and non-homogeneous Neumann condition are necessary to impose. Other types of direct numerical simulation can require to derive other types of constitutive relations. For example, the continuation of a tensile

experiment in the non-linear regime would require plasticity laws in the direct numerical simulation. Nonetheless, the derivations and fundamentals are somewhat similar and can be found in the textbooks.

3.2 Direct numerical simulation using strain gradient continuum theory

Kinematics

In contrast to the classical continuum theory, strain gradient theory introduces an additional micro-volume Ω' with boundary Γ' attached to every material point as shown in Figure 3.5.

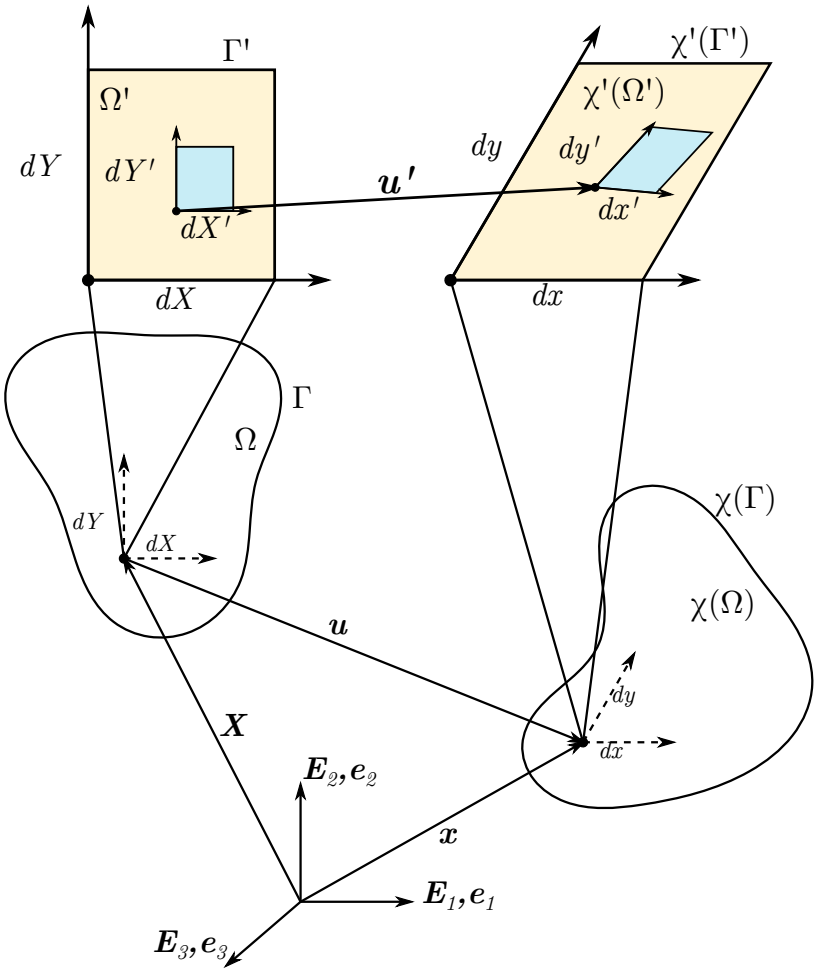

Figure 3.5: Motion of material point and micro-volume in strain gradient continuum.

In this frame, the initial micro-point coordinate $\boldsymbol{X}'$ is pushed to its deformed configuration $\boldsymbol{x}'$ with the help of micro-deformation mapping χ'. Analagously to the classical kinematic relation, the micro-displacement vector $\boldsymbol{u}'$ is then defined as follows:

$$\boldsymbol{u}' \equiv \boldsymbol{x}' - \boldsymbol{X}' \tag{3.12}$$

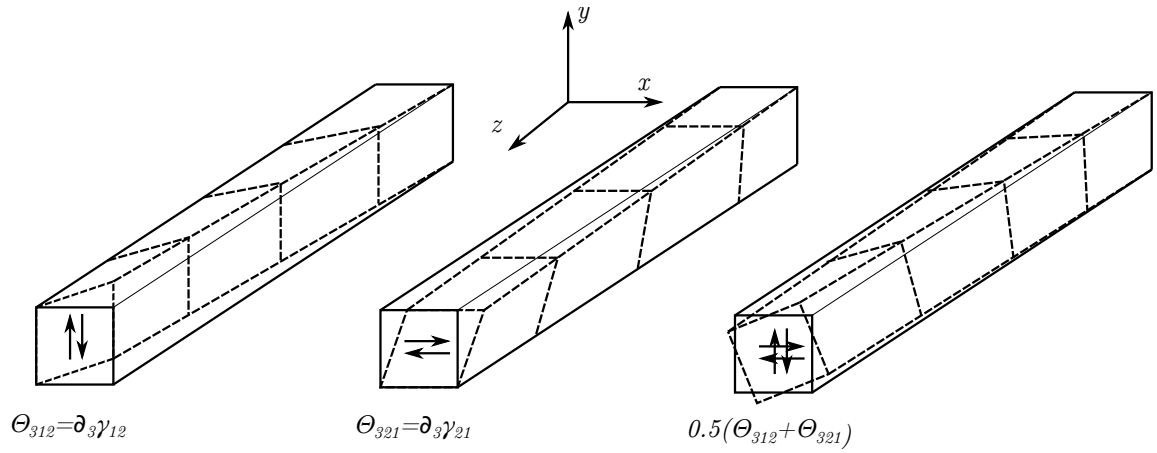

Figure 3.6: An example of micro-deformations (adapted by permission from Springer Nature Customer Service Centre GmbH: Springer Nature, Archive of Rational Mechanics and Analysis [110]).

The micro-deformations are also assumed to be small. Thus, the micro-strain tensor $\boldsymbol{\gamma}$ can be formulated as

$$\boldsymbol{\gamma} \equiv \frac{1}{2}\left(\nabla' \boldsymbol{u}' + (\nabla' \boldsymbol{u}')^T\right) \tag{3.13}$$

with ∇' being the vector differential operator in micro-coordinates. Apart from defining the microscopic kinematic relations, one additional connection must be established. In particular, the connection between classic continuum scale and microscale can be described using the following equation:

$$\boldsymbol{\varkappa} \equiv \nabla \boldsymbol{u} - \boldsymbol{\gamma} \tag{3.14}$$

This describes the relative deformation $\boldsymbol{\varkappa}$ of a microscopic point with respect to a macroscopic one. Similarly, the micro-deformation gradient can be formulated as

$$\boldsymbol{\Theta} \equiv \nabla \boldsymbol{\gamma} \tag{3.15}$$

An example of few entries to this micro-deformation gradient tensor $\boldsymbol{\Theta}$ are shown in Figure 3.6.

Constitutive relations

The strain energy density formulated for a classical Cauchy continuum as in Equation 3.5 is enriched for the micromorphic continuum $\mathcal{W}_{MM}$ by assuming it to be dependent on macro-strain $\boldsymbol{\varepsilon}$, relative deformation between the scales $\boldsymbol{\varkappa}$ and micro-deformation gradient $\boldsymbol{\Theta}$ as follows:

$$\mathcal{W}_{MM} = \mathcal{W}_{MM}(\boldsymbol{\varepsilon}, \boldsymbol{\varkappa}, \boldsymbol{\Theta}) \tag{3.16}$$

providing the definitions of standard Cauchy stress $\boldsymbol{\sigma}$, relative stress $\boldsymbol{\xi}$ and double stress $\boldsymbol{\iota}$ as

$$\boldsymbol{\sigma} = \frac{\partial \mathcal{W}_{MM}(\boldsymbol{\varepsilon}, \boldsymbol{\varkappa}, \boldsymbol{\Theta})}{\partial \boldsymbol{\varepsilon}}, \qquad \boldsymbol{\xi} = \frac{\partial \mathcal{W}_{MM}(\boldsymbol{\varepsilon}, \boldsymbol{\varkappa}, \boldsymbol{\Theta})}{\partial \boldsymbol{\varkappa}}, \qquad \boldsymbol{\iota} = \frac{\partial \mathcal{W}_{MM}(\boldsymbol{\varepsilon}, \boldsymbol{\varkappa}, \boldsymbol{\Theta})}{\partial \boldsymbol{\Theta}} \tag{3.17}$$

Overall, there are 1764 independent constitutive coefficients in a fully anisotropic case. For isotropic elasticity, this number is reduced to 18 independent variables.

The next important simplification is the introduction of vanishing relative deformation between the scales, i.e., the micro-medium merges with the macro-medium gradient and $\boldsymbol{\varkappa}= \mathbf{0}$ [185]. This allows to express the strain energy density in terms of macroscopic displacements $\boldsymbol{u}$. This implies that

$$\boldsymbol{\gamma} = \nabla \boldsymbol{u}, \qquad \boldsymbol{\Theta} = \nabla \boldsymbol{\varepsilon} \tag{3.18}$$

With this in mind, the strain energy density $\mathcal{W}_{II}(\cdot)$ is only dependent on the macroscopic strain and the third-order micro-deformation gradient tensor $\boldsymbol{\Theta}$:

$$\mathcal{W}_{II} = \mathcal{W}_{II}(\boldsymbol{\varepsilon}, \boldsymbol{\Theta}) = \frac{1}{2}\boldsymbol{\varepsilon} : \boldsymbol{C} : \boldsymbol{\varepsilon} + \frac{1}{2}\boldsymbol{\Theta} \vdots \boldsymbol{A} \vdots \boldsymbol{\Theta} \tag{3.19}$$

which is known as the strain energy density of Mindlin's Form II gradient elasticity [110]. Mathematical operations of contractions are defined such that Equation 3.19 is written in the index notation as follows:

$$\mathcal{W}_{II} = \frac{1}{2}C_{ijkl}\varepsilon_{ij}\varepsilon_{kl} + \frac{1}{2}A_{mijnkl}\partial_m\varepsilon_{ij}\partial_n\varepsilon_{kl} \tag{3.20}$$

where $\boldsymbol{C}$ is the standard elasticity tensor and $\boldsymbol{A}$ is the sixth-order gradient-elastic tensor. Assuming linear isotropic material, the gradient-elastic tensor $\boldsymbol{A}$ has five gradient-elastic constants, or also called *length scale parameters*. This tensor holds the information about both material anisotropy and anisotropy of length scale effects [93].

The high-order material parameters are usually difficult to determine, which, in turn, complicates the use of strain gradient elasticity for large-scale applications. Thus, another assumption is usually made. This is the assumption of weak non-locality [93], or, separation of material and length scale anistropy. In this context, the high-order material tensor $\boldsymbol{A}$ can be decomposed as a product of elasticity tensor $\boldsymbol{C}$ and a length scale matrix $\boldsymbol{\Psi}^s$:

$$\boldsymbol{A} = \boldsymbol{P}_1\boldsymbol{\Psi}^s \otimes \boldsymbol{C}\boldsymbol{P}_2 \tag{3.21}$$

with $\boldsymbol{P_1}$ and $\boldsymbol{P_2}$ being permutation tensors such that $A_{ijklmn} = \Psi^s_{il}C_{jkmn}$, and $\boldsymbol{\Psi}^s$ having dimensions of m^2. This length scale matrix reflects the discrete nature of continuum and is not present in standard anisotropic elasticity. The properties of this tensor are related to non-local anisotropic effects at the micro-scale [94]. For example, the length scale tensor can indicate different crystal symmetries. For a cubic crystal symmetry it takes the form:

$$\boldsymbol{\Psi}^s = \begin{bmatrix} \Psi^2 & 0 & 0 \\ 0 & \Psi^2 & 0 \\ 0 & 0 & \Psi^2 \end{bmatrix} \tag{3.22}$$

Finally, plugging in Equation 3.21 into Equation 3.19 yields the simplified form of the strain gradient elasticity theory formulation.

Boundary value problem

Similar to Equation 3.7, the strong form of the strain gradient elastostatic equilibrium equations can be formulated as follows:

$$\nabla \cdot (\boldsymbol{\sigma} - \nabla \cdot \boldsymbol{\iota}) + \boldsymbol{b} = 0 \qquad \text{on} \qquad \Omega \tag{3.23}$$

with $\boldsymbol{\iota}$ being the double stress tensor defined in Equation 3.17 with Equation 3.19. The boundary conditions are extended to the following form [8, 49]:

$$\begin{aligned}
&\boldsymbol{n} \cdot (\boldsymbol{\sigma} - \nabla \cdot \boldsymbol{\iota}) - \nabla_{surf} \cdot (\boldsymbol{n} \cdot \boldsymbol{\iota}) + (\nabla_{surf} \cdot \boldsymbol{n})\, \boldsymbol{n} \otimes \boldsymbol{n} : \boldsymbol{\iota} = \hat{\boldsymbol{t}} \qquad \text{on} \qquad \Gamma_{N,cl} \\
&\boldsymbol{u} = \hat{\boldsymbol{u}} \qquad \text{on} \qquad \Gamma_{D,cl} \\
&\boldsymbol{n} \otimes \boldsymbol{n} : \boldsymbol{\iota} = \hat{\boldsymbol{q}} \qquad \text{on} \qquad \Gamma_{N,II} \\
&\boldsymbol{n} \cdot \nabla \delta \boldsymbol{u} = d\hat{\boldsymbol{u}}_n \qquad \text{on} \qquad \Gamma_{D,II}
\end{aligned} \tag{3.24}$$

where $\nabla_{surf} = \nabla - \boldsymbol{n} \otimes \boldsymbol{n} \cdot \nabla$ is the surface gradient operator, $\hat{\boldsymbol{q}}$ is the prescribed double stress traction vector, and $d\hat{\boldsymbol{u}}_n$ is the prescribed normal directional derivative of the displacement $\boldsymbol{u}$. The boundary is composed of four parts as $\Gamma = \Gamma_{D,cl} \cup \Gamma_{N,cl} \cup \Gamma_{D,II} \cup \Gamma_{N,II}$. The Neumann part of the domain boundary is then formed as $\Gamma_D = \Gamma_{D,II} \cup \Gamma_{D,cl}$ and the Dirichlet part as $\Gamma_N = \Gamma_{N,II} \cup \Gamma_{N,cl}$. Similar to the classical elasticity theory: $\Gamma_D \cap \Gamma_N = \emptyset$. These boundary conditions resemble the classical boundary conditions defined in Equation 3.8. In particular, the first two indicate the traction and displacement boundary conditions, while the last two correspond to non-classical traction and displacement derivative conditions.

Galerkin approach

Equation 3.23 indicates the presence of high order derivatives. Thus, the Galerkin method should comply with this high regularity condition. In particular, the Non-Uniform Rational B-Splines (NURBS) basis function could be employed to resolve this problem. More details about the derivation of the weak form and the requirements can be found in [120]. The demand of higher continuity shape functions makes the numerical solutions of full-scale 3D strain gradient problems scarce. In this work, the use of strain gradient elasticity theory will be limited to dimensionally reduced models in bending. Thus, all the details about the numerical solution of 3D strain gradient elastostatic equations are omitted.

3.3 Classical and strain gradient beam theories[g]

Some engineering problems allow to apply simplified numerical models. For example, bending rigidity characterizes the structural resistance to bending deformation. Typically, it can be determined by a three-point bending experiment schematically depicted in Figure 3.3. In this case, well-established beam theories are preferred to the full 3D analysis. The most common approaches are to employ the Euler-Bernoulli or the Timoshenko beam model. When slender beams with a small thickness-to-length ratio are considered, an Euler-Bernoulli model is more suitable to evaluate bending rigidity. By contrast, the Timoshenko beam theory is more appropriate when shear effects are not

negligible. Detailed derivation and thorough discussion on these techniques can be found in, e.g., [174]. In the following, only the fundamental relations needed for this work are recalled.

For example, the full 3D model of a three-point bending test as in Figure 3.3 can be reduced to a simplified 2D problem where the structure deforms in the xz-plane (see the 2D sketch of the problem in Figure 3.7).

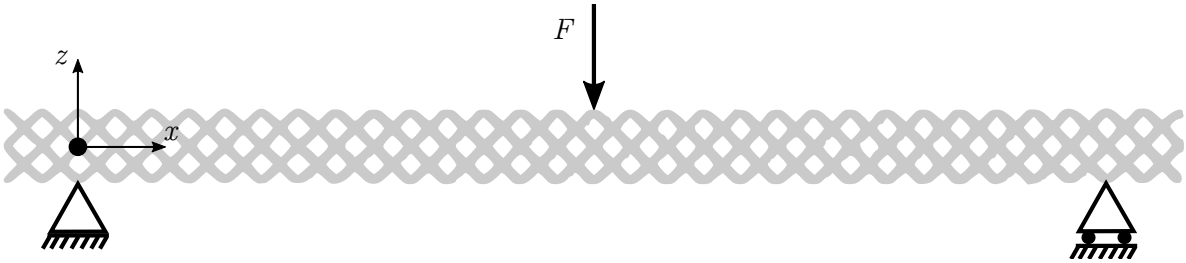

Figure 3.7: A 2D sketch of a three-point bending setup [83].

The displacement components $\boldsymbol{u}= (u_x, u_y, u_z)$ are assumed to obey the following relationships:

$$u_x = -z\frac{\partial w(x)}{\partial x}, \qquad u_y = 0, \qquad u_z = w(x) \tag{3.25}$$

where x is the coordinate along the main axis of the beam, z is the direction perpendicular to it, and y is the out-of-plane coordinate, as depicted in Figure 3.7. This leaves the transverse deflection w as the only unknown.

When utilizing the symmetry of this test set up in the axial direction and, accordingly, modelling the left half of the structure as a uniaxial beam bending problem, the boundary conditions of the resulting beam problem read as follows:

$$w(x=0) = 0, \qquad M(x=0) = 0, \qquad w'\left(x=\frac{L}{2}\right) = 0, \qquad Q\left(x=\frac{L}{2}\right) = \frac{F}{2} \tag{3.26}$$

where the x-coordinate runs along the central (neutral) axis of the beam and $x = 0$ is the coordinate of a fixed left support, w is the deflection of a central axis of the beam, F is the total applied force (evaluated from the distributed traction $\hat{\boldsymbol{t}}$ applied in 3D case Figure 3.3) at the symmetry point $x = L/2$, L is the distance between supports, whereas M and Q, respectively, are the standard bending moment and shear force of the beam.

3.3.1 Classical beam theories

Given the previously defined bending problem, the dimensional reduction to the Euler-Bernoulli beam theory is performed. The classical Euler-Bernoulli solution delivers the maximum deflection at $x = L/2$:

$$w^{EB} = \frac{FL^3}{48E^*I} \tag{3.27}$$

where L is the length of the beam between supports, E^* is the effective Young's modulus, and $I = (bh^3)/12$ is defined as an effective moment of inertia of a rectangluar cross section having the outer dimensions (width b and height h) of the original structure. The last two effective quantities are not straightforward to obtain when lattice structures are considered. The two most common ways to determine them are to perform experiments or to use a first-order numerical homogenization. The latter will be in details discussed in chapter 5 of this thesis.

To account for shear deformations for higher thickness-to-length ratios, the solution of classical Timoshenko beam theory for three-point bending can be formulated as follows:

$$w^T = \frac{FL^3}{48E^*I} + \frac{FL}{4G^*A} \tag{3.28}$$

where G^* is the effective shear modulus and A is the cross-sectional effective area. Then, the main characteristic of the bending behavior is the bending stiffness or bending rigidity D. It defines the resistance of the specimens to bending deformations:

$$D = \frac{F}{w} \tag{3.29}$$

where F is the applied load and w the determined displacement.

With the help of the classical beam theories solutions, this quantity can be determined analytically when all other parameters are known. The classical Euler-Bernoulli bending rigidity D^{EB} for the considered problem yields:

$$D^{EB} = \frac{F}{w^{EB}} = \frac{48E^*I}{L^3} = \frac{4E^*bh^3}{L^3} \tag{3.30}$$

where b is the depth and h is the height of the homogenized rectangular cross section. Analogously, the classical bending rigidity using the Timoshenko beam theory D^T is defined as:

$$D^T = \frac{F}{w^T} = \frac{D^{EB}}{1 + \dfrac{12E^*I}{G^*AL^2}} = \frac{D^{EB}}{1 + \dfrac{E^*}{G^*}\left(\dfrac{h}{L}\right)^2} \tag{3.31}$$

Equation 3.31 shows that for a fixed length L, the bending rigidity D^T approaches D^{EB} when thickness approaches zero, whereas for constant thickness-to-length ratios, the Timoshenko and Euler-Bernoulli rigidities stay apart.

3.3.2 Strain gradient beam theories

The formulation of the strain gradient Euler-Bernoulli beam theory starts with the same displacement relations as defined in Equation 3.25. The strain gradient energy density has been formulated above in Equation 3.19. In this case, the only non-zeros strain and stress components are ε_{xx} and $\sigma_{xx} = C_x\varepsilon_{xx}$ with $C_x = C_{xxxx}$. Accordingly, the strain

gradient model has to incorporate strain gradients components $\varepsilon_{xx,x}$ and $\varepsilon_{xx,z}$ only, with the corresponding two high-order elasticity constants $A_x = A_{xxxxxx}$ and $A_z = A_{xxzzxz}$ of a full high-order material tensor defined in Equation 3.19 [161]. Thus, the variation of the strain energy density defined corresponding to Equation 3.19 simplifies to:

$$\delta \int_{\Omega} \mathcal{W}_{II} d\Omega = \int_{\Omega} \left(C_x \varepsilon_{xx} \delta\varepsilon_{xx} + A_x \varepsilon_{xx,x} \delta\varepsilon_{xx,x} + A_z \varepsilon_{xx,z} \delta\varepsilon_{xx,z} \right) d\Omega \tag{3.32}$$

and further to a 1D energy expression over the main axis of the beam:

$$\delta \int_{\Omega} \mathcal{W}_{II} d\Omega = \int_{0}^{L} \left(M + g_z^2 R \right) \frac{\partial^2 (\delta w)}{\partial x^2} dx + \int_{0}^{L} g_x^2 \frac{\partial M}{\partial x} \frac{\partial^3 (\delta w)}{\partial x^3} \tag{3.33}$$

with a generalized moment $R{=}R(x)$ written out as follows:

$$R(x) = \int_{A} \frac{\partial \sigma_{xx}(x,y,z)}{\partial z} dA = C_x A \frac{d^2 w}{dx^2} \tag{3.34}$$

where A is the cross-sectional area of the beam.

Applying Hamilton's principle the strong formulation of the two-parameter strain gradient Euler-Bernoulli elasticity model can be formulated. The differential equation reads in terms of moments, or in terms of deflection with constant material parameters, respectively, as follows:

$$(M + g_z^2 R - (g_x^2 M')')'' = f \qquad \text{or} \qquad (E^* I + g_z^2 E^* A) w'''' + g_x^2 E^* I w'''''' = f \qquad \forall x \in (0, L) \tag{3.35}$$

where f is the externally applied transversal loading and $E^* I$ stands for the classical bending rigidity with $E^* = C_x$, whereas the two length scale parameters g_x and g_z are defined following the weak non-locality approximation defined in Equation 3.21 as $A_x = g_x^2 E^*$ and $A_z = g_z^2 E^*$, respectively. The higher-order term $((g_x^2 M')')''$, $\left(\text{or } g_x^2 E^* I w''''''\right)$, can be related to boundary layer effects specific for certain boundary conditions and the crucial stiffening effect can be traced back essentially to the additional lower-order term $g_z^2 R$, $\left(\text{or } g_z^2 E^* A w''''\right)$ (see [119]). The governing equation can be written in a simple lower-order form [79, 80]:

$$(E^* I + E^* A g^2) w'''' = f \qquad \forall x \in (0, L) \tag{3.36}$$

where only one length scale parameter $g = g_z$ is present.

The analytical solution of Equation 3.36 under the absence of body load with the boundary conditions described in Equation 3.26 takes the form:

$$w_{gr}^{EB} = \frac{F L^3}{48 \left(E^* I + E^* A g^2 \right)} \tag{3.37}$$

Equation 3.37 compared to the solution of the classical Euler-Bernoulli theory in Equation 3.27 leaves the only intrinsic length scale parameter g which acts as a representative

high-order material parameter of length scale matrix $\mathbf{\Psi}^s$ defined in Equation 3.21. This parameter depends on the unit cell's microstructure and characterizes the size-dependent beam behavior when the beams with a low thickness-to-length ratio show a stiffening effect.

The solution of the strain gradient Timoshenko beam theory can be derived in a similar manner taking into account the respective assumptions [79, 80]:

$$w_{gr}^{T} = \frac{FL^3}{48\left(E^* I + E^* A g^2\right)} + \frac{FL}{4G^* A} \tag{3.38}$$

Equation 3.38 is also similar to the solution of the classical Timoshenko theory except for the presence of the intrinsic material parameter g. The bending rigidities (with rectangular cross sections $A = bh$) corresponding to these deflections can be shown to follow, respectively, the formulae:

$$\begin{aligned} D_{gr}^{EB} &= D^{EB}\left(1 + 12\left(\frac{g}{h}\right)^2\right) \\ D_{gr}^{T} &= D^{T}\left(1 + 12\left(\frac{g}{h}\right)^2\right) \end{aligned} \tag{3.39}$$

revealing the size effect for decreasing values of h with a fixed value of g.

To sum up, both the classical and the strain-gradient theories could provide a quick estimate of the considered beam-like lattice structures' bending behavior. In the scope of this thesis, the predictions provided by these theories will be compared to the full 3D numerical and experimental analysis in chapter 6. Furthermore, their accuracy and applicability will be evaluated with the help of experimental three-point bending tests.

Chapter 4

Finite Cell Method for image-based numerical characterization

[g]As explained in section 2.3 the as-manufactured geometries are often acquired via computed tomography. Such geometrical models challenge the meshing procedure of the conventional FEM approach. To perform a direct numerical simulation described in chapter 3, a suitable 3D model must be reconstructed. Then, a boundary conforming mesh must be generated. However, these two steps involve a lot of manual labor and necessary computational power. Furthermore, when the lattice structures are analyzed, the high level of microstructural details makes the preparation to the numerical analysis very costly. Hence, to address these challenges, the Finite Cell Method, an immersed boundary method [38, 39, 129], is introduced. This approach allows not only to circumvent the challenge of incorporation the CT-based geometrical models into the numerical analysis but also to exploit the inherent structure of the CT scans to make the numerical analysis of as-manufactured geometries efficient and feasible. In the following, only the main ideas of the FCM are recapitulated.

4.1 The main concept[g]

The main idea of the Finite Cell Method is illustrated in Figure 4.1.

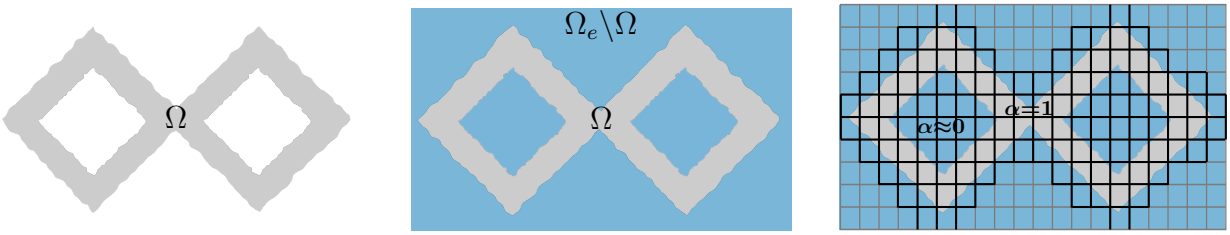

(a) Physical domain Ω (b) Extended domain Ω_e (c) FCM mesh (in bold) and indicator function

Figure 4.1: The idea of the Finite Cell Method [83].

First, a complex domain Ω is immersed in a simplified box-like domain Ω_e. Note that the strong and the weak formulation of the elastostatic problems as in Equations 3.7 and 3.9 are defined on the physical domain Ω. Due to the simplicity of the fictitious domain Ω_e, it can be trivially discretized with a structured grid of cuboids, further referred to as *finite cells*. As opposed to the conforming finite element mesh, the finite cell mesh does not aim at approximating the boundary of the physical domain Γ. In turn, it just discretizes a simple cuboid. These elements provide the support for shape functions which are chosen to be integrated Legendre polynomials of order p as mentioned in section 3.1.

Second, the original boundary value problem must be recovered on the actual, physical domain. To achieve such a result, an indicator function $\alpha(\boldsymbol{x})$ is introduced into the problem formulation. It is defined to be equal to one on all points of the physical domain Ω and to a small positive value in the domain $\Omega_e \backslash \Omega$. Then, the classic weak formulation defined in Equation 3.9 is modified as follows:

$$\text{Find } \boldsymbol{u} \in \mathcal{S} \text{ such that } \mathcal{B}_e^{\alpha}(\boldsymbol{v}, \boldsymbol{u}) = \mathcal{F}_e^{\alpha}(\boldsymbol{v}) \;\; \forall\, \boldsymbol{v} \in \mathcal{V} \tag{4.1}$$

$$\text{where} \quad \mathcal{B}_e^{\alpha}(\boldsymbol{v}, \boldsymbol{u}) = \int_{\Omega_e} \boldsymbol{\varepsilon}(\boldsymbol{v}) : \alpha(\boldsymbol{x}) \boldsymbol{C}(\boldsymbol{x}) : \boldsymbol{\varepsilon}(\boldsymbol{u}) \, d\Omega_e$$

$$\mathcal{F}_e^{\alpha}(\boldsymbol{v}) = \int_{\Omega_e} \boldsymbol{v} \cdot \alpha(\boldsymbol{x}) \boldsymbol{b} \, d\Omega + \int_{\Gamma_N} \boldsymbol{v} \cdot \hat{\boldsymbol{t}} \, d\Gamma_N$$

The introduction of the indicator function $\alpha(\boldsymbol{x})$ in this formulation ensures equivalency of Equation 4.1 to the classical formulation Equation 3.9 in terms of energy with the modeling error proportional to $\sqrt{\alpha}$. The mechanical meaning of this function can be described as the value of $\alpha(\boldsymbol{x}) \; \forall \, \boldsymbol{x} \in \Omega_e \backslash \Omega$ corresponds to the addition of a material with vanishing stiffness in the void domain $\Omega_e \backslash \Omega$.

As the geometries under consideration stem from CT images, the spatial scalar function $\alpha(\boldsymbol{x})$ can be conveniently related to the acquired Hounsfield Units. After applying the single thresholding technique explained in section 2.3, the threshold value of Hounsfield units HU_{thres} can directly be used to define the indicator function as follows:

$$\alpha(\boldsymbol{x}) = \begin{cases} 1 & \text{if } HU \geq HU_{\text{thres}} \\ << 1 & \text{if } HU < HU_{\text{thres}} \end{cases} \tag{4.2}$$

Although the indicator function simplifies the meshing procedure drastically, it also introduces additional challenges to the numerical procedure. In particular, four major points needs to be discussed:

- Boundary condition application
- Refinement strategies
- Accurate integration of cut finite cells
- Conditioning problems

As mentioned above, the finite cells do not approximate the geometrical boundary of the domain. However, on the physical domain boundary Γ, the boundary conditions are defined (see Equation 3.8). Like in the conventional FEM, homogeneous Neumann boundary condition is automatically satisfied by choosing the indicator function close

to zero. Non-homogeneous Neumann conditions are also naturally incorporated in the formulation of Equation 4.1. However, the essential boundary conditions are not possible to be applied traditionally. As opposed to the conforming nodes at the domain boundary in FEM, the geometric boundary does not contain the necessary degrees of freedom. Thus, the most common approach is to apply Dirichlet boundary conditions in a weak sense by using Nitsche's method (see, e.g., [121]), Lagrange multipliers (e.g., [60]) or Penalty approach [6]. The latter will be further used in this work.

The traditional refinement procedures, such as *h*- or *p*-refinement, can also be applied in the Finite Cell Method. Similarly, the background grid's size can be reduced, or the polynomial degree of the shape functions can be elevated. Furthermore, the *hp*-refinement is also possible and can be advantageous when singular solutions are considered or local solution features have to be resolved. This technique has been extensively studied in the scope of FCM by [149, 184].

As indicated in Equation 4.1, the indicator function can make the domain integrands discontinuous. In the extended domain, there are so-called *cut cells*, which are overlapping both the physical domain Ω and the fictitious domain $\Omega \backslash \Omega_e$. In this case, a special integration technique must be applied to achieve a reasonable accuracy of the domain integrals. For this purpose, multiple techniques have been proposed (see, e.g., [1, 90]). However, as the geometrical domains in this thesis stem from CT scans, the underlying voxel structure can be exploited to perform this integration efficiently. This scheme will be discussed further.

Finally, the presence of cut cells, especially when the portion of the fictitious overlap is large, can lead to a high condition number of the stiffness matrix. This is particularly challenging when iterative solvers are used to obtain the numerical solution. As in this thesis most of the problems are large, the iterative solver remains the best possible choice for the solution of linear systems. Thus, the solution to this conditioning problem will be briefly mentioned in the following sections.

4.2 Efficient numerical integration of discontinuous integrands[a]

For numerical domains stemming from CT scans and linear physical problems, the computational efficiency of the FCM can be optimally exploited using a pre-integration technique on a voxel level introduced in [180]. Consider a 3D voxel-based domain of size $l_x \times l_y \times l_z$ length units. A slice of this domain is depicted in Figure 4.2 as an example. The numerical domain is discretized with $n_x \times n_y \times n_z$ finite cells. Every cell contains $v_x \times v_y \times v_z$ voxels with dimensions $s_x \times s_y \times s_z$ length units.

The Hounsfield Units are piecewise constant in a voxel. Hence, the domain integrand in Equation 4.1 is discontinuous at the boundary of the voxels within every finite cell. Therefore, the integration is carried out piecewise, i.e., in a composed fashion on each voxel separately. Then, the composed integration of the cell stiffness matrix after dis-

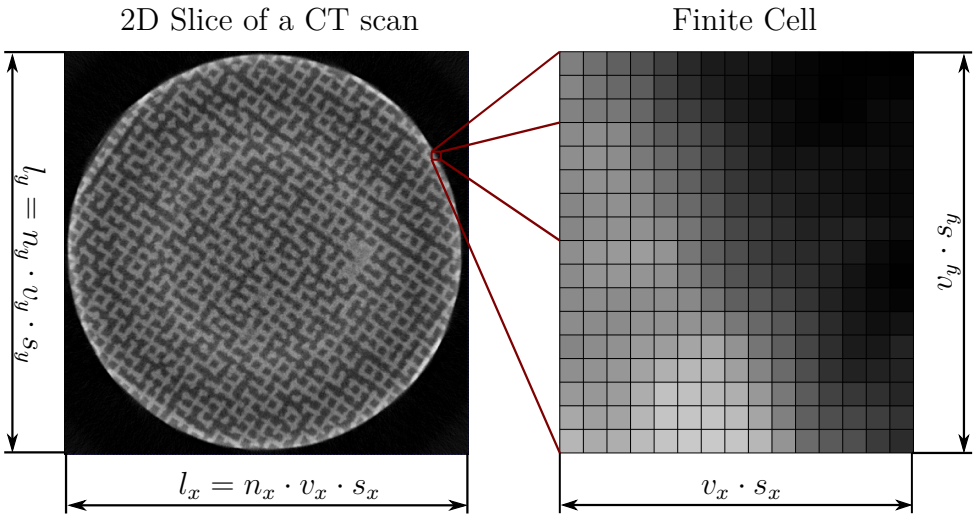

Figure 4.2: 2D Slice of a CT scan with an example of a finite cell.

cretizing Equation 4.1 reads:

$$\boldsymbol{K}_c = \int_{\Omega_c} \boldsymbol{B}^T \left(\alpha(\boldsymbol{x})\boldsymbol{C}(\boldsymbol{x})\right) \boldsymbol{B}\, d\Omega_c = \sum_{v_x}\sum_{v_y}\sum_{v_z} \int_{\Omega_v} \boldsymbol{B}^T \left(\alpha(\boldsymbol{x})\boldsymbol{C}(\boldsymbol{x})\right) \boldsymbol{B}\, d\Omega_v \tag{4.3}$$

where $\boldsymbol{B}$ is the matrix containing shape functions derivatives, Ω_c is the finite cell domain, and Ω_v is the domain of one voxel.

Transferring Equation 4.3 to a local coordinate system of one finite cell, the integral can be written as follows:

$$\begin{aligned} \boldsymbol{K}_c &= \int_{-1}^{1}\int_{-1}^{1}\int_{-1}^{1} \boldsymbol{B}^T \left(\alpha(\boldsymbol{x})\boldsymbol{C}(\boldsymbol{x})\right) \boldsymbol{B} det\boldsymbol{J}\, drdsdt \\ &= \sum_{v_x}\sum_{v_y}\sum_{v_z} \left(\int_{k_r}\int_{k_s}\int_{k_t} \boldsymbol{B}^T \left(\alpha(\boldsymbol{x})\boldsymbol{C}(\boldsymbol{x})\right) \boldsymbol{B} det\boldsymbol{J}\, drdsdt \right) \end{aligned} \tag{4.4}$$

where k_r,k_s and k_t indicate the local coordinate limits of integration for every voxel within a finite cell. They depend on the number of considered voxels per dimension $v_x \times v_y \times v_z$.

Then, exploiting the structure of the integral indicated in Equation 4.4, the voxel stiffness matrix contributions can be pre-computed in an offline stage using a standard $(p+1)^3$ Gaussian quadrature rule resulting in $v_x(p+1) \times v_y(p+1) \times v_z(p+1)$ integration points per finite cell. These contributions are then multiplied with the indicator function $\alpha(\boldsymbol{x})$ defined through the Hounsfield Units in Equation 4.2.

This pre-integration technique allows for fast integration of the global stiffness matrix. However, the storage of the dense $v_x \times v_y \times v_z$ matrices increases the memory consumption (see [180]). In this thesis's scope, the memory cost for storing these matrices is negligible compared to that of the rest of the simulation (e.g., the storage of the global stiffness matrix).

4.3 Linear system solution and conditioning considerations

Although the Finite Cell Method combined with a voxel-based pre-integration technique provides a powerful tool to perform numerical analysis directly on CT images, the linear systems size, especially for the DNS tests, remains considerable. To address this issue, a hybrid parallelization of the high-order FCM is used. This parallelization strategy is based on a modified version of the approach presented in [74, 75]. In this section, only the novelty of the utilized parallel framework will be briefly highlighted.

The main idea of the hybrid parallelization framework is based on both distributed and shared memory parallelism. The numerical solution is obtained on different computational units, or *nodes*. The original technique proposed in [74] and employed in [75] was replicating the entire mesh data structure on all participating nodes, i.e., every computational node, the entire finite cell mesh in all detail, and only selects a subset of these elements for further processing. This method was employed in [74, 75] due to its simplicity. It automatically delivers consistent management of all degrees of freedom of discretization. However, it not only requires a large amount of memory to store the mesh structure, but the size of the largest computable problem is limited by the amount of memory one single node can allocate. This memory limitation does not allow for a DNS computation of the examples discussed in chapter 6.

In the scope of this thesis, a new version of this approach is employed. The limitations of the techniques presented in [74, 75] is lifted by an advanced mesh handling strategy. This strategy is based on a fully-parallel adaptive Cartesian mesh and is similar to the parallel mesh generation routines in packages such as P4est[19]. At the start of the mesh generation process, a coarse lightweight Cartesian grid is generated, see Figure 4.3a. This grid structure is computationally inexpensive to create and store as it only holds every grid cell's location indices. It allows determining the mesh part containing the geometrical model's physical domain Ω and discard possible inactive coarse grid cells. Then, these grids are partitioned among the computational nodes, as indicated in Figure 4.3b. Each node then "forgets" the overall mesh structure, storing only the domain's necessary part. Every computational unit can independently refine its local grid cells until a predefined depth to capture more geometrical details, as shown in Figure 4.3c. After this refinement, some processes can end up with a larger number of grid cells than others. Hence, a second load balancing step is performed on the refined grid cells using Zoltan to eliminate this imbalance. Finally, a numerical simulation can be performed independently on every computational node. The only remaining ingredient to complete this framework is to allow a suitable communication of numerical data among the processes. In the current implementation, overlapping ghost layers, as shown in Figure 4.3d, provide an analysis-suitable discretization in which every degree of freedom has a unique global number. This parallelization strategy uses the concept of *ghost elements*, an additional overlapping element layer between the computational nodes. Therefore, the distributed linear system of equations can be computed without communication. At this point, the new algorithms nicely allow for subsequent usage of the methodologies for the distributed solution of equations as presented in [75].

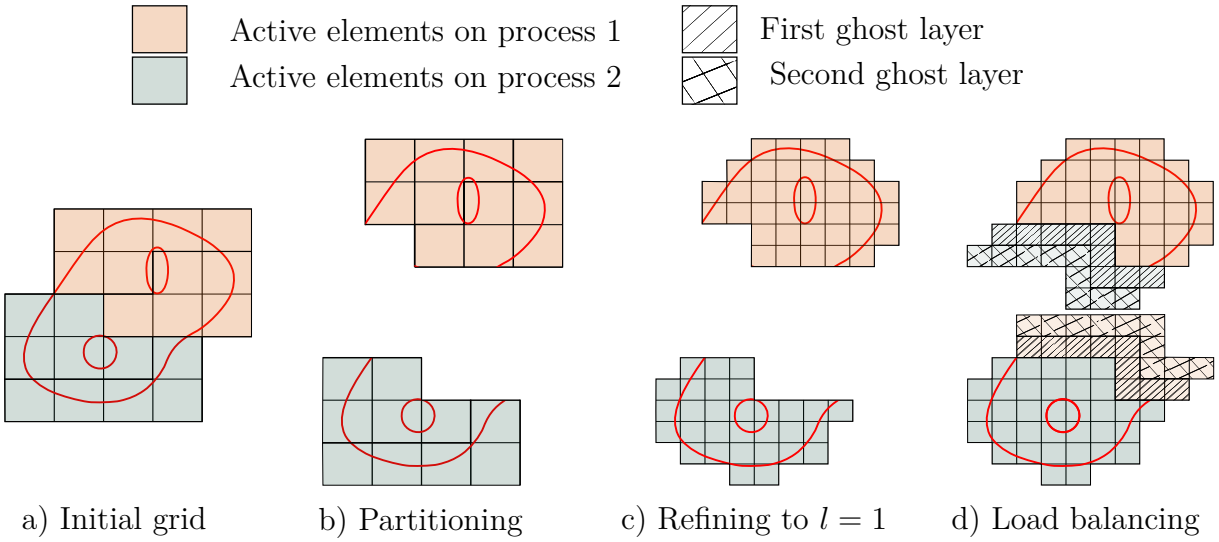

Figure 4.3: An example of parallel mesh handling for two computational nodes.

To solve these distributed systems, highly optimized parallel linear algebra capabilities of `Trilinos` for parallel matrix-vector multiplications and matrix storage are extensively used. Nonetheless, the conditioning issues arising due to the small fraction cut cells still have to be addressed. To this extent, the parallel Conjugate Gradient solvers from Trilinos library are extended with the custom Additive Schwarz-based preconditioner, which was specifically designed to treat conditioning problems associated with the cut elements in FCM. A detailed description of this approach can be found in [29, 75].

Chapter 5

Computational homogenization

This chapter describes computational homogenization as a numerical tool to characterize the macroscopic material behavior of complex structures. Computational homogenization is a cheaper alternative to direct numerical testing addressed in chapter 2.

The effective material properties can be either determined analytically or numerically. However, only a few analytical solutions for unique geometrical configurations exist. The most generic approximations of effective properties applicable to any setup are described in section 5.1.

When the effective material properties are determined numerically, the computational homogenization theory is applied. According to [118], this method includes the following main ingredients:

- The concept of Representative Volume Element (RVE)
- Principle of separation of scales
- Averaging theorems
- The Hill-Mandel macro-homogeneity principle
- Boundary conditions

In sections 5.2 to 5.5, each of these crucial concepts is discussed in greater detail.

Although computational homogenization is widely used to characterize the linear and non-linear behavior of materials, porous non-periodic structures' material characterization remains challenging. In this case, the homogenization boundary conditions become crucial for the accuracy of the obtained homogenized quantities. Furthermore, when the voids are randomly crossing the boundary, averaging theorems and application of boundary conditions becomes rather cumbersome [33, 116, 158]. This issue is addressed in section 5.6, where a novel solution provided by the FCM is presented.

An alternative way to homogenize non-periodic porous structures is to employ the window method, eliminating the need for specific void treatment. This method was introduced and employed in [58, 150, 189]. However, it shows a few limitations, which are extensively discussed in section 5.7.

In the following, the concepts of computational homogenization are described based on linear elasticity. Generally, thermal, permeability or viscoelastic homogenization is performed in the same way. However, the important differences are briefly discussed in section 5.8.

While numerical homogenization does not require any prior assumptions on a macroscopic material law and provides a complete macroscopic material tensor at once, the final result is governed by the applied boundary conditions and might not deliver the best approximate. Numerical examples at the end of this chapter (see section 5.9) investigate these phenomena in greater detail and provide an extensive discussion on the applicability of the computational homogenization theory. The examples are chosen such that the two most common groups of the materials are considered. In particular, structures consisting of one material with voids and composites are investigated. The first group is represented by considering a periodic cubic cell with a cubical void. In this case, the internal void's size is not fixed but varied throughout the studies. To further verify the computational homogenization results, the larger structure is artificially constructed by a cubic cell's periodic repeating. The composites are considered by investigating a two-material particle reinforced cubic cell. Similar to the first example, this cell is considered to be ideally periodic.

5.1 Analytical bounds

To determine the effective behavior of materials with complex microstructure analytically, only a handful of solutions exist. In the following, only Voigt and Reuss bounds and the Hashin-Shtrikman bounds are recapitulated. They rely solely on the macroscopic porosity and do not consider any geometrical or topological specifications of the microstructure. These bounds are considered the simplest models to evaluate the range where the effective properties fall.

There are more analytical estimates to determine effective properties, such as Mori-Tanaka model, Dilute distribution, Differential scheme, Self-consistency method, etc. [55]. These estimates do not provide the bounds but a value approximation for specific microstructures. These models require knowledge about inclusion's position, form, properties, and influence on one another. These assumptions limit its application in the scope of this work and will not be considered further.

Voigt and Reuss bounds (Hill bounds)

Consider a matrix (Ω_m) and another material (Ω_h)m which are perfectly bonded together (see Figure 5.1).

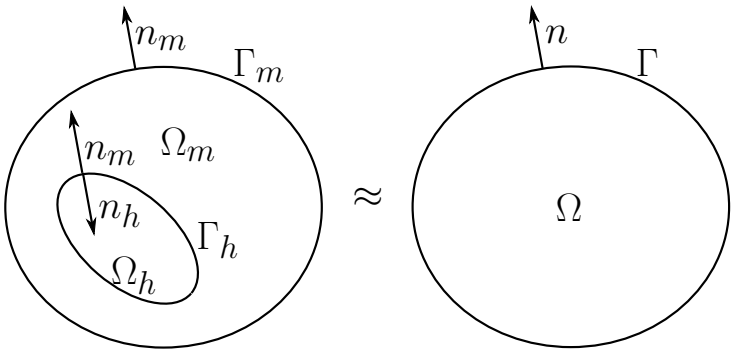

Figure 5.1: Representative volume domain, boundaries and normals definitions.

As the volume consists of two phases, the overall average stress can be written out using the subdomain expansion as follows:

$$\begin{aligned} \langle \boldsymbol{\sigma} \rangle_{\Omega} &= \sum_{\alpha=1}^{n} c_{\alpha} \langle \boldsymbol{\sigma} \rangle_{\Omega_{\alpha}} \\ \langle \boldsymbol{\varepsilon} \rangle_{\Omega} &= \sum_{\alpha=1}^{n} c_{\alpha} \langle \boldsymbol{\varepsilon} \rangle_{\Omega_{\alpha}} \end{aligned} \tag{5.1}$$

where α is a considered phase,
n is the total number of phases. i.e subdomains, in this case $n = 2$,
c_{α} - volume fraction of a subdomain:
$c_{\alpha} = \frac{\Omega_{\alpha}}{\Omega}$ and $\sum_{\alpha=1}^{n} c_{\alpha} = 1$,
$< \cdot >$ is a volume averaging operator.

If the considered volume is representative of the overall macroscopic behavior, a unique relation between an average quantity within the mixture and a single phase exists:

$$\begin{aligned} \langle \boldsymbol{\varepsilon} \rangle_{\Omega_m} &= \boldsymbol{L}_m \langle \boldsymbol{\varepsilon} \rangle_{\Omega} & \langle \boldsymbol{\sigma} \rangle_{\Omega_m} &= \boldsymbol{M}_m \langle \boldsymbol{\sigma} \rangle_{\Omega} \\ \langle \boldsymbol{\varepsilon} \rangle_{\Omega_h} &= \boldsymbol{L}_h \langle \boldsymbol{\varepsilon} \rangle_{\Omega} & \langle \boldsymbol{\sigma} \rangle_{\Omega_h} &= \boldsymbol{M}_h \langle \boldsymbol{\sigma} \rangle_{\Omega} \end{aligned} \tag{5.2}$$

where $\boldsymbol{L}$ and $\boldsymbol{M}$ are fourth-order influence tensors expressing the dependence of the field average over one subdomain on the prescribed macroscopic quantity [55]. Substituting Equation 5.2 into Equation 5.1 gives:

$$\langle \boldsymbol{\sigma} \rangle_{\Omega} = \boldsymbol{C}^{*} : \langle \boldsymbol{\varepsilon} \rangle_{\Omega} \qquad \text{where} \qquad \boldsymbol{C}^{*} = c_h \boldsymbol{C}_h \boldsymbol{L}_h + c_m \boldsymbol{C}_m \boldsymbol{L}_m \tag{5.3}$$

or equivalently for the strains:

$$\langle \boldsymbol{\varepsilon} \rangle_{\Omega} = \boldsymbol{D}^{*} : \langle \boldsymbol{\sigma} \rangle_{\Omega} \qquad \text{where} \qquad \boldsymbol{D}^{*} = c_h \boldsymbol{D}_h \boldsymbol{M}_h + c_m \boldsymbol{D}_m \boldsymbol{M}_m \tag{5.4}$$

If an average uniform strain through the mixture is assumed ($\boldsymbol{L}_h = \boldsymbol{L}_m = \boldsymbol{I}$), Equation 5.3 reduces to the Voigt estimate [173]:

$$\langle \boldsymbol{\sigma} \rangle_{\Omega} = \boldsymbol{C}^{*}_{V} : \langle \boldsymbol{\varepsilon} \rangle_{\Omega} \qquad \text{where} \qquad \boldsymbol{C}^{*}_{V} = c_h \boldsymbol{C}_{\boldsymbol{h}} + c_m \boldsymbol{C}_{\boldsymbol{m}} \tag{5.5}$$

While for the average uniform stress state in the mixture ($\boldsymbol{M}_h = \boldsymbol{M}_m = \boldsymbol{I}$), Equation 5.4 is a Reuss estimate [142]:

$$\langle \boldsymbol{\sigma} \rangle_{\Omega} = \boldsymbol{C}^{*}_{R} : \langle \boldsymbol{\varepsilon} \rangle_{\Omega} \qquad \text{where} \qquad \frac{1}{\boldsymbol{C}^{*}_{R}} = \frac{c_h}{\boldsymbol{C}_h} + \frac{c_m}{\boldsymbol{C}_m} \tag{5.6}$$

When the void phase is present in the mixture, the lower bound can be estimated as follows:

$$\langle \boldsymbol{\sigma} \rangle_{\Omega} = \boldsymbol{0} \qquad \boldsymbol{C}^{*}_{R} = \lim_{\boldsymbol{C}_h \to 0} \frac{\boldsymbol{C}_h \boldsymbol{C}_m}{c_h \boldsymbol{C}_m + c_m \boldsymbol{C}_h} = \boldsymbol{0} \tag{5.7}$$

Physically, the Voigt estimate implies that tractions at the phase boundaries are not in equilibrium, while the Reuss approximation suggests that inclusion and matrix are not remaining bonded.

Both Reuss and Voigt estimates provide a wide range of bounds for a general type of mixture. In case one phase is either rigid or weak, compared to the other, the difference between these two values becomes quite large [68]. The Voigt and Reuss bounds provide an exact solution only for the special cases depicted in Figure 5.2.

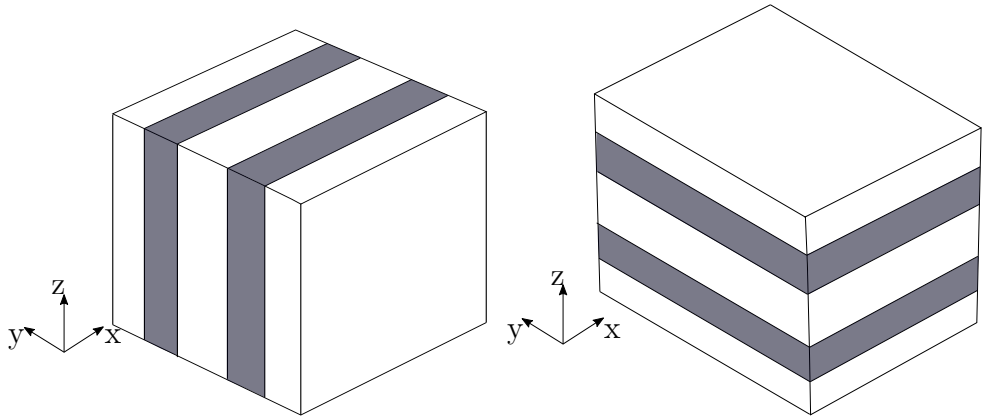

(a) Exact Voigt Bound (b) Exact Reuss Bound

Figure 5.2: Special cases for which Voigt and Reuss bounds provide exact effective properties (load is applied in z-direction) [111].

Nevertheless, it was proven that the Voigt and Reuss estimates are always bounding the effective elasticity tensor as follows [67]:

$$\boldsymbol{C}_R^* \leq \boldsymbol{C}^* \leq \boldsymbol{C}_V^* \tag{5.8}$$

Hashin-Shtrikman bounds

The base of variational Hashin-Shtrikman bounds is the comparison of a microscopically fluctuating response with a homogeneous reference material [61]. These bounds are exact for a composite sphere assemblage.

If the mixture consists of n phases with bulk modulus K_n and shear modulus G_n, the Hashin-Shtrikman bounds are written as follows:

$$\begin{aligned} K_{HSB} &\gtrless K_0 + \frac{A}{1+\alpha_0 A} \\ G_{HSB} &\gtrless G_0 + \frac{1}{2}\frac{B}{1+\beta_0 B} \end{aligned} \tag{5.9}$$

where K_0, G_0 are either the largest material characteristics of a phase in the mixture yielding an upper bound, or the smallest mixture characteristics leading to a lower bound.

And α_0, β_0, A, and B are constants defined as follows:

$$\begin{aligned}
\alpha_0 &= -\frac{3}{3K_0 + 4G_0} \\
\beta_0 &= -\frac{3\,(K_0 + 2G_0)}{5G_0\,(3K_0 + 4G_0)} \\
A &= \sum_{r=1}^{r=n} \frac{c_r}{\frac{1}{K_r - K_0} - \alpha_0} \\
B &= \sum_{r=1}^{r=n} \frac{c_r}{\frac{1}{2(G_r - G_0)} - \beta_0}
\end{aligned} \tag{5.10}$$

Substituting $n = 2$, $K_1 > K_0$ and $G_1 > G_0$ for a two-phase mixture in Equation 5.9, the following equation for the effective bulk and shear moduli can be obtained:

$$\begin{aligned}
K_{HSB^-} &= K_0 + \frac{c_1}{\frac{1}{K_1 - K_0} + \frac{3c_0}{3K_0 + 4G_0}} \\
G_{HSB^-} &= G_0 + \frac{c_1}{\frac{1}{G_1 - G_0} + \frac{6(K_0 + 2G_0)c_0}{5G_0(3K_0 + 4G_0)}}
\end{aligned} \tag{5.11}$$

$$\begin{aligned}
K_{HSB^+} &= K_1 + \frac{c_0}{\frac{1}{K_0 - K_1} + \frac{3c_1}{3K_1 + 4G_1}} \\
G_{HSB^+} &= G_1 + \frac{c_0}{\frac{1}{G_0 - G_1} + \frac{6(K_1 + 2G_1)c_1}{5G_1(3K_1 + 4G_1)}}
\end{aligned} \tag{5.12}$$

If one of the phases has vanishing stiffness $K = 0$, $G = 0$, then the limits can be simplified as follows:

$$\begin{aligned}
K_{HSB^-} &= \lim_{K_0, G_0 \to 0} K_0 + \frac{c_1}{\frac{1}{K_1 - K_0} + \frac{3c_0}{3K_0 + 4G_0}} = \\
&= \lim_{K_0, G_0 \to 0} K_0 + \frac{c_1\,(K_1 - K_0)\,(3K_0 + 4G_0)}{3K_0 + 4G_0 + K_1 - K_0} = 0 \\
G_{HSB^-} &= G_0 + \frac{c_1}{\frac{1}{G_1 - G_0} + \frac{6(K_0 + 2G_0)c_0}{5G_0(3K_0 + 4G_0)}} = \\
&= \lim_{K_0, G_0 \to 0} G_0 + \frac{5c_1 G_0\,(3K_0 + 4G_0)\,(G_1 - G_0)}{5G_0\,(3K_0 + 4G_0) + G_1 - G_0} = 0
\end{aligned} \tag{5.13}$$

$$\begin{aligned}
K_{HSB^+} &= K_1 + \frac{c_0}{-\frac{1}{K_1} + \frac{3c_1}{3K_1 + 4G_1}} \\
G_{HSB^+} &= G_1 + \frac{c_0}{-\frac{1}{G_1} + \frac{6(K_1 + 2G_1)c_1}{5G_1(3K_1 + 4G_1)}}
\end{aligned} \tag{5.14}$$

For the case of a void phase Equation 5.14 and Equation 5.13 provides the same estimate as the Reuss model (see Equation 5.7). As an example of this distribution, consider a

two-phase material with $E = 200\,GPa$, $\nu = 0.3$ with the voids. As shown in Figure 5.3, when the voids are present, the lower Hashin-Shtrikman bounds and the Reuss bound provide the same results. However, the overall Hashin-Shtrikman bounds provide a tighter estimate of the overall effective properties for materials not following any special cases mentioned before.

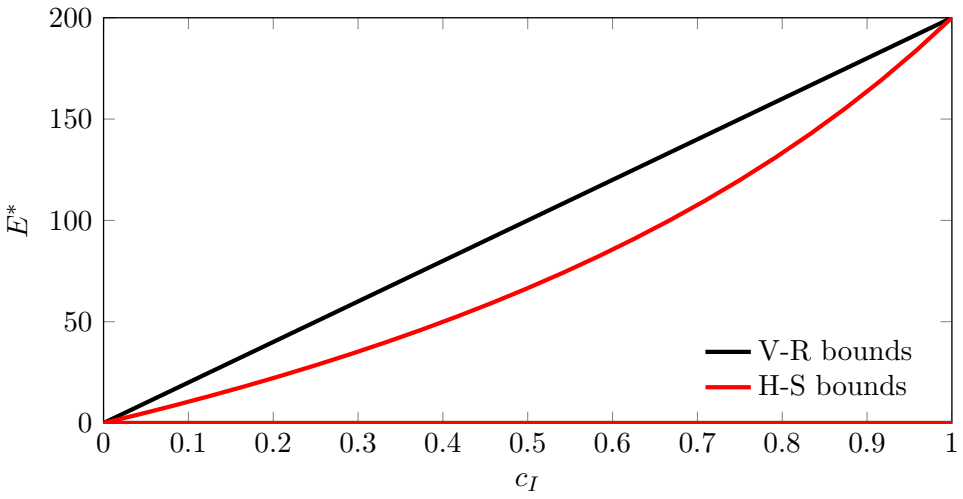

Figure 5.3: Hashin-Shtrikman and Voigt and Reuss bounds for two-phase material with the voids.

5.2 Representative Volume Element

The overall macroscopic behavior of complex structures is strongly influenced by the defects arising on different levels. Defects cause inhomogeneous stress and strain distribution through the material, which is called *eigenstress* and *eigenstrain* respectively. The eigenstress is defined as stress in a body with the applied surface or body forces [140]. Eigenstrains can be defined as nonelastic strains from thermal expansion, phase transformation, initial strains, plastic strains, or misfit strains [112].

Thus, the following classification of inhomogeneities by nature of eigenstrain can be considered [55]:

- *Inclusions* and *dislocations*, which are the sources of eigenstrains and eigenstresses themselves. These, for example, can be inclusions with the same elastic properties as the matrix but undergoing some internal deformations.
- *Inhomogeneities*, which are the sources of equivalent eigenstrain and eigenstress. It can be, for example, a crack or void in a homogeneous matrix. Such material's total mechanical response is composed of a uniform field induced in a defect-free material and a fluctuating field generated by the defect presence. The fluctuating fields in such materials are called the *equivalent eigenstrains or equivalent eigenstresses* [55].

When macroscopically homogeneous structures have microstructural inclusions or inhomogeneities, the mechanical or flow problems become challenging and can be solved analytically only in exceptional cases. As this work focuses on the macroscopic behavior of additively manufactured structures, the most common defects in the structures are

inhomogeneities. The changes in microstructural geometries and their properties may seriously affect the effective behavior and change macroscopic response, e.g., microstructural damage and crack propagation. For this case, only a handful of analytical solution exists, which is not directly applicable to all considered cases.

A common concept to determine the macroscopic response of heterogeneous components is *homogenization*. In this method microstructures are treated as a macroscopic material point characterized by *effective material properties* (see Figure 5.4). The response of these microstructures is "communicated" to the structure by appropriate averaging procedures and is referred to as *homogenization* [55].

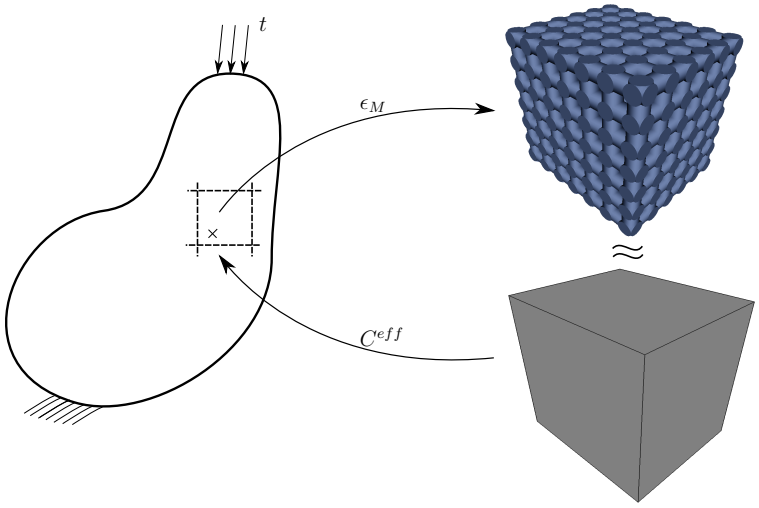

Figure 5.4: Concurent homogenization concept.

The central concept of the homogenization theories is RVE. An RVE must fulfill the following prerequisites [68]:

- Be representative of the macroscopic object on average.
- Contain a sufficient number of inhomogeneities to determine the overall behavior, which is independent of the surface values of traction and displacement.
- The effective response should be independent of the chosen macroscopic location and the size and shape of the chosen volume.

When the structure is highly irregular, the last requirement imposes an RVE to contain a statistically large number of defects and has a much larger dimension. The size of the RVE (l_{RVE}) should be chosen in such a way that it contains a sufficient number of heterogeneities (l) to represent an overall macroscopic behavior. At the same time, an RVE corresponds to a material point on the macroscopic scale (L). Therefore, the following scale separation principle can be formulated

$$l << l_{RVE} << L \tag{5.15}$$

A characteristic dimension of a microstructure is a defects' size or a distance between them. Then, fluctuations in the microstructure's internal fields vary with the so-called "wavelength" l. A dimension L is identifying the size of the macroscopic structure.

Such strict bounds on a dimension of RVE questions its existence in some cases. Furthermore, the size of an RVE depends on the macroscopic loading conditions, the boundary conditions imposed on the RVE and the presence of local physical phenomena, e.g., strain localization. If the size of representative volume element cannot be determined, a volume of a smaller size is usually extracted. In this case, the macroscopic mechanical properties obtained by performing homogenization on this smaller volume are called *apparent properties*.

5.3 Averaging theorems[a]

The homogenization theory's central postulate is that an RVE is a macroscopic material point. Thus, its fluctuating fields *on average* should be equal to those present on a macroscopic scale [55]:

$$\begin{aligned} \boldsymbol{\sigma}^M &= \langle \boldsymbol{\sigma} \rangle_\Omega = \frac{1}{\Omega} \int_\Omega \boldsymbol{\sigma}(\boldsymbol{x}) d\Omega \\ \boldsymbol{\varepsilon}^M &= \langle \boldsymbol{\varepsilon} \rangle_\Omega = \frac{1}{\Omega} \int_\Omega \boldsymbol{\varepsilon}(\boldsymbol{x}) d\Omega \end{aligned} \tag{5.16}$$

The notation $(\cdot)^M$ identifies the fields on the macroscopic level, while the fields without a superscript refer to those on the microscopic level. It is important to note that the averaging volume Ω is the total microscopic volume occupied by the matrix Ω_m and the heterogeneities Ω_h, i.e., $\Omega = \Omega_m \cup \Omega_h$. Such heterogeneities may be inclusions, voids, cracks, etc. (see Figure 5.1, where m indicates matrix material and h - heterogeneities).

The divergence theorem plays an important role in the homogenization theory. Integrals stated in Equation 5.16 can be transformed to surface integrals fulfilling necessary requirements. The divergence theorem can be formulated as follows:

If Ω is the volume bounded by a closed surface $d\Gamma$ and $\boldsymbol{A}$ is a vector function of position with continuous derivatives, then:

$$\int_\Omega \nabla \cdot \mathbf{A} \, d\Omega = \int_{d\Gamma} (\mathbf{A} \cdot \boldsymbol{n}) \, d\Gamma \tag{5.17}$$

where $\boldsymbol{n}$ is the positive normal vector to $d\Gamma$ [156].

According to the separation of scales defined in Equation 5.15, the RVE is small, the inertial and body forces are neglected at the microscopic scale. Thus, assuming $\sigma_{ik,k} = 0$ and $x_{j,k} = \delta_{jk}$, the following equation holds:

$$(x_j \sigma_{ik})_{,k} = x_{j,k} \sigma_{ik} + x_j \sigma_{ik,k} = \sigma_{ij} \tag{5.18}$$

where the coordinate system is positioned in the center of the RVE. If the volume Ω is closed and bounded, has a piecewise smooth boundary and the stress field $\boldsymbol{\sigma}$ is continuously differentiable within the domain $\boldsymbol{\sigma}$, then Equation 5.16 for the stresses can be

formulated in terms of a surface integral:

$$\begin{aligned}\boldsymbol{\sigma}^{\boldsymbol{M}} = \langle \sigma_{ij} \rangle_{\Omega} = \frac{1}{\Omega} \int\limits_{\Omega} \sigma_{ij}(\boldsymbol{x}) d\Omega = \frac{1}{\Omega} \int\limits_{\Omega} (x_j \sigma_{ik})_{,k} d\Omega = \\ = \frac{1}{\Omega} \int\limits_{d\Gamma} x_j \sigma_{ik} n_k \, d\Gamma = \frac{1}{\Omega} \int\limits_{dV} t_i x_j \, d\Gamma = \frac{1}{\Omega} \int\limits_{d\Gamma} \boldsymbol{t} \otimes \boldsymbol{x} \, d\Gamma\end{aligned} \tag{5.19}$$

where the definition of traction forces $t_i = \sigma_{ik} n_k$ is used.

In order to convert the volumetric integral over the strain field to a surface one, assume that the tensor F_{ijk} exists, which is defined as $F_{ijk} = u_i \delta_{jk}$. Then multiplying this tensor by a normal vector $\boldsymbol{n}$ yields:

$$\boldsymbol{F} \cdot \boldsymbol{n} = F_{ijk} n_k = u_i \delta_{jk} n_k = u_i n_j = \boldsymbol{u} \otimes \boldsymbol{n} \tag{5.20}$$

where $\otimes$ indicates the Kronecker product of two vectors. Applying the divergence theorem from Equation 5.17 to a divergence of tensor F_{ijk}, the following equality can be written:

$$\int\limits_{\Omega} \nabla \cdot \boldsymbol{F} d\Omega = \int\limits_{d\Gamma} (\mathbf{F} \cdot \boldsymbol{n}) \, d\Gamma \tag{5.21}$$

Using the definition of the tensor F_{ijk}, left side of the Equation 5.21 can be simplified as follows:

$$\int\limits_{\Omega} \nabla \cdot \boldsymbol{F} d\Omega = \int\limits_{\Omega} \sum_k \frac{\partial F_{ijk}}{\partial x_k} \, d\Omega = \int\limits_{\Omega} \sum_k \frac{\partial (u_i \delta_{jk})}{\partial x_k} \, d\Omega = \int\limits_{\Omega} \frac{\partial u_i}{\partial x_j} \, d\Omega = \int\limits_{\Omega} \nabla \boldsymbol{u} \, d\Omega \tag{5.22}$$

If the right side of the Equation 5.22 is replaced by Equation 5.20, the following equation can be formed:

$$\int\limits_{\Omega} \nabla \boldsymbol{u} \, d\Omega = \int\limits_{d\Gamma} (\mathbf{u} \otimes \boldsymbol{n}) \, d\Gamma \tag{5.23}$$

If vector $\boldsymbol{u}$ in Equation 5.23 is considered to be a displacement vector, then strains $\boldsymbol{\varepsilon}$ can be defined as follows:

$$\boldsymbol{\varepsilon} = \varepsilon_{ij} = \frac{1}{2} (u_{i,j} + u_{j,i}) = \nabla_s \boldsymbol{u} \tag{5.24}$$

where operator ∇_s is a symmetric gradient of vector $\boldsymbol{u}$. Thus, using Equation 5.23 the weighted average integral of the strains over the volume can be expressed similar to the integral over stress field:

$$\boldsymbol{\varepsilon}^{\boldsymbol{M}} = \langle \varepsilon_{ij} \rangle_{\Omega} = \frac{1}{\Omega} \int\limits_{\Omega} \boldsymbol{\varepsilon}(\boldsymbol{x}) \, d\Omega = \frac{1}{\Omega} \int\limits_{V} \nabla_s \boldsymbol{u} \, d\Omega = \frac{1}{\Omega} \int\limits_{d\Gamma} (\boldsymbol{u} \otimes_s \boldsymbol{n}) \, d\Gamma \tag{5.25}$$

where $\otimes_s$ is a symmetric Kronecker product.

Equation 5.19 and Equation 5.25 can be used to compute volumetric averages of strains and stresses over the RVE. The main assumption of continuously differentiable stress

and strain fields does not necessarily hold for heterogeneous materials due to a material discontinuity over the boundary Γ_h (see Figure 5.1). However, applying the sub-domain expansion as in Equation 5.1 and assuming equilibrium and displacement continuity along the surface Γ_h ($t_i^m \stackrel{!}{=} t_i^h$ and $u_i^h \stackrel{!}{=} u_i^m$), the general form of Equation 5.19 and Equation 5.25 remains valid.

To prove this, consider two domains with discontinuous material properties $\boldsymbol{C_h} \neq \boldsymbol{C_m}$ shown in Figure 5.1. The volumetric stress integral must be first split in two integrals over the volume Ω_h and Ω_m. The divergence theorem applied to the volumetric integral over Ω_m will consist of two integrals over the surface Γ_h and Γ_m [156]:

$$\int_{\Omega} (\cdot)\, d\Omega = \int_{\Omega_h} (\cdot)\, d\Omega + \int_{\Omega_m} (\cdot)\, d\Omega = \int_{\Gamma_h} (\cdot)\, d\Gamma + \left(\int_{\Gamma_m} (\cdot)\, d\Gamma + \int_{\Gamma_h} (\cdot)\, d\Gamma \right) \tag{5.26}$$

In Equation 5.26 the integral over the surface Γ_h comes twice, however it is different only by the normal vector $\boldsymbol{n}$ of this surface. Considering $n_h = -n_m$ Equation 5.19 can be rewritten:

$$\begin{aligned} \frac{1}{\Omega} \int_{\Omega} \sigma_{ij}(\boldsymbol{x}) d\Omega &= \frac{1}{\Omega} \left(\int_{\Omega_h} \sigma_{ij}(\boldsymbol{x}) d\Omega + \int_{\Omega_m} \sigma_{ij}(\boldsymbol{x}) d\Omega \right) = \\ &= \frac{1}{\Omega} \left(\int_{\Gamma_h} t_i x_j \, d\Gamma + \left(\int_{\Gamma_m} t_i x_j \, d\Gamma - \int_{\Gamma_h} t_i x_j \, d\Gamma \right) \right) = \\ &= \frac{1}{\Omega} \left(\int_{\Gamma_m} t_i x_j \, d\Gamma + \int_{\Gamma_h} \left(t_i^h - t_i^m \right) x_j \, d\Gamma \right) \end{aligned} \tag{5.27}$$

Under the condition that the equilibrium along surface Γ_h is fulfilled ($t_i^m \stackrel{!}{=} t_i^h$), the second surface integral in Equation Equation 5.27 vanishes and the following equality for two domains with different material properties holds:

$$\frac{1}{\Omega} \int_{\Omega} \sigma_{ij}(\boldsymbol{x}) d\Omega = \frac{1}{\Omega} \int_{\Gamma_m} t_i x_j \, d\Gamma \tag{5.28}$$

Equation 5.25 can be rewritten analogously:

$$\begin{aligned}\frac{1}{\Omega}\int_{\Omega}\varepsilon_{ij}(\boldsymbol{x})d\Omega &= \frac{1}{\Omega}\left(\int_{\Omega_h}\varepsilon_{ij}(\boldsymbol{x})d\Omega+\int_{\Omega_m}\varepsilon_{ij}(\boldsymbol{x})d\Omega\right)= \\ &= \frac{1}{\Omega}\int_{\Gamma_h}\frac{1}{2}\left(u_i n_j+u_j n_i\right)\,d\Gamma+ \\ &+\frac{1}{\Omega}\left(\int_{\Gamma_m}\frac{1}{2}\left(u_i n_j+u_j n_i\right)\,d\Gamma-\int_{\Gamma_h}\frac{1}{2}\left(u_i n_j+u_j n_i\right)\,d\Gamma\right)= \\ &= \frac{1}{\Omega}\left(\int_{\Gamma_m}\frac{1}{2}\left(u_i n_j+u_j n_i\right)\,d\Gamma+\int_{\Gamma_h}\frac{1}{2}\left(\left(u_i^h-u_i^m\right)n_j+\left(u_j^h-u_j^m\right)n_i\right)\,d\Gamma\right)\end{aligned} \tag{5.29}$$

The last integral accounting for the jump in the displacements vanishes due to the continuity requirement over the interface Γ_h ($u_i^h \stackrel{!}{=} u_i^m$) and the following boundary integral is valid:

$$\frac{1}{\Omega}\int_{\Omega}\varepsilon_{ij}(\boldsymbol{x})d\Omega = \frac{1}{\Omega}\int_{\Gamma_m}\frac{1}{2}\left(u_i n_j+u_j n_i\right)\,d\Gamma \tag{5.30}$$

Considering yet a Finite Element or Finite Cell approximation, a continuous equilibrium is not necessarily established along Γ_h if the displacement-based approximations are applied to obtain the primary variables. While C^0 continuity across the primary variables' element boundaries is guaranteed, only discontinuous stresses and strain fields can be expected. Taking into consideration Equations 5.19 and 5.25, displacements and tractions at the boundary of evaluation need to be continuous. The direct computation of the tractions in the boundary integral of Equation 5.19 involves a lower degree of the stress extrapolation than the order of the shape functions used for the discretization of the primary variables. This results in poor accuracy and a lower convergence rate of the first derivatives of the primary variables.

This problem can be tackled by many approaches, for example using NURBS as basis functions to ensure higher continuity between the elements. However, as the nodal force equilibrium always holds for any finite element or finite cell mesh for standard approximations [12], the following equation is used:

$$\langle\boldsymbol{\sigma}\rangle_{\Omega} = \frac{1}{\Omega}\int_{d\Omega}\boldsymbol{t}\otimes\boldsymbol{x}\,d\Gamma = \frac{1}{\Omega}\sum_{i=1}^{n_{nodes}}\boldsymbol{t}\otimes\boldsymbol{x} \tag{5.31}$$

where

$$\boldsymbol{t}_{el} = \int_{\Omega_{el}}\boldsymbol{B}^T\boldsymbol{\sigma}\,d\Omega_{el} \tag{5.32}$$

For numerical reasons, it is convenient to evaluate Equation 5.32 after the computation of the finite cell solution as $\mathbf{K}\boldsymbol{u}$ and extract the corresponding nodal tractions during a postprocessing step. This approach is described in a greater detail in [27].

5.4 Hill-Mandel macro-homogeneity principle[a]

In order to connect macroscopic and microscopic quantities the Hill-Mandel condition can be formulated. The general Hooke's law on a microscopical level is expressed by:

$$\sigma_{ij}(\boldsymbol{x}) = C_{ijkl}(\boldsymbol{x})\varepsilon_{kl}(\boldsymbol{x}) \tag{5.33}$$

Given the definition of the effective material properties in Equation 5.16 the effective elasticity tensor C^*_{ijkl} can be introduced relating the macroscopic fields:

$$\sigma^M_{ij} = C^*_{ijkl}\varepsilon^M_{kl} \tag{5.34}$$

To allow an interpretation of C^*_{ijkl} as a material characteristic on the macroscopic level, the condition of strain energy equality must be satisfied [55]. The average strain energy density in the Representative Volume Element Ω must be equal to the strain energy density in the macroscopic point:

$$\frac{1}{2}\sigma^M_{ij}\varepsilon^M_{kl} = \int_\Omega \frac{1}{2}\sigma_{ij}\varepsilon_{kl}d\Omega \tag{5.35}$$

Equation 5.35 can be rewritten using the definition in Equation 5.16 as:

$$\langle\sigma_{ij}\rangle_\Omega \langle\varepsilon_{kl}\rangle_\Omega = \langle\sigma_{ij}\varepsilon_{kl}\rangle_\Omega \tag{5.36}$$

Equation 5.36, known as a Hill condition [68] can be expressed in a more conventional form. Let us assume that a split of total microscopic fields on an average and a fluctuating part exists:

$$\begin{aligned}\sigma_{ij}(\boldsymbol{x}) &= \langle\sigma_{ij}\rangle_\Omega + \widetilde{\sigma}_{ij}(\boldsymbol{x})\\ \varepsilon_{ij}(\boldsymbol{x}) &= \langle\varepsilon_{ij}\rangle_\Omega + \widetilde{\varepsilon}_{ij}(\boldsymbol{x})\end{aligned} \tag{5.37}$$

Inserting Equation 5.37 into Equation 5.36 yields:

$$\begin{aligned}\Big\langle\big(\langle\sigma_{ij}\rangle_\Omega + \widetilde{\sigma}_{ij}(\boldsymbol{x})\big)\big(\langle\varepsilon_{ij}\rangle_\Omega + \widetilde{\varepsilon}_{ij}(\boldsymbol{x})\big)\Big\rangle_\Omega &= \langle\sigma_{ij}(\boldsymbol{x})\rangle_\Omega \langle\varepsilon_{kl}(\boldsymbol{x})\rangle_\Omega\\ \langle\widetilde{\sigma}_{ij}(\boldsymbol{x})\widetilde{\varepsilon}_{ij}(\boldsymbol{x})\rangle_\Omega + \langle\sigma_{ij}\rangle_\Omega \langle\widetilde{\varepsilon}_{ij}(\boldsymbol{x})\rangle_\Omega &+\\ \langle\widetilde{\sigma}_{ij}(\boldsymbol{x})\rangle_\Omega \langle\varepsilon_{ij}\rangle_\Omega + \langle\sigma_{ij}(\boldsymbol{x})\rangle_\Omega \langle\varepsilon_{kl}(\boldsymbol{x})\rangle_\Omega &= \langle\sigma_{ij}(\boldsymbol{x})\rangle_\Omega \langle\varepsilon_{kl}(\boldsymbol{x})\rangle_\Omega\end{aligned} \tag{5.38}$$

As the average strain fluctuations and average stress fluctuations are zero due to the definition of RVE, Equation 5.38 is reduced to the following equation:

$$\langle\widetilde{\sigma}_{ij}(\boldsymbol{x})\widetilde{\varepsilon}_{ij}(\boldsymbol{x})\rangle_\Omega = 0 \tag{5.39}$$

Equation 5.39 requires the stress fluctuations not to do any work on the strain fluctuations on average.

Consider Equation 5.18, Equation 5.23 and the following identity of tensor calculus:

$$div\,(\boldsymbol{A}\boldsymbol{b}) = div\,(\boldsymbol{A}) \cdot \boldsymbol{b} + \boldsymbol{A} : grad\,(\boldsymbol{b}) \tag{5.40}$$

where the commutativity of the double-dot product allows a swap of the last term to $grad\,(\boldsymbol{b}) : \boldsymbol{A}$ [24]. Rewriting Equation 5.39, the following can be obtained (for simplicity $\sigma_{ij}(\boldsymbol{x})$ and $\varepsilon_{ij}(\boldsymbol{x})$ are replaced by σ_{ij} and ε_{ij}):

$$\begin{aligned}
&\frac{1}{\Omega}\int_{\Omega}\left(\sigma_{ij} - \langle\sigma_{ij}\rangle_{\Omega}\right)\left(\varepsilon_{ij} - \langle\varepsilon_{ij}\rangle_{\Omega}\right) d\Omega = 0\\
&\frac{1}{\Omega}\left(\int_{\Omega}\sigma_{ij}\varepsilon_{ij}\,d\Omega - \int_{\Omega}\langle\sigma_{ij}\rangle_{\Omega}\,\varepsilon_{ij}\,d\Omega - \int_{\Omega}\sigma_{ij}\,\langle\varepsilon_{ij}\rangle_{\Omega}\,d\Omega + \int_{\Omega}\langle\sigma_{ij}\rangle_{\Omega}\,\langle\varepsilon_{ij}\rangle_{\Omega}\,d\Omega\right) = 0\\
&\frac{1}{\Omega}\left(\int_{\Omega}(u_i\sigma_{ij})_{,j}\,d\Omega - \int_{\Omega}\langle\sigma_{ij}\rangle_{\Omega}\,\frac{1}{2}\left(u_{i,j} + u_{j,i}\right)\,d\Omega\right) -\\
&\qquad - \frac{1}{\Omega}\left(\int_{\Omega}\left(x_k\sigma_{ij}\right)_{,j}\langle\varepsilon_{ik}\rangle_{\Omega}\,d\Omega + \int_{\Omega}x_{k,j}\,\langle\sigma_{ij}\rangle_{\Omega}\,\langle\varepsilon_{ik}\rangle_{\Omega}\,d\Omega\right) = 0\\
&\frac{1}{\Omega}\left(\int_{\Gamma}u_i\sigma_{ij}n_j\,d\Gamma - \int_{\Gamma}\langle\sigma_{ij}\rangle_{\Omega}\,\frac{1}{2}\left(u_in_j + u_jn_i\right)\,d\Gamma\right) -\\
&\qquad - \frac{1}{\Omega}\left(\int_{\Gamma}x_k\sigma_{ij}n_j\,\langle\varepsilon_{ik}\rangle_{\Omega}\,d\Gamma + \int_{\Gamma}x_kn_j\,\langle\sigma_{ij}\rangle_{\Omega}\,\langle\varepsilon_{ik}\rangle_{\Omega}\,d\Gamma\right) = 0\\
&\frac{1}{\Omega}\int_{\Gamma}\left(u_i\sigma_{ij} \;- u_i\,\langle\sigma_{ij}\rangle_{\Omega} - \sigma_{ij}\,\langle\varepsilon_{ik}\rangle_{\Omega}\,x_k + \langle\sigma_{ij}\rangle_{\Omega}\,\langle\varepsilon_{ik}\rangle_{\Omega}\,x_k\right)n_j\,d\Gamma = 0\\
&\frac{1}{\Omega}\int_{\Gamma}\left(u_i - \langle\varepsilon_{ik}\rangle_{\Omega}\,x_k\right)\left(\sigma_{ij} - \langle\sigma_{ij}\rangle_{\Omega}\right)n_j\,d\Gamma = 0
\end{aligned} \tag{5.41}$$

Equation 5.41 shows that the fluctuations of the micro-fields along the boundary of an RVE must be energetically equivalent to their averages (see Figure 5.5).

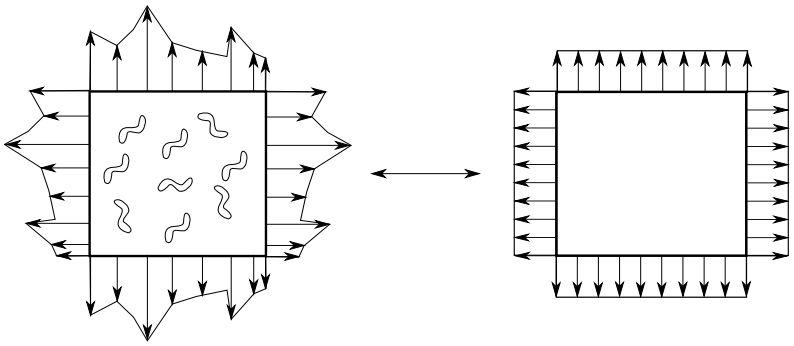

Figure 5.5: Equivalence of the fluctuating fields and average ones.

5.5 Boundary conditions in homogenization theory[a]

The Hill-Mandel macro-homogeneity principle can be satisfied a priori defining appropriate boundary conditions for the microscopic initial boundary value problem [68]. The following boundary conditions are widely used and are further referred as *conventional boundary conditions* in this thesis [128]:

- Kinematic Uniform Boundary Conditions (KUBC)

$$\boldsymbol{u}|_\Gamma = \boldsymbol{\varepsilon}^M \boldsymbol{x} \tag{5.42}$$

- Static Uniform Boundary Conditions (SUBC)

$$\boldsymbol{t}|_\Gamma = \boldsymbol{\sigma}^M \boldsymbol{n} \tag{5.43}$$

- Periodic Boundary Conditions (PBC)

$$\begin{aligned} \boldsymbol{u}(\boldsymbol{x}^+)|_\Gamma - \boldsymbol{u}(\boldsymbol{x}^-)|_\Gamma &= \boldsymbol{\varepsilon}^M \Delta\boldsymbol{x} \\ \boldsymbol{t}(\boldsymbol{x}^+)|_\Gamma + \boldsymbol{t}(\boldsymbol{x}^-)|_\Gamma &= 0 \end{aligned} \tag{5.44}$$

The averaging stress theorem (see Equation 5.19) is only meaningful if self-equilibrating forces are applied through Equation 5.43 (see [113]). However, for the uniform kinematic condition as in Equation 5.42, a requirement of them to be self-compatible is not necessary. Furthermore, it was proven that the rigid-body rotations or translations' presence does not influence the relation between the average stresses and strains [113].

It is important to note that there is a group of Mixed uniform boundary conditions (MUBC), which also satisfy the Hill condition. However, this group is finely tuned for a specific RVE structure and the material tensor symmetries (e.g., [63]). Therefore, they will not be considered in this work.

Although, all three boundary conditions satisfy the Hill-Mandel principle a priori, they do not lead to the same effective estimates. The size of the RVE as it is stated in section 5.2 is influenced by applied boundary conditions. Only under the condition that the numerical volume is an actual representative volume element, all of the estimates converge to the effective tensor [144]:

$$\boldsymbol{C}_{SUBC} = \boldsymbol{C}_{KUBC} = \boldsymbol{C}_{PBC} = \boldsymbol{C}^* \tag{5.45}$$

However, in most applications, the size of RVE is not known a priori and sometimes even hard to be defined. But there exist inequalities relating the results of the effective estimates via different boundary conditions [64]. The so-called *boundary conditions hierarchy* provides bound estimates for the analyzed volumes' intermediate size. The first relation indicates that an effective elasticity tensor is always bounded by the apparent tensors estimated by KUBC and SUBC:

$$\boldsymbol{C}_{SUBC} \leq \boldsymbol{C}^* \leq \boldsymbol{C}_{KUBC} \tag{5.46}$$

Operator $\leq$ in Equation 5.46 for Voigt notation means that the matrix quadratic forms:

$$Q_1 = \boldsymbol{\sigma}^T \left(\boldsymbol{C}^* - \boldsymbol{C}_{SUBC} \right) \boldsymbol{\sigma} \tag{5.47}$$

$$Q_2 = \boldsymbol{\sigma}^T \left(\boldsymbol{C}_{KUBC}{}^* - \boldsymbol{C}^* \right) \boldsymbol{\sigma} \tag{5.48}$$

should be positive semi-definite [64]. The semi-positive definiteness of the quadratic forms can be determined either by the eigenvalues or the semi-positivity of the principal minors of the matrix $\left(\boldsymbol{C}^* - \boldsymbol{C}_{SUBC}\right)$ and $\left(\boldsymbol{C}_{KUBC} - \boldsymbol{C}^*\right)$.

Next, for periodic microstructures, the exact effective stiffness can be estimated with the application of PBC (see e.g. [127, 147]). The gap between $\boldsymbol{C}_{KUBC}$ and $\boldsymbol{C}_{SUBC}$ remains significant [157]. The hierarchy relation is then summarized as follows:

$$\boldsymbol{C}_{SUBC} \leq \boldsymbol{C}_{PBC} \leq \boldsymbol{C}_{KUBC} \tag{5.49}$$

Thus, KUBC always overestimates, while SUBC underestimates the effective properties for the volumes smaller than an actual RVE size. The position of the PBC concerning the effective material tensor is not known. Only for fully periodic structures, they deliver an exact estimate, i.e., $C^* = C_{PBC}$. However, it is widely accepted that the periodic conditions can also be applied to non-periodic geometries, thus, leading to reliable estimates also in this case [115].

Although the definition of the appropriate boundary conditions completes the formulation of the homogenization theory, it is important to identify, how they are applied to compute the whole material tensor. In a general case, an anisotropic effective elasticity tensor $\boldsymbol{C}^*$ contains 36 (21 unknowns due to the considered symmetry) unknown constants:

$$\begin{bmatrix} \sigma^M_{11} \\ \sigma^M_{22} \\ \sigma^M_{33} \\ \sigma^M_{12} \\ \sigma^M_{23} \\ \sigma^M_{13} \end{bmatrix} = \begin{bmatrix} C^*_{1111} & C^*_{1122} & C^*_{1133} & C^*_{1112} & C^*_{1123} & C^*_{1113} \\ C^*_{2211} & C^*_{2222} & C^*_{2233} & C^*_{2212} & C^*_{2223} & C^*_{2213} \\ C^*_{3311} & C^*_{3322} & C^*_{3333} & C^*_{3312} & C^*_{3323} & C^*_{3313} \\ C^*_{1211} & C^*_{1222} & C^*_{1233} & C^*_{1212} & C^*_{1223} & C^*_{1213} \\ C^*_{2311} & C^*_{2322} & C^*_{2333} & C^*_{2312} & C^*_{2323} & C^*_{2313} \\ C^*_{1311} & C^*_{1322} & C^*_{1333} & C^*_{1312} & C^*_{1323} & C^*_{1313} \end{bmatrix} \begin{bmatrix} \varepsilon^M_{11} \\ \varepsilon^M_{22} \\ \varepsilon^M_{33} \\ 2\varepsilon^M_{12} \\ 2\varepsilon^M_{23} \\ 2\varepsilon^M_{13} \end{bmatrix} \tag{5.50}$$

The shear strains are multiplied with two in Equation 5.50 due to the transition to Voigt notation. By applying one of the above-mentioned boundary conditions, only one pair of $\langle\boldsymbol{\sigma}\rangle_\Omega$ and $\langle\boldsymbol{\varepsilon}\rangle_\Omega$ will be obtained, which leads to 6 equations with 21 unknowns. Therefore, usually 6 independent loading cases need to be constructed [189]. The following is an example of construction of such cases for KUBC (see Equation 5.42), where the initial macroscopic strains are varied by a small increment $\delta\varepsilon$:

$$\boldsymbol{\varepsilon}_l = \boldsymbol{\varepsilon}^M + \delta\varepsilon \boldsymbol{e}_l \tag{5.51}$$

where vector $\boldsymbol{e}_l$ denotes the vector with a 1 in the $l-$th coordinate and 0's elsewhere. Other types of boundary conditions are applied in the same way.

The first approach to solve the problem of determining an effective elasticity tensor $\boldsymbol{C}^*$ is to construct the following system of equation:

$$\langle\boldsymbol{\sigma}\rangle_l = \boldsymbol{C}^* \cdot \langle\boldsymbol{\varepsilon}\rangle_l \tag{5.52}$$

where $\langle\boldsymbol{\sigma}\rangle_l, \langle\boldsymbol{\varepsilon}\rangle_l$ are matrices with every column representing the averaged stress and strain fields for load case l. In this case, there are enough equations to have $\boldsymbol{C}^*$ uniquely defined via a *direct inversion*.

Another approach is to apply a *finite difference scheme*, where 7 loading cases are constructed with an addition of a "no-increment" loading case to the ones from above. As an example, by subtracting the response of case 0 from case 1, the following relation can be obtained:

$$\langle \boldsymbol{\sigma} \rangle_l - \langle \boldsymbol{\sigma} \rangle_0 = \boldsymbol{C}^* \cdot \delta\varepsilon \boldsymbol{e}_l \tag{5.53}$$

which can be uniquely reduced to the following generalized equation:

$$C_{ij,l} = \frac{\langle \sigma_{ij} \rangle_{l,\Omega} - \langle \sigma_{ij} \rangle_{l-1,\Omega}}{|| \langle \boldsymbol{\varepsilon} \rangle_{l,\Omega} - \langle \boldsymbol{\varepsilon} \rangle_{l-1,\Omega} ||_{L_2}} \tag{5.54}$$

where l - indicates the column of the elasticity tensor and the corresponding load case. The denominator of Equation 5.54 is considered as an L_2 norm of a vector difference of two load cases, which in an ideal case would reduce to the small increment $\delta\varepsilon$ from Equation 5.53.

These two approaches will provide an equivalent solution up to numerical precision for a linear elastic homogenization using conventional boundary conditions. However, when the window method is used, the last approach will deliver a slightly different result, which will be discussed in section 5.7.

5.6 Voids in the Representative Volume Element

Voids as inhomogeneities in an RVE require special consideration.

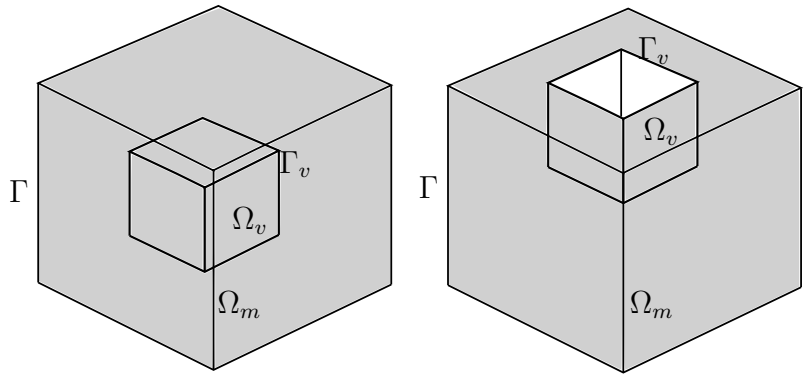

Figure 5.6: Voids in the Representative Volume Element.

For simplicity, first, consider an RVE with the cavity, completely enclosed in the volume (see Figure 5.6, left). Following [157] voids are assumed to be an infinitely soft heterogeneity with vanishing stiffness:

$$\boldsymbol{C}_h = \boldsymbol{C}_v \approx \boldsymbol{0} \tag{5.55}$$

The total volume of an RVE (Ω) consist of the volume of the void (Ω_v) and the matrix (Ω_m):

$$\Omega = \Omega_m \cup \Omega_v \tag{5.56}$$

The boundary of the void (Γ_v) does not intersect the boundary of an RVE (Γ), i.e. $\Gamma_v \cap \Gamma = \emptyset$. The matrix' volume boundary Γ_m consists of two parts: an outer boundary which coincides with the boundary of the RVE Γ, and an interior boundary, which coincides with the boundary of the void. For clarification, Figure 5.7 shows a 2D view on this problem with the definition of the normals (adapted from [113]). The normals are defined as positive if they point outwards of the volume they bound – and as negative otherwise. The notation in Figure 5.7 should not be confused with the gap between domains, i.e., Γ_v and Γ_m are coinciding, however, depicted with the gap in order to clarify the $\boldsymbol{n}$ definitions.

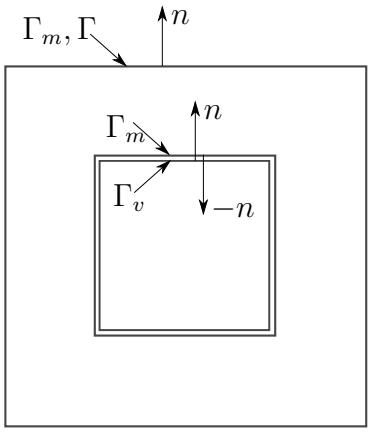

Figure 5.7: Definition of normals and boundaries.

If the cavity is truly void, the strain field in the cavity is ambiguous. However, using the definition of the void from Equation 5.55 and the sub-domain expansion Equation 5.16, the strain average over the total volume can be rewritten as follows:

$$\begin{aligned}
\langle \sigma_{ij} \rangle_\Omega &= c_m \langle \sigma_{ij} \rangle_{\Omega_m} + c_v \cancelto{0}{\langle \sigma_{ij} \rangle_{\Omega_v}} = c_m \langle \sigma_{ij} \rangle_{\Omega_m} = \int_\Gamma t_i x_j d\Gamma + \int_{\Gamma_M} \cancelto{0}{t_i} x_j d\Gamma = \int_\Gamma t_i x_j d\Gamma \\
\langle \varepsilon_{ij} \rangle_\Omega &= c_m \langle \varepsilon_{ij} \rangle_{\Omega_m} + c_v \langle \varepsilon_{ij} \rangle_{\Omega_v} = c_m \langle \varepsilon_{ij} \rangle_{\Omega_m} + \int_{\Gamma_v} \frac{1}{2} (u_i n_j + u_j n_i) \, d\Gamma = c_m \langle \varepsilon_{ij} \rangle_{\Omega_m} + \langle \varepsilon \rangle_{\Omega_c} = \\
&= \int_\Gamma \frac{1}{2} (u_i n_j + u_j n_i) \, d\Gamma - \int_{\Gamma_m} \frac{1}{2} (u_i n_j + u_j n_i) \, d\Gamma + \int_{\Gamma_v} \frac{1}{2} (u_i n_j + u_j n_i) \, d\Gamma \\
&= \int_\Gamma \frac{1}{2} (u_i n_j + u_j n_i) \, d\Gamma
\end{aligned} \tag{5.57}$$

If the cavities are traction free, then the average macro-stress is equal to the weighted stress average in a matrix. However, the strains are not vanishing within the cavity subdomain and can be called a cavity strain ε_c (see Section 5 in [113]). The cavity strain is an average of additional strain fluctuations induced by the deformation of the cavity boundary compared to the deformation state of a purely homogeneous domain [48].

Thus, the cavity strain represents an equivalent eigenstrain as introduced by Eshelby (refer to [55] and [113]).

Equation 5.57 shows that when cavities are completely inside an RVE and do not intersect with its boundaries, overall average strains and stresses are entirely determined through the fields residing at the outer boundary of the RVE Γ_m.

When an intersection between a boundary of a void and a boundary of an RVE is not empty, i.e., $\Gamma_v \cap \Gamma \neq \emptyset$, the averaging relations in Equation 5.57 remain valid. However, its definitions in terms of boundary integrals become rather cumbersome as a split into $\Gamma_v \cap \Gamma$, and $\Gamma/(\Gamma_v \cap \Gamma)$ needs to be considered.

Nevertheless, the definition of the void as an infinitely soft medium provides a unique definition of the strain and stress fields in the required segment $\Gamma_v \cap \Gamma$. Using the Finite Cell Method described in chapter 4 for this case is advantageous as it mimics the assumption of the voids being a material with vanishing stiffness (see Equation 5.55). The indicator function $\alpha(\boldsymbol{x})$ in the Finite Cell Formulation can be interpreted as the inclusion of an infinitely soft material. A displacement field in the void domain is, thus, computed naturally. An extension of a displacement field to the void domain must be consistent with the formulation of the boundary value problem. Thus, strain energy consistency is preserved naturally in the Finite Cell Method [129].

The boundary conditions mentioned in section 5.4 are also affected by the presence of the voids at the RVE boundary. The Kinematic Uniform Boundary Conditions are not required to be self-compatible (see section 5.4) and can be applied to the cases with the voids in the boundary in a standard way. In this case, the average macroscopic strain is defined naturally in terms of the macro-strains applied at the boundary:

$$\langle \boldsymbol{\varepsilon} \rangle_\Omega = \int_\Gamma \boldsymbol{\varepsilon}^M \boldsymbol{x} d\Gamma = \boldsymbol{\varepsilon}^M \tag{5.58}$$

assuming a compatible extension of the displacement field to the void domain.

The case of antisymmetric positioning of the voids on the boundary of an RVE was mentioned in [33], where the specific mixed boundary conditions were proposed. As KUBC are usually overestimating the effective stiffness (see Equation 5.46), the mixed boundary conditions could take advantage of the order relation and get a closer approximation. However, for the case of random voids intersection, this condition is complex to derive.

Static Uniform Boundary Conditions are very difficult to apply in such cases. When the voids are crossing the boundaries antisymmetric, the only meaningful way to prescribe this boundary condition is as follows:

$$\begin{aligned} \boldsymbol{t} &= \boldsymbol{\sigma}^M \boldsymbol{n} \quad && on \quad && \Gamma/(\Gamma_v \cap \Gamma) \\ \boldsymbol{t} &= \boldsymbol{0} \quad && on \quad && \Gamma_v \cap \Gamma \end{aligned} \tag{5.59}$$

Then the SUBC are not fulfilling the requirement of the static equilibrium and are not self-equilibrating as described in section 5.4:

$$\int_\Gamma \boldsymbol{\sigma} \boldsymbol{n} \, d\Gamma = \boldsymbol{0} \tag{5.60}$$

When the voids are symmetrically crossing the boundary of the RVE, the static equilibrium is fulfilled, and the applied loads are self-equilibrating. However, by applying this condition to the material with vanishing stiffness, the numerical solution is almost unattainable. Furthermore, the average strain can only be computed if an extension of the displacement field into the void domain is assumed (see Equation 5.57). Even when the volumetric integral is expressed with the help of a boundary integral, the part of this integral over $\Gamma_v \cap \Gamma$ has to be computed (see, e.g., [17]).

The Periodic Boundary Conditions are widely used even if the periodicity requirement does not hold (see [115] and the literature therein). The application of the PBC requires identical meshes on the polar RVE surfaces ($\boldsymbol{x}^+$ and $\boldsymbol{x}^-$, see Figure 5.8). This becomes rather cumbersome and sometimes even impossible when the RVE has a non-periodic microstructure. There is broad research in this field. The periodic boundary condition for the problems with the arbitrary non-conforming meshes was studied by [183] through a master/slave concept, by [91] using weak enforcement of PBC and by [170] using the local implementation. However, these methods do not solve the problem of PBC when there are many voids present at the boundary. Nguyen introduced a method treating such cases based on a polynomial interpolation [117].

Nevertheless, the finite cell mesh consists of Cartesian grids with coupled nodes on all six surfaces of an RVE independently on its microstructure. Figure 5.8 shows a simplified representation of a volume with an immersed mesh of 4×4 elements. The boundaries opposite to each other are indicated as Γ^+ and Γ^-. On these boundaries, the $\boldsymbol{n}$ vectors are pointing in the opposite directions. However, they are of the same size. Due to a natural construction of the mesh, the nodes $\boldsymbol{x}^+$ and $\boldsymbol{x}^-$ are always coupled. This simplifies the search of such coupled nodes and allows to apply PBC without any additional effort.

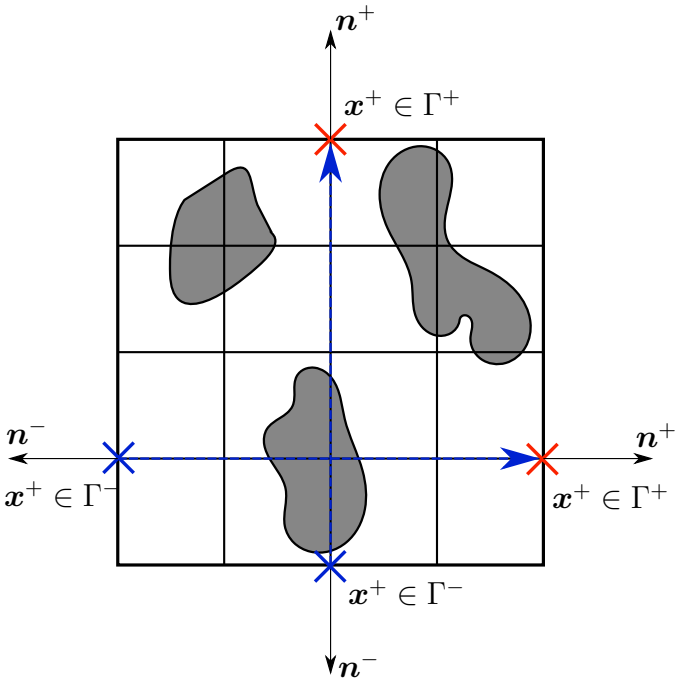

Figure 5.8: Application of Periodic Boundary Conditions with FCM (adapted from [115]).

5.7 Window method

Another method to perform numerical homogenization on the RVE with random pores at the boundary is to apply *window method*. This method was extensively studied by Hain [58], and Sehlhorst [150] and in the literature cited therein.

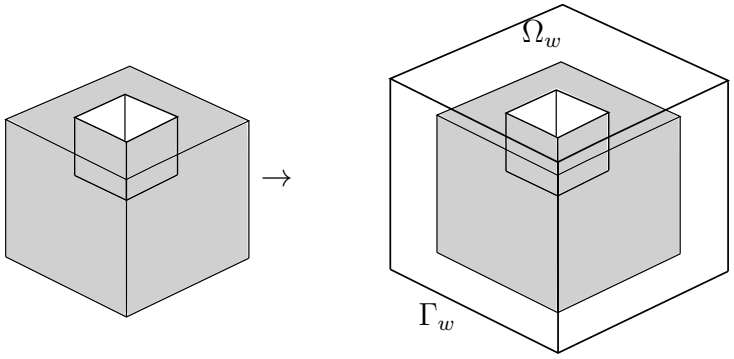

Figure 5.9: The concept of a window method.

The window method resembles the self-consistency approach from analytical homogenization techniques. An RVE Ω is embedded into a larger domain Ω_w with a priori unknown effective properties, which have to be determined iteratively. Then, the following boundary value problem for a micro-structure can be formulated:

$$\begin{aligned} div\,(\boldsymbol{\sigma}) &= 0 \qquad \text{on } \Omega_w \cup \Omega \\ \boldsymbol{\sigma} &= \begin{cases} \boldsymbol{C}(\boldsymbol{x}) : \boldsymbol{\varepsilon} & \text{on } \Omega_w \\ \boldsymbol{C}^* : \boldsymbol{\varepsilon} & \text{on } \Omega \end{cases} \\ \boldsymbol{\varepsilon} &= \nabla_s \boldsymbol{u} \\ \boldsymbol{u}^{I-VI}|_{\Gamma_w} &= \boldsymbol{\varepsilon}^M \boldsymbol{x} \quad \text{on } \Gamma_w \end{aligned} \tag{5.61}$$

The boundary conditions in Equation 5.61 can be replaced by any other boundary condition satisfying Hill criteria, e.g. Equation 5.43, Equation 5.44 etc.. The only difference is that the boundary conditions are now applied on the window domain's outer boundary Γ_w. In the following, these boundary conditions will be referred to as *window boundary conditions*.

This is advantageous for non-periodic RVEs, as the window domain is homogeneous and void-free. Thus, the boundary conditions are straightforward to apply. Furthermore, it is proven that the boundary effects causing large dispersion between KUBC and SUBC with the increase of the window size vanish:

$$\boldsymbol{C}^{w(0)}_{SUBC} \leq \boldsymbol{C}^{w(1)}_{SUBC} \leq \boldsymbol{C}^{w(2)}_{SUBC} \leq ... \leq \boldsymbol{C}^* \leq ... \leq \boldsymbol{C}^{w(2)}_{KUBC} \leq \boldsymbol{C}^{w(1)}_{KUBC} \leq \boldsymbol{C}^{w(0)}_{KUBC}$$

where window size $w(i)$ is smaller than $w(i+1)$. Therefore, even for a KUBC applied at the window's boundary, the effective properties converge faster towards the effective estimate.

Moreover, the same hierarchy of the boundary conditions holds [165]:

$$\boldsymbol{C}_{SUBC} \leq \boldsymbol{C}^{w}_{SUBC} \leq \boldsymbol{C}^{w}_{PBC} \leq \boldsymbol{C}^{w}_{KUBC} \leq \boldsymbol{C}_{KUBC} \tag{5.62}$$

The position of an apparent elasticity tensor $\boldsymbol{C}_{PBC}$ in the order relation is unknown [165].

An important requirement of the window method is the self-consistency of the window. The elastic property of the window must be $\boldsymbol{C}^{*}$ under convergence of the iterations. Only if this condition is satisfied, the domain of averaging can be either Ω or $\Omega \cup \Omega_w$. Following [166] and assuming no self-consistency holds:

$$\begin{aligned} \langle \boldsymbol{\sigma} \rangle_{\Omega \cup \Omega_w} &= c_w \langle \boldsymbol{\sigma} \rangle_{\Omega_w} + c_{RVE} \langle \boldsymbol{\sigma} \rangle_{\Omega} = c_w \boldsymbol{C}_w : \langle \boldsymbol{\varepsilon} \rangle_{\Omega_w} + c_{RVE} \boldsymbol{C}^{*} : \langle \boldsymbol{\varepsilon} \rangle_{\Omega_w} = \\ &= \boldsymbol{C}^{*} \left(c_w \boldsymbol{C}_w \boldsymbol{C}^{*-1} \langle \boldsymbol{\varepsilon} \rangle_{\Omega_w} + c_{RVE} \langle \boldsymbol{\varepsilon} \rangle_{\Omega_w} \right) \neq \boldsymbol{C}^{*} : \langle \boldsymbol{\varepsilon} \rangle_{\Omega \cup \Omega_w} \end{aligned} \tag{5.63}$$

As the averaging needs to be performed at every iteration, the domain of averaging during the iteration procedure must be the RVE itself to satisfy the Hill condition in Equation 5.36. The averages of the strain and stress fields are, thus, computed according to Equation 5.25 and Equation 5.19. It is important to note that when the voids cross the boundary, the average strains can be determined considering the window's inner boundary instead of the outer boundary of the RVE. This is valid due to the compatibility of the displacement fields across the boundary. However, the stress fields must be computed on the outer boundary of the RVE itself.

As mentioned before, the homogenized quantity can be determined either using a direct inversion of constructed average stress and strain matrices as in Equation 5.52 or using a finite difference scheme from Equation 5.54. These two approaches lead to an equivalent result if $(\boldsymbol{\varepsilon}_l - \boldsymbol{\varepsilon}_{l-1}) \approx \beta \boldsymbol{e}_l$. However, this does not hold for the iterative process when the window domain is present. Therefore, the denominator in Equation 5.54 is formulated in the L_2 norm. This formulation will provide an approximation to a $\boldsymbol{C}^{*}$, which is quite close to the one computed by a direct inverse. However, this approach must be carefully considered for the window method as the order relation formulated in Equation 5.62 does not hold anymore. Although the error is relatively small, the bounds in Equation 5.62 are swapped. This phenomenon will be further illustrated in the numerical examples.

Together with the self-consistency requirement the window method is complete in its formulation. However, this makes the boundary value problem in Equation 5.61 a nonlinear one. The most-straightforward approach to solve this is to use the fixed-point iterations:

Algorithm 1 Determine $\boldsymbol{C}^*$ with the fixed-point iteration

Set $\boldsymbol{C}^*_0$
while $e_{C,Frob} > TOL$ **do**
Solve boundary value problem as in Equation 5.61 with 6 loading cases as in Equation 5.51
Average field quantities over the RVE domain using Equation 5.19 and Equation 5.25
Estimate effective material tensor $\boldsymbol{C}^*_n$ with Equation 5.52
Compute an error as e.g. $e_{C,Frob} = \frac{\left|\left|\boldsymbol{C}^*_n - \boldsymbol{C}^*_{n-1}\right|\right|_{Frob}}{\boldsymbol{C}^*_n}$
end while

The first estimate of the effective material tensor is governing the convergence speed of this algorithm. A better approximation for the starting point is the Hashin-Shtrikman bound. The fixed-point iterations could converge slow, especially if the first guess is far from the effective value. In this case, the Aitken Δ^2 can lead to a faster convergence process (see [66]). The iteration results can be written in a sequence form:

$$S = \{\boldsymbol{C}^*_0, \boldsymbol{C}^*_1, ..., \boldsymbol{C}^*_{n-1}, \boldsymbol{C}^*_n\} \tag{5.64}$$

where $\boldsymbol{C}^*$ is written as a vector containing all elasticity tensor values.

Although the window method overcomes the shortcomings of the boundary condition applications and the non-periodicity of the RVEs, it should be applied prudently. Resembling the self-consistent analytical homogenization, the window method provides reasonable estimates for the low volume fractions of inhomogeneities [2, 189]. In case the inhomogeneities are voids, unrealistic results are obtained for the volume fraction larger than 50%. For the case of infinitely rigid inclusions, the estimates are not valid after the volume fraction reaches 40%. The window method's effects were not investigated earlier and will be shown in few examples in the consequent section.

5.8 Other types of computational homogenization

The homogenization procedure described above is valid for any type of linear physics, i.e., thermal problems, permeability, or viscoelasticity. As an example, the permeability homogenization is briefly discussed. In order to determine effective permeability of the produced specimen, the microscopic initial boundary value problem based on Darcy's law is solved:

$$\begin{aligned} \nabla(-\mathbf{K}\nabla p) &= 0 && \text{on } \Omega \\ p &= p_D && \text{on } \Gamma_D \\ \boldsymbol{v}\cdot\boldsymbol{n} &= v_N && \text{on } \Gamma_N \end{aligned} \tag{5.65}$$

where $\mathbf{K}$ is Darcy's permeability tensor
p_D is the prescribed pressure
v_N is the prescribed Darcy's velocity

In contrast to linear elastic homogenization boundary conditions, the application of the prescribed strains (see Equation 5.42) is replaced with the pressure boundary condition as follows:

$$p|_\Gamma = \nabla \boldsymbol{p}^M \boldsymbol{x} \tag{5.66}$$

For SUBC, the following equation is used:

$$(\boldsymbol{v} \cdot \boldsymbol{n})|_\Gamma = \boldsymbol{v}^M \boldsymbol{n} \tag{5.67}$$

Displacement-driven Periodic Boundary Conditions are then reformulated as follows:

$$\begin{aligned} p(\boldsymbol{x}^+)|_\Gamma - p(\boldsymbol{x}^-)|_\Gamma &= \nabla \boldsymbol{p}^M \boldsymbol{x} \\ (\boldsymbol{v} \cdot \boldsymbol{n})(\boldsymbol{x}^+) + (\boldsymbol{v} \cdot \boldsymbol{n})(\boldsymbol{x}^-) &= 0 \end{aligned} \tag{5.68}$$

Similarly, the effective permeability is formulated in terms of the microscopic averages:

$$< v >_\Omega = -\mathbf{K}_{eff} < \nabla p >_\Omega \tag{5.69}$$

In this case, only four load cases are required to determined the effective permeability tensor.

To sum up, linear computational homogenization presented in this thesis can be similarly formulated for any other problem. The corresponding averaging theorems and homogenization boundary conditions should be adjusted accordingly. Furthermore, the number of necessary load cases strongly depends on the considered field quantity, i.e. the number of the field components.

5.9 Numerical investigations[a]

In this section, numerical examples to verify and investigate the numerical homogenization are shown. The numerical homogenization was implemented in the in-house code AdhoC++.

To test correctness of the implementation, two unit test cases must be considered for all types of homogenization, i.e., linear elastic, thermal or viscoelastic. The first setting is a homogenization of a homogeneous cube with arbitrary dimensions. In this case, the result of any conventional or window boundary condition should coincide with the bulk material properties. For example, the homogenization of a linear elastic isotropic homogeneous cube with Young's Modulus $E = 200$ GPa and Poisson's ratio $\nu = 0.3$ should lead to the same values independent of the applied boundary conditions. The second setup considers two special cases of layered composites depicted in Figure 5.2. These two setups have an analytical solution shown in Equation 5.5 and Equation 5.6. These cases will not be detailed in the following. Instead, more complex setups are considered.

5.9.1 Unit cell with a cubical void

In the following, an example of a cubic RVE with a cubic pore is considered. The material of the matrix has a Young's modulus $E = 190\,GPa$ and a Poisson's ratio $\nu = 0.294$. The cubical RVE has the size of $10 \times 10 \times 10$ mm.

Integration of homogenized quantities

As described in section 5.6, the integration of the homogenized quantities can become especially important in the case of the voids crossing the boundary of the RVE. Thus, the different integration techniques are compared. In this study, the centered cubic pore is set to $8 \times 8 \times 8$ mm. This corresponds to a moderate porosity of $\phi = 0.512$.

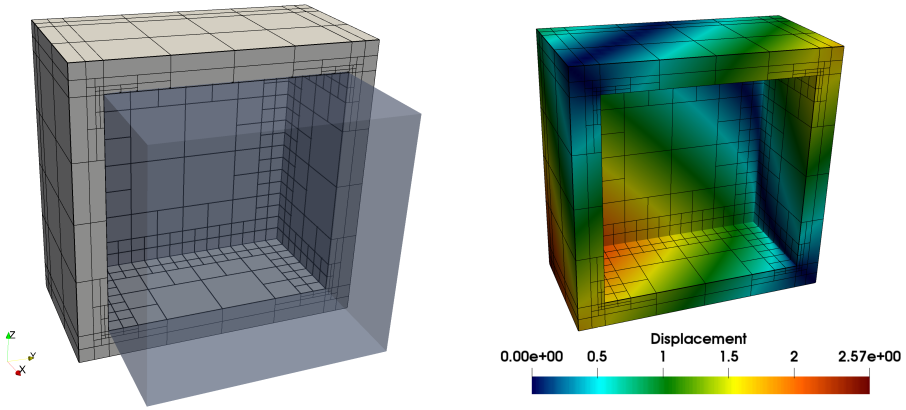

(a) Finite Element mesh

(c) Displacement field

(b)Finite cell mesh

(d) Von Mises stress field

Figure 5.10: Unit cell with a cubical void: numerical approximation of the displacement magnitude and von Mises stresses without the window under KUBC ($8 \times 8 \times 8$ elements, $p = 5$, $d = 2$).

First, the example is solved using FEM with a high-order mesh of polynomial degree $p = 5$, which boundary conforms to the boundary of the void (see Figure 5.10a). To resolve the singularities at the edges of the void, an $hp-$refinement with depth $k = 3$ is performed. Figures 5.10b and 5.10d show representative displacement field in the shear load case under KUBC and the corresponding von Mises stress distribution.

Second, the unit cell with the cubic hole is discretized in an immersed way utilizing FCM. RVE is meshed with $6 \times 6 \times 6$ finite cells of polynomial degree $p = 5$ with the same $hp-$refinement towards the singular edges. The inner cells in the void are not filtered. The indicator function is $\alpha(\boldsymbol{x}) = 10^{-6}$, which imitates the void being a very soft material

as stated in section 5.6.

The KUBC are applied directly to the unit cell outer boundary. In this case, the prescribed macroscopic strain tensor is required to be equal to the average strain values over the RVE boundary or over the whole volume as shown in Equation 5.25. Thus, the integration of the homogenized strain is performed in the following way:

- Strain integration over the RVE volume - referred to as "Volume int." (first part of Equation 5.25)
- Strain integration over the RVE boundary - referred to as "Surface int." (second part of Equation 5.25)
- Strain integration over the RVE volume combined with the surface integration over the internal pore boundary - referred to as "Combined int."(as in Equation 5.57)

The immersed study, in turn, has only the volumetric integration and the surface integration available.

$\boldsymbol{\varepsilon}$	$\boldsymbol{\varepsilon}_{exp}$, mm	$<\boldsymbol{\varepsilon}>$, mm - FEM			$<\boldsymbol{\varepsilon}>$, mm - FCM	
		Volume int.	Surface int.	Combined int.	Volume int.	Surface int.
ε_{11}	0.1000	0.029 (71%)	0.1000	0.1000	0.1000	0.1000
ε_{22}	0.1000	0.029 (71%)	0.1000	0.1000	0.1000	0.1000
ε_{33}	0.1000	0.029 (71%)	0.1000	0.1000	0.1000	0.1000
ε_{12}	0.1000	0.028 (72%)	0.1000	0.1000	0.1000	0.1000
ε_{23}	0.1000	0.028 (72%)	0.1000	0.1000	0.1000	0.1000
ε_{13}	0.1000	0.028 (72%)	0.1000	0.1000	0.1000	0.1000

Table 5.1: Unit cell with a cubical void: Comparison of the different integration approaches for the FEM and the FCM discretization of the prescribed KUBC for constant macroscopic strain of 0.1 mm.

Table 5.1 summarizes the results of the homogenized strain integration. The boundary conforming discretization shows that only the surface integration or the volumetric integration and the integration over the pore's inner surface deliver the expected result. This observation supports the definition of the cavity strain as in Equation 5.57. The volumetric integration in the absence of the elements in the void provides a lower value of the homogenized strain.

However, due to the natural definition of the void as a continuum with a vanishing stiffness for the FCM discretization (see Figure 5.10c), the volume averaging can be performed with the same precision as the surface integral over the outer boundary. The formulation of the averaging theorems becomes consistent with the discretization method used, and the knowledge about the inner boundaries is not required. The stress comparison for any of the boundary conditions is not shown here as the stress is not affected by the internal voids' presence.

To gain a further understanding of this phenomena, consider the same setup but with a shifted cubic void of $8 \times 8 \times 8$ mm as depicted in Figure 5.11.

The example is studied in the same manner as above. For the FEM computation, it is assumed that the displacement field in the void is zero as proposed in [33]. For the FCM complete numerical field, including the fictitious part is taken for averaging the fields.

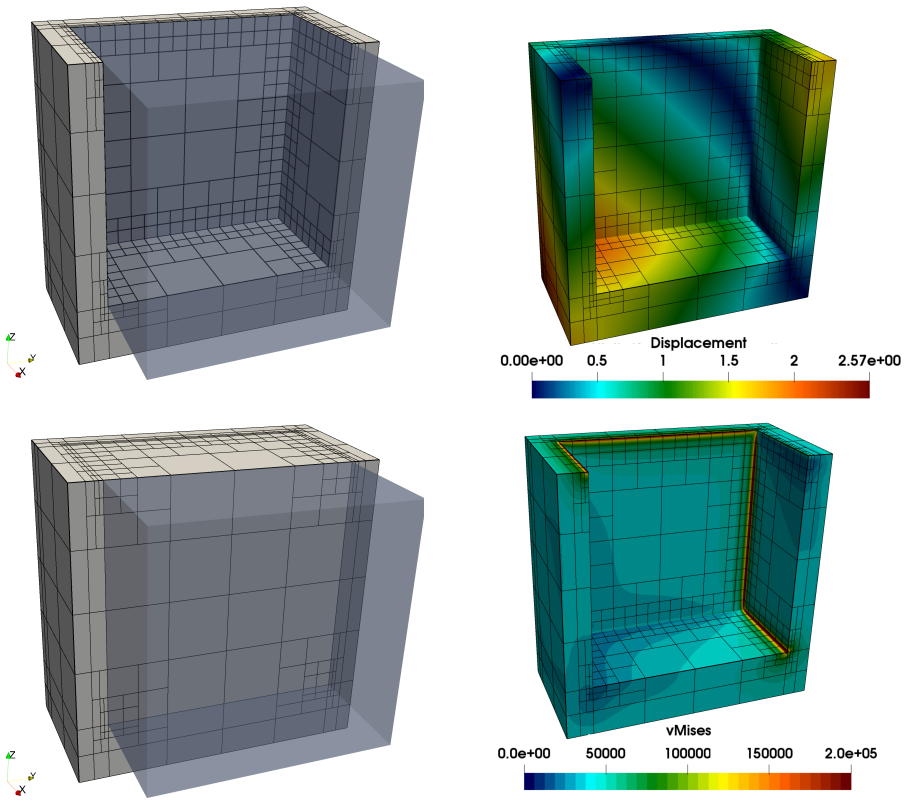

(a) Meshes for FEM and FCM

(b) Displacement and von Mises stress fields

Figure 5.11: Unit cell with a shifted cubical void: numerical approximation of the displacement magnitude and von Mises stresses without the window under KUBC ($8 \times 8 \times 6$ cells, $p = 5$, $d = 2$).

Table 5.2 shows that one needs reasonable assumptions for the displacement fields in the void for the Finite Element discretization. The surface integration in the area where the void is crossing the boundary does not provide the expected quantities. If the displacement is assumed to be zero in the void, then the homogenized strain values do not agree with the prescribed macroscopic ones. A more elaborated way would be to introduce a prolongation of the displacement fields in the void by extrapolating the computed values from the cavity boundary. This approximation can be achieved via, e.g., a polynomial interpolation. However, in the case of complex void networks crossing the boundaries, this assumption becomes impractical. In contrast, the FCM provides the natural extension of the primary fields into the void domain, thus removing the correct interpolation necessity.

Overall, this study shows the importance of the correct integration of the strain fields. When PBC or KUBC are applied directly to the RVE boundary, evaluation of the homogenized strain is not necessary. These values are naturally equivalent to the macroscopic strains applied at the boundary and set a priori. However, the integration approach becomes essential for a few cases.

$\boldsymbol{\varepsilon}$	$\boldsymbol{\varepsilon}_{exp}$, mm	$<\boldsymbol{\varepsilon}>$, mm - FEM			$<\boldsymbol{\varepsilon}>$, mm - FCM	
		Volume int.	Surface int.	Combined int.	Volume int.	Surface int.
ε_{11}	0.1000	0.0293 (71%)	0.1000	0.1000	0.1000	0.1000
ε_{22}	0.1000	0.0293 (71%)	0.1000	0.1000	0.1000	0.1000
ε_{33}	0.1000	0.0305 (69%)	0.068 (32%)	0.068 (32%)	0.1000	0.1000
ε_{12}	0.1000	0.0286 (71%)	0.1000	0.1000	0.1000	0.1000
ε_{23}	0.1000	0.0311 (69%)	0.084 (16%)	0.084 (16%)	0.1000	0.1000
ε_{13}	0.1000	0.0311 (69%)	0.084 (16%)	0.084 (16%)	0.1000	0.1000

Table 5.2: Unit cell with a shifted cubical void: Comparison of the different integration approaches for the FEM and the FCM discretization of the prescribed KUBC of constant macroscopic strain of 0.1 mm

First, when SUBC is directly imposed on the boundary of the RVE, the computation of the homogenized strain tensor is required. The quality of the achieved results depends on the correctness of the integration procedure. In particular, if a volumetric integration is chosen, the necessity of complex treatment of the inner boundaries arises. For a cheaper surface integration, one needs to account for the void crossing the RVE boundary.

Second, when the PBC, KUBC or SUBC are applied at the window, both homogenized strains and stresses must be evaluated over the internal RVE boundary. This averaging can be done by evaluating the quantities at the window's internal boundary in the boundary conforming FEM, which mixes the micro-macro separation concept. Moreover, as mentioned in [165], the domain of integration for the window method can be either, window or an RVE, only on the convergence of iterations. The FCM provides a remedy for such problem by introducing a material with vanishing stiffness and removing the problems computing the strain integral within the void zone.

Brief summary:

- Correct strain integration is crucial for the quality of the homogenization when voids cross the RVE boundary.
- Surface integration is the most efficient approach for both, FEM and FCM to obtain homogenized quantities.
- For PBC or KUBC without a window, the homogenized strain is equivalent to the macroscopic strain tensor.
- SUBC without a window requires strain integration. In this case, a surface integration is recommended. In the FCM the elements adjacent to the RVE boundary should not be filtered. Such an approach provides the correct strain values.
- KUBC, PBC, SUBC with the window require strain and stress integration over the RVE boundary. Again, a surface integration is recommended. The same holds for the adjacent elements in the FCM. The best results are achieved when they are not filtered.

Direct numerical tensile test: reference values

For verifications purposes a tensile experiment is performed. The unit cell remains the same as shown in Figure 5.10 with the exception of the size of the internal void. The size of the void is increased to $9 \times 9 \times 9$ mm. This corresponds to a porosity state of $\phi = 0.729$. To achieve reliable homogenization results, the tensile specimen is constructed by repeating this unit cell $10 \times 3 \times 3$ times. The tensile loading is then applied along the longest direction of the specimen. For the speed and simplicity of this test, a voxel geometry representation is chosen. In this way, an efficient pre-integration technique can be utilized as described in section 4.2. Every unit cell is represented with $100 \times 100 \times 100$ voxels allowing for an exact representation of the void. An example of the deformed state under tensile loading is shown in Figure 5.12.

The tensile sample is discretized with $100 \times 30 \times 30$ finite cells of degree $p = 5$ with $10 \times 10 \times 10$ integration partitions. The integration partitions correspond to the voxels of the considered geometry. In every partition, then, the standard integration rule with $(p+1)^3$ Gauss points per partition. The bulk material properties are kept at $E = 190$ GPa and $\nu = 0.294$. In this load case, only a directional Young's modulus can be computed. The following homogenized Young's modulus has been determined:

$$E^* = 38\,446.12 \text{ MPa}$$

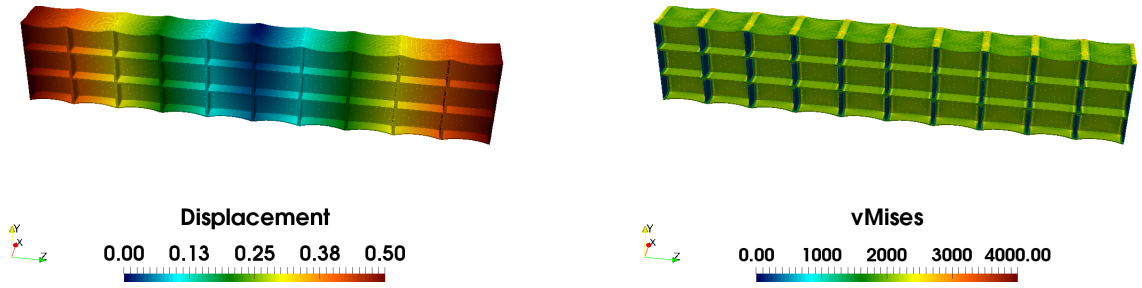

Figure 5.12: Numerical tensile test of a fully periodic specimen with cubical voids of size $l_h = 9.0$ mm (deformed state is scaled with the factor of 20).

Conventional boundary conditions: influence of the porosity value on the homogenized elasticity tensor

The cubical RVE has the size of $10 \times 10 \times 10$ mm. The discretization is kept the same as in the case of direct tensile test, i.e. $10 \times 10 \times 10$ finite cells of order $p = 5$ with $10 \times 10 \times 10$ integration partitions.

First, the same porosity value of $\phi = 0.729$ is solved with different boundary conditions. Figure 5.13 shows observed deformation patterns in tension under different boundary conditions. KUBC and PBC show a similar deformation pattern to the one observed in the tensile specimen Figure 5.12. However, the SUBC shows a different deformation state that does not resemble the full specimen's deformation state.

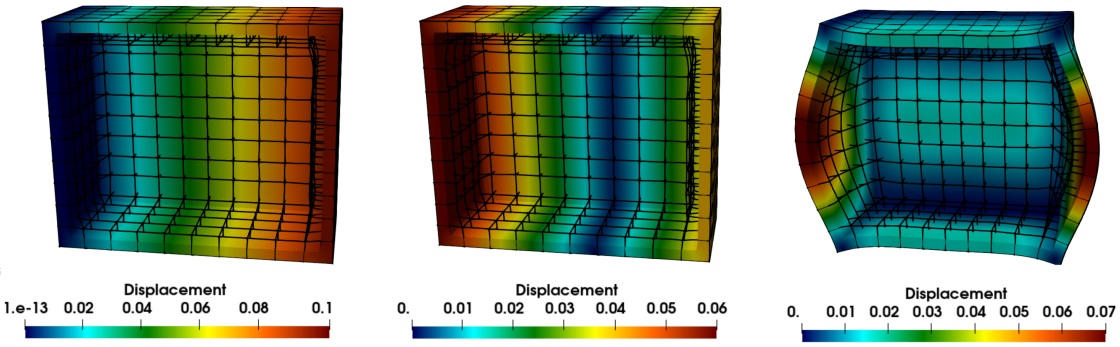

(a) KUBC (b) PBC (c) SUBC

Figure 5.13: Unit cells with a cubical void: Deformation patterns under different boundary conditions of a unit cell with a cubical void of size 9.0 mm in tension (scale factor for deformations is 20).

Then, the homogenized Young's modulus obtained by different boundary conditions is compared. The following results are obtained:

$$E^*_{KUBC} = 38\,945.72 \text{ MPa} \quad E^*_{PBC} = 38\,404.53 \text{ MPa} \quad E^*_{SUBC} = 2\,014.61 \text{ MPa}$$

An example of a homogenized tensor for porosity $\phi = 0.729$ with PBC is shown below:

$$C^* = \begin{bmatrix} 41117.46 & 8212.73 & 8117.19 & 0.00 & 0.00 & 0.00 \\ 8117.19 & 41117.46 & 8117.19 & 0.00 & 0.00 & 0.00 \\ 8117.19 & 8117.19 & 41117.46 & 0.00 & 0.00 & 0.00 \\ 0.00 & 0.00 & 0.00 & 8073.21 & 0.00 & 0.00 \\ 0.00 & 0.00 & 0.00 & 0.00 & 8073.21 & 0.00 \\ 0.00 & 0.00 & 0.00 & 0.00 & 0.00 & 8073.21 \end{bmatrix}$$

Curiously, the result obtained using KUBC is close to the solution delivered by PBC. When compared to the quantities computed via DNS, the PBC shows a relative error of 0.10%, while the kinematic conditions - 0.13%. The SUBC results are much further apart, highly underestimating the homogenized quantity. These results are closely related to the observed deformation patterns of the unit cell.

Finally, the influence of the porosity value on the computed homogenized quantities is investigated. As in this case, there are no reference solutions available, the obtained results are compared to the analytical Voigt, and upper Hashin-Shtrikman bounds described in section 5.1. As the second phase of this unit cell is the void, the lower bounds deliver zero. In the following, two entries of the homogenized elastic tensor, C_{1111} and C_{1313}, are monitored.

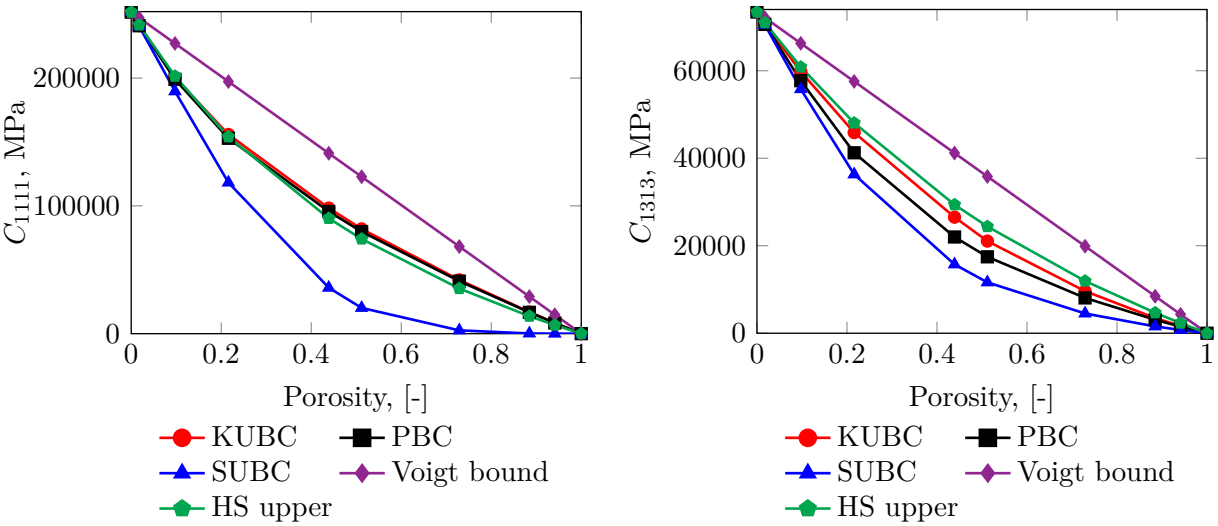

Figure 5.14: Unit cells with a cubical void: Sensitivity study of homogenized properties to the conventional boundary conditions.

Figure 5.14 summarizes the achieved results. The first important observation is that the Voigt bound delivers a conservative prediction of the homogenized quantities. This is an "ultimate" upper bound. As all other numerical solutions lay underneath the curve, the results agree with the literature. The next interesting result is that the Hashin-Shtrikman bound seems to deliver a result in the first homogenized entry, which is quite close to the one determined in the numerical studies with PBC and KUBC. However, when the shear-dominated entry is observed, the analytical approximation is getting further apart. Lastly, all numerical boundary conditions are following the expected hierarchy, i.e. $\boldsymbol{C}_{SUBC} \leq \boldsymbol{C}_{PBC} \leq \boldsymbol{C}_{KUBC}$. A gap between the kinematic and periodic boundary conditions is not observed in the tension-dominated entry, while for the shear one - the conditions are apart from each other.

Brief summary:

- All numerical boundary conditions follow the expected boundary condition hierarchy.
- PBC homogenization solution entirely agrees with the direct tensile test performed on the full specimen.
- For larger porosity states, the influence of the applied homogenization boundary conditions is significant.
- The shear dominated entries are more sensitive to the applied boundary conditions.

Conventional boundary conditions: sensitivity of the homogenized quantities to the number of unit cells

To further understand the importance of the applied boundary conditions, the effect of the number of considered unit cells is studied. In the following, the size of the cubic void

is fixed to 9 mm, which leads to a porosity state $\phi = 0.729$. The unit cells are discretized with the same parameters as in the study above. Then, the number of unit cells is increased from 1 to 4 in every direction. This means that for 3 unit cells per direction, nine cubic cells with a cubic void are composed together, after which the homogenization procedure is performed.

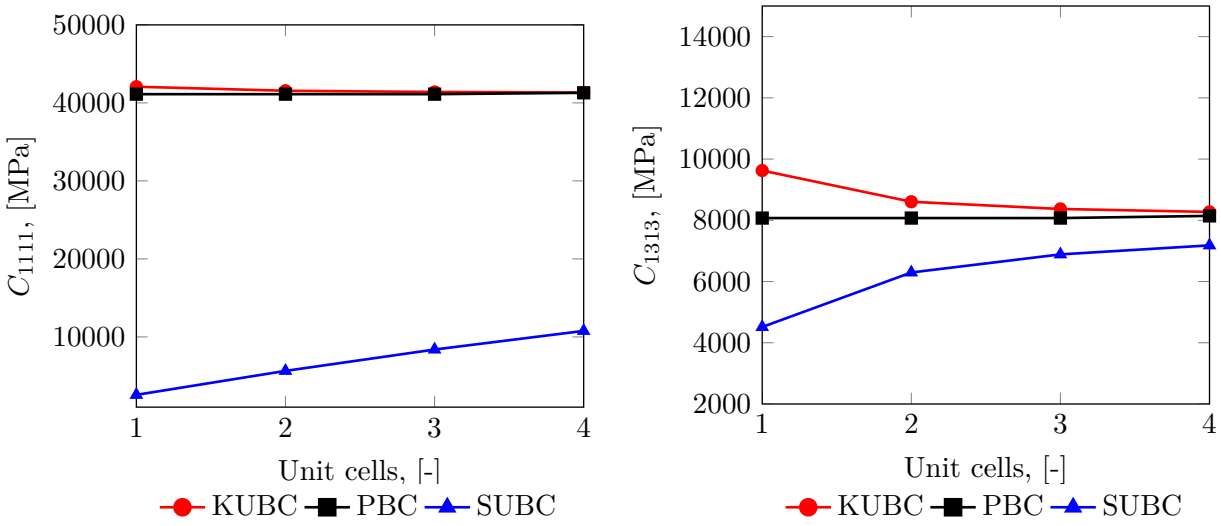

(a) No window (b) No window

Figure 5.15: Unit cells with a cubical void: Sensitivity study of homogenized properties to the number of considered unit cells.

Figure 5.15 shows the achieved numerical results. First, it is important to note that the PBC result remains constant independent of the considered number of unit cells. As it was mentioned in section 5.4, the periodic conditions are the most accurate when periodic structures are considered. They are independent of the considered number of cells and deliver the exact result, demonstrated in this study. Second, as expected, with the increase in the number of considered unit cells, all boundary conditions tend to converge to the same value. A very significant change is observed when the SUBC are applied. As KUBC already deliver similar results to the periodic conditions, the homogenized result seems to converge to the PBC faster. Finally, the same difference in the tensile- and shear-driven behavior of the homogenized quantity is observed. The hierarchy of the boundary conditions is more pronounced in the shear term of the effective tensor. The gap between the KUBC, PBC and SUBC is larger when one cell is considered. Only at the end of the study, the kinematic conditions seem to deliver a similar result to the PBC one.

Brief summary:

- PBC homogenization result remains independent on the number of considered unit cells.
- The gap between the KUBC and SUBC is reducing with the increase of the unit cells.

Window boundary conditions: sensitivity of the homogenized quantities to the window width

As explained in section 5.7, the window method can be advantageous when the voids randomly cross the boundary of the RVE. However, it is important to investigate the window width's influence on the homogenized values and verify the achieved results. For this study, the porosity $\phi = 0.729$ is considered. The discretization level is the same as in the previous studies. Then, the window width l_w is varied from 0 to 20 mm. This value indicates the window box's width in every direction, i.e., with the window size of $l_w = 10$ mm, the computational domain becomes $30 \times 30 \times 30$ mm. Finally, all boundary conditions - KUBC, PBC and SUBC - are applied at the window frame. According to Equation 5.52 and Equation 5.54 the final homogenized tensor can be computed either by finite difference or by direct inversion. Figure 5.16 shows the achieved homogenized quantities when Equation 5.52 is used, while Figure 5.17 represent the solution when the homogenized quantities are computed with Equation 5.54.

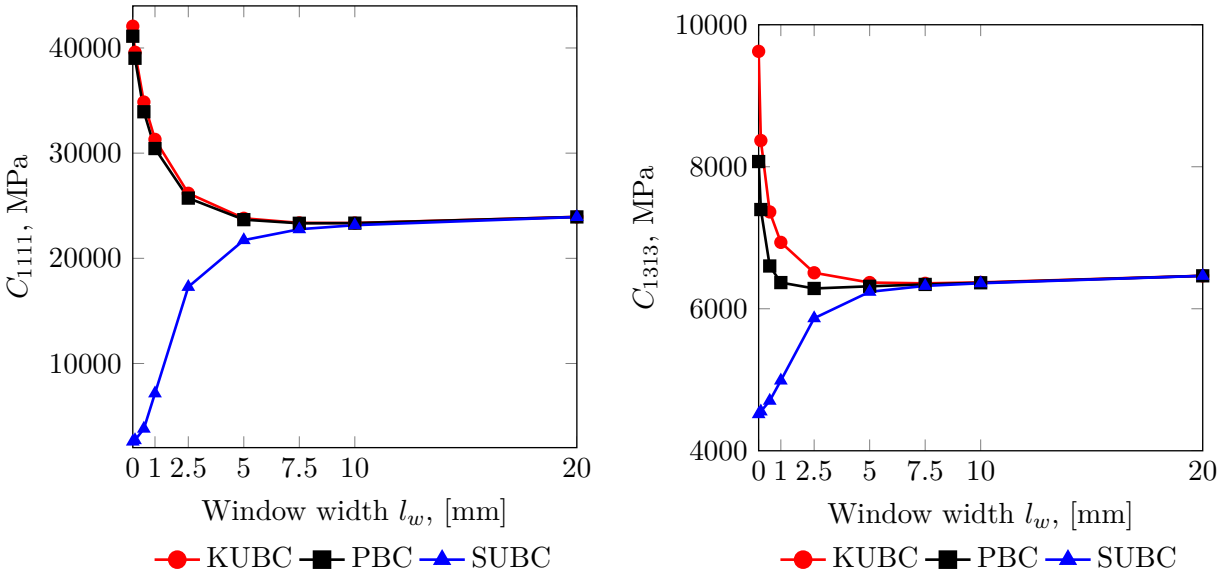

Figure 5.16: Unit cell with a cubical void: effect of the window width on the homogenized quantities computed by direct inversion.

These graphs show that with the window size increase, the problem becomes insensitive to the applied boundary conditions. Already at the window size nearly equal to the overall RVE dimension, all three results deliver almost the same value. Interestingly, both direct and approximate inversion leads to similar homogenized quantities for this setup. One observes no visual difference between the two figures.

However, as noted in Equation 5.62 when the window method is applied, the hierarchy of the boundary conditions must be preserved. To further check this requirement, the eigenvalues of two homogenized tensor differences is computed as indicated in Equation 5.48. While the eigenvalues of the difference of homogenized tensors are always

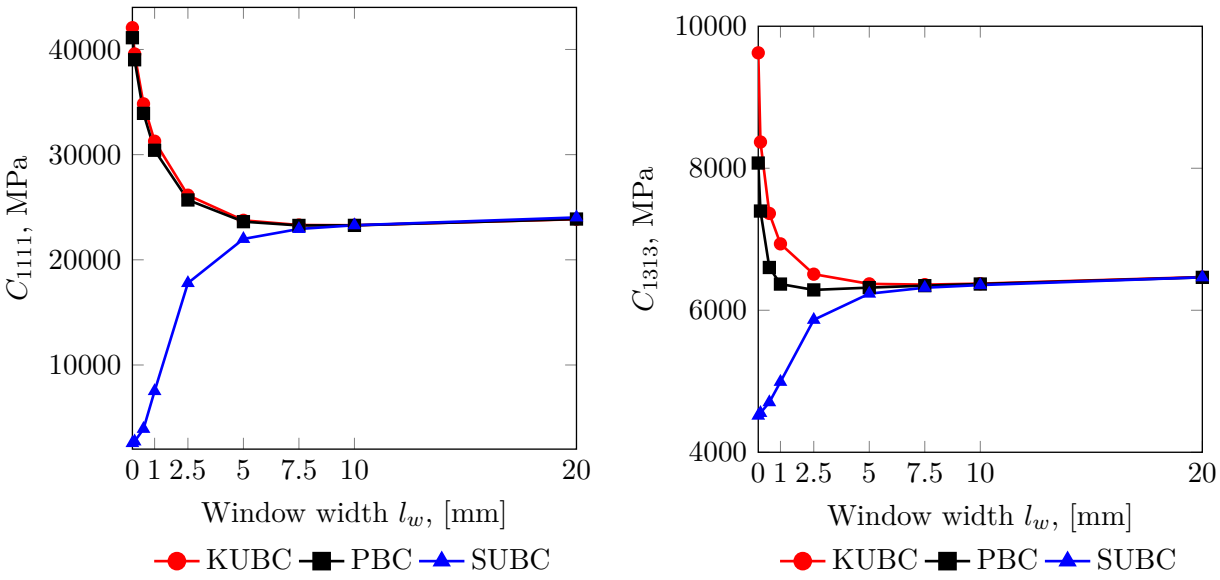

Figure 5.17: Unit cell with a cubical void: effect of the window width on the homogenized quantities computed by numerical differentiation.

positive for direct inversion as shown in Figure 5.18a, approximate inversion leads to a reverse hierarchy of the boundary conditions as depicted in Figure 5.18b. For window sizes bigger than half of the size of RVE, the results violate the expected hierarchy of the boundary conditions (see Equation 5.62). Moreover, for window size $l_w = 10$ and $l_w = 20$ mm there are difficulties reaching convergence of the window method with the tolerance of $1e^{-5}$. However, for the direct inversion, neither of these phenomena are observed (see Figure 5.18a).

Finally, as all boundary conditions deliver almost the same value when the window size is large, the deformation patterns and the homogenized tensor at a window size of $l_w = 10$ mm applying KUBC are compared to the one achieved with conventional BCs. Figure 5.19 shows a distinct deformation pattern compared to the one observed in Figure 5.13 and in a direct numerical tensile test. The presence of the window allows the RVE to deform unconstrained. Thus, a "bubble" deformation is seen when tension is applied. However, this pattern does not seem to resemble the one observed in the tensile experiment.

The following homogenized tensor is computed for this setup:

$$C^* = \begin{bmatrix} 23358.58 & 2860.33 & 2860.33 & 0.00 & 0.00 & 0.00 \\ 2860.33 & 23358.58 & 2860.33 & 0.00 & 0.00 & 0.00 \\ 2860.33 & 2860.33 & 23358.58 & 0.00 & 0.00 & 0.00 \\ 0.00 & 0.00 & 0.00 & 6371.38 & 0.00 & 0.00 \\ 0.00 & 0.00 & 0.00 & 0.00 & 6371.38 & 0.00 \\ 0.00 & 0.00 & 0.00 & 0.00 & 0.00 & 6371.38 \end{bmatrix}$$

which corresponds to $E_{KUBC,w} = 22\,734.49$ MPa.

This result is 41% lower than the one achieved by the direct numerical tensile experiment and by homogenization without the window. The reason for such a large difference is

the applicability of the self-consistent methods for high-porosity values as mentioned in section 5.7. As the porosity is high for the considered case, the final tensor is mainly underestimating the homogenized tensor. This will be further investigated in the next study.

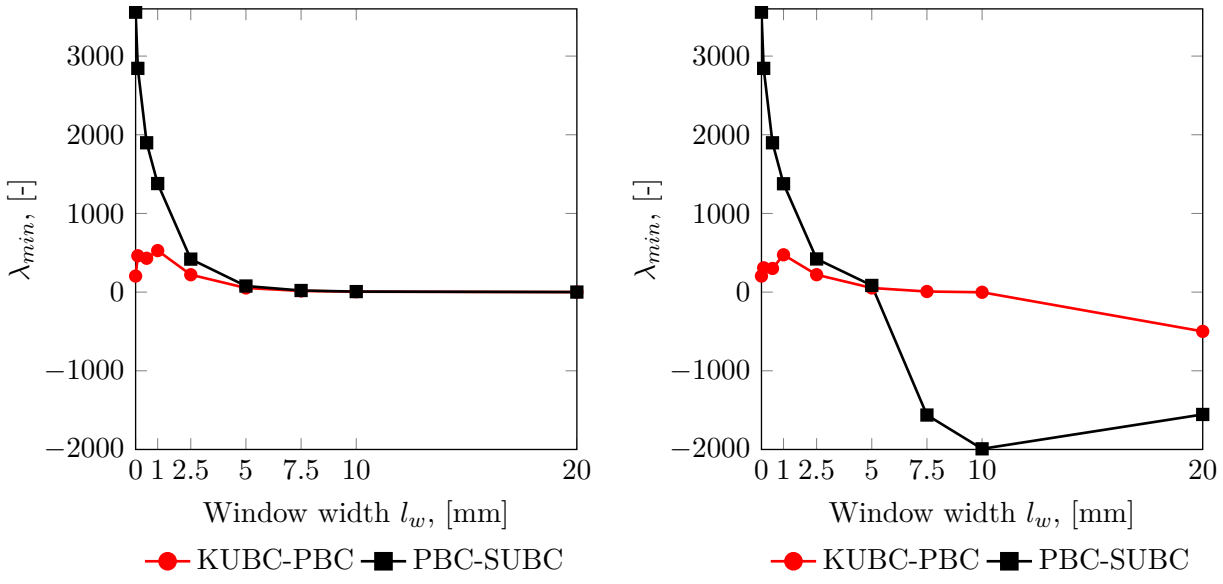

(a) Direct inverse

(b) Approximate inverse

Figure 5.18: Unit cell with a cubical void: Smallest eigenvalue of the tensor differences.

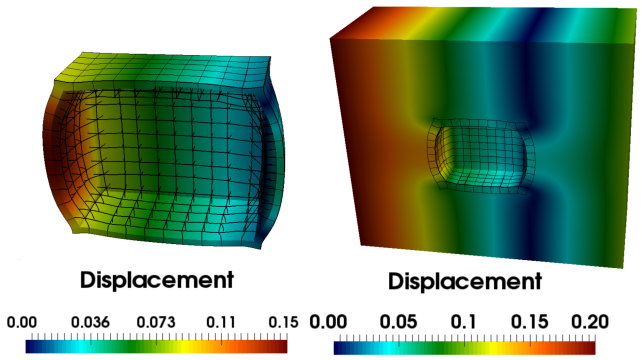

Figure 5.19: Unit cells with a cubical void: Deformation patterns of a unit cell with a cubical void of size 9.0 mm in tension with window boundary conditions (scale factor for deformations is 20).

Brief summary:

- Homogenization results become independent of the applied boundary condition for a larger window width (as a rule of thumb for a window size larger than the size of the RVE itself).

- The deformation pattern obtained with the window boundary conditions does not resemble the one observed in a direct numerical tensile test.
- Inversion through numerical differentiation violates the prescribed hierarchy of the boundary conditions.
- For high porosity states, the window method significantly underestimates the effective quantities.

Window boundary conditions: Sensitivity of the homogenized quantities to the porosity states

In the following, the size of a cubical void is varied. The discretization parameters are the same as in the previous study. As it was demonstrated above, all boundary conditions at large window width deliver similar results. Thus, in the following only KUBC are applied at the window frame. The width of the window is fixed to $l_w = 10$ mm, which corresponds to one size of the RVE $l_w/l_{RVE} = 1$.

Figure 5.20 summarizes the homogenization results for a few porosity states. The results achieved by applying conventional PBC without a window are shown for comparison.

This study confirms that for lower porosity states, the homogenized quantities agree well with the conventional boundary conditions. However, when the porosity is increased, the window boundary conditions deliver lower values. Interestingly, the behavior is different for tensile and shear-driven homogenized entries. Underestimation of the homogenized quantities appears earlier for the first entry to the effective stiffness tensor C_{1111} than for entry C_{1313}.

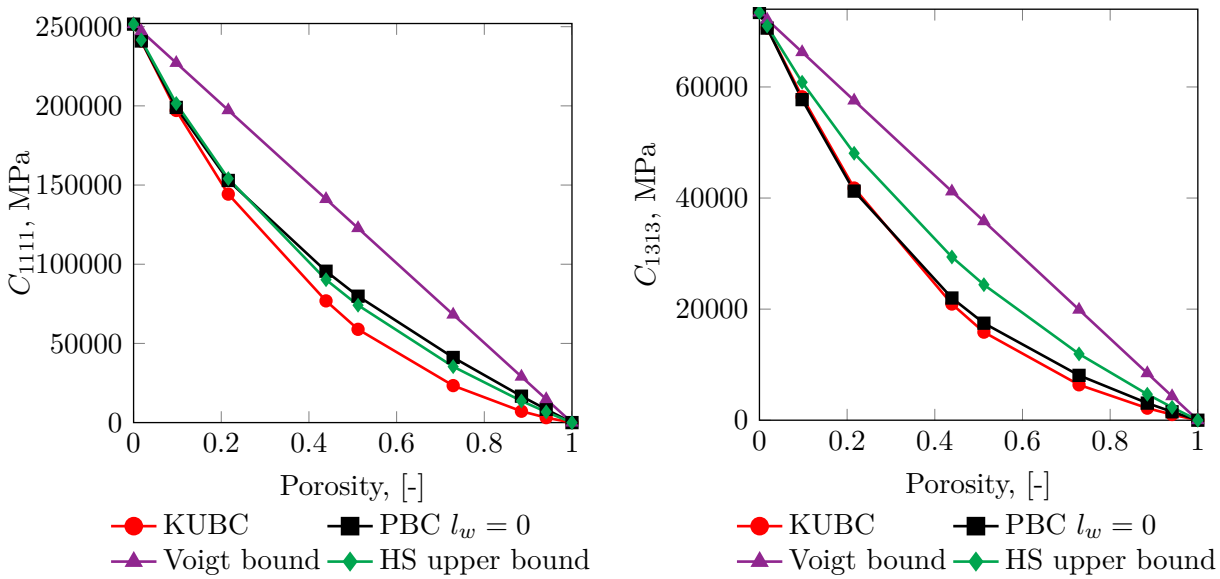

(a) Window size $l_w/l_{RVE} = 1$

(b) Window size $l_w/l_{RVE} = 1$

Figure 5.20: Unit cell with a cubical void: Sensitivity study of homogenized quantities to the window boundary conditions.

Brief summary:

- There is a good agreement between conventional and window boundary conditions for lower porosity.
- Both the tensile- and shear-driven quantities are underestimated for higher porosity states. However, there is larger gap in the tensile-driven elasticity tensor entry.

Window boundary conditions: Sensitivity of the homogenized quantities to the number of unit cells.

Finally, the effect of the number of unit cells on the effective tensor is studied. Unit cell is discretized with $10 \times 10 \times 10$ finite cells of polynomial degree $p = 5$. Then, the number of cells is increased in every direction. The window size is modified such that $l_w/l_{RVE} = 1$ for all cases. This, in turn, significantly increases the number of degrees of freedom with every additional cell per direction.

Figure 5.21 shows that with the increase of the number of unit cells, the results achieved applying window boundary conditions tend to converge to a lower value than the one achieved with conventional PBC. Although there is a convergence towards the correct homogenized value, the results even at $4 \times 4 \times 4$ unit cells are lower. This configuration is very computational demanding due to the presence of the window. Any further increase in the domain size would result in prohibitively high computational costs.

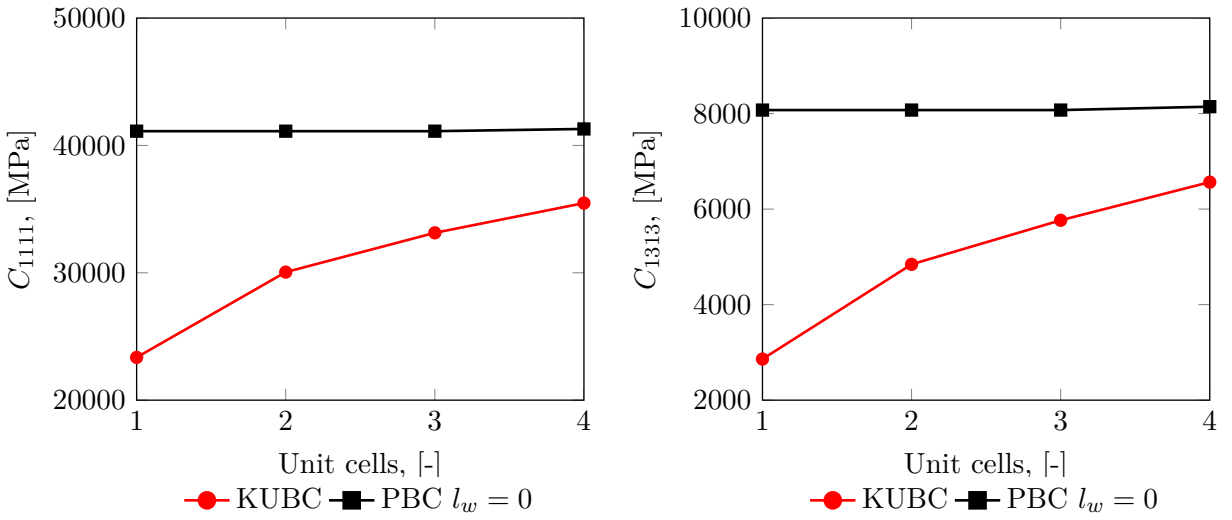

(a) No window (b) No window

Figure 5.21: Unit cell with a cubical void: Sensitivity study of homogenized properties to the increase of the unit cells applying window boundary conditions.

Brief summary:

- The window boundary conditions converge to a lower value than the one delivered with the conventional PBC.
- Large configurations with the window boundary conditions become prohibitively costly.

5.9.2 Two-phase particle reinforced composite

An example of a centered rigid spherical inclusion inside a soft cubic unit cell is considered. This example covers a slightly different area when no voids are present in an RVE. The setup used for the following numerical investigations is indicated in Figure 5.22. The reference solutions are taken from [57, 108].

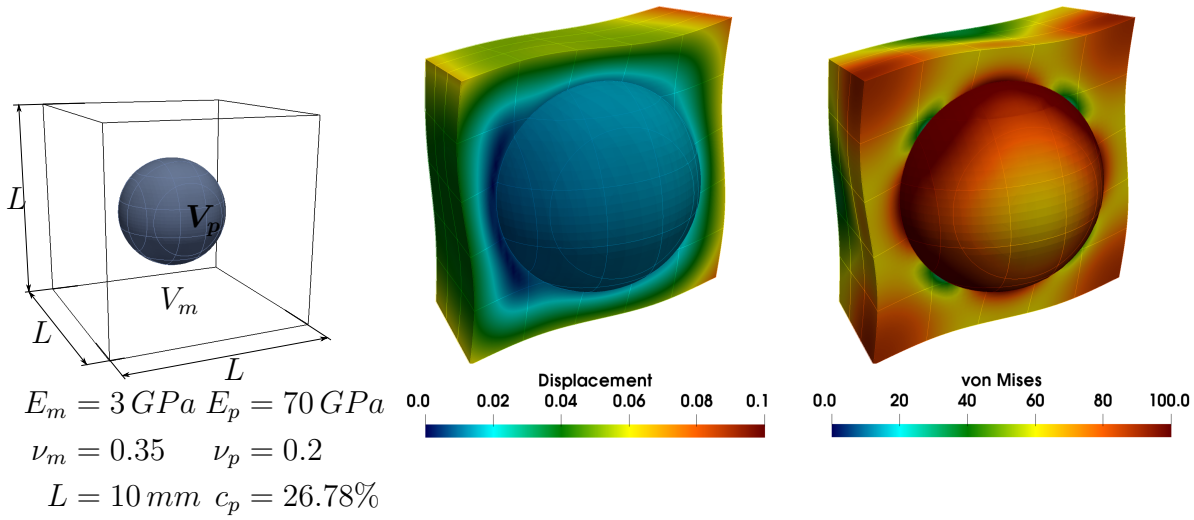

(a) Setup (b) Representative displacement field (c) Representative von Mises stress distribution

Figure 5.22: Hard spherical inclusion in a soft matrix.

This periodic unit cell is computed using the high-order Finite Cell Method (chapter 4) in combination with the Smart-Octree integration described in [90]. Due to the presence of a material interface, two meshes are employed to discretize the problem. The interface condition between the two materials is enforced weakly with a penalty parameter of $\beta = 10^8$, while the fictitious indicator function is kept as $\alpha(\boldsymbol{x}) = 10^{-9}$ [42].

Conventional boundary conditions: convergence study and verification of the developed method

The convergences curves using $4 \times 4 \times 4$ and $5 \times 5 \times 5$ cells are presented in Figure 5.23. The polynomial degree is raised from $p = 1$ to $p = 7$.

Figure 5.23 shows that the Finite Cell Method combined with the Smart-Octree integration benefits from an exact resolution of geometry on the integration level. The error between the computed homogenized quantity applying PBC with 4000 DOFs and the reference solution is smaller than 5% for C_{1111} and less than 1% for C_{2211}. In this setting, the best resolution is achieved with an accuracy of 0.22% in the effective elastic tensor of C_{1111} and the insignificant difference in the off-diagonal entry C_{2211} with 50 736 DOFs for five finite cells of polynomial order $p = 7$. As the errors in the achieved results are relatively small for configurations with more than 4000 DOF, in further studies, the

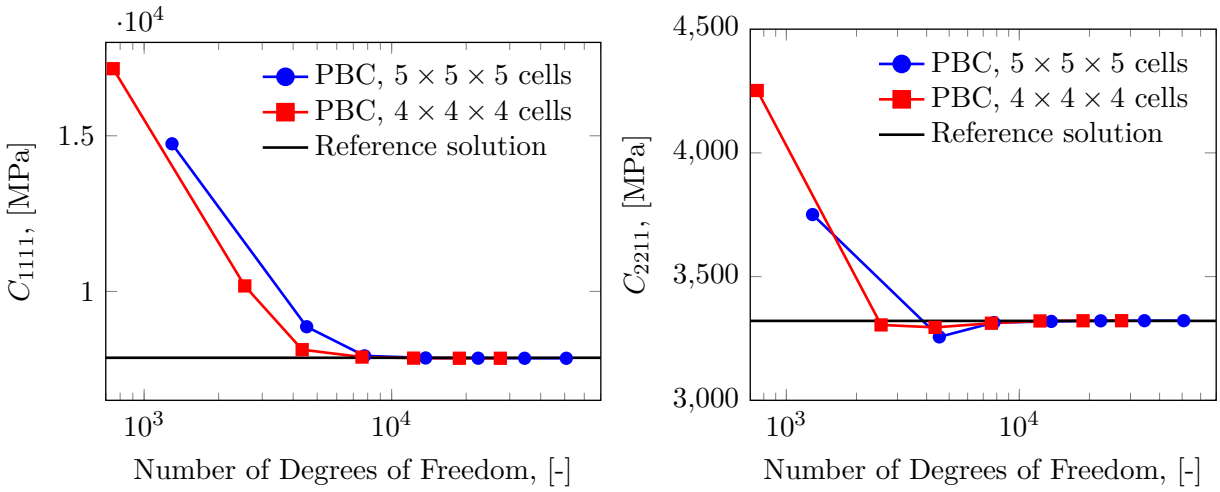

Figure 5.23: Convergence studies of two entries into the elasticity tensor C_{1111}, C_{2211}.

discretization with $5 \times 5 \times 5$ finite cells of polynomial degree $p = 5$ resulting in 22356 DOF is fixed.

	c_p $[-]$	N	C^*_{1111} $[GPa]$	C^*_{2211} $[GPa]$	C^*_{2222} $[GPa]$	C^*_{3333} $[GPa]$	C^*_{1212} $[GPa]$	C^*_{2323} $[GPa]$	C^*_{1313} $[GPa]$
[57]	0.2678	$\approx 3.4 \cdot 10^4$ tet./sphere	8.069	-	8.075	8.072	1.839	1.834	1.835
[108]	0.2678	240^3 pixels	7.867	3.321	-	-	-	-	-
This work	0.2678	50 736 DOFs	7.851	3.321	7.851	7.851	1.780	1.780	1.780

Table 5.3: Two-phase composite: homogenized elastic constants ([57], [108])

The achieved results are summarized in Table 5.3 to show the achieved homogenization quantities quantitatively.

Brief summary:

- Homogenized results for two-phase composite with PBC agree well with the reference values.
- For implicit geometries homogenization with Smart-Octree provides a reliable solution with few DOFs to determine effective quantities.

Conventional boundary conditions: sensitivity of the homogenized quantities to different volume fraction states

In the following, the radius of the inclusion is varied. The maximum inclusion volume fraction is $\phi_I = 0.52$, where the sphere is nearly touching the unit cell's boundary. The

radius of the sphere is $r = 4.99$ mm while the cell size is $l_{RVE} = 10$ mm. Then, conventional BCs are applied for all achievable volume fractions.

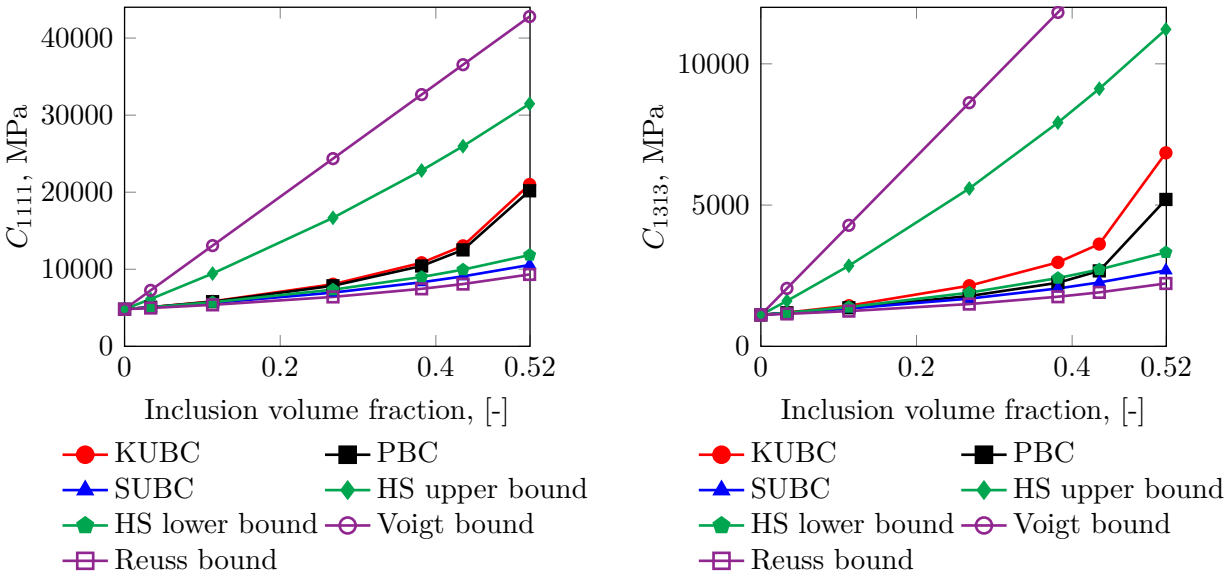

Figure 5.24: Two-phase composite: homogenized quantities for different porosity states.

Figure 5.24 shows the numerical results achieved with conventional boundary conditions together with the analytical bounds from section 5.1. In this case, as both phases are not voids, the Reuss and the lower Hashin-Shtrikman approximations are computed. Overall, all conventional boundary conditions deliver reasonable estimates between the Voigt and Reuss bounds and between a tighter approximation of Hashin-Shtrikman bounds. Similar to the example of a cell with a cubical void, the boundary conditions' hierarchy is more pronounced in the shear-driven effective quantity. Curiously, the SUBC does not have such a pronounced gap as in the cubical void. These boundary conditions also deliver the estimates which are close to the other solutions.

Brief summary:

- Similar to the cubical void unit cell shear-driven effective quantities show a more distinct hierarchy of boundary conditions.
- All numerical results lay between the analytical bounds.
- SUBC underestimates the homogenized quantities. However, its values are closer to the other boundary condition results than the RVE where the second phase is a void.

Window boundary conditions: sensitivity of the homogenized quantities to the window size

In this study, the window boundary conditions are investigated for two volume fractions of the hard inclusion, in particular $\phi_I = 0.2678$ and $\phi_I = 0.521$. In contrast to the

previous example, only the direct inversion is used to provide reliable estimates of the final quantities.

Figure 5.25 depicts two homogenized quantities C_{1111} and C_{1313} with respect to the chosen window width for all BCs for the first volume fraction. The results for the increased size of the inclusion are shown in Figure 5.26.

Similarly to the example of a cubical void, all window BCs converge to one value with the increasing window size. The results do not change significantly after the window size $l_w = 10$ mm which corresponds to one RVE size. Furthermore, the change in the inclusion size does not change the necessary window size. Thus, this parameter can be considered independent of the problem type. Finally, the results are compared quantitatively with the results delivered by conventional PBC. In the case of a small inclusion, the difference with the PBC is 3% for C_{1111} and 7% for C_{1313}. However, for a larger inclusion size, the results are further apart with a difference of 18% in C_{1111} and 4% for C_{1313}. These results support the observation made in the case of a cubic void. With the increase of the volume fraction inclusion, the window boundary conditions tend to underestimate the homogenization results independently of the phase type (e.g., void or another material).

Brief summary:

- The window width is independent of the inclusion size.
- Window BCs deliver close results to the one achieved with conventional PBC.
- The gap between the window BCs and conventional periodic ones increases with increasing the inclusion size.

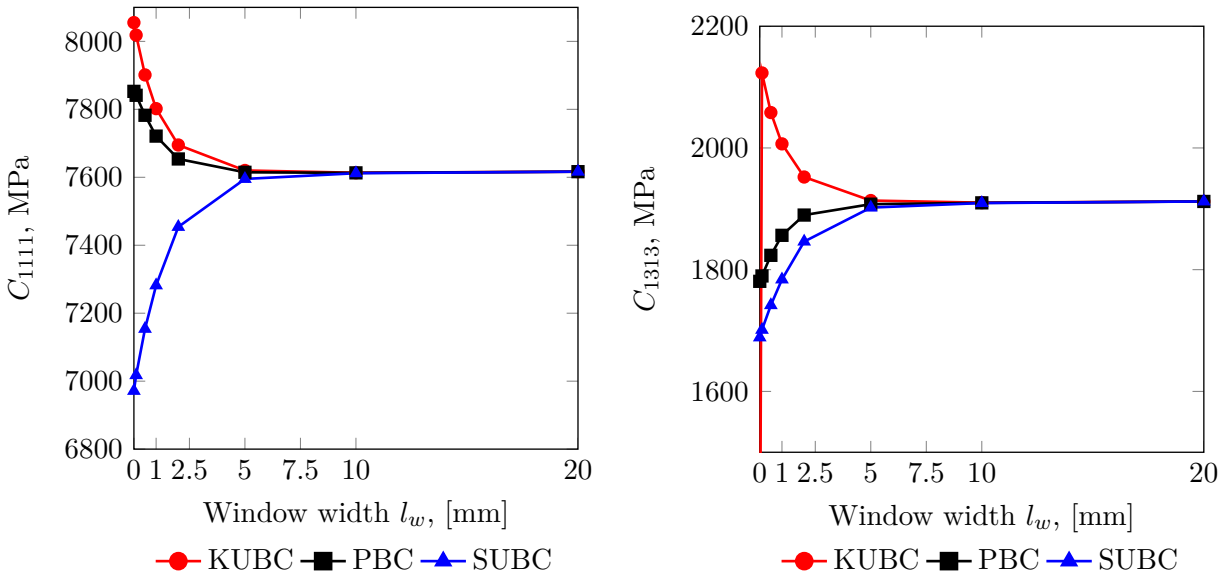

Figure 5.25: Two-phase composite: window size sensitivity for $\phi_I = 0.2678$.

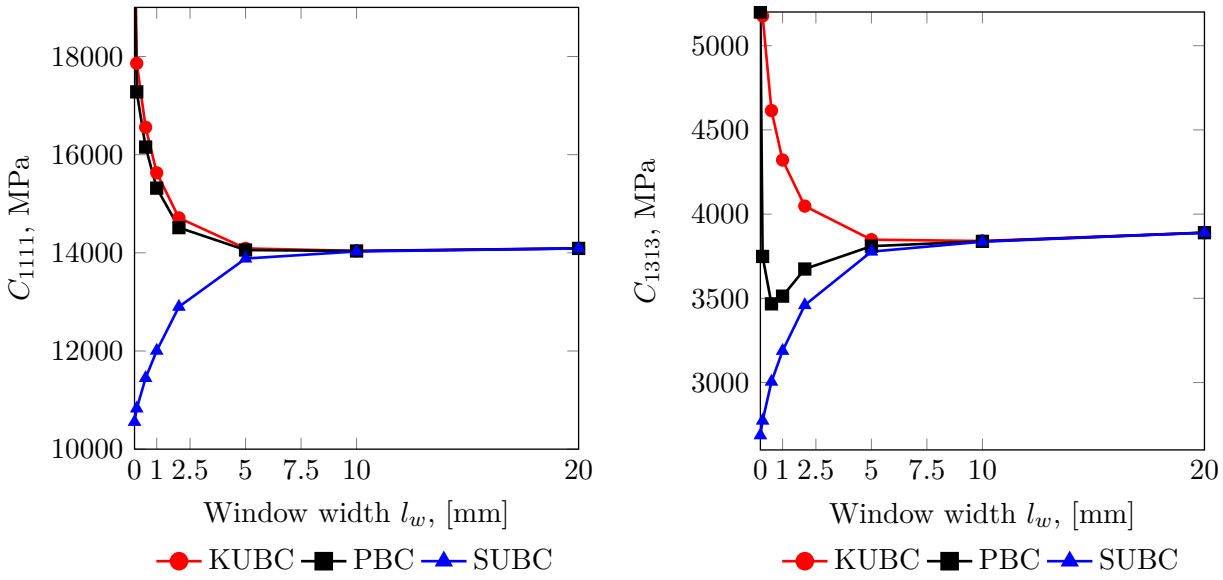

Figure 5.26: Two-phase composite: window size sensitivity for $\phi_I = 0.521$.

Window boundary conditions: sensitivity of the homogenized quantities to the volume fraction states

To further investigate the homogenized quantities' behavior when window boundary conditions are applied, the size of the inclusion in the unit cell is varied to a maximum value of $r = 4.99$ mm. The window size is fixed such that $l_w/l_{RVE} = 1$. As the boundary conditions are not important in the window method, KUBC are applied.

Figure 5.27 shows that good agreement between the homogenized quantities for low volume fraction values is achieved. Curiously, the volume fraction's value, where the window boundary conditions start to underestimate the results, is lower compared to the cubical void example. Thus, it is problem-dependent. In the literature, as indicated in section 5.7 it is emphasized that when the second phase of the unit cell is void, incorrect results can be observed for the volume fraction larger than 50%. While for rigid inclusions, the homogenized quantities are not valid after the volume fraction reaches 40%. This statement entirely agrees with the results observed in Figure 5.27. The tensile-driven homogenized entry starts to diverge at about 40% of the inclusion volume fraction.

Brief summary:

- The window method provides good estimates for two-phase unit cells only with a low volume fraction of the inclusion.

Window boundary conditions: sensitivity of the homogenized quantities to the inclusion hardness

Self-consistency methods are also considered to be sensitive to the inclusion hardness. This can be characterized by a ratio $E_{inclusion}/E_{matrix}$. For all examples above, this ratio was

fixed to 23.33. In the following, the Young's Modulus of the inclusion is varied to achieve different inclusion hardness. The radius of the spherical inclusion is kept at $r = 4.77$ mm. This corresponds to the volume fraction $\phi_I = 0.435$ in Figures 5.24 and 5.27. The window size is kept so that $l_w/l_{RVE} = 1$.

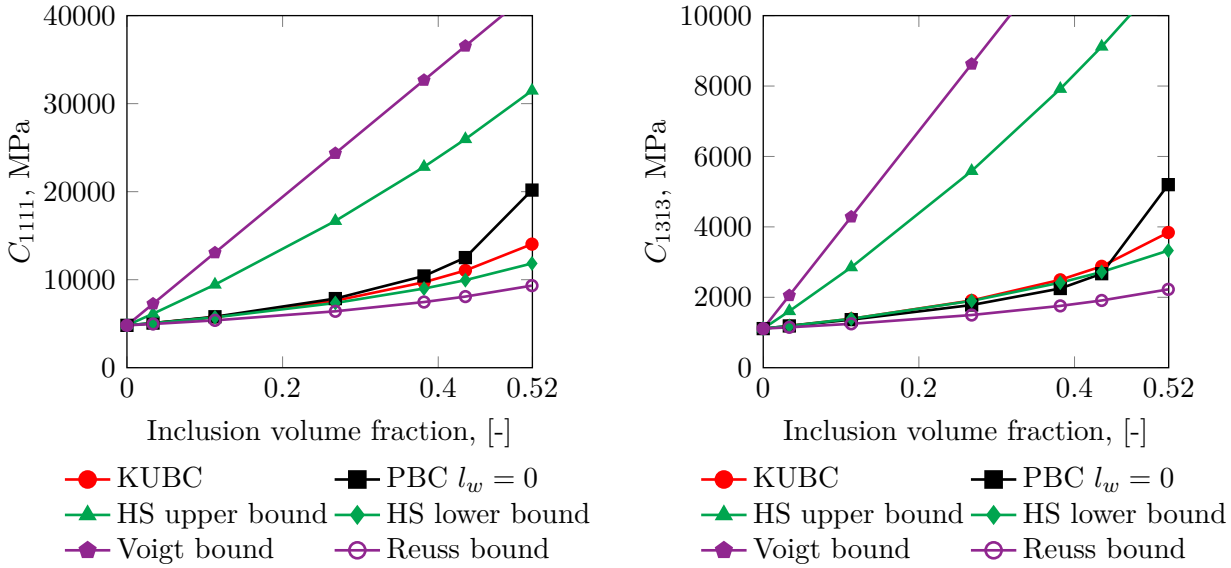

Figure 5.27: Two-phase composite: homogenized quantities for different porosity states using window BCs.

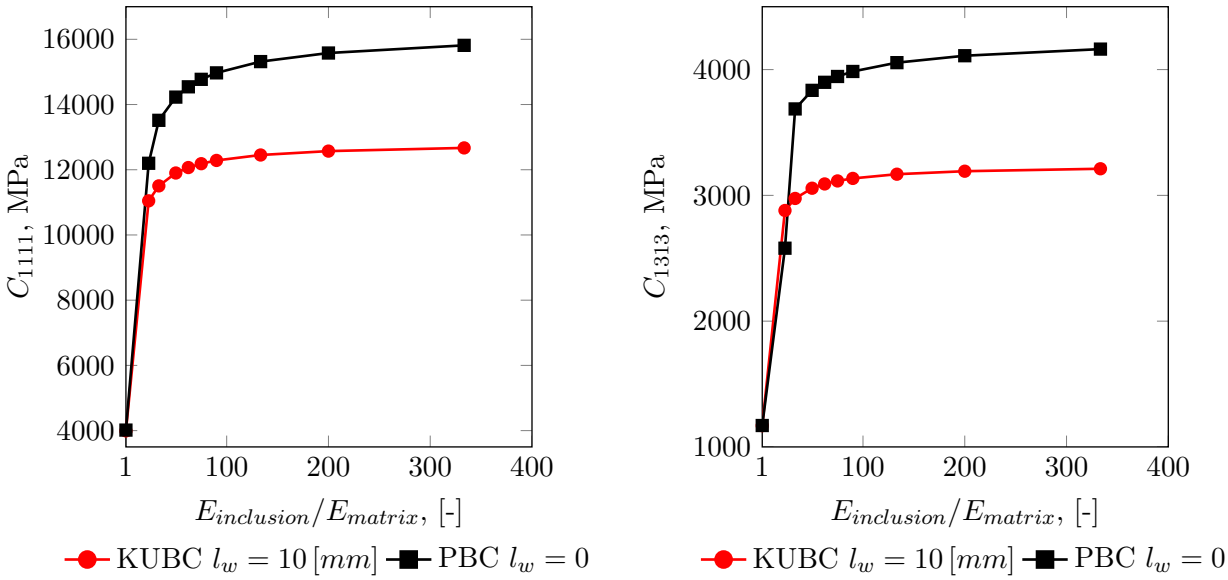

Figure 5.28: Two-phase composite: influence of the ratio $\frac{E_{inclusion}}{E_{matrix}}$ on the homogenized properties.

Figure 5.28 indicates that with the increase of the ratio between the Young's Modulus of the inclusion and the matrix, the gap between the homogenized value obtained by conventional PBC without the window and KUBC with the window also increases. Thus, the applicability of the window method also depends on the properties of the considered inclusion.

Brief summary:

- The applicability of the window method depends on multiple factors. These are type of the inclusion (e.g. void or another material), volume fraction and inclusion hardness (void is an infinitely soft inclusion).
- Overall, the window boundary conditions deliver reasonable estimates for smaller volume fractions and smaller inclusion hardness.

Chapter 6

Validation and verification of additive manufacturing product simulation

As mentioned in chapter 2, the metal additive manufacturing process often introduces geometrical and topological variations in the final parts. These process-induced defects depend not only on the process parameters but also on the printed scale. The smaller the scale of the smallest features, the less reproducible the result of the manufacturing process becomes. Thus, in the following, the representative structures of two opposite groups will be considered.

The first example is a periodic octet-truss lattice structure discussed in section 6.1. This part is produced at a scale, which allows for good control of the process parameters. The size of the smallest design feature is 0.4 mm. This dimension for the considered metal steel powder leads to a reproducible structure with preserved geometrical features. Furthermore, it allows for better control of the experimental investigations. Thus, it provides a strong basis for validating the proposed numerical workflow shown in Figure 2.6.

The second example is the grid-like microarchitectured structure demonstrated in section 6.2. In this case, the size of the printed struts is 96 μm. In contrast, to the first example, this scale is microscopic in the additive manufacturing process. The consequences of choosing such small geometrical features and the numerical and experimental results will be briefly discussed in section 6.2.

6.1 Periodic octet-truss lattice structure[b,c]

The work described in this section was carried out in close collaboration with Computational Mechanics and Advanced Material group at the University of Pavia and Department of Civil Engineering at Aalto University. Their contribution, in particular, of Massimo Carraturo, PhD, Gianluca Alaimo, PhD, Prof. Ferdinando Auricchio, Prof. Alessandro Reali, Seyeed Bahram Hosseini and Prof. Jarkko Niiranen is gratefully acknowledged.

A few samples of a periodic octet-truss lattice structure have been produced to validate the proposed numerical workflow for material characterization experimentally. The de-

tails on the design and the additive manufacturing process are provided in section 6.1.1. Then, these specimens have been experimentally investigated. Three main characteristics have been measured: macroscopic porosity of the printed structures, effective Young's Modulus, and the bending rigidity. The experimental setup is further explained in the consequent section 6.1.2.

Although the considered periodic octet-truss lattices are produced at a larger scale, the manufacturing process causes significant deviations from the designed geometry. Thus, the designed CAD models are compared to the printed specimens in section 6.1.3. The comparison is performed qualitatively via a visual identification of the overall geometrical variations and quantitatively by estimating the geometric characteristics, such as macroscopic porosity.

Then, the material characterization numerical workflow is applied to evaluate the mechanical behavior of the considered lattice. In the following, the path indicated with green arrows in Figure 2.6 is closely followed. In particular, all proposed techniques are applied and compared to both the experimental values and the path results indicated with black arrows.

The comparison starts by investigating the octet-truss lattices' behavior in tension in section 6.1.4. Numerical simulations of the tensile test are performed on both as-manufactured and as-designed geometries and compared to experimental values. The former is analyzed employing FCM introduced in chapter 4, whereas the latter using conforming mesh finite elements based on the CAD geometry. Furthermore, the first-order homogenization technique presented in chapter 5 is also employed to simulate the tensile test again using both as-manufactured and as-designed geometries and compare them to DNS results.

Numerical homogenization faces a few significant difficulties when applied to these octet-truss samples. In contrast to the examples shown in section 5.9, the structures under consideration are not strictly periodic. Due to the geometrical irregularities, the octet-truss lattices can only be considered macroscopically periodic, i.e., within and between the unit cells, there is a broad spectrum of the observed variations. Moreover, the octet-truss lattice shows many irregular voids crossing the boundary of RVE. Following the conclusions from the simplified examples discussed in section 5.9 and despite in a strict sense non-periodic underlying geometry, the best estimate of the effective Young's Modulus can be achieved via the application of the periodic boundary conditions. In this case, their application in the conventional mesh-conforming way would be rather tricky. Instead, the proposed way to apply the PBC (see section 5.6) is employed. This approach allows for flexibility in the geometrical variations of the considered volumes. Furthermore, it is essential to mention that the octet-truss lattices under investigation have a large macroscopic porosity. Thus, in the following, the window method will not be employed.

Finally, the bending behavior of the octet-truss structures is studied in section 6.1.5. Like the tensile test, the direct numerical three-point bending test results on both as-manufactured and as-designed geometries are validated against the experimental values. Further, using the first-order numerical homogenization results from section 6.1.4, applicability of the beam theories described in section 3.2 is investigated. Both the classical and the strain-gradient Euler-Bernoulli and Timoshenko beam theories are applied to

analyze the behavior of both as-designed and as-manufactured octet-truss lattice beams.

6.1.1 Manufacturing of octet-truss lattices

The numerical and experimental investigations are carried out on an octet-truss lattice structure. The specimens for experimental testing were produced in the laboratory 3DMetal@UniPV. The contribution of Eng. Alberto Cattenone and Prof. Stefania Marconi of the 3DMetal laboratory of the Department of Civil Engineering and Architecture of the University of Pavia for providing facilities for additive manufacturing and experimental testing is gratefully acknowledged. The manufacturing and experimental testing is performed by Gianluca Alaimo, PhD, and Massimo Carraturo, PhD, at the University of Pavia. Their effort is gratefully acknowledged.

The specimens were produced with SS316L metal powder, using a Renishaw AM400 LPBF system. The adopted LPBF process parameters are detailed in Table 6.1; in particular, a 200 W laser power is used, and a layer thickness of 50 μm.

Process parameters	Value
Build plate temperature	170°C $\pm$ 1°C
Chamber temperature	35°C $\pm$ 5°C
Layer thickness	50 μm $\pm$ 1 μm
Hatch spacing	110 μm $\pm$ 2 μm
Scan speed	1200 mm/s $\pm$ 2 mm/s
Laser power	200 W $\pm$ 0.1 W
Laser spot size	70 μm $\pm$ 1 μm

Table 6.1: Process parameters for octet-truss manufacturing [84].

The unit cell is shown in Figure 6.1 with three orthogonal views indicating main dimensions. The overall cell size is 4×4 mm, the horizontal strut thickness is 0.8 mm, and the inclined struts are 0.4 mm.

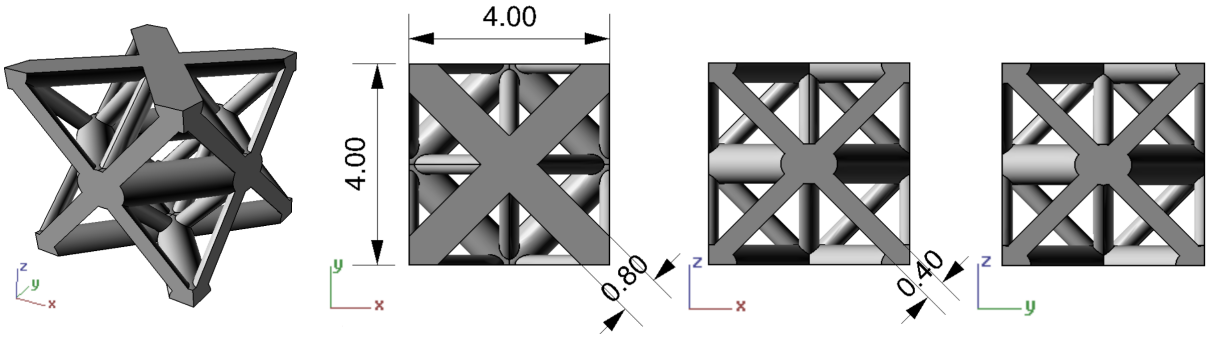

Figure 6.1: Octet-truss unit cell (dimensions are shown in mm) [84].

The first goal of these numerical and experimental investigations is to validate the material characterization workflow in tension. Thus, a tensile specimen is constructed from $12 \times 2 \times 1$ unit cells. As one of the further objectives of this work is the investigation of

the lattice bending behavior, an octet-truss unit cell indicated in Figure 6.1 is also used to construct the four beam-like structures shown in Figure 6.2. These beams have the same length of 128 mm (32 cells) and the same width of 8 mm (2 cells) but different heights (thicknesses): 4, 8, 12, and 16 mm, respectively (1, 2, 3, and 4 unit cells). Then, the upper and the lower side of the beams was completed to contain the full strut size of 0.8 mm (see zoomed side of a representative specimen in Figure 6.3). These complements were added for the printing resolution and for the assumption that possible applications would most probably include such complements. According to CAD-based FE-simulations, trusses with and without these complements behave almost identically, both qualitatively and quantitatively. Therefore, the total heights of the specimens are 4.8, 8.8, 12.8, and 16.8 mm. Thus, the constructed thickness-to-length ratios are 0.03, 0.06, 0.09, and 0.13 respectively.

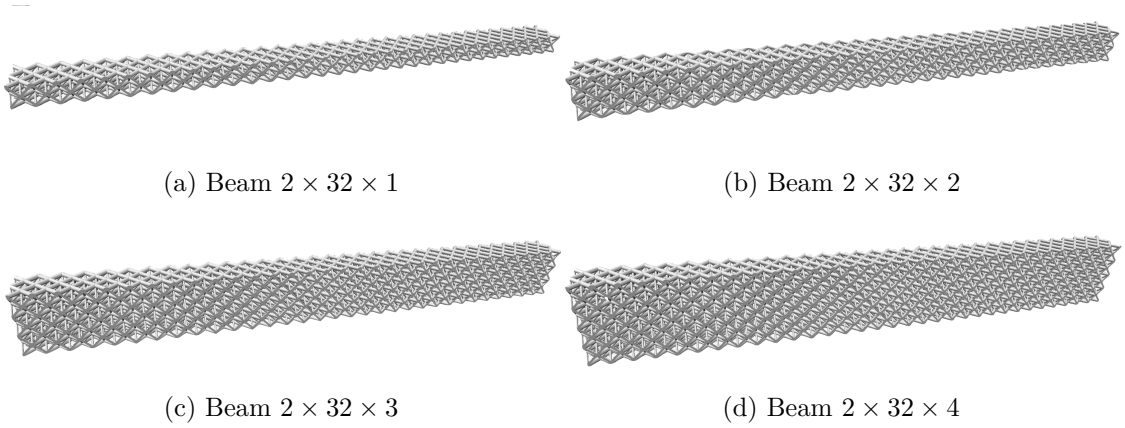

(a) Beam $2 \times 32 \times 1$ (b) Beam $2 \times 32 \times 2$

(c) Beam $2 \times 32 \times 3$ (d) Beam $2 \times 32 \times 4$

Figure 6.2: Investigated CAD models of the octet-truss beam structures [83].

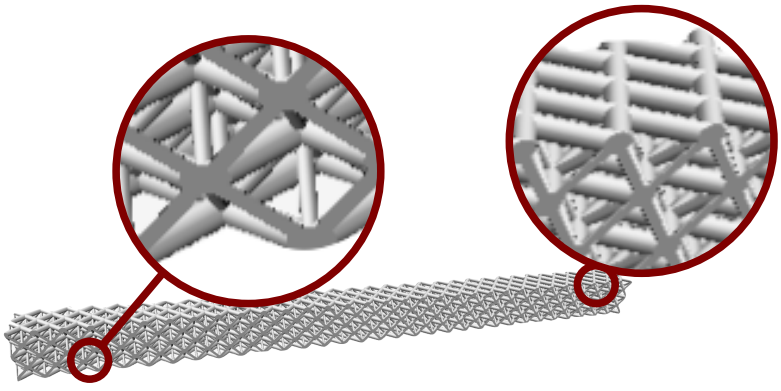

Figure 6.3: Zoom on the completed upper and lower struts of the beam $2 \times 32 \times 2$ [83].

According to the material data sheet provided by the powder producer [141], the considered setup leads to a bulk material with Young's modulus 190 GPa $\pm$ 10GPa along the longitudinal direction with the density of $\rho = 7.99\, g/cm^3$. This value as indicated in the

data sheet depends on the printing direction. In the orthogonal direction to the printing the Young's modulus is reported to be 197 GPa ± 4GPa. As these two values are fairly close to each other, in the following an isotropic material with the Young's modulus being 190 GPa is assumed.

The produced tensile specimens after heat treatment at $400°C$ in the chamber Nabertherm LH120/12 for 2 hours are shown in Figure 6.4. The bending specimens are depicted in Figure 6.5.

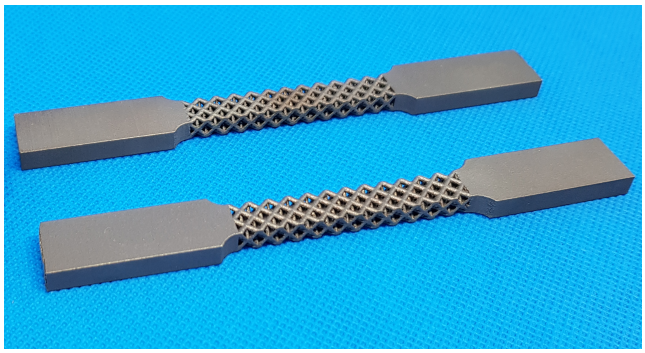

Figure 6.4: Printed tensile specimens after heat treatment [84].

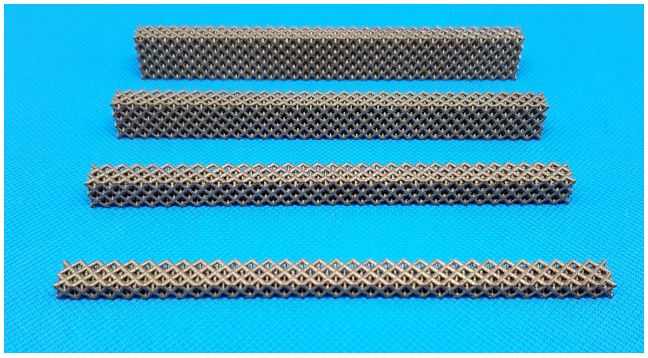

Figure 6.5: Printed bending specimens after heat treatment [83].

After printing, tensile and bending specimens were subjected to a computed tomography before experimental testing. The geometry acquisition was performed with the CT scanner Phoenix V. The tensile specimen was scanned resulting in a voxel resolution of 27 μm, while the bending specimens were acquired with 61 μm.

6.1.2 Experimental setup

For a comprehensive experimental study of the printed specimens four main investigations are undertaken. First, to evaluate the difference between overall as-manufactured and as-designed structures, the samples dimensions are measured. Second, to characterize as-manufactured macroscopic geometrical variations the overall porosity is measured. Third, the tensile specimens are tested under tensile loading to evaluate the effective directional Young's modulus. Finally, the bending rigidities of four printed bending specimens are measured [84, 83].

As-manufactured samples dimensions

As deviation of the as-manufactured from as-designed overall dimensions is expected, the corresponding measurements are performed experimentally. In particular, an overall width, height and the length of the printed beam specimens is measured with the help of a digital caliper. Table 6.2 summarizes the experimentally determined values together with the designed characteristics. As there is no repetitive measurement available, the measurement uncertainty of the used instrumentation is provided. The measurement uncertainty is computed according to [73] using the uncertainty propagation of the used instrument's precision. As the dimensions of the as-manufactured samples are measured with the digital calipers, the instrumentation error of this device is used to evaluate the measurement error. The results are indicated in Table 6.2.

Specimen	Width, [mm]		Height, [mm]		Length, [mm]	
	D	M	D	M	D	M
$2 \times 32 \times 1$	8.00	8.22 ± 0.001	4.80	4.96 ± 0.002	128.00	$128.82 \pm 1e-4$
$2 \times 32 \times 2$	8.00	8.22 ± 0.001	8.80	8.89 ± 0.002	128.00	$128.83 \pm 1e-4$
$2 \times 32 \times 3$	8.00	8.22 ± 0.001	12.80	12.89 ± 0.001	128.00	$128.91 \pm 1e-4$
$2 \times 32 \times 4$	8.00	8.22 ± 0.001	16.80	16.96 ± 0.001	128.00	$128.91 \pm 1e-4$

Table 6.2: Dimension comparison of the beam specimens (D stands for as-designed, M stands for as-manufactured) [83].

The values shown in Table 6.2 are used in this thesis to compute the effective cross-sectional area A and the effective cross-sectional moment of inertia I of the as-designed and as-manufactured specimens. Both, A and I are determined by using the outer dimensions of the beams. Furthermore, these values are used to identify the as-manufactured porosity as described in the following paragraph.

Porosity of the printed structures

The overall porosity of the lattice structures is measured for two reasons. The first motivation is to compare the experimentally determined porosity value to the as-designed CAD-based ones, thus, providing the first estimate on the geometrical variations of the as-manufactured geometries with respect to the original CAD models shown in Figure 6.1 and Figure 6.2. The second reason is to experimentally verify the porosity values determined from the acquired CT scan of tensile specimen and beams.

The porosity values are determined for the beam specimens by evaluating their mass m. Then, considering the printed density ρ indicated in [141] the overall porosity can be calculated as:

$$\phi = 1 - \frac{V_m}{V} = 1 - \frac{m}{\rho V} \tag{6.1}$$

The overall volume V was then determined by measuring the dimensions of the bending specimens. The volume occupied by the material V_m was computed in two steps. First,

the printed specimens were weighted to determine their mass. Then, the volume was calculated according to the bulk density specified by the powder producer [141]. The measurement uncertainty of the porosity values ϕ was estimated based on the accuracy of the used instrumentation.

Tensile experiment

To experimentally validate the proposed numerical framework for the mechanical evaluation of lattice components, a tensile test was performed. For the aim of this work, only the elastic regime was investigated. Herein a brief description of the experimental setup is provided.

The lattice specimen was tested under displacement control, at room temperature, on an MTS Insight test system, with computer control and data acquisition. The strain is measured with a video extensometer (ME-46 video extensometer, with 1 mm resolution and a camera field of view of 200 mm) at the mid-section of the specimen (gage section). Following ASTM E111 recommendations, the displacement rate is set to 2 mm/min and it is selected to produce failure between 1 and 10 minutes. The Young's Modulus was then computed according to ASTM E111 standard [5] with the corresponding measurement error.

Bending rigidity

The final experimentally determined value is the bending rigidity of the octet-truss lattice beams as defined in Equation 3.29. This quantity describes the characteristic overall (global) resistance of the structure against the bending deformation. The values of bending rigidity of the four 3D printed structures of Figure 6.4 is experimentally measured by a three-point bending test under quasi-static conditions and displacement-controlled velocity (see Figure 6.6). The span (L) between the supports is 120 mm, while the applied point load (F) is transferred in the middle of the span of the beam. During the experiment, the imposed displacement and the corresponding force are recorded. The bending rigidities of the beams are then computed by using Equation 3.29. All tests are performed in both elastic and plastic regime. However, for the aim of this work only the elastic characteristics are considered. Experimental results will be discussed together with the numerical values in the following sections.

6.1.3 Geometrical comparison of as-designed and as-manufactured specimens

At first, the as-manufactured tensile specimen is compared to the as-designed CAD model used for its printing. The CT scan, obtained with the help of single thershold technique described in section 2.3, was converted to a point cloud and overlayed with the designed CAD model. To achieve the best possible fit of these two models, a two-step procedure is employed. First, a coarse alignment of the point cloud to a CAD model is performed. In this step, the model bounding boxes are aligned, followed by the point pairs picking. Then, the fine registration is run to achieve the best possible fit of the two models.

The geometrical manipulations are performed with the open-source software CloudCompare. The distance between the point cloud and the CAD model is computed as the nearest neighbor distance (see Figure 6.8). The specimen was printed in the $x-$direction shown in Figure 6.8. An important observation is that there are partially melted powder particles hanging on the diagonal struts (having axes out of the yz-plane) as depicted in Figure 6.8c,d and, on the horizontal struts in Figure 6.7.

Then, the as-manufactured geometry of bending specimens extracted from CT scan images and the as-designed geometric model are compared in Figure 6.9. The following geometrical features of as-manufactured geometry can be observed in the bending specimens compared to the as-designed ones:

- larger truss thickness;
- partially melted material powder particles in overhanging surfaces opposite to the build direction;
- excess material collection in the nodes.

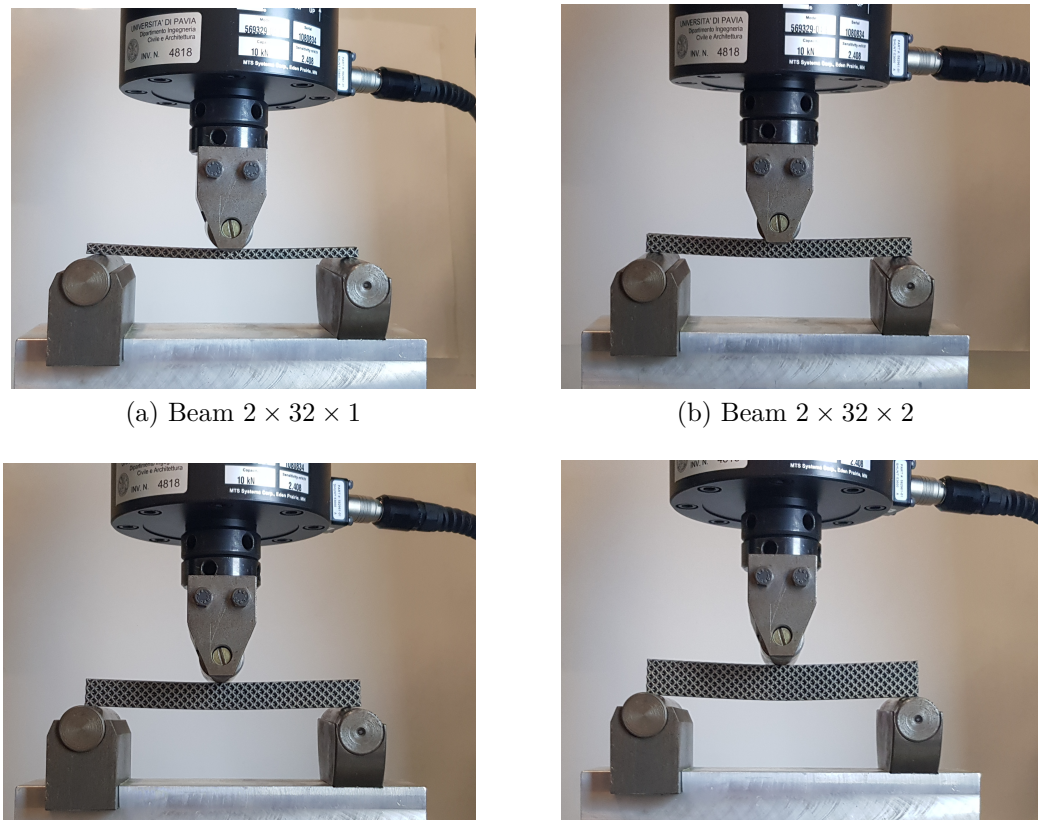

(a) Beam $2 \times 32 \times 1$

(b) Beam $2 \times 32 \times 2$

(c) Beam $2 \times 32 \times 3$

(d) Beam $2 \times 32 \times 4$

Figure 6.6: Bending of beam specimens [83].

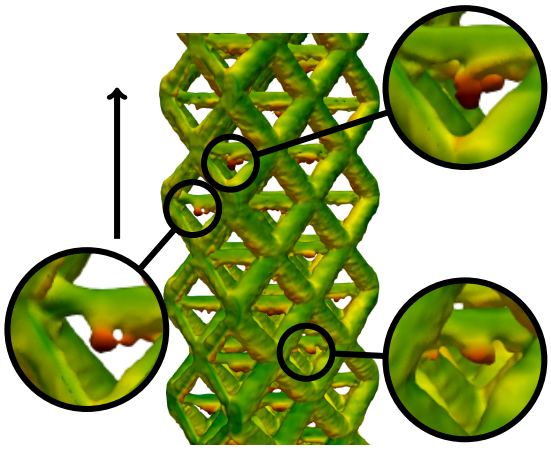

Figure 6.7: Partially melted powder grains attached to the horizontal struts in the octet-truss tensile specimen. The arrow is pointing in the build direction [84].

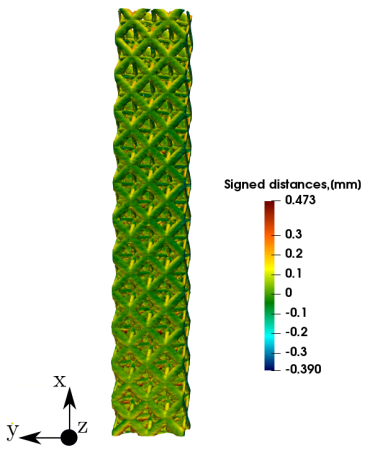

(a) Front view

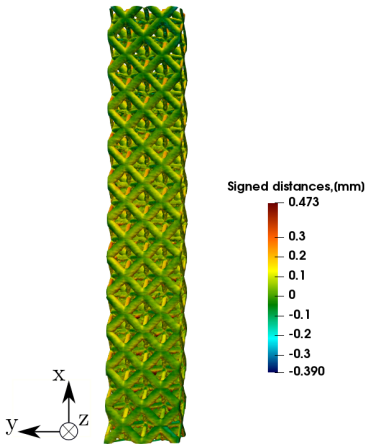

(b) Back view

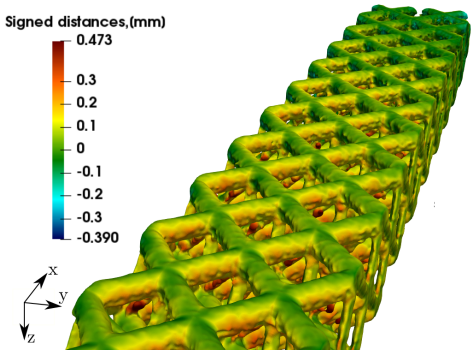

(c) View from the bottom

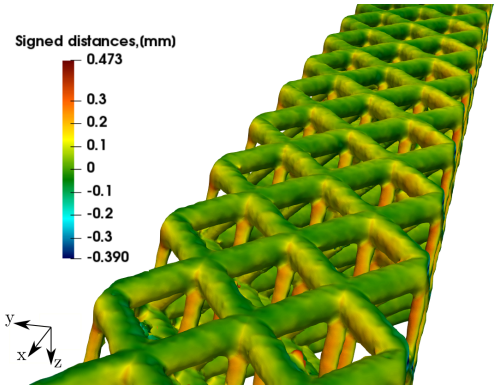

(d) View from the top

Figure 6.8: Comparison of as-manufactured and as-designed tensile specimen [84].

These features are well-known side effects of the LPBF printing process. It is also established in literature [21, 37], that these geometrical features have a strong influence on the numerical results, and thus as-designed models lead to a quite inaccurate prediction of the mechanical behavior of lattice structures.

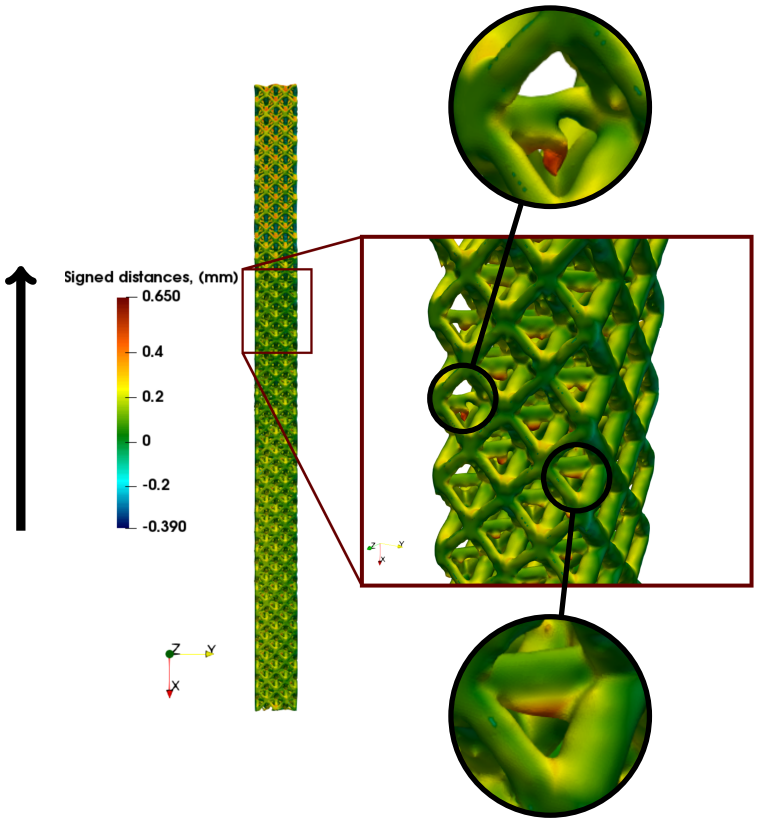

Figure 6.9: Comparison of as-manufactured and as-built octet-truss bending specimen $2 \times 32 \times 2$ (build direction marked with the black arrow) [83].

Then, the CT-based porosity is compared with the CAD-based and experimental values in Table 6.3. The experimental results together with the estimated instrumentation error are determined according to the procedure described in section 6.1.2. The CAD-based porosity is measured using an as-designed geometrical model of the specimens as shown in section 6.1.1. The CT-based results are obtained similarly using computed tomographic images of the corresponding as-manufactured specimens.

As expected, the CAD-based porosity is always larger than the printed one. This is also supported by the geometrical comparison of the CAD and CT-based model (e.g., Figures 6.7 and 6.9). One of the reasons why the as-designed parts have higher porosity values is that the struts with axes in the yz-plane are always larger in the printed components than in the designed ones. This is because partially melted powder particles remain attached to the surface of the manufactured component opposite to the build direction. Such defects are a well-known natural side-effect of the melting process together with the excess material collection in the nodes, where higher temperatures occur. Overall, the CT-based porosity is in good agreement with the experimental values, making us confident in the sufficient accuracy of the as-manufactured geometry representation provided by CT

scan measurements. However, the porosity value of the thickest beam differs from the experimentally determined value by 6.5%. Although there is a certain possibility to vary the threshold value of the CT scan, the experimental porosity value cannot be achieved within a reasonable range of variation of HU_{thres}. Curiously, the beam with $2 \times 32 \times 3$ cells indicates an increase in the experimental porosity compared to other specimen, which is also observed in the CT scan. This tendency, however, seems to be reversed in the case of the thickest beam.

Specimen	CAD-based porosity, [-]	Experimental porosity, [-]	CT-based porosity, [-]
$2 \times 32 \times 1$	0.756	0.638 ± 0.006	0.647
$2 \times 32 \times 2$	0.770	0.630 ± 0.004	0.639
$2 \times 32 \times 3$	0.775	0.677 ± 0.003	0.679
$2 \times 32 \times 4$	0.777	0.630 ± 0.002	0.671
Tensile	0.756	0.646 ± 0.002	0.668

Table 6.3: Porosity comparison of the printed specimens [84, 83].

6.1.4 Numerical tensile test of an octet-truss lattice structure

CT-based direct numerical simulation of a tensile test

Herein, the computed tomography of the tensile specimen is investigated numerically by using FCM as described in chapter 4. The middle part of the obtained CT scan is presented in Figure 6.10. To correctly compute the numerical results, the value of the spatial scalar function $\alpha(\boldsymbol{x})$ defined in Equation 4.2 needs to be accurately evaluated. In the present work - as the material of the product is metal - the indicator function can be directly deduced from the CT scan since the contrast between material and void is very high. To distinguish among the holes where the indicator function $\alpha(\boldsymbol{x})$ is set to 10^{-11} for further numerical investigations and the metal where $\alpha(\boldsymbol{x}) = 1$, the threshold level of the Hounsfield units is set to be 14 500. The standard single thresholding technique described in section 2.3 was sufficient in this case and resulted in the model with the porosity indicated in Table 6.3. All gray values above the limit are considered to be material, while everything below is classified as void.

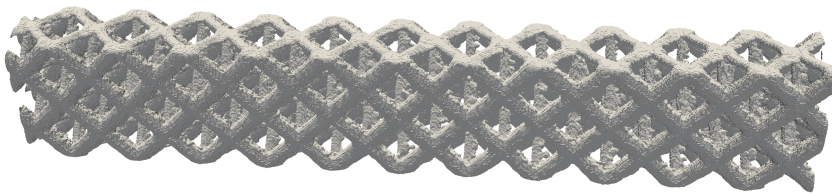

Figure 6.10: CT scan data image of the middle part of the tensile specimen [84].

Having defined the indicator function, a convergence study of the effective Young's modulus is performed. The results of this analysis are summarized in Figure 6.12. Given two different FCM discretizations with $73 \times 44 \times 442$ and $146 \times 88 \times 884$ (i.e., embedding

$4 \times 4 \times 4$ and $2 \times 2 \times 2$ voxels in one finite cell, respectively), a convergence study is carried out increasing the polynomial order of the approximation space. An example of the displacement and stress field arising in such specimen is shown in Figure 6.11. In the following, the numerical results obtained directly computing a tensile experiment on the full specimen are referred to as CT-based DNS results. The relative error is determined with respect to an overkill numerical resolution, where every voxel is an element with the polynomial degree of $p = 2$ resulting in 390 112 737 DOFs. The reference solution, in this case, has a value of 12 736 MPa, and took about 22 min on 90 compute nodes. This overkill result was computed on the SuperMUC cluster of TUM[†].

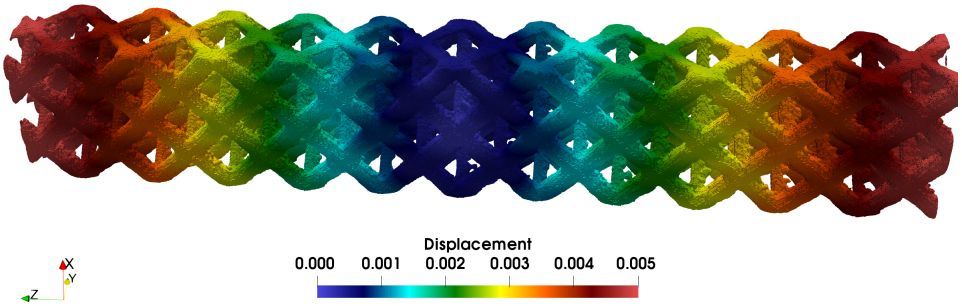

(a) Displacement field along the build direction (z-axis) in mm

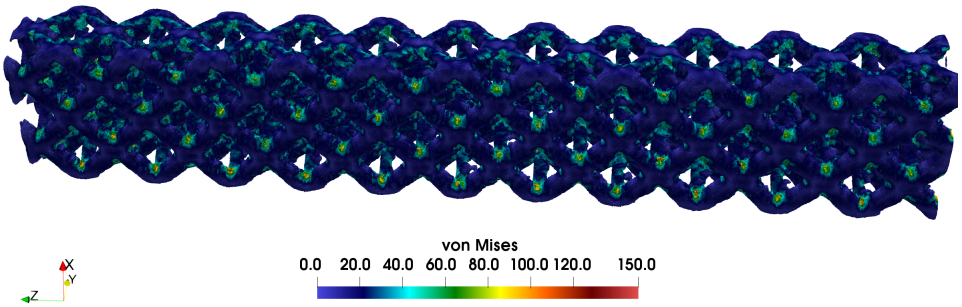

(b) Von Mises stress distribution in MPa

Figure 6.11: CT-based numerical analysis: Representative displacement and stress fields in the middle part of the tensile specimen [84].

The final results for the CT-based numerical simulations are shown together with the experimental and CAD-based values in Table 6.4. As a final estimate, Young's modulus of 13 081 MPa is chosen. This value corresponds to a Finite Cell discretization of $146 \times 88 \times 884$ cells of polynomial degree $p = 3$ resulting in 98 316 435 DOFs. Overall simulation time

[†]The authors gratefully acknowledge the Gauss Centre for Supercomputing e.V. (www.gauss-centre.eu) for funding this project by providing computing time on the GCS Supercomputer SuperMUC-NG at Leibniz Supercomputing Centre (www.lrz.de).

for this case is 52 min on 40 nodes on the CoolMUC cluster of TUM[‡]. The final numerical value is 4.4% different from the experimental value and within the limits of the estimated instrumentation error. Moreover, the results of these analyses show a clear convergence trend of the numerical solution and the method presents a robust behavior even for coarse and low-order discretizations. The above observation confirms the possibility to adopt such an approach for material characterization of as-manufactured AM lattice structures.

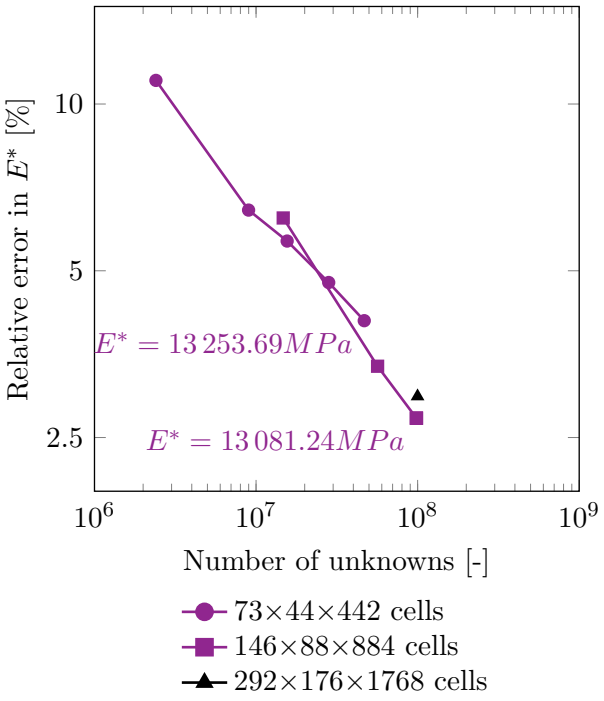

Figure 6.12: Convergence of the effective Young's modulus E^* [84].

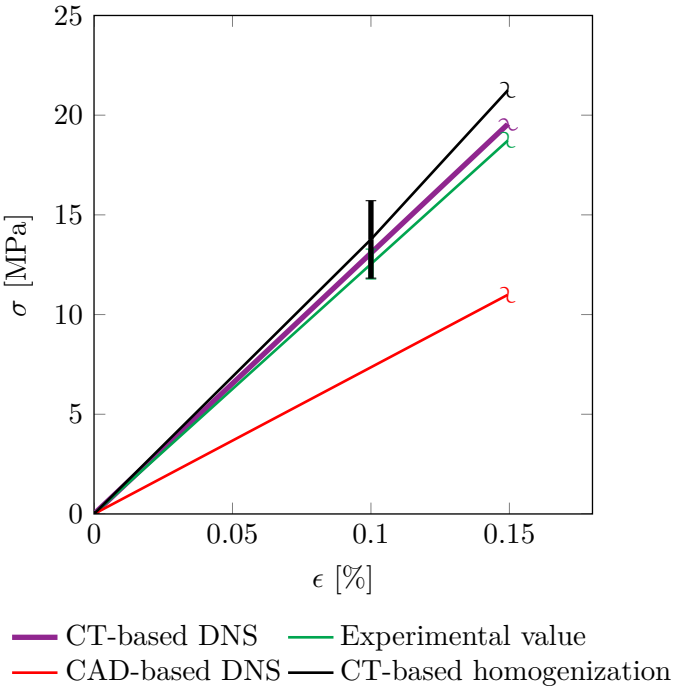

Figure 6.13: Stress-strain curve of the octet-truss lattice structure [84].

Specimen	CAD-based E, [MPa]	Experimental E, [MPa]	CT-based E, [MPa]
Octet-truss	7 356	12 533 ± 751	13 081

Table 6.4: Comparison of experimentally and numerically determined Young's modulus of the octet-truss specimen [84].

CT-based numerical homogenization results

Due to the high computational costs of the DNS numerical analysis, it was decided to investigate less demanding (at least from a computational point of view) approaches. The first-order homogenization technique using the Periodic Boundary Conditions described in chapter 5 is employed. However, the unit cells of the octet-truss lattices are not strictly periodic. In contrast to the numerical examples considered in section 5.9, the periodicity

[‡]The authors gratefully acknowledge the Leibniz Supercomputing Centre for funding this project by providing computing time on its Linux-Cluster.

requirement does not necessarily hold for these samples. The unit cells, due to the manufacturing process, strongly differ from one another. Furthermore, the tensile specimen is very thin in two directions. Thus, the Periodic Boundary conditions are expected to deliver only *apparent* properties, i.e., represent an approximation of the effective behavior. It is important to note that the order relation of the boundary conditions indicated in Equation 5.49 always holds. Thus, the obtained results should be the closest estimate to the effective tensile behavior. To further relax the periodicity requirement and account for the unit cells' variability in the structure, several volumes n are extracted from the whole structure. Then, every unit cell is homogenized which delivers an apparent material tensor $\boldsymbol{C}_n^*$. The whole structure's final response is then determined as a statistical average of all computed tensors together with the standard deviation, indicating the spread of the quantities in the whole domain. The statistical average can be computed in two ways. The first approach is to determine an element-wise mean value of the homogenized elasticity tensor. The second approach is to invert the computed effective material tensors, extract the directional effective Young's Modulus, and then average this quantity. The latter will be further used in this thesis.

The results of all tests are shown together in the stress-strain graph in Figure 6.13. The homogenization is performed on $n = 24$ existing unit cells and the mean value and standard deviation is indicated with the black line in Figure 6.13. The deviation from the mean value is computed by considering the spread of the homogenized Young's modulus through the computed unit cells. An example of the displacement and stress distribution in one of the as-manufactured unit cells is shown in Figure 6.14.

The homogenized material tensor for the depicted unit cell is determined as follows:

$$C^*_{n=12} = \begin{bmatrix} 22665 & 4967 & 14366 & -328 & -66 & 328 \\ 4967 & 13396 & 5968 & -287 & -65 & -50 \\ 14366 & 5968 & 23035 & -7 & 84 & 300 \\ -328 & -287 & -7 & 5351 & -80 & -9 \\ -66 & -65 & 84 & -80 & 6280 & 5 \\ 328 & -50 & 300 & -9 & 5 & 13120 \end{bmatrix}$$

The depicted tensor suggests that the octet-truss unit cell possesses the orthotropic material symmetry. The off-diagonal entries in lines 4–6 are relatively small and can be treated as zero. When all of the unit cells are considered, it can be observed that the mean value of the homogenized numerical solution deviates by 5.3% from the one determined by using DNS tensile test on the CT scan, but - due to the large geometrical variations in the as-manufactured specimen - the octet-truss unit cells provide a considerable standard deviation from the mean value as shown in Figure 6.13 and in Table 6.5. The resulting interval of confidence includes both experimental and CT-based DNS simulation results. The homogenization with FCM is a less memory expensive operation than homogenization with Voxel-FEM. Furthermore, it does not require high-performance computing resources in contrast to the DNS simulation (see Table 6.5). In light of the above results, it can be concluded that the first-order homogenization based on the statistically periodic as-manufactured geometry can be a reliable technique to predict the tensile behavior of AM lattice structures.

Homogenization setup	E^*,[MPa]	Computational nodes	CPU per node	Wall-clock time
FCM	13769 ± 1942	1	40	80 min
Voxel-FEM‡	13804 ± 1985	1	40	82 min

Table 6.5: Comparison of the results and the computational resources for numerical homogenization (‡ - memory extensive computation) [84].

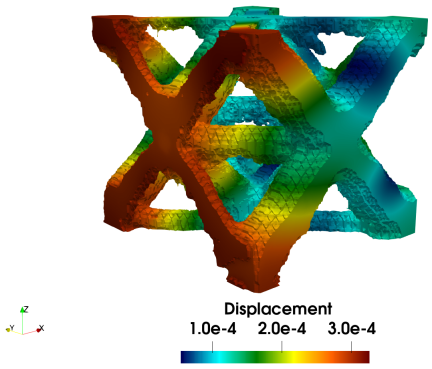

(a) Displacement field for the load case in $x-$direction

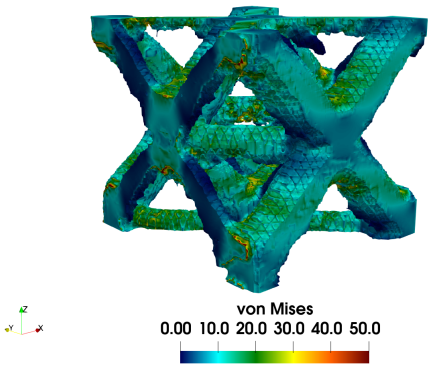

(b) Von Mises stress distribution in MPa

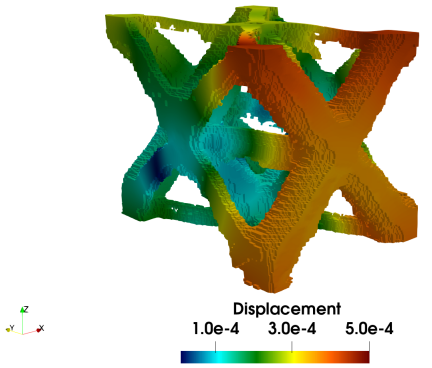

(c) Displacement field for the load case in $yz-$plane

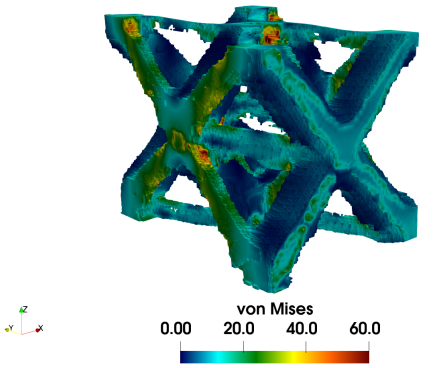

(d) Von Mises stress distribution in MPa

Figure 6.14: CT-based numerical homogenization: Representative displacement and stress fields on one unit cell for tensile and shear load case [84].

CAD-based direct numerical simulation of a tensile test

As a next step, the same numerical studies are performed on the original CAD model used for specimen printing. For the direct numerical simulation, quadratic solid tetrahedral elements are chosen to perform analysis in Ansys®†. The converged solution shown

†The numerical computations of the full tensile specimen in Ansys were performed by Gianluca Alaimo at the University of Pavia. His contribution is gratefully acknowledged.

in Table 6.4 is achieved with 10 954 356 DOFs. The total number of DOFs, in this case, is considerably lower than the one used for the CT-based computations. This arises due to the geometrical complexity of the considered CT scan. In the as-manufactured geometry many more small features are present, such as e.g. overhangs as indicated in Figure 6.7. Thus, a higher resolution is required to capture the mechanical contribution of such geometrical details to an overall part behavior.

As expected from the higher porosity value measured in section 6.1.3, the ideal CAD model delivers a much smaller Young's modulus than the experimental one. This relates to the geometrical differences of the as-manufactured and as-designed specimens presented in section 6.1.3. This already demonstrates that the high discrepancy between as-manufactured and as-designed porosity values lead to an inaccurate prediction of Young's modulus based on CAD geometries (see Table 6.4). The values of the Young's moduli are even further appart than the difference between as-manufactured and as-designed porosity.

CAD-based homogenization with an equivalent porosity

To investigate in detail the observed discrepancy among CAD-based results and experimental measurements a further study on the CAD geometry is undertaken. The geometrical features of the unit cell depicted in Figure 6.1 are varied linearly to achieve different porosity states ϕ. Such a study can be performed using different approaches. The main geometrical feature of the considered unit cell is the strut diameter. In Figure 6.1 all struts horizontal to a printing direction are 0.8 mm, while the struts inclined to the printing direction are 0.4 mm. Thus, the dimensions of the struts could be varied freely to achieve different porosity values. However, to reduce the dimension of the undertaken study both strut diameters are increased by the same increment, e.g. 0.2 mm. In particular, the diameter of the smallest struts is increased from 0.4 to 1.0 while the largest diameter - from 0.8 to 1.4.

Then, the first-order homogenization technique described in chapter 5 in combination with the Finite Cell Method is applied to evaluate the effective Young's modulus based on the modified CAD models. The dependency of the homogenized Young's modulus E^* on the porosity is depicted in Figure 6.15. As expected from the literature, a change in the porosity does not cause the same change in the Youngs modulus. Instead, the obtained relation $E^*(\phi)$ is indirectly proportional but its exact determination is too elaborate to be predicted analytically.

Under the assumption that the overall porosity is the only determining factor for Young's modulus, an experimentally determined porosity of 0.668 delivers a value of 16 178 MPa. This is much higher than the results of CT-based numerical analysis (13 081 MPa) as well as the experimentally measured value of 12 533 MPa. Therefore, the porosity can not be the only determining factor.

The strong variability in the printed struts and nodes could explain this difference raising the importance of the incorporation of the precise as-manufactured geometries into the numerical analysis. First of all, there is a significant geometrical deviation of the printed struts from as-designed boundaries. Next, the non-homogeneity of material properties of the manufactured component, due for instance to voids and inclusions is

present within the printed structure. These inhomogeneities are shown in Figure 6.16 on one of the slices of the obtained CT scan.

These topological and geometrical defects introduce an additional level of complexity in the mechanical characterization of AM lattice structures, which cannot be merely modeled with an equivalent CAD-based geometrical model, but it necessarily requires a numerical approach (DNS or homogenization) able to take into account the actual geometry of the manufactured part. The presented numerical framework naturally incorporates the as-manufactured components thus considering the arising defects.

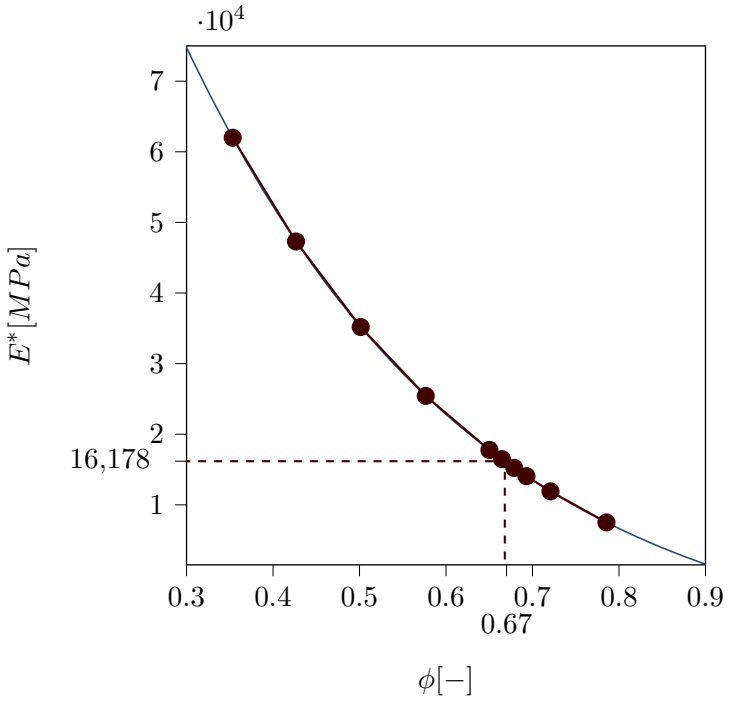

Figure 6.15: Porosity study of the ideal CAD-based unit cell using the Finite Cell Method [84].

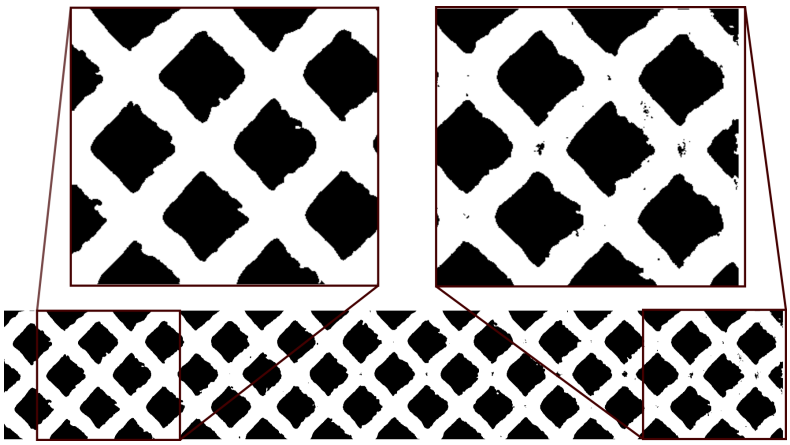

Figure 6.16: Representative slice of the CT scan with a zoom on arising inhomogeneities [84].

6.1.5 Numerical bending test of an octet-truss lattice structure

Direct numerical simulation of three-point bending test

In order to further support the above observations, a numerical simulation of the three-point bending test described in section 6.1.2 was carried out. Numerical experiments are performed for each one of the four specimens on both as-designed (CAD) and as-manufactured (CT) geometrical models. In both cases, the same boundary conditions and load cases are applied as in the experimental setup. The simulation of the as-designed geometry is carried out by using Comsol™ with quadratic tetrahedral Finite Elements[†], whereas as-manufactured geometry is simulated using the high-order Finite Cell Method as described in chapter 4 with finite cells of polynomial degree $p = 3$ containing $2 \times 2 \times 2$ voxels. A representative discretization is depicted in Figure 6.17. The latter is performed directly on the complete CT image. A complete scan of every beam specimen is immersed in a grid of finite cells of polynomial degree $p = 3$ containing $2 \times 2 \times 2$ voxels. An example of the used discretization for the analysis of the beam specimen in Figure 6.9 is depicted in Figure 6.17. Figure 6.17 shows a complete finite cell mesh with two consequent zooms on the corner of this model. As an example, for this specimen a total number of $51 \times 524 \times 32$ cells is used. It should be emphasized, that no simplifications are carried out to incorporate the as-manufactured geometry in the direct numerical analysis.

Representative displacement and von Mises stress distributions for an as-manufactured beam specimen are shown in Figure 6.18.

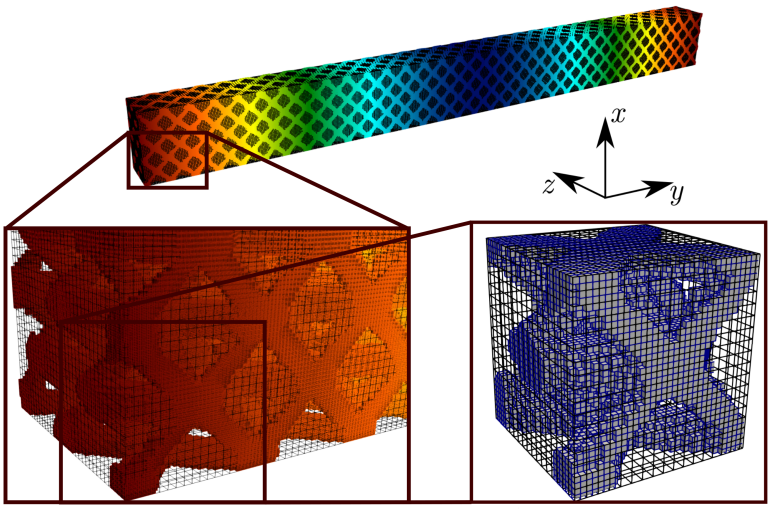

Figure 6.17: Finite Cell mesh with $51 \times 524 \times 32$ cells for $2 \times 3 \times 32$ beam specimen [83].

The numerical bending rigidities are, then, computed using Equation 3.29 and their values are compared to the experimental ones in Figure 6.19. To provide an insight into the necessary computational resources, the simulation of the as-designed beam of

[†]The CAD-based numerical experiments were performed by Seyyed Bahram Hosseini at Aalto University. His contribution is gratefully acknowledged.

$2 \times 3 \times 32$ is performed on a standard workstation with i7-9700K processor and 64GB of RAM using shared memory parallelism. The total wall clock time for the computation amounts to 2 minutes including pre- and postprocessing. By contrast, the simulation of the as-manufactured geometry on the cluster using the distributed memory parallelism on 40 28-way Haswell-based nodes with 64GB RAM takes 37 minutes. This large difference is due to the fact that the latter model incorporates many more small scale details.

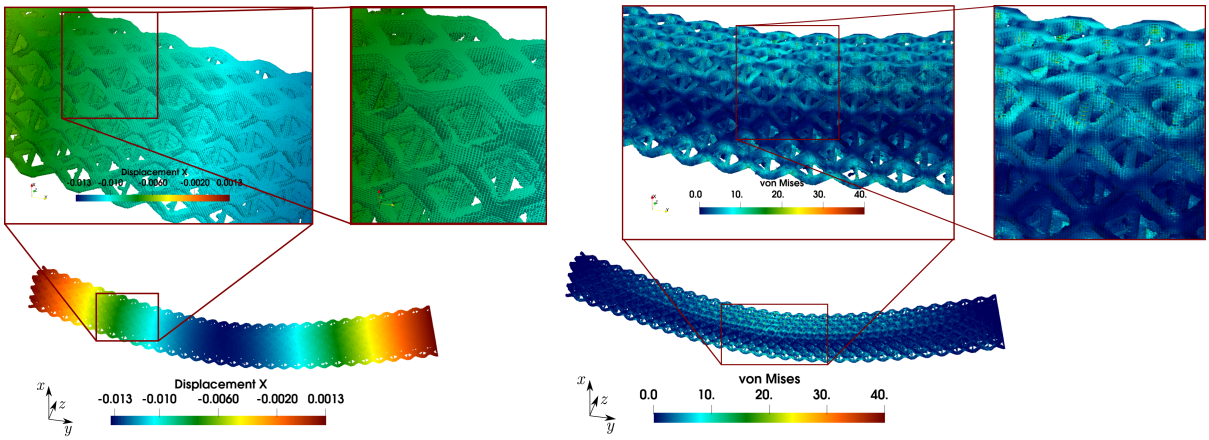

(a) Displacement field in mm in the load direction

(b) Von Mises stress in MPa

Figure 6.18: Displacement and von Mises stress distributions for as-printed beam $2 \times 3 \times 32$ utilizing the Finite Cell Method [83].

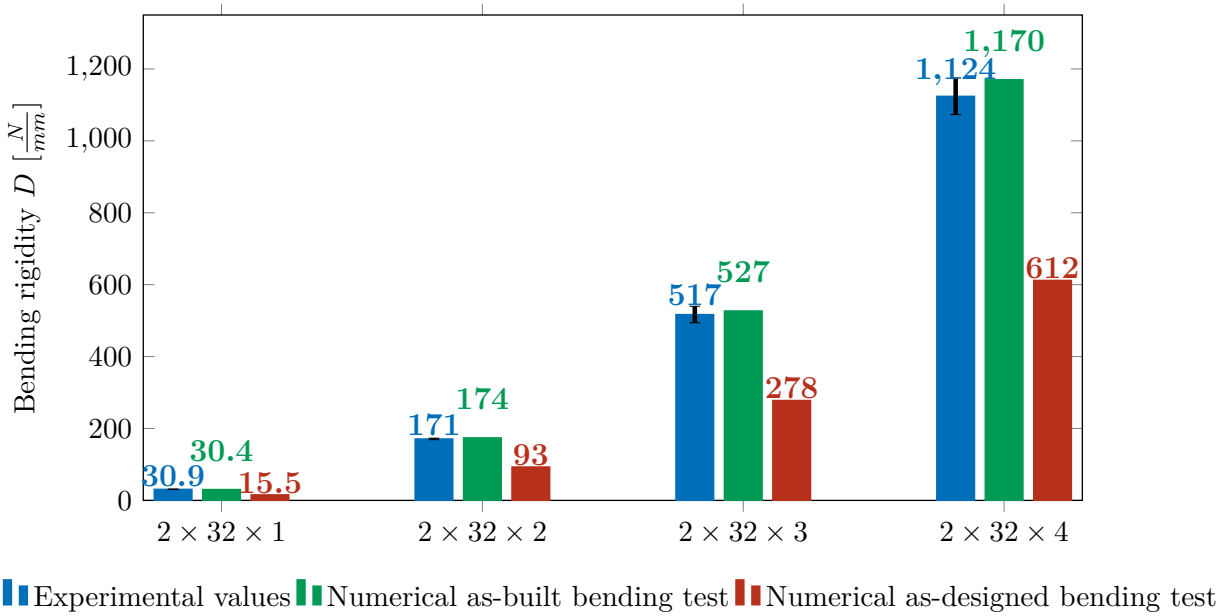

Figure 6.19: Comparison of bending rigidity obtained by numerical bending tests on the original as-designed geometry and on the as-manufactured geometry obtained from CT scan data [83].

The qualitative comparison of these results shows that the as-designed and as-manufactured geometries follow the same tendency of a higher rigidity value for thicker beams. Nevertheless, quantitatively the relative errors of as-designed bending rigidity value are always above 40%. This gap is largely driven by the geometrical difference between the as-manufactured and as-designed geometries. As the CT-based and experimental porosity values shown in Table 6.3 are lower than the designed ones, the as-designed bending rigidity should agree with this trend. According to the results in Figure 6.19 the as-manufactured bending rigidity is larger than the designed one, thus, supporting the described tendency. Furthermore, the numerical simulation on the printed geometry via computed tomography provides an excellent agreement with the experimental tests, with a relative error always below 4%. Interestingly, although the porosity determined by a CT scan for the thickest beam is lower than the porosity determined experimentally (see Table 6.3), the numerical bending rigidity for this specimen is slightly higher than the experimental value. The dependency between the porosity and the bending rigidity of the samples is, in general, non-linear. This is similar to the tensile characteristics, such as the homogenized Young's modulus (see [84]). However, the results are "reversed" in this case. As the experimental value is obtained by measuring one specimen, this could suggest that the CT-based porosity provides a more accurate estimate. Furthermore, this would support the trend of a slightly higher porosity value for thicker beam setups as described in the previous section.

Experimental validation of strain gradient beam theory for octet-truss lattices

Since in a three-point bending it is often desired to predict the mechanical behavior by dimensionally reduced beam models, a more careful investigation of the applicability of the beam models described in section 3.2 to octet-truss lattice structures is undertaken.

The beam models rely on the identification of effective quantities, such as Young's modulus E^* and shear modulus G^*. There are two ways to obtain the necessary quantities. For the as-designed geometries, only the first-order homogenization can be applied, as there is no possibility to perform experimental tests on it, while for the as-manufactured structures, the effective Young's and shear modulus can be measured experimentally. The as-manufactured Young's modulus of octet-truss lattices was experimentally evaluated in earlier section, whereas the effective as-manufactured shear modulus is now determined by means of the first-order homogenization technique described in chapter 5. To account for non-periodic as-manufactured cells, homogenization is performed through the whole structure, taking the mean value of the homogenized shear modulus similar to the identification procedure of the homogenized Young's modulus described earlier in section 6.1.4. Table 6.6 summarizes the effective quantities used in the following.

Furthermore, to apply the beam theories described in section 3.3 the effective cross-sectional area A and the moment of inertia I have to be computed. These quantities are dependent on the overall dimensions of the beam specimens. The as-designed and as-manufactured values as indicated in Table 6.2 are different. Thus, the values indicated with D in Table 6.2 are used to compute the effective geometrical characteristics of as-designed models, while the ones indicated with M in Table 6.2 of as-manufactured shapes.

Effective quantity	As-designed	As-manufactured
E^*, MPa	7 356	$12\,533 \pm 751^\dagger$
G^*, MPa	2 742	5 651

Table 6.6: Effective mechanical quantities of the octet-truss specimens (†Experimental measure) [83].

Figure 6.20 shows the normalized bending rigidity D/D^{EB} with respect to the beam height h (see Equation 3.30). The normalization is performed following the Euler-Bernoulli bending rigidity D^{EB} solution as follows:

$$\frac{D}{D^{EB}} = \frac{Dw^{EB}}{F} = \frac{w^{EB}}{w} \tag{6.2}$$

where w^{EB} is the classical Euler-Bernoulli solution for three-point bending as in Equation 3.27, w is the experimentally recorded maximum deflection, and D is the compared bending rigidity.

As the as-manufactured and as-designed geometries have different effective properties, the bending rigidities are normalized with the Euler-Bernoulli solutions using the respective quantities from Table 6.6 and, thus, they are plotted separately in Figures 6.20a and 6.20b.

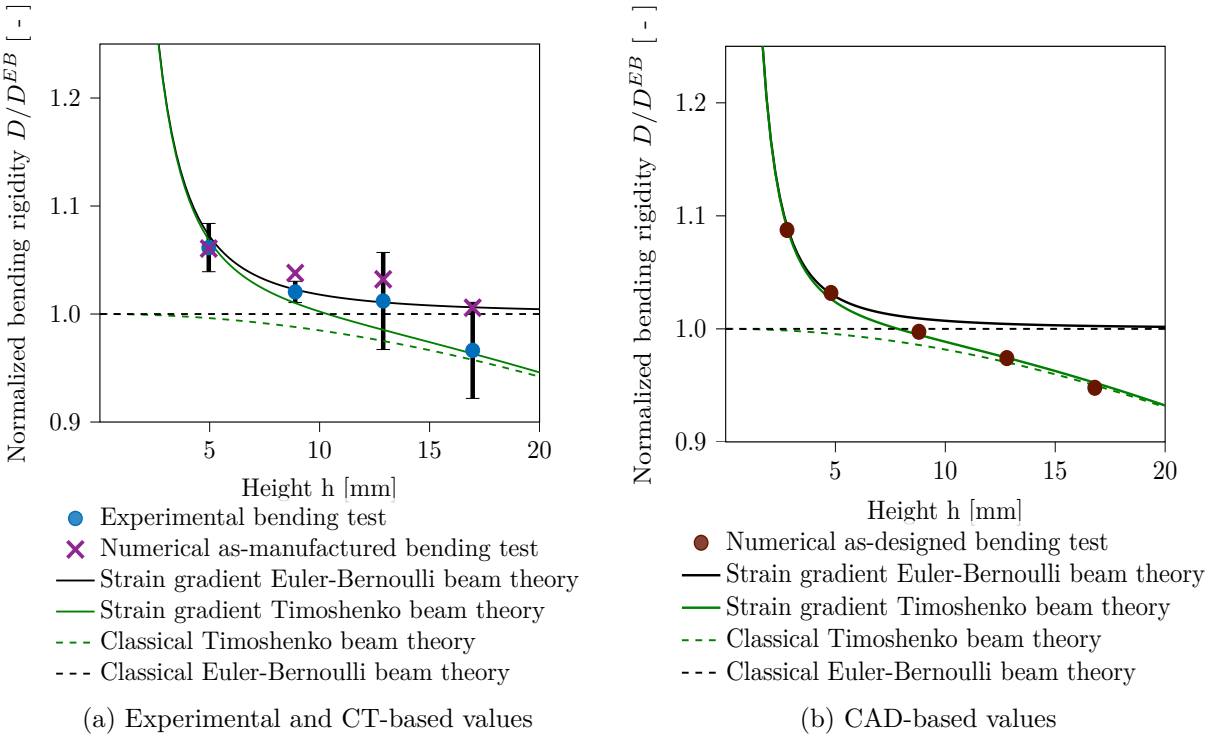

(a) Experimental and CT-based values

(b) CAD-based values

Figure 6.20: Normalized bending rigidities of the octet-truss lattice beams with respect to the beam height [83].

In both plots of Figure 6.20, the bending rigidity values are normalized with the analytical Euler-Bernoulli solution using the as-manufactured effective Young's modulus

from Table 6.6. The brown dots in Figure 6.20b indicate the CAD-based results of the numerical bending test and again the results are normalized with the Euler-Bernoulli solution with the as-designed effective Young's modulus from Table 6.6. Since as-designed geometry allows for further reduction of the considered thickness-to-length ratios, an extra point is added at the height of 2.4 mm. This setup leads to a thickness-to-length ratio of 0.015.

Classical beam theory using as-manufactured and as-designed geometry

As the normalization is performed with respect to the corresponding classical Euler-Bernoulli solution, the dashed black lines remain at the value 1 for both as-manufactured and as-designed geometries. If the octet-truss lattice beams were to follow this behavior, all bending rigidities would lay on a straight line. However, neither as-manufactured nor as-designed values comply with the assumptions of the Euler-Bernoulli theory. Thus, the classical Euler-Bernoulli theory cannot be applied to the characterization of the bending behavior of the considered octet-truss lattices.

The classical Timoshenko beam theory indicated with the green dashed line converges to the Euler-Bernoulli theory with the decreasing beam height. These states correspond to extremely slender beams, thus, making shear effects of minor importance. The as-manufactured geometry results as shown in Figure 6.20a propose that only the thickest specimen with $2 \times 32 \times 4$ cells and the thickness-to-length ratio of 0.13 follows the Timoshenko theory. However, the rest of the points do not follow this curve. The as-designed bending behavior as depicted in Figure 6.20b shows a similar trend, where for the thickest specimens the points lay on the curve. Although the Timoshenko beam theory provides a better solution compared to Euler-Bernoulli, none of them can capture the observed bending behavior well.

Strain gradient beam theory using as-manufactured geometry

Figure 6.20a indicates the presence of a stiffening effect. When the height of the beam is close to the characteristic size of the unit cell, the size effects affect the macroscopic bending behavior of the components and cause stiffer behavior in comparison to a standard prediction of the classical beam theories. This size-dependent bending phenomenon is precisely captured by the strain gradient beam theories on the as-manufactured geometries.

The strain gradient beam theories as described in section 3.2 introduce an additional material parameter g. This high-order parameter is unknown a priori and can only be determined by a calibration of the solid lines to the obtained numerical and experimental solutions (or by other generalized homogenization procedures [70]). As mentioned in [79], this intrinsic length parameter behaves as a material parameter and it is independent of loading, problem type, or the beam model. This quantity only depends on the underlying geometry. Thus, it must be the same for both strain gradient Timoshenko and Euler-Bernoulli theories. The value of the high-order material parameter g is determined as 0.349 mm for the as-manufactured octet-truss lattice (see Table 6.7). This intrinsic length parameter characterizes the size effects in the octet-truss lattice structures via both Euler-Bernoulli and Timoshenko strain gradient beam theories. Its order is close to the smallest

strut size diameter of the unit cell of 0.4 mm.

Although both strain gradient beam theories capture an overall stiffening trend, it is important to know which theory is applicable. The numerical solution indicated with crosses seems to rather follow the Euler-Bernoulli approximation. However, the experimental data indicated with blue dots do not give a clear direction of which theory to follow. The first three points lay on the strain gradient Euler-Bernoulli theory, while the last point corresponding to the thickness-to-length ratio 0.13 is away from it. This can suggest that for the last configuration the strain-gradient Timoshenko theory is more appropriate. However, the measurement error bars on the experimental data indicate that both theories could be applicable for this setup and the last point can as well lay on the black solid line. Furthermore, the CT-based porosity value for the thickest beam is further away from the experimental one. Thus, it could lead to uncertainty in the computed bending rigidity. To further clarify this let us look at the as-designed results.

	As-designed g, [mm]	As-manufactured g, [mm]
Octet-truss beam	0.244	0.349

Table 6.7: Comparison of as-designed and as-manufactured high-order intrinsic length parameter of the octet-truss specimen [83].

Strain gradient beam theory using as-designed geometry

As already pointed out, the effective quantities obtained on the as-designed model are far from the experimentally determined bending rigidity and are depicted separately in Figure 6.20b.

Curiously, for the as-designed geometry, a weaker stiffening effect is observed. For the thickness-to-length ratio of 0.03 (i.e., for the thinnest beam), the CAD-based results show about 8.4% stiffening compared to the thickest observation, while the as-printed analysis indicated 9.5%.

This is also reflected in the intrinsic high-order material parameter g. It is determined as $g = 0.244$ mm in the same manner as for the as-manufactured geometries (see Table 6.7). The most remarkable observation is that this high-order material parameter is lower than the one for as-manufactured geometries, similarly to the behavior already observed in the porosity values, the effective quantities, and the bending rigidity of the octet-truss specimens.

Furthermore, the as-designed numerical results clearly follow the strain gradient Timoshenko theory, whereas the strain gradient Euler-Bernoulli curve does not provide an accurate solution to the overall bending behavior. Although it should be noticed that for the thickness-to-length ratios of two thinnest specimens ($h < 5$ mm) the strain gradient beam models are already very close to each other.

Comparison between as-manufactured and as-design results

All in all, the overall stiffening tendency is similar to the one observed from the experimental and as-manufactured numerical analysis. But the as-manufactured values are about 50% higher than the designed ones as shown in Figure 6.19. The as-manufactured

computations always lie within the uncertainty range of the experimental measurements, whereas as-designed numerical results never fall in this range. This rather large difference has been observed in similar studies conducted by the same authors on tensile behaviors of octet-truss lattices [84].

Moreover, when a closer study on the as-manufactured and as-designed geometries is undertaken, the stiffening trend differs. First, it was observed that the considered octet-truss beams experience size effects, such that classical beam theories are not applicable to approximate the bending behavior, whereas strain gradient beam theories provide a much more accurate description. Secondly, the as-manufactured bending rigidities show a stronger stiffening effect than the designed ones, as also reflected in the intrinsic material parameter determined for both geometries. This observation correlates well to all other material characteristics determined for the octet-truss lattice structure.

6.2 Square grid microarchitectured structure[a]

To further identify the proposed methodology's opportunities and limitations, lattices at a much smaller scale are investigated. Specimens 300 and 600 are produced using Inconel®718 powder with the in-plane square grid cell. The samples' names are given to identify an overall grid size of 300 μm and 600 μm, respectively. As shown in Figure 6.21a, specimen 300 has a square grid rotated in-plane. In comparison, the other sample is produced entirely orthogonal to the printing direction (see Figure 6.21b). The designed strut size in both cases is 96 μm.

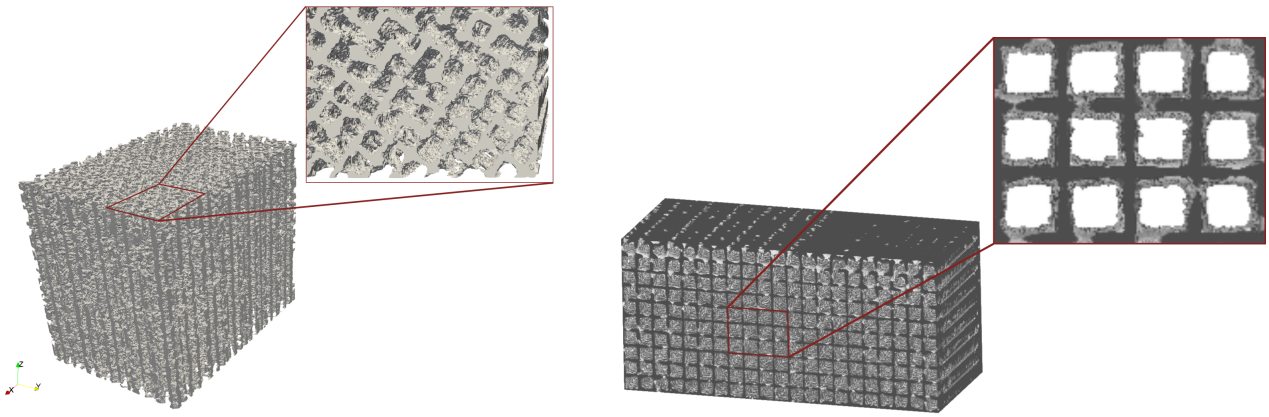

(a) Specimen 300 (b) Specimen 600

Figure 6.21: Overview of the printed specimens with square grid microstructure [85].

In the following, only the key findings are discussed. The numerical and experimental approach for analyzing these specimens is similar to the one described in section 6.1. Thus, the details about the experimental testing setup, the acquired CT data, and the numerical methods are omitted in this section. The full description of this example can be found in [85]. The work described in this section was carried out in close collaboration with Research and Technology Center of Siemens AG Corporate Technology. Lattice manufacturing together with its experimental testing and CT scanning was realized in

their facilities. Their contribution, in particular, of Dr. Daniel Reznik, is gratefully acknowledged.

Manufacturing at a microscopic scale

As the designed lattice structures have a much smaller scale of geometric features than the ones present in the octet-truss lattice, the manufacturing process faces multiple challenges. The process parameters for the LPBF are much harder to control to manufacture a reproducible microstructure. In particular, except for a common set of process-induced defects discussed in section 6.1.3, the structures show a very high irregularity, grid breakages, and trapped powder.

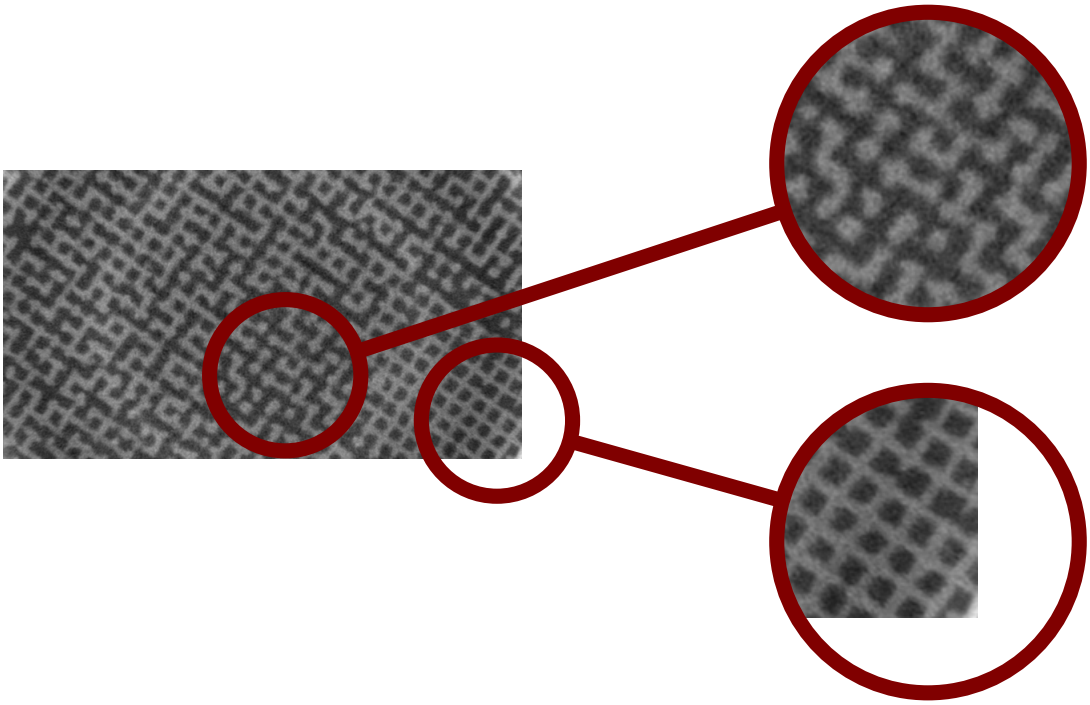

(a) Slice 1: Breakages in the grid structure

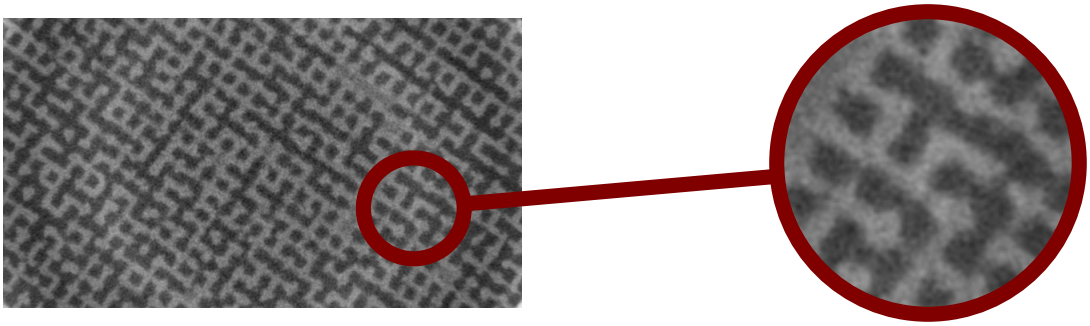

(b) Slice 2: Trapped powder in the middle of the specimen

Figure 6.22: Specimen 300: 2D slices of a square grid microstructure.

The samples have the strut thickness of 96μm, thus requiring the laser tracks to be narrow. In particular, if the laser input is lowered, the width of the molten pool becomes

small. This, in turn, can result in an insufficient overlap of the laser tracks and lead to the lack of fusion [186]. Such unmelted parts can further propagate their effects in the build direction, causing severe breakages in the lattice. Figure 6.22a shows an example of a 2D slice from specimen 300. The as-designed square grid can be achieved only in particular areas of the specimen (shown at the bottom), while in the remaining part of the sample there is a very high grid's irregularity (shown at the top).

Furthermore, there is a considerable effect due to the small distance of 300μm between the center of the struts. Because of the nature of the manufacturing process, there are unmelted particles attached to the melted tracks, which are usually removed in the post-treatment stage. However, as the cell size is microscopic, it is difficult to remove the powder from the specimen, especially in the middle slices. Figure 6.22b shows the trapped powder areas in the lattice. In turn, this effect complicates the CT imaging and, consequently, the numerical analysis.

In contrast, the specimen with a larger grid size does not have trapped powder inside the sample. In this case, the grid structure is better preserved with a fewer breakages occurring (see Figure 6.23).

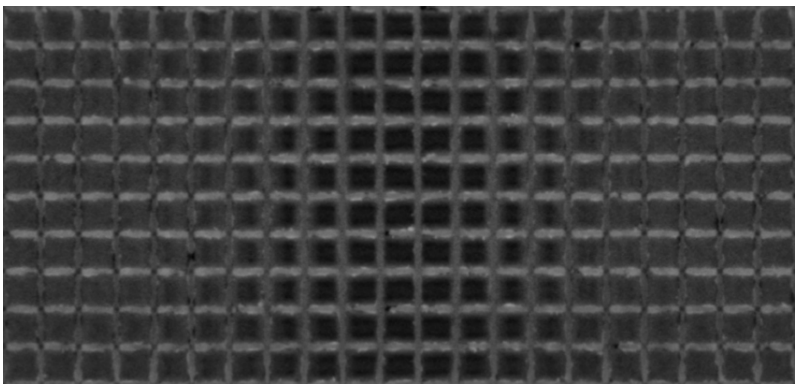

Figure 6.23: Specimen 600: 2D slice of a square grid microstructure [85].

Experimental testing of square grid lattices

The experiments are performed on three similar specimens from both sizes, i.e., specimen 300 (S1-S3) and 600 (L1-L3). The tensile testing is held with optical microscopy, where two orthogonal cameras are installed tracking the lateral extension. One camera is frontal to the specimen, following the extension of the region of interest at the wide side of the sample. Simultaneously, the other camera is tracking the extension from the narrow side of the testing specimen. The experimental results are summarized in Table 6.8.

As it is depicted in Table 6.8, the square grid lattices exhibit significant variations in the final mechanical properties. This is again due to the difficulty in controlling the process parameters at the microscopic level. As shown above, the manufactured lattices have significant deviations from the as-designed geometries. Although only one CT image from every group is available, a considerable inter-specimen geometrical variability is expected. The same process parameters and the same nominal geometry could lead to a different as-manufactured geometry, causing a large spread in the mechanical quantities.

Specimens	E^*, [MPa]	ν_1^*, [-]	ν_2^*, [-]
300 S1-S3	18 844 – 32447	0.27 – 0.35	0.23 – 0.32
600 L1-L3	15 339 – 26 731	-0.04 – 0.13	0.05 – 0.14
600 L2 narrow	20 851	-0.04	0.08
600 L2 wide	25 915	-	-

Table 6.8: Square grid lattice: Experimental results of a tensile test [85].

CT images of microscopic metal lattices

The microscopic scale of the considered specimens and the presence of trapped powder also significantly affect the acquired CT images. For both square lattices, one CT scan is taken from each group. It is important to note that the images for specimen 300 are obtained from a similar sample, which was not tested experimentally, i.e., it does not belong to S1 – S3 in Table 6.8. In contrast, for large grid size, the CT is taken from specimen 600 L2 before the tensile testing as shown in Table 6.8.

In both samples low contrast of Hounsfield units is observed (see 2D slices in Figure 6.22 and Figure 6.23). It is well-known that such imaging issues can occur when metal objects are scanned [14, 15, 105]. Severe metal artifacts, such as ring artifacts, noise, beam hardening, etc., obscure these specimens' geometrical borders. They arise due to the high attenuating material properties of the metal itself and the metal edges. Especially when the microscopic scale is considered, the effects can be significant. Thus, it is difficult to detect the object's shape and prepare it for further numerical analysis. Furthermore, the presence of the trapped powder as indicated in Figure 6.22b leads to the Hounsfield units of the metal powder to be very close to the ones of fully melted material. Thus, the identification of the melted object's geometrical boundary in these areas is cumbersome. A single thresholding technique would assign these areas together with the trapped powder to be fully melted. However, the unmelted powder does not contribute to the tensile behavior of these parts. Thus, such segmentation would negatively affect the accuracy of numerical results.

To overcome these imaging artifacts, the deep learning segmentation technique described in section 2.3 is applied. As opposed to the single thresholding technique, this approach leads to a reliable geometrical model suitable for numerical analysis.

Numerical investigation of tensile behavior

Similar to the analysis of the octet-truss lattices in section 6.1.4, both a direct numerical tensile test and numerical homogenization are performed on the square grid structures.

The results for specimen 300 are summarized in Table 6.9. The homogenized Young's modulus determined via a CT-based direct numerical tensile test is different from the experimental values. However, as the analyzed CT scan does not belong to any of the specimens S1 – S3, these deviations are to be expected. The inter-specimen geometrical variability can lead to a significant spread in the mechanical properties. This conclusion can be drawn from already available experimental test results on three similar specimen. Although they have the same as-designed geometry and the same process parameters, the mechanical response of these samples significantly differs from one another. Thus,

to achieve accurate results of the numerical analysis, an exact as-manufactured geometry should be incorporated. Once more, it supports the importance of the process-induced geometrical defects in the numerical modeling of as-manufactured lattices.

Method	E_{mean}, [MPa]	CV, [%]
Experiment	18 884 – 32 447	-
CT-based DNS($100 \times 60 \times 124$ cells, $p = 5$)	39 351.31	-
CT-based homogenization with PBC	38 417.80	15.50

Table 6.9: Specimen 300: Quantitive comparison of the numerical results for the homogenized Young's modulus E^* and its coefficient of variation CV [85].

To reduce the required the computational resources to perform a numerical tensile test on a full specimen, the numerical homogenization technique described in chapter 5 is applied. Although the as-designed geometry is periodic, the as-manufactured structure is highly irregular due to multiple breakages. As opposed to the octet-truss lattices, it is difficult to define a unit cell, which is statistically repeated throughout the sample. Thus, the RVE size and its existence become questionable. Hence, the homogenization procedure for specimen 300 is performed on 168 RVEs of the size $84 \times 84 \times 80$ voxels independently of the underlying microstructure. To estimate the quality of the obtained results, a coefficient of variation is computed as follows:

$$CV = \frac{\sigma}{\mu} \tag{6.3}$$

where σ is the standard deviation of the homogenized Young's modulus in a statistical set of 168 homogenized values, and μ is the mean value of this quantity through the whole set. As mentioned in [44] when this coefficient is up to 15%, the size of the RVE is considered to be satisfactory for the numerical analysis. Certainly, when the size of the homogenized volumes is increased, the coefficient of variation should decrease. As shown in Table 6.9, the homogenized Young's modulus variability is within these bounds, thus it can be accepted as a final result. Despite the discrepancies between numerical and experimental results, an accurate agreement between the effective Young's modulus determined by the tensile test and the homogenization procedure is observed. The Periodic Boundary Conditions delivered the estimate, which deviates from the numerical tensile experiment by 2.4%.

In the case of larger grid size, the analyzed CT scan corresponds to the specimen L2, which is tested before numerical investigations. It is noteworthy that the CT-based DNS results are now in an exceptional agreement with the experimental tests as shown in Table 6.10. These findings suggest that the difference between the numerical and experimental results for the previously described specimen 300 indeed arise from the expected geometrical variability in the printed structure. When as-manufactured geometrical models are incorporated, the proposed workflow delivers a good agreement with the experimental tests.

In this case, the CT-based homogenization also delivers results, that are less than 5% different from the DNS values (see Table 6.10). The coefficient of variation for specimen

600 is also smaller. In particular, the orthogonal grid structure with fewer breakages allows making a better guess on the size of the RVE.

Method	E_{mean}, [MPa]	CV, [%]
Experiment	20 851 – 25 915	-
CT-based DNS($200 \times 92 \times 200$ cells, $p = 6$)	25 881.40	-
CT-based homogenization with PBC	27 176.42	12.20

Table 6.10: Specimen 600: Quantitative comparison of the numerical results for the homogenized Young's modulus E^* and its coefficient of variation CV [85].

All in all, the investigations on the lattices manufactured at the microscopic scale have indicated that the proposed workflow can be applied at any size of the structure. Both the direct numerical simulation of the whole specimen and numerical homogenization show an excellent agreement with each other. Thus, both methods can be used to perform material characterization of lattice structures. Furthermore, incorporating the process-induced defects into the numerical analysis undoubtedly leads to a better prediction of the mechanical behavior of as-manufactured parts. However, the main challenges at a smaller scale are the manufacturing process and image acquisition. These aspects strongly affect the quality of the numerical results. It was demonstrated that a good agreement could be achieved only when an exact geometrical description of the analyzed specimen is available.

Chapter 7

Uncertainty quantification of process-induced defects[d]

The previous chapters have presented a numerical framework to perform numerical characterization of printed structures. This deterministic evaluation of the AM product mechanical behavior provides an insight into the achieved quality of the final structure and allows to compare the designed and achieved quantities. This final chapter aims to extend this numerical framework such that an uncertainty quantification of the process-induced defects is possible. In particular, this extension should enable the evaluation of the variability of the mechanical response subject to geometrical uncertainties in the underlying microstructure.

To begin with, a binary random field model is proposed in section 7.1. This model allows generating statistically similar geometrical models to the printed structures. In particular, the only necessary input to this approach is the CT image of the analyzed structure. Through the fitting procedure described in section 7.2 the design parameter space of the binary random field can be determined. These parameters control the periodicity of the underlying structure, smoothness, internal voids, and other small geometrical features. A numerical procedure to generate the statistically similar geometries is described in section 7.3. Once these geometries are generated, the remaining point to be discussed is how they can be analyzed. In this work, a Multilevel Monte Carlo (MLMC) approach is employed in section 7.4. This approach is slightly different from the traditional way of estimating the mean values of the quantity of interest. In particular, this study aims to estimate the variability of the mean value of the homogenized Young's modulus of AM products and its standard deviation. Furthermore, other higher-order central moments could be of interest when the effects of the process-defects on the mechanical behavior are investigated. Thus, a specific formulation of MLMC is introduced, allowing to incorporate the estimation of arbitrary order of central moments in the analysis. Finally, the proposed model is evaluated in section 7.5 on the examples of octet-truss and square grid lattices described in the previous chapter. The work described in this chapter was carried out in close collaboration with Engineering Risk Analysis Group of Technical University of Munich. Their contribution, in particular, of Dr.-Ing. Iason Papaioannou, is gratefully acknowledged.

7.1 Binary random field model for geometrical description of periodic structures

As discussed in section 2.3, after applying the single thresholding segmentation technique the CT images have a clear distinction between metal and void. Thus, only of values 0 and 1 are present in the final segmented images, with 1 indicating metal and 0 indicating void. Two lattices structures described in chapter 6 are considered in the following. Their representative two-dimensional slices are shown in Figure 7.1.

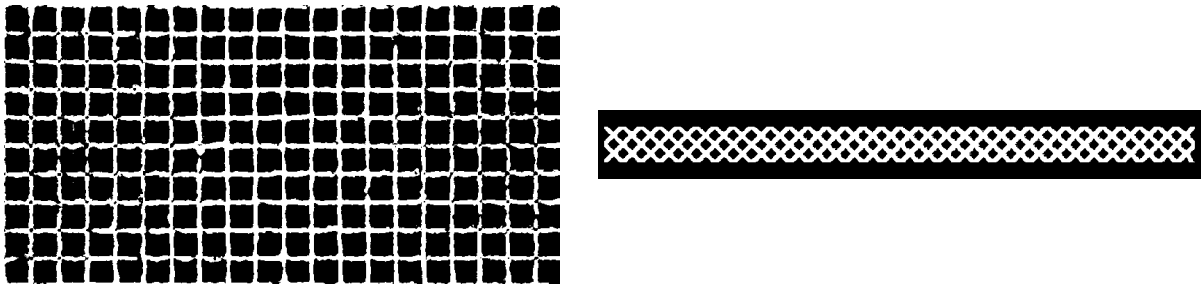

(a) Square grid lattice (b) Octet-truss lattice

Figure 7.1: 2D slices of the segmented CT scans of AM periodic lattice structures (white pixels represent material and black pixels represent void) [86].

A natural choice to describe such geometrical models is through a binary random field model. A binary random field $V(\boldsymbol{x})$ represents an infinite collection of binary random variables, i.e., variables taking outcomes in $\{0, 1\}$, indexed by a spatial coordinate $\boldsymbol{x} \in \Omega$, where $\Omega \subset \mathbb{R}^n$ denotes a spatial domain [172]. This model is then used to generate realizations, i.e., artificial geometries which are statistically similar to a physical structure recorded through CT images. The properties of the random field model should be such that the generated realizations retain certain important geometrical features while their remaining characteristics are varying. In particular, the lattices considered in this work are periodic as shown in Figures 6.4 and 6.23. Thus, the proposed model should preserve a general repetitive periodic cell structure, while the individual small features within a cell, e.g., surface roughness, internal porosity, strut sizes, should vary.

A common way to formulate the binary random field is to define a parent (or latent) underlying continuous random field, which is clipped in the consequent step with the pre-defined threshold d. The parent field is assumed to be a real-valued homogeneous Gaussian random field $U(\boldsymbol{x})$ with zero mean value $\mu_U = 0$, unit standard deviation $\sigma_U = 1$, and auto-correlation function $\rho_{UU}(\boldsymbol{x}_1, \boldsymbol{x}_2)$. Commonly, the cut-off level d is assumed to be homogeneous, i.e., constant with respect to the spatial coordinate (see, e.g., [97, 81, 87, 123, 135, 172]). However, the use of homogeneous threshold would lead to a random porous geometrical model. The generation of periodic structures as shown in Figures 6.4 and 6.23 would not be possible. Thus, in this work, the threshold is chosen to vary with respect to the spatial location, i.e., $d(\boldsymbol{x})$, which allows us to control the overall periodic structure of the lattices. Hence, the binary random field $V(\boldsymbol{x})$ can be

expressed in terms of the Gaussian field $U(\boldsymbol{x})$ as

$$V(\boldsymbol{x}) = \begin{cases} 0 & \text{for } U(\boldsymbol{x}) \in (-\infty, d(\boldsymbol{x})) \\ 1 & \text{for } U(\boldsymbol{x}) \in [d(\boldsymbol{x}), \infty) \end{cases} \tag{7.1}$$

where $d(\boldsymbol{x})$ is the truncation threshold depending on the spatial location. As the Gaussian random field $U(\boldsymbol{x})$ has zero mean and unit variance, $U(\boldsymbol{x})$ is completely characterized by its auto-correlation function $\rho_{UU}(\boldsymbol{x}_1, \boldsymbol{x}_2) = \mathbb{E}\left[U(\boldsymbol{x}_1)U(\boldsymbol{x}_2)\right]$. Hence, the binary random field $V(\boldsymbol{x})$ is defined by the threshold function $d(\boldsymbol{x})$ and the function $\rho_{UU}(\boldsymbol{x}_1, \boldsymbol{x}_2)$. These functions should be identified such that the generated geometrical models attain a similar lattice structure. A graphical illustration of the proposed model is given in Figure 7.2. The figure shows the process of generation of a random realization from the binary random field $V(\boldsymbol{x})$ for a single unit cell of lattice structure. Given the function $\rho_{UU}(\boldsymbol{x}_1, \boldsymbol{x}_2)$, realizations from the Gaussian field $U(\boldsymbol{x})$ can be generated, which can be transformed to realizations of the field $V(\boldsymbol{x})$ based on the threshold function $d(\boldsymbol{x})$. The parameters $\boldsymbol{l}$ and $\boldsymbol{\nu}$ shown in Figure 7.2 are parameters of the function $\rho_{UU}(\boldsymbol{x}_1, \boldsymbol{x}_2)$, which will be discussed in detail further below.

The design parameter space of the binary random field model, including the threshold level $d(\boldsymbol{x})$ and the auto-correlation function $\rho_{UU}(\boldsymbol{x}_1, \boldsymbol{x}_2)$, can be identified based on matching sample estimates of the first and second moment functions of $V(\boldsymbol{x})$ obtained from the CT images of sample structures. In the following, the expressions for these functions in terms of the model parameters are provided. Note, that for the case of a homogeneous threshold, expressions for the second moment function of the binary field as a function of $\rho_{UU}(\boldsymbol{x}_1, \boldsymbol{x}_2)$ and the (homogeneous) threshold d are given, e.g., in [167, 78, 135, 97].

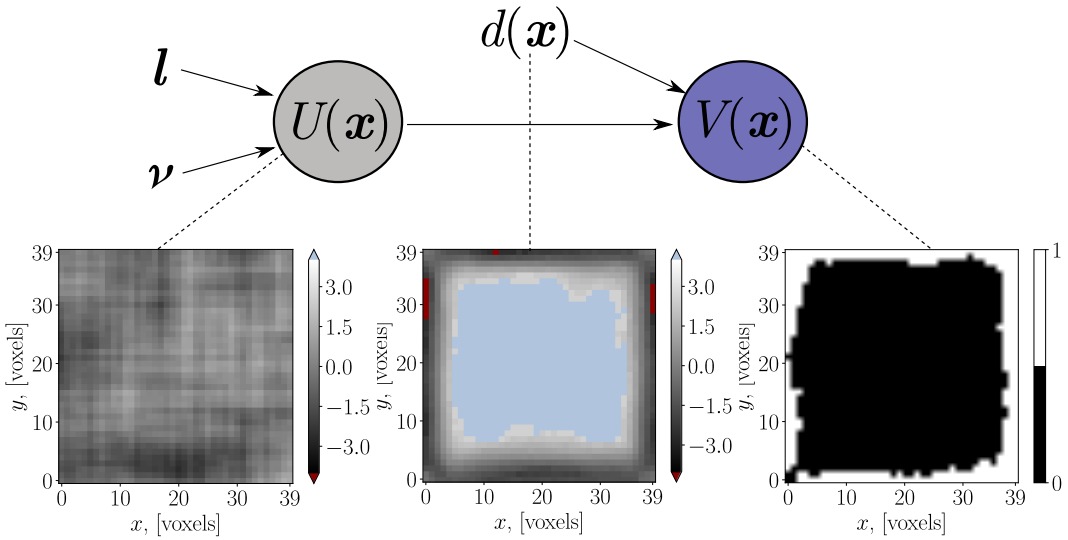

Figure 7.2: Graphical illustration of the proposed non-homogeneous binary random field model and the process of generation of a random realization from the model (in dark red: $-\infty$ values, light blue: ∞ values). Lower left: one realization of the Gaussian random field $U(\boldsymbol{x})$; lower middle: threshold function $d(\boldsymbol{x})$ acquired from CT image of a sample; lower right: one realization of a binary random field $V(\boldsymbol{x})$ [86].

The marginal probability mass function (PMF) of $V(\boldsymbol{x})$ is

$$p_V(v, \boldsymbol{x}) = \begin{cases} \Phi(d(\boldsymbol{x})) & \text{for } v = 0 \\ 1 - \Phi(d(\boldsymbol{x})) & \text{for } v = 1 \end{cases} \tag{7.2}$$

where Φ is the standard normal cumulative distribution function (CDF). Hence, the mean of $V(\boldsymbol{x})$ is given as follows:

$$\mu_V(\boldsymbol{x}) = 1 - \Phi(d(\boldsymbol{x})) \tag{7.3}$$

and the variance function is:

$$\sigma_V^2(\boldsymbol{x}) = [1 - \Phi(d(\boldsymbol{x}))]\, \Phi(d(\boldsymbol{x})) \tag{7.4}$$

The covariance of the binary random field with spatially varying thresholds can be written as

$$\Gamma_{VV}(\boldsymbol{x}_1, \boldsymbol{x}_2) = \int_0^{\rho_{UU}(\boldsymbol{x}_1, \boldsymbol{x}_2)} \frac{1}{2\pi\sqrt{1 - z^2}} \exp\left[-\frac{d(\boldsymbol{x}_1)^2 + d(\boldsymbol{x}_2)^2 - 2d(\boldsymbol{x}_1)d(\boldsymbol{x}_2)z}{2(1 - z^2)} \right] dz \tag{7.5}$$

A full derivation of this result can be summarized as follows. The second-order PMF of $V(\boldsymbol{x})$ is given as (cf. [172])

$$p_{VV}(v_1, \boldsymbol{x}_1; v_2, \boldsymbol{x}_2) = \begin{cases} F_{UU}\left(d(\boldsymbol{x}_1), \boldsymbol{x}_1; d(\boldsymbol{x}_2), \boldsymbol{x}_2\right) & \text{for } v_1 = v_2 = 0 \\ \Phi(d(\boldsymbol{x}_2)) - F_{UU}\left(d(\boldsymbol{x}_1), \boldsymbol{x}_1; d(\boldsymbol{x}_2), \boldsymbol{x}_2\right) & \text{for } v_1 = 1, v_2 = 0 \\ \Phi(d(\boldsymbol{x}_1)) - F_{UU}\left(d(\boldsymbol{x}_1), \boldsymbol{x}_1; d(\boldsymbol{x}_2), \boldsymbol{x}_2\right) & \text{for } v_1 = 0, v_2 = 1 \\ 1 - \Phi(d(\boldsymbol{x}_2)) - \Phi(d(\boldsymbol{x}_1)) + F_{UU}\left(d(\boldsymbol{x}_1), \boldsymbol{x}_1; d(\boldsymbol{x}_2), \boldsymbol{x}_2\right) & \text{for } v_1 = v_2 = 1 \end{cases} \tag{7.6}$$

where $F_{UU}(u_1, \boldsymbol{x}_1; u_2, \boldsymbol{x}_2) = \Phi_2\left(u_1, u_2, \rho_{UU}(\boldsymbol{x}_1, \boldsymbol{x}_2)\right)$ is the second-order CDF of $U(\boldsymbol{x})$ and $\Phi_2(\cdot, \cdot, r)$ is the joint CDF of the bivariate standard normal distribution with correlation parameter r. Hence, the mean-of-product function $\mathbb{E}\left[V(\boldsymbol{x}_1)V(\boldsymbol{x}_2)\right]$ is given as:

$$\begin{aligned} \mathbb{E}\left[V(\boldsymbol{x}_1)V(\boldsymbol{x}_2)\right] &= \sum_{i=0}^{1}\sum_{j=0}^{1} v_i v_j p_{VV}(v_i, \boldsymbol{x}_1; v_j, \boldsymbol{x}_2) \\ &= 1 - \Phi(d(\boldsymbol{x}_2)) - \Phi(d(\boldsymbol{x}_1)) + \Phi_2\left(d(\boldsymbol{x}_1), d(\boldsymbol{x}_2), \rho_{UU}(\boldsymbol{x}_1, \boldsymbol{x}_2)\right) \end{aligned} \tag{7.7}$$

For the auto-covariance function of $V(\boldsymbol{x})$, $\Gamma_{VV}(\boldsymbol{x}_1, \boldsymbol{x}_2) = \mathrm{Cov}(V(\boldsymbol{x}_1), V(\boldsymbol{x}_1))$, it holds:

$$\Gamma_{VV}(\boldsymbol{x}_1, \boldsymbol{x}_2) = \mathbb{E}\left[V(\boldsymbol{x}_1)V(\boldsymbol{x}_2)\right] - \mu_V(\boldsymbol{x}_1)\mu_V(\boldsymbol{x}_2) \tag{7.8}$$

Plugging in Equation 7.7 and Equation 7.3 into Equation 7.8 the following result is obtained:

$$\Gamma_{VV}(\boldsymbol{x}_1, \boldsymbol{x}_2) = \Phi_2\left(d(\boldsymbol{x}_1), d(\boldsymbol{x}_2), \rho_{UU}(\boldsymbol{x}_1, \boldsymbol{x}_2)\right) - \Phi(d(\boldsymbol{x}_1))\Phi\left(d(\boldsymbol{x}_2)\right) \tag{7.9}$$

The bivariate joint CDF can be expressed in terms of a single-fold integral, as follows [126]:

$$\Phi_2\left(u_1, u_2, r\right) = \int_0^r \frac{1}{2\pi\sqrt{1-z^2}} \exp\left[-\frac{u_1^2 + u_2^2 - 2u_1u_2z}{2(1-z^2)}\right] dz + \Phi(u_1)\Phi(u_1) \tag{7.10}$$

Then, combining Equation 7.10 with Equation 7.9 leads to the final equation for the covariance of the binary random field in Equation 7.5.

The auto-correlation function of $V(\boldsymbol{x})$ is then obtained as:

$$R_{VV}(\boldsymbol{x}_1, \boldsymbol{x}_2) = \frac{\Gamma_{VV}(\boldsymbol{x}_1, \boldsymbol{x}_2)}{\sigma_{VV}(\boldsymbol{x}_1)\sigma_{VV}(\boldsymbol{x}_2)} \tag{7.11}$$

with $\sigma_{VV}(\boldsymbol{x})$ as defined in Equation 7.4.

The functions $d(\boldsymbol{x})$ and $\rho_{UU}(\boldsymbol{x}_1, \boldsymbol{x}_2)$, which define the binary field $V(\boldsymbol{x})$, can be estimated by comparing sample estimates of the mean and auto-covariance functions of $V(\boldsymbol{x})$ with the expressions in Equations 7.3 and 7.5. Such estimates can be obtained based on CT images of manufactured AM products. Before describing this identification procedure, the modeling process can be further simplified by introducing a parametric correlation model for the function $\rho_{UU}(\boldsymbol{x}_1, \boldsymbol{x}_2)$, based on the Matérn model. The one-dimensional Matérn correlation model reads [59]:

$$\rho_M\left(x_1, x_2\right) = \frac{2^{1-\nu_x}}{\Gamma(\cdot)(\nu_x)} \left(\sqrt{2\nu_x}\frac{\Delta x}{l_x}\right)^{\nu_x} K_{\nu_x}\left(\sqrt{2\nu_x}\frac{\Delta x}{l_x}\right) \tag{7.12}$$

where $\Delta x = |x_1 - x_2|$ indicates the spatial lag, l_x is the correlation length parameter, ν_x is a non-negative smoothness parameter, $\Gamma(\cdot)$ is the gamma function, and $K_\nu(\cdot)$ is the modified Bessel function of the second kind. The design space for the one-dimensional Matérn correlation model includes two parameters, namely the correlation length l_x and smoothness parameter ν_x. The smoothness parameter provides great flexibility to describe spatial correlations. When ν_x tends to zero, the spatial variation is rather rough, while large values of ν_x lead to a smooth spatial process. Furthermore, it combines a wide range of other parametric correlation models. For example, for $l_x = 0.5$ the exponential model is recovered, while for $l_x \to \infty$ the Gaussian correlation kernel is obtained.

The separability assumption on the correlation function is introduced, such that as discussed in section 7.3 the generation of the random field $U(\boldsymbol{x})$ is greatly simplified. The product family of the correlation kernels can be formulated as follows [145]:

$$\rho_{UU}(\boldsymbol{x}_1, \boldsymbol{x}_2) = \rho_M\left(x_1, x_2\right)\rho_M\left(y_1, y_2\right)\rho_M\left(z_1, z_2\right) \tag{7.13}$$

Thus, the design space for the binary model in Equation 7.1 with Equations 7.12 and 7.13 consists of the following set of parameters: the threshold function $d(\boldsymbol{x})$, the correlation length vector $\boldsymbol{l} = (l_x, l_y, l_z)$ and the smoothness vector $\boldsymbol{\nu} = (\nu_x, \nu_y, \nu_z)$ as depicted in Figure 7.2. Given CT scans of the produced lattice structures, these parameters can be determined directly from the segmented images. The procedure for the parameter identification will be described in the following section.

7.2 CT-based binary random field model parameter identification

The next step is to select the design parameters d, $\boldsymbol{l}$, and $\boldsymbol{\nu}$ of the proposed random binary field model that lead to geometric models that are statistically similar to the structures depicted in Figures 6.4 and 6.23. Thus, a procedure to identify these parameters is established such that the overall macroscopic periodic structure, together with the process-induced defects, are retained by the model in a statistical sense. The available CT images of already produced lattices serve as a basis to learn these features because they contain all necessary data to proceed with the model generation.

First, the threshold d can be identified from available CT images. As mentioned in section 7.1, this function primarily controls a general macroscopic shape of the structure. As an example, if the threshold level $d = \text{const}$, it regulates a macroscopic volume fraction of the voids or inclusions in the generated geometry. In contrast, when it is dependent on the spatial coordinate, structure-specific information can be incorporated. In the considered case, the periodicity of the lattice cells must be retained. Thus, the threshold level can be identified by taking advantage of the repetition of the unit cells.

A local unit cell is introduced with the attached local coordinate system $\boldsymbol{x}^l = (x^l, y^l, z^l)$. This is shown in Step 1 of Figure 7.3 on a two-dimensional slice. The size of this cell depends on the design geometry of the structure. The mapping between the local and the global coordinate system is defined inherently due to the existing periodicity. Then, the underlying voxel structure of the CT scan can be exploited (Step 2 in Figure 7.3). In particular, as the segmented values are constant within one voxel, the threshold d becomes piece-wise constant. It can be evaluated at a discrete set of local coordinates $\boldsymbol{\mathcal{X}}^l = [\boldsymbol{x}_1^l; \ldots; \boldsymbol{x}_{n_l}^l]$ located at the center of every voxel (see step 2 in Figure 7.3).

Then, as the CT image consists of many local unit cells N_{cells}, all of them can be collected in a pool of realizations of the binary random field defined at the voxels of the local cells $\{v_i^l(\boldsymbol{\mathcal{X}}^l), i = 1, \ldots, N_{\text{cells}}\}$. In this way, the mean function of V at the discrete grid points $\boldsymbol{\mathcal{X}}^l$ in the local coordinate system can be estimated as follows (step 3 in Figure 7.3):

$$\hat{\mu}_V(\boldsymbol{\mathcal{X}}^l) = \frac{1}{N_{\text{cells}}} \sum_{i=1}^{N_{\text{cells}}} v_i^l(\boldsymbol{\mathcal{X}}^l) \tag{7.14}$$

where $\hat{(\cdot)}$ indicates the estimated quantity. Note that the computed mean values coincide with the estimates of the probabilities $\Pr(V(\boldsymbol{\mathcal{X}}^l) = 1)$. In particular, the black voxels in step 3 in Figure 7.3 indicate that there is always a void at these locations in all periodic cells. By contrast, the white-coloured voxels are always filled with the material in the whole structure. This grey value distribution is considered representative of the AM process for the considered lattice structure itself.

The global mean values $\hat{\mu}_V(\boldsymbol{\mathcal{X}})$, are then obtained through performing the inverse mapping of the local coordinate system to the global one (step 4 in Figure 7.3). Using Equation 7.3, the thresholds $d(\boldsymbol{x})$ then are piece-wise constant with the values evaluated at the set of coordinates $\boldsymbol{\mathcal{X}}$ as follows:

$$\hat{d}(\boldsymbol{\mathcal{X}}) = \Phi^{-1}(1 - \hat{\mu}_V(\boldsymbol{\mathcal{X}})) \tag{7.15}$$

where Φ^{-1} is the inverse of the standard normal CDF.

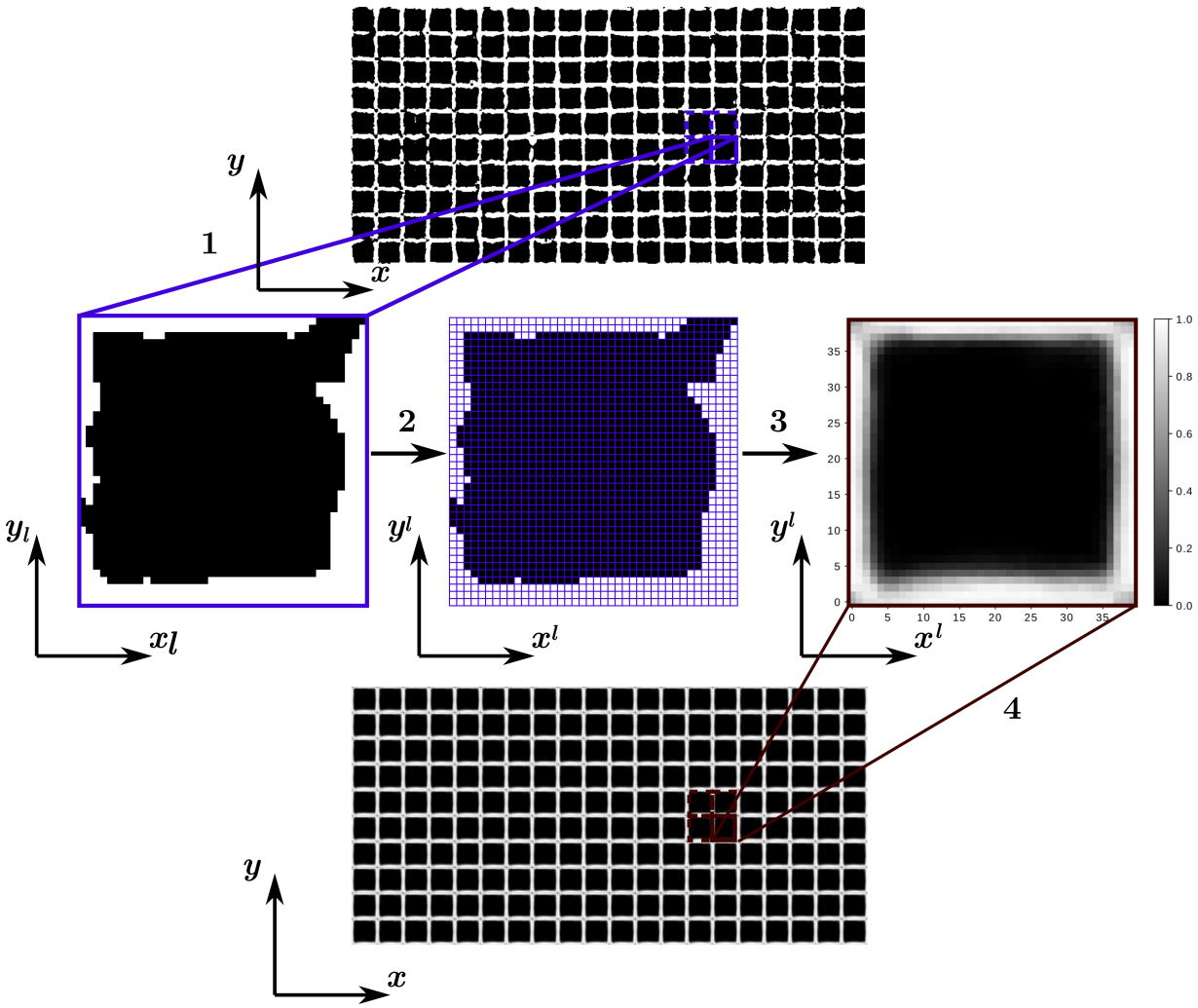

Figure 7.3: Threshold workflow identification [86].

Second, a correlation structure similar to the one occurring in the manufactured lattice should be identified. The correlation parameters $(\boldsymbol{l}, \boldsymbol{\nu})$ control an overall smoothness of the lattice grid. For example, the combination of a large correlation length with large smoothness values would lead to a smooth surface, while low values would be associated with rough lattice surfaces. Following Equation 7.13, the correlation kernel is assumed to be separable. Thus, the correlation fit can be performed separately in every spatial direction. In the following, the procedure only for spatial direction x is explained, where the design parameters to be determined are (l_x, ν_x). The other directions are fitted analogously.

The covariance function of the binary random field can be estimated from the CT image for each local coordinate pair $(\boldsymbol{x}_i^l, \boldsymbol{x}_j^l)$ having a certain spatial lag $|\boldsymbol{x}_i^l - \boldsymbol{x}_j^l| = (\Delta x_{(ij)}, 0, 0)$. The spatial lag in x direction, $\Delta x x_{(ij)}$, can attain the minimum value of one voxel and runs until the width of the local unit cell. Since the threshold values are repeated in each

unit cell, an estimate of the covariance for a given lag $\Delta x_{(ij)}$ is obtained as follows:

$$\hat{\Gamma}_{VV}(\boldsymbol{x}_i^l, \boldsymbol{x}_j^l) = \frac{1}{N_{\text{cells}}} \sum_{k=1}^{N_{\text{cells}}} \left(v_k^l(\boldsymbol{x}_i^l) - \hat{\mu}_V(\boldsymbol{x}_i^l)\right) \left(v_k^l(\boldsymbol{x}_j^l) - \hat{\mu}_V(\boldsymbol{x}_j^l)\right) \tag{7.16}$$

The auto-covariance of the binary random field is stored as a vector depending on the spatial lag $\Delta x_{(ij)}$ together with the corresponding threshold values $\hat{d}(\boldsymbol{x}_i^l)$ and $\hat{d}(\boldsymbol{x}_j^l)$. For a certain spatial lag $\Delta x_{(ij)}$, there is a total of $(k_x - n_{\text{lags}})k_y k_z$ covariance entries with k_x,k_y,k_z being the number of voxels in every spatial direction within one unit cell and n_{lags} being the total number of considered lags (see Step 2 in Figure 7.3). The problem can be further reduced by only considering the points with intermediate probability values larger than zero and smaller than one. For voxels with probability zero or one, correlation is not defined. This filtering interval is further enlarged to remove the extreme data sets, i.e., the sets for which $\hat{\mu}_V(\boldsymbol{x}_i^l) < 0.1$ and $\hat{\mu}_V(\boldsymbol{x}_i^l) > 0.9$.

Assume, that the covariance data after filtering the extreme data sets has the total size N_{data}. Hence, the collected data set consists of the estimated covariance of the binary field $\hat{\Gamma}_{VV}(\boldsymbol{x}_{1m}^l, \boldsymbol{x}_{2m}^l$ at the respective pair of spatial coordinates $(\boldsymbol{x}_{1m}^l, \boldsymbol{x}_{2m}^l)$ with $m = 1, \ldots, N_{\text{data}}$. The set is fitted to the considered analytical Matérn model by inserting Equation 7.12 into Equation 7.13 and then plugging into Equation 7.5. The optimization problem is then formulated as a standard least-square minimization:

$$\min\left(S^2(l_x, \nu_x)\right) = \min\left(\sum_{m=1}^{N_{\text{data}}} r_m^2(l_x, \nu_x)\right) = \min\left(\sum_{m=1}^{N_{\text{data}}} \left(\hat{\Gamma}_{VV}(\boldsymbol{x}_{1m}^l, \boldsymbol{x}_{2m}^l) - \Gamma_{VV}(\boldsymbol{x}_{1m}^l, \boldsymbol{x}_{2m}^l)\right)^2\right) \tag{7.17}$$

where S indicates the total formulated residual, $\hat{\Gamma}_{VV}(\boldsymbol{x}_{1m}^l, \boldsymbol{x}_{2m}^l)$ is the estimated covariance of the observed binary random field according to Equation 7.16, and $\Gamma_{VV}(\boldsymbol{x}_{1m}^l, \boldsymbol{x}_{2m}^l)$ is the chosen model correlation computed by combining Equation 7.12 with Equation 7.13 and plugging in to Equation 7.5.

7.3 Efficient random field simulation for large data sets

To analyze the impact of the random microstructure on the output quantities of interest, realizations of the binary random field as in Equation 7.1 need to be generated. The latter requires the simulation of the underlying standard Gaussian random field $U(\boldsymbol{x})$. This can be done by a number of methods – a comprehensive review is given in [99]. Unlike methods based on approximate representations of the random field (e.g., Fourier representations [154], Karhunen-Loève expansion [13]), the Cholesky decomposition method generates samples from the true random field at a number of spatial locations [177]. However, this approach is rarely used as its computational cost is $\mathcal{O}(n^3)$, with n denoting the number of locations, which is prohibitively expensive for large n. Furthermore, the necessary memory storage for the whole covariance matrix before its decomposition is exceptionally large for practical examples. The size of the problems at hand results in a

simulation of more than 100 million random variables in three dimensions. This would not be feasible unless approximation methods are used or the assumption of separability as in Equation 7.13 is made. If the covariance function is assumed to be separable, the exact stepwise technique based on the covariance matrix decomposition proposed in [96] can be applied. This approach drastically reduces the computational costs and memory requirements for the generation of a three-dimensional Gaussian random field. In the following, the main steps of this method are recapitulated.

Recall that the Gaussian random field $U(\boldsymbol{x})$ is to be simulated at a number n of spatial points $\boldsymbol{\mathcal{X}} = [\boldsymbol{x}_1; \ldots; \boldsymbol{x}_n]$, corresponding to the voxel centers. This requires the simulation of a Gaussian random vector $\boldsymbol{U}$ with zero mean, unit variance and prescribed correlation matrix $\boldsymbol{R} = [\rho_{UU}(\boldsymbol{x}_i, \boldsymbol{x}_j)]_{n\times n}$. The vector $\boldsymbol{U}$ can be decomposed as follows:

$$\boldsymbol{U} = \boldsymbol{L}\boldsymbol{W} \tag{7.18}$$

where $\boldsymbol{W}$ is the vector of n-independent standard normal variables and $\boldsymbol{L}$ is the lower triangular matrix derived from the Cholesky decomposition $\boldsymbol{R} = \boldsymbol{L}\boldsymbol{L}^{\mathrm{T}}$ [46]. Since the correlation function is assumed to be separable as in Equation 7.13, the total correlation matrix $\boldsymbol{R}$ can be written as a Kronecker product of correlation matrices corresponding to 1D correlation functions:

$$\boldsymbol{R} = \boldsymbol{R}_z \otimes \boldsymbol{R}_y \otimes \boldsymbol{R}_x \tag{7.19}$$

where $\otimes$ is the Kronecker product, $\boldsymbol{R}_x = [\rho_x(x_i, x_j)]_{n_x\times n_x}$, $\boldsymbol{R}_y = [\rho_y(y_i, y_j)]_{n_y\times n_y}$, $\boldsymbol{R}_z = [\rho_z(z_i, z_j)]_{n_z\times n_z}$ and $\boldsymbol{x}_i = [x_i, y_i, z_i]$. In contrast to the size of the total correlation matrix $\boldsymbol{R}$ of $(n_x n_y n_z \times n_x n_y n_z)$, the matrices corresponding to the one-dimensional correlation models have a much smaller size of $(n_z \times n_z)$, $(n_y \times n_y)$, and $(n_x \times n_x)$.

Using the mixed-product property of the Kroenecker product, the lower triangular matrix $\boldsymbol{L}$ can be written as the Kroenecker product of the lower triangular matrices of the Cholesky decompositions corresponding to each one-dimensional model:

$$\boldsymbol{L} = \boldsymbol{L}_z \otimes \boldsymbol{L}_y \otimes \boldsymbol{L}_x \tag{7.20}$$

Equation 7.20 simplifies the computation of the Cholesky decomposition of a large matrix, which is both time-consuming and prone to round-off errors due to the poor conditioning of the covariance matrix [46]. Inserting Equation 7.20 into Equation 7.18 gives:

$$\boldsymbol{U} = (\boldsymbol{L}_z \otimes \boldsymbol{L}_y \otimes \boldsymbol{L}_x)\, \boldsymbol{W} \tag{7.21}$$

Equation 7.21 is still rather expensive, as a large matrix multiplication is involved. However, if matrix-array multiplication is introduced the equation can be written out in its equivalent form as follows [96]:

$$\underline{\boldsymbol{U}} = \boldsymbol{L}_z \times_3 [\boldsymbol{L}_y \times_2 (\boldsymbol{L}_x \times_1 \underline{\boldsymbol{W}})] \tag{7.22}$$

where $\underline{\boldsymbol{U}}$ and $\underline{\boldsymbol{W}}$ are vectors $\boldsymbol{U}, \boldsymbol{W}$ respectively reshaped to the matrices of size $(n_x \times n_y \times n_z)$ and $\times_i$ is the matrix-array multiplication defined in the following generic way:

$$\begin{aligned} c_{jpq} &= \sum_k a_{jk} b_{kpq} \text{ if } i = 1 \\ c_{pjq} &= \sum_k a_{jk} b_{pkq} \text{ if } i = 2 \\ c_{pqj} &= \sum_k a_{jk} b_{pqk} \text{ if } i = 3. \end{aligned} \tag{7.23}$$

This approach reduces the computational costs of the covariance decomposition to $\mathcal{O}(n_x^3 + n_y^3 + n_z^3)$ and of the random field generation to $\mathcal{O}\left[n_x n_y n_z (n_x + n_y + n_z)\right]$ [96]. Moreover, it avoids evaluation and storage of the full correlation matrix $\boldsymbol{R}$. Hence, it enables generating the large scale Gaussian random fields required in this work. The required computational times will be further addressed in section 7.5.

7.4 Multilevel Monte Carlo method for AM product characterization

For a given realization of the binary random field representing the material microstructure, the Quantity of interest (QoI), $\mathcal{Q}$, or in this case the homogenized Young's modulus, can be approximated numerically. In particular, the setup shown in Figure 3.2 can be used to characterize a homogenized tensile behavior of the lattices, with $\hat{\boldsymbol{u}}$ denoting the applied uni-axial displacement. Then, the homogenized Young's Modulus in the applied displacement direction can be computed by dividing the average occurring stress by the applied strain.

The effect of microstructural variability on the effective Young's modulus can be evaluated by application of the Monte Carlo (MC) method. In the crude MC method, the statistical moments of the QoI (e.g., mean and variance) are estimated based on repeated evaluations of the QoI for a number of realizations of the uncertain geometrical input. Due to the large overall size of the considered structures and the small scale of the local geometrical variations, in a traditional FEM a detailed resolution is typically required to achieve an accurate approximation of the QoI. Thus, the numerical analysis for each realization with standard FEM results in significant manual labour and high computational cost. This is because every change of the underlying geometry would require a new mesh generation to resolve the generated geometry. Furthermore, the realization and the original specimens are CT images that bring an additional level of complexity to the traditional FEM for numerical analysis. In particular, before the mesh for a model can be generated, a complex geometry reconstruction must be run, which results in a large manual involvement. Thus, the Finite Cell Method described in chapter 4 is applied. However, the computational effort for estimating the statistical moments using a combination of the FCM with the crude MC method still remains high. The necessary computational cost for obtaining accurate moment estimates can be further reduced by employing the MLMC method. Instead of evaluating a large number of samples with a

fixed fine discretization of the QoI, the MLMC method considers a hierarchy of $(\mathcal{L}+1)$ numerical approximation levels. Every subsequent level has a better approximation quality. The levels can be chosen, e.g., such that every subsequent level has a finer mesh or a higher polynomial degree of the element shape functions. MLMC reduces the overall computational cost for a target accuracy of the obtained moment estimates by performing many numerical simulation runs at low approximation levels while decreasing the required runs on every subsequent level. Thus, only a few solves at high levels are necessary.

For the characterization of the variability of the homogenized Young's Modulus, both the mean value $\mu_{\mathcal{Q}} = \mathbb{E}[\mathcal{Q}]$ and the second central moment, i.e. the variance, $\mu_{2,\mathcal{Q}} = \mathbb{E}[(\mathcal{Q}-\mu_{\mathcal{Q}})^2] = \mathrm{Var}[\mathcal{Q}]$, are considered. The MLMC method is well established for estimating the mean value (or other raw moments) of the QoI (e.g [25, 164]). However, the estimation of central moments is not trivial. Recently, MLMC was extended to include the estimation of central moments of the QoI of any order [89]. In the following this method is reviewed, starting with a summary of the standard MLMC procedure for the mean value estimation.

The MLMC estimator for the mean value $\mu_{\mathcal{Q}} = \mathbb{E}[\mathcal{Q}]$ can be written as follows:

$$m_1^{MLMC} = \sum_{\ell=0}^{\mathcal{L}} \left(\widehat{\mathcal{Q}}^{\ell}_{N_\ell, M_\ell} - \widehat{\mathcal{Q}}^{\ell}_{N_\ell, M_{\ell-1}} \right) \tag{7.24}$$

where

$$\widehat{\mathcal{Q}}^{\ell}_{N_\ell, M_\ell} = \frac{1}{N_\ell} \sum_{i=1}^{N_\ell} \mathcal{Q}_{i, M_\ell} \tag{7.25}$$

and $\widehat{\mathcal{Q}}^{0}_{N_0, M_{-1}} := 0$; $\boldsymbol{\mathcal{Q}}^{\ell}_{N_\ell, MM_\ell} = (\mathcal{Q}_{i,M_\ell})_{i=1,\dots,N_\ell}$ is the collection of N_ℓ independent and identically distributed (i.i.d.) realizations of the quantity of interest $\mathcal{Q}_{M_\ell}$ at numerical approximation level ℓ and M_ℓ is the corresponding number of degrees of freedom at level ℓ. The estimator quantities with the same superscript ℓ are computed with the same input samples whereas estimators with different superscripts are computed with a different set of i.i.d. input samples.

The accuracy of the estimator in Equation 7.24 can be assessed by the mean-square error, which is formulated as:

$$\mathrm{MSE}(m_1^{MLMC}) = (\mu_{\mathcal{Q}_{M_\mathcal{L}}} - \mu_{\mathcal{Q}})^2 + \sum_{\ell=0}^{\mathcal{L}} \mathrm{Var}\left[\widehat{\mathcal{Q}}^{\ell}_{N_\ell, M_\ell} - \widehat{\mathcal{Q}}^{\ell}_{N_\ell, M_{\ell-1}} \right] \tag{7.26}$$

where $\mu_{\mathcal{Q}_{M_\mathcal{L}}}$ denotes the mean of the QoI at the final approximation level $\mathcal{L}$. The first term in Equation 7.26 is the bias contribution and evaluates the approximation error at level $\mathcal{L}$, while the second term is the sampling (statistical) error. The bias contribution for the mean value can be approximated as follows:

$$\left| \mu_{\mathcal{Q}_{M_\mathcal{L}}} - \mu_{\mathcal{Q}} \right| \approx \left| \widehat{\mathcal{Q}}^{\ell}_{N_\ell, M_\ell} - \widehat{\mathcal{Q}}^{\ell}_{N_\ell, M_{\ell-1}} \right| \tag{7.27}$$

The variance terms can be estimated using the available samples through the standard variance estimator.

The number of approximation levels $\mathcal{L}$ and the number of samples at each level N_ℓ can be determined such that a small mean-square error is achieved with a low computational cost. To approach this problem, an assumption is typically made on the behavior of the bias, variance and computational cost at each level. In particular, they are assumed to follow relations:

$$\begin{aligned} \left|\mu_{\mathcal{Q}_{M_\ell}} - \mu_{\mathcal{Q}}\right| &\leq c_\alpha (M_\ell)^{-\alpha} \\ V_\ell &\leq c_\beta (M_\ell)^{-\beta} \\ \text{cost}(\mathcal{Q}_{M_\ell}) &\leq c_\gamma (M_\ell)^{\gamma} \end{aligned} \tag{7.28}$$

where M_ℓ is the number of degrees of freedom for level ℓ, $V_\ell := N_\ell \text{Var}\left[\widehat{\mathcal{Q}}^l_{N_\ell,M_\ell} - \widehat{\mathcal{Q}}^l_{N_\ell,M_{\ell-1}}\right]$, $\text{cost}(\mathcal{Q}_{M_\ell})$ is the computational cost of evaluating the QoI at level ℓ, and $c_\alpha, \alpha, c_\beta, \beta, c_\gamma, \gamma$ are the problem-dependent constants. These constants are determined by employing a screening procedure. An initial small number of samples N_ℓ are evaluated at a few coarse levels $\bar{\mathcal{L}}$. Then, the constants are fit via a least-squares procedure and used to extrapolate the costs and variance at the subsequent levels.

The number of degrees of freedom at the maximum level $\mathcal{L}$, $M_\mathcal{L}$, can be estimated for a prescribed relative tolerance ε_r through:

$$M_\mathcal{L} \geq \left(\frac{\varepsilon}{c_\alpha \sqrt{2}}\right)^{-\frac{1}{\alpha}} \tag{7.29}$$

where $\varepsilon \approx \varepsilon_r \cdot m^{MLMC}_{\mu_\mathcal{Q}}$. Then, by solving an optimization problem to minimize the variance of the estimator for a fixed computational cost, the optimal sample size at every level can be estimated as:

$$N_\ell \geq \left\lceil \frac{2}{\varepsilon^2} \sqrt{\frac{V_\ell}{\text{cost}(\mathcal{Q}_{M_\ell})}} \sum_{k=0}^{\mathcal{L}} \sqrt{\text{cost}(\mathcal{Q}_{M_k}) V_k} \right\rceil \tag{7.30}$$

where the terms V_ℓ and $\text{cost}(\mathcal{Q}_{M_\ell})$ can be estimated with Equation 7.28.

Having described the standard MLMC procedure for estimating the mean value of the QoI, the estimation of its central moments can be discussed. The most important quantity is the second central moment, i.e., the variance of the QoI, which is a measure of its variability. It is possible to employ the standard MLMC estimator for these cases if the central moments are expressed in terms of raw moments. However, an approximation of the r-th central moments through the raw moments can lead to a large sampling error. In [89] an MLMC estimator of central moments is proposed that employs h-statistics. The h-statistics is an unbiased central moment estimator, which provides a minimal variance for the level contributions. This approach allows to evaluate any central moment using closed-form expressions. In this approach, the MLMC estimator for the r-th central moment (with $r \geq 2$) is expressed as follows:

$$m_r^{MLMC} = \sum_{\ell=0}^{\mathcal{L}} \Delta_\ell h_r = \sum_{\ell=0}^{\mathcal{L}} \left(h_r \left(\boldsymbol{\mathcal{Q}}^\ell_{N_\ell,M_\ell} \right) - h_r(\boldsymbol{\mathcal{Q}}^\ell_{N_\ell,M_{\ell-1}}) \right) \tag{7.31}$$

where $h_r(\boldsymbol{\mathcal{Q}})$ is the r-th order h-statistic of $\boldsymbol{\mathcal{Q}}$ and $h_r(\boldsymbol{\mathcal{Q}}^0_{N_0,M_{-1}}) := 0$.

The difference of two h-statistics between two consecutive levels for the second central moment is formulated as:

$$\Delta_\ell h_r = \frac{N_\ell S^\ell_{1,1} - S^\ell_{0,1} S^\ell_{1,0}}{(N_\ell - 1) N_\ell} \tag{7.32}$$

In Equation 7.32 a power sum notation $S^l_{a,b}$ between the levels is introduced. It can be computed via the sample sum $\boldsymbol{S}^{\ell,+}_{N_\ell}$ and the sample difference $\boldsymbol{S}^{l,-}_{N_\ell}$ as follows:

$$S^l_{a,b} := S_{a,b}(\boldsymbol{S}^{l,+}_{N_\ell}, \boldsymbol{S}^{l,-}_{N_\ell}) = \sum_{i=1}^{N_\ell} (S^{l,+}_{i,N_\ell})^a (S^{l,-}_{i,N_\ell})^b \tag{7.33}$$

with

$$\boldsymbol{S}^{\ell,+}_{N_\ell} = \boldsymbol{\mathcal{Q}}^\ell_{N_\ell,M_\ell} + \boldsymbol{\mathcal{Q}}^\ell_{N_\ell,M_{\ell-1}}$$
$$\boldsymbol{S}^{\ell,-}_{N_\ell} = \boldsymbol{\mathcal{Q}}^\ell_{N_\ell,M_\ell} - \boldsymbol{\mathcal{Q}}^\ell_{N_\ell,M_{\ell-1}}$$

The mean-square error of the MLMC estimator of section 7.4 can then be formulated:

$$\mathrm{MSE}(m_r^{MLMC}) = \left(\mu_{r,\mathcal{Q}_{M_\mathcal{L}}} - \mu_{r,\mathcal{Q}}\right)^2 + \sum_{\ell=0}^{\mathcal{L}} \mathrm{Var}\left[\Delta_\ell h_r\right] \tag{7.34}$$

where $\mu_{r,\mathcal{Q}_{M_\mathcal{L}}}$ is the r-th central moment of the QoI at level $\mathcal{L}$. The expressions for the bias contribution and the variance terms for central moments of any order r can be found in [89].

The optimal number of the levels and the required sample number can be determined through a similar screening procedure to the one described above. In particular, Equation 7.28 can be used to fit the problem-dependent constants, the only difference being the expressions for the estimation of the bias and the variance terms.

7.5 Numerical investigations

In this section, the proposed workflow is applied to previously analyzed lattices in sections 6.1 and 6.2. The binary random field model parameter fitting and generation of statistically equivalent CT images are performed on a standard workstation with $i7-6500U$ CPU and 16 GB of RAM. The numerical simulations of mechanical behavior of all specimens has been performed on the Linux Cluster CoolMUC-2 at Leibniz Supercomputing Centre of Technical University of Munich[‡].

[‡]The authors gratefully acknowledge the Leibniz Supercomputing Centre for funding this project by providing computing time on its Linux-Cluster.

7.5.1 Octet-truss lattice

To gain confidence in the proposed workflow, an octet-truss lattice structure is considered. The size of the considered example is $292 \times 176 \times 1768$ voxels with the spacing of $2.69\mu m$.

3D model parameter identification

First, the local probabilities of the underlying local cell are evaluated. The size of the unit cell is $146 \times 176 \times 146$ voxels as indicated in Figure 7.4. Overall, 20 cells are extracted to evaluate the probabilities at every local coordinate according to to Equation 7.14.

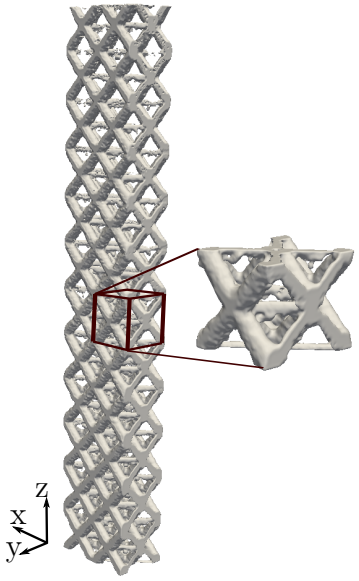

Figure 7.4: An example of a periodic unit cell with its local coordinate system in the 3D octet-truss lattice [86].

Second, the correlation parameters are determined. In this case, convergence was not achieved for any number of considered spatial lags. It appears that with the increase of the number of lags, the smoothness parameter $\boldsymbol{\nu}$ is continuously increasing. Such behavior was observed in all directions. Thus, to gain further insight into the behavior of the residual in Equation 7.17, the residual on the grid of correlation length and smoothness values is evaluated. The objective function's behavior in all directions is somewhat similar. Figure 7.5 shows an apparent plateau in the smoothness parameter, explaining the lack of convergence. As the residual appears to decrease with increase of the smoothness parameter, the Gaussian model is chosen to be fitted, which is a particular case of Matérn correlation function when $\boldsymbol{\nu} \to \infty$.

Having fixed the smoothness parameter, the convergence study on the achieved correlation length is performed. Figure 7.6 shows that the convergence in x direction can be achieved relatively quickly as the correlation length parameter changes only slightly with the increasing number of lags. However, there is a significant change in other directions. The results converge after 100 spatial lags.

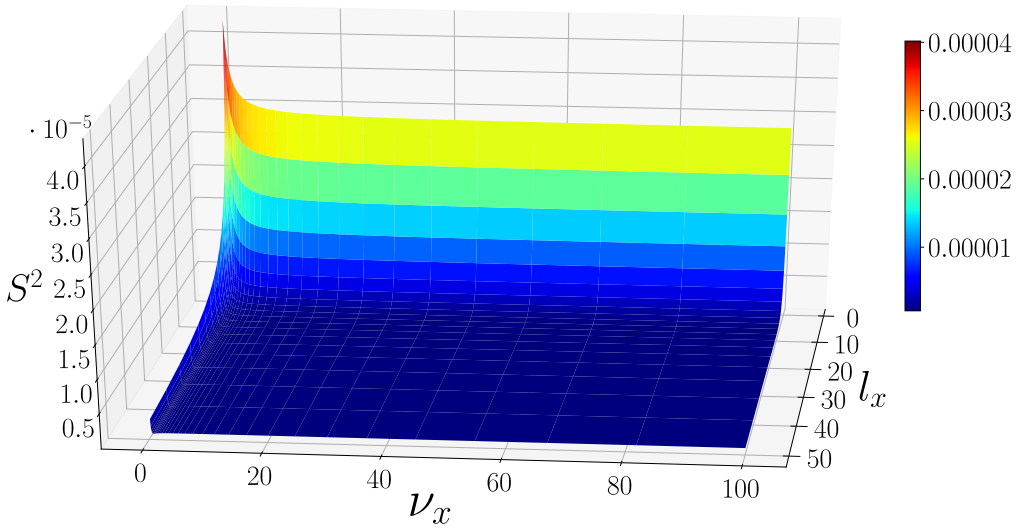

Figure 7.5: Objective function for an octet-truss lattice in x-direction with 100 lags [86].

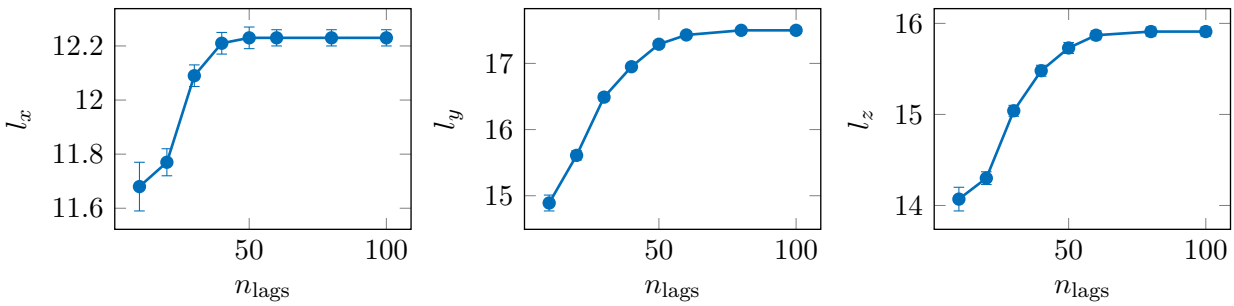

Figure 7.6: Convergence of the estimated correlation parameters for the octet-truss lattice [86].

The qualitative fitting as shown in Figure 7.7 shows that the trend is only captured on average. The extreme values of the observed binary correlation are not well contained in the proposed structure. It is important to note, that due to a very large size of the data set, it is hard to visualize it. The computed correlation coefficients for every lag follow a distribution, i.e. large amount of data points are concentrated around a value. The fitting procedure captures this value, or homogenizing the spread of the possible correlation parameters. Quantitatively, the results presented in Table 7.1 seem to have a relatively small standard deviation indicating a good fit.

Considered lags	$l_x, [voxels]$	$l_y, [voxels]$	$l_z, [voxels]$
100 lags	12.23 ± 0.03	17.50 ± 0.05	15.91 ± 0.05

Table 7.1: Correlation parameter identification for the octet-truss lattice [86].

Based on the fitted parameters, 3D samples of the microstructure are generated ac-

cording to the procedure described in section 7.3. One sample takes about 10 seconds to be generated. A representative realization is compared to the original image in three orthogonal views in Figures 7.8 to 7.10. Visually, the structures are similar to the original image and the periodic structure of the underlying octets is well-captured.

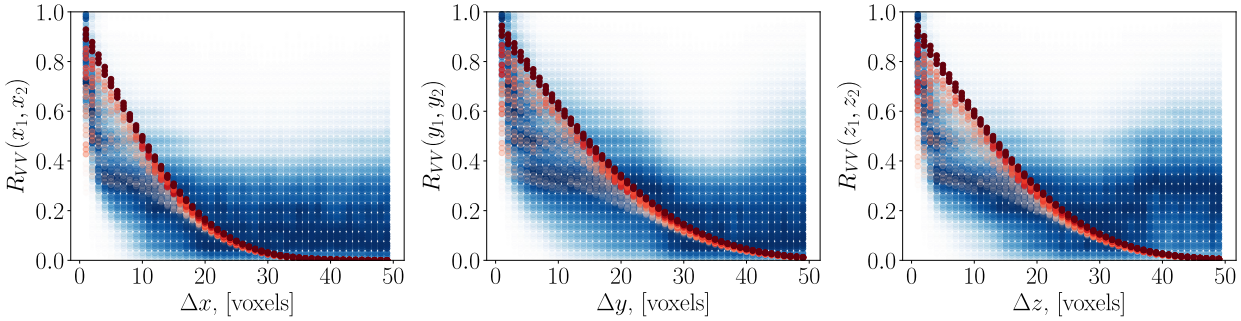

Figure 7.7: Fitted and computed auto-correlation of the octet-truss structure (blue - sample correlation; red - squared exponential model fit) [86].

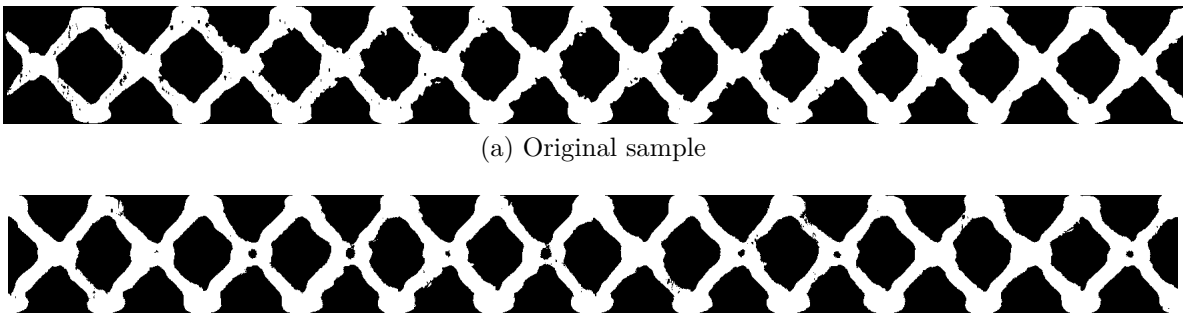

(a) Original sample

(b) Realization

Figure 7.8: An example of a realization based on fitted correlation parameters: coronal slice 290 of the octet-truss lattice [86].

(a) Original sample (b) Realization

Figure 7.9: An example of a realization based on fitted correlation parameters: axial slice 872 of the octet-truss lattice [86].

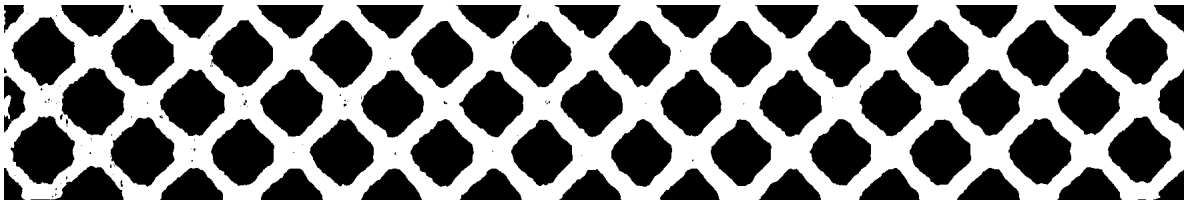

(a) Original sample

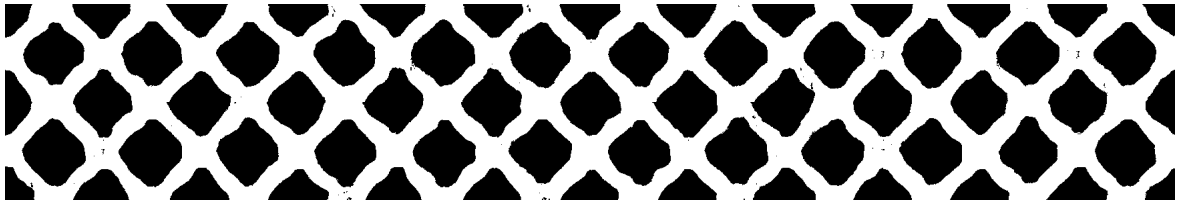

(b) Realization

Figure 7.10: An example of a realization based on fitted correlation parameters: axial slice 77 of the octet-truss lattice [86].

Multilevel Monte Carlo analysis of the homogenized mechanical behavior

The original octet-truss lattice is analyzed both experimentally and numerically. The results for deterministic evaluation are shown in section 6.1. The numerical analysis of the CT scan of the octet-truss lattice was performed with fewer hierarchy levels than the example above. The coarsest discretization level $\mathcal{L} = 0$ consists of $73 \times 44 \times 442$ finite cells with the polynomial degree $p = 1$. At the level $\mathcal{L} = 1$ h-refinement is performed to obtain $146 \times 88 \times 884$ finite cells with the polynomial degree $p = 1$. With every higher level, $\mathcal{L} > 2$, the finite cells' polynomial degree is raised from $p = 1$ to $p = 3$. The results achieved based on the analysis of the original CT scan are presented in section 6.1.

To evaluate the number of necessary samples for the MLMC, the screening was performed (see Figure 7.12). The procedure showed that four hierarchy levels with the sample numbers larger than $N_\ell \geq (5413, 298, 145, 27)$ are required to achieve a relative error of 2.5% for the estimated variance. The mean value can be evaluated with the same relative error with four levels and sample numbers larger than $N_\ell \geq (70, 3, 1, 1)$. The number of samples for the mean estimation is much smaller as a fast convergence for provided discretization is expected. Again, both estimates are combined and the number of samples is updated during the computation procedure to achieve a relative accuracy of $\varepsilon_r = 0.025$ for both the mean and the variance, which results in the number of samples $N_\ell = (5479, 396, 166, 43)$ meaning 5479 simulations with the coarsest and 43 simulations with the finest discretization. To get a better understanding of the final distribution, the third and the fourth moments are estimated without evaluating the optimal sample number for these central moments.

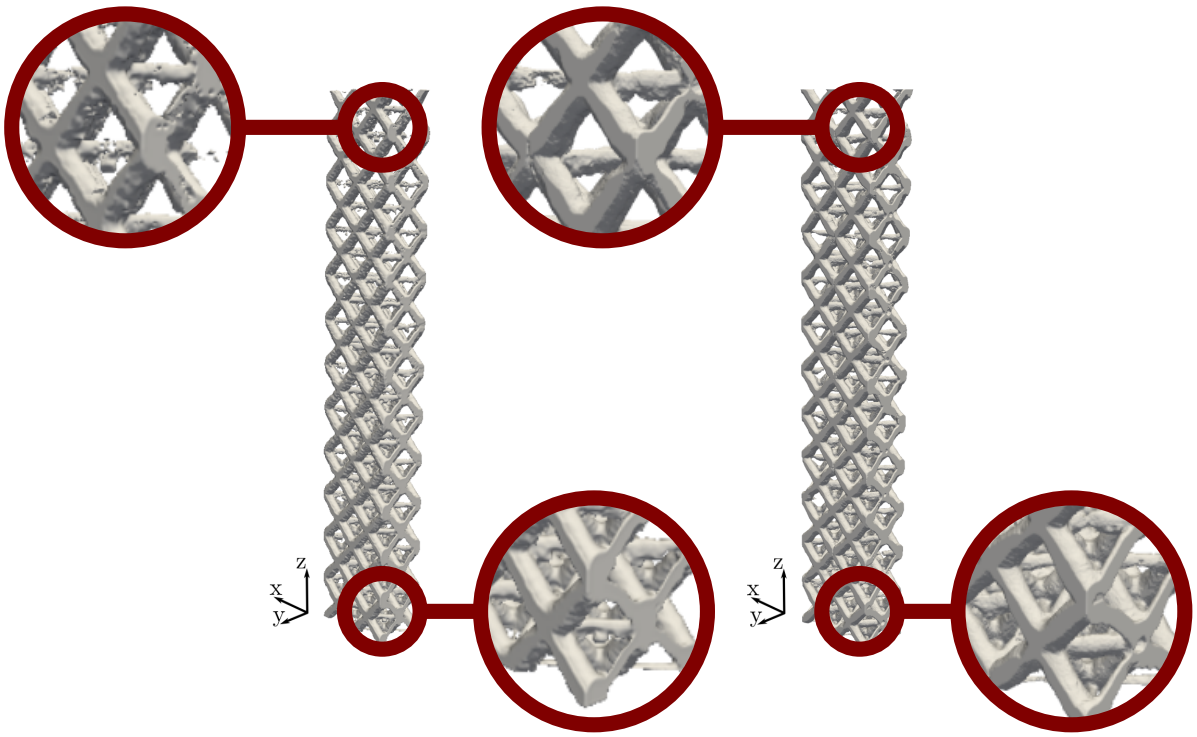

(a) Original sample (b) Realization

Figure 7.11: An example of a realization based on fitted correlation parameters: full 3D model of the octet-truss lattice [86].

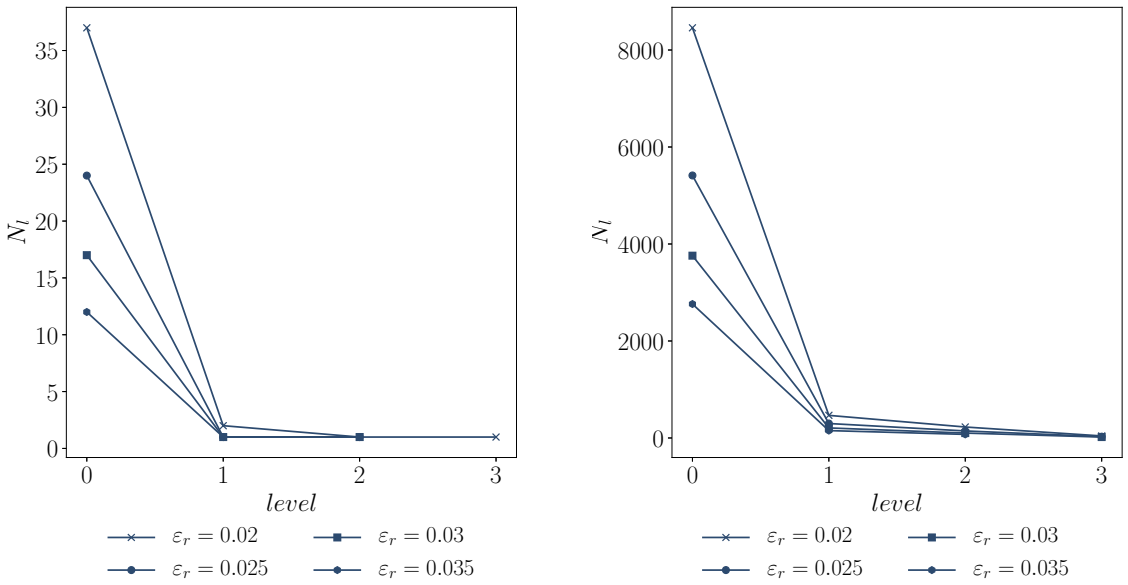

(a) Mean estimation (b) Variance estimation

Figure 7.12: Results of MLMC screening procedure for the octet-truss lattice [86].

Table 7.2 summarized the achieved results. To get a visual overview of the estimated distribution, it is approximated with the normal distribution based on the estimated first and second moments. The estimated skewness and kurtosis as indicated in Table 7.2 are close to the values for the normal distribution.

μ, [MPa]	σ, [MPa]	γ,[-]	κ,[-]
12 807	164	-0.16	3.66

Table 7.2: The estimated moments from the MLMC procedure for the octet-truss lattice (γ indicates skewness, whereas κ kurtosis) [86].

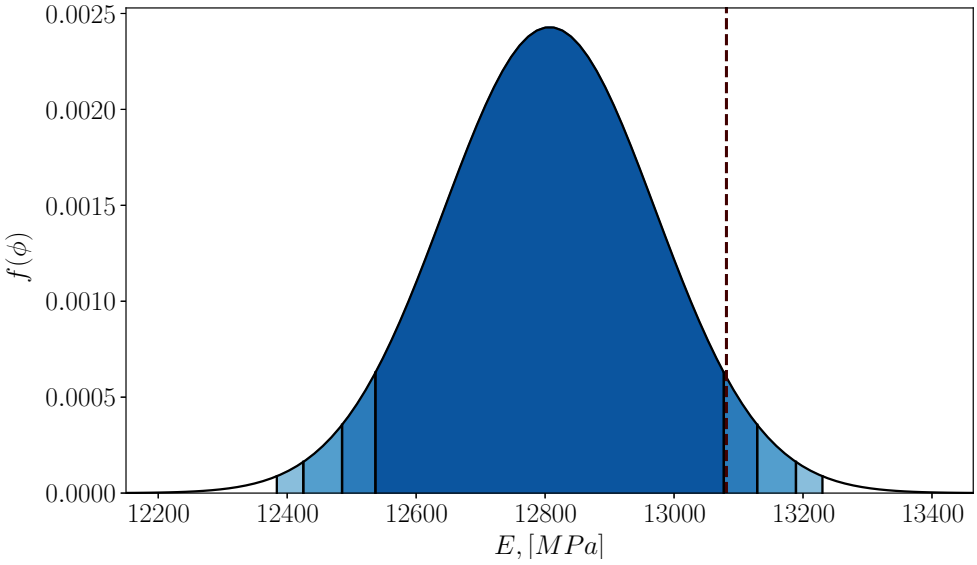

Figure 7.13: Results of MLMC on the homogenized Young's modulus for the octet-truss lattice. Normal fit based on the estimates of the first two moments. The shaded areas plot the intervals covering the 90%, 95%, 98%, and 99% of the probability mass [86].

For this example, the Young's modulus evaluated numerically with the original specimen is at the border of the estimated 90% interval. The estimated mean value agrees well with the experimentally obtained values. However, the standard deviation appears to be relatively small $\sigma = 164$. This phenomenon points once more to the nature of the additive manufacturing process. As indicated, the octet-truss lattice is produced at a much larger scale than the square one. Thus, the as-manufactured geometries are expected to exhibit smaller relative variability than for the square grid lattice structure. This behavior is mirrored in the results of the MLMC procedure: a much smaller variability is observed in the final homogenized Young's modulus due to the present geometrical variations. The considered structure is much smoother with a smaller number of geometrical and topological defects.

7.5.2 Square grid lattice

3D model parameter identification

First, the whole CT scan of the square lattice structure is analyzed using the proposed model (section 6.2). The total size of the considered model is $400 \times 800 \times 368$ voxel with the same voxel spacing $14.71\mu m$. The size of the local cell is $40 \times 40 \times 368$ voxels with local coordinates $x^l \in [0, 39]$, $y^l \in [0, 39]$ and $z^l \in [0, 368]$ (see Figure 7.14).

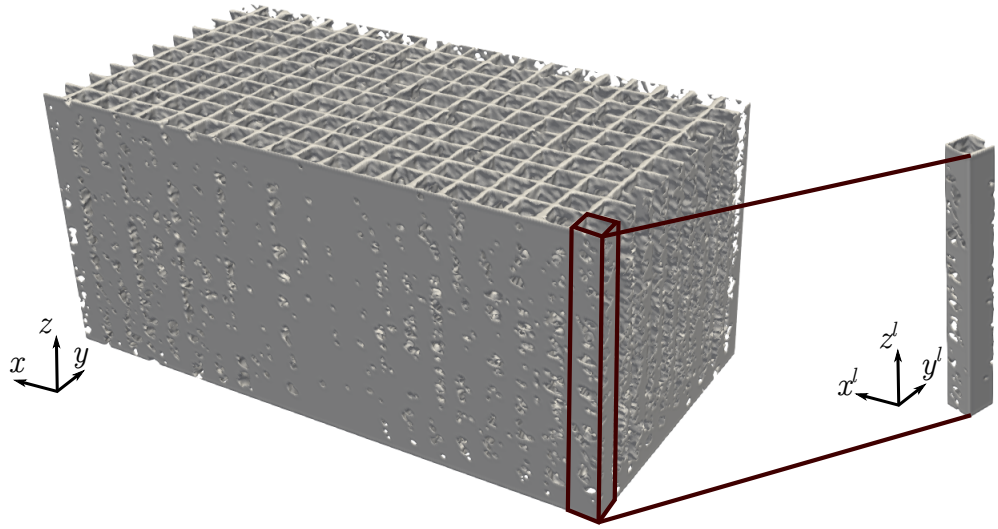

Figure 7.14: An example of a periodic unit cell with its local coordinate system in the 3D square lattice structure [86].

The local probabilities are computed in a similar manner as for the 2D case considering the local unit cells extracted from the volume. As the data set already becomes very large, not all spatial lags can be considered in the fitting procedure for the parameters of the correlation model. To estimate the necessary number of spatial lags, a convergence study on the correlation parameters is performed. To this end, the number of spatial lags is increased in every direction and observe the estimated correlation parameters' behavior.

Figure 7.15 indicates that after 30 spatial lags both the correlation length and the smoothness parameters in x and y directions do not change significantly. Thus, for further computations 30 spatial lags are considered. However, Figure 7.16 shows that the correlation length in z direction is constantly increasing with the number of considered lags. The smoothness parameter ν_z can be considered converged after 300 lags. This could potentially indicate that the objective function in Equation 7.17 is rather flat in the achieved minimum of the smoothness parameter. Thus, the change in the correlation length for the fixed smoothness parameter does not change the behavior of the residual significantly. To further investigate this, the residual as in Equation 7.17 is computed for 300 lags on a pre-defined grid of values for correlation length and smoothness parameter. Figure 7.17 reveals a manifold of near-optimal values of (l_z, ν_z), indicating that there is a number of combinations of the two parameters that leads to near-optimal parameter fit. The non-identifiability of unique smoothness and correlation length parameters of correlation models belonging to the Matérn class has been discussed elsewhere, e.g., in [28].

The plot also shows that there exists a minimum for the smoothness parameter, which corresponds well to the results obtained above. However, the objective function remains almost constant once the smoothness minimum is achieved for $l_z \in (2000, 10000)$. The large values of the correlation length in z direction are related to the technique used to generate the AM product. In particular, the square grid structure is produced such that the in-plane grid is extruded in z direction. Thus, it is natural to expect a larger correlation length in this direction. The optimal value obtained in this case is $(l_z, \nu_z) = (0.104, 4187)$. For further computations the number of spatial lags in z direction is fixed to 300.

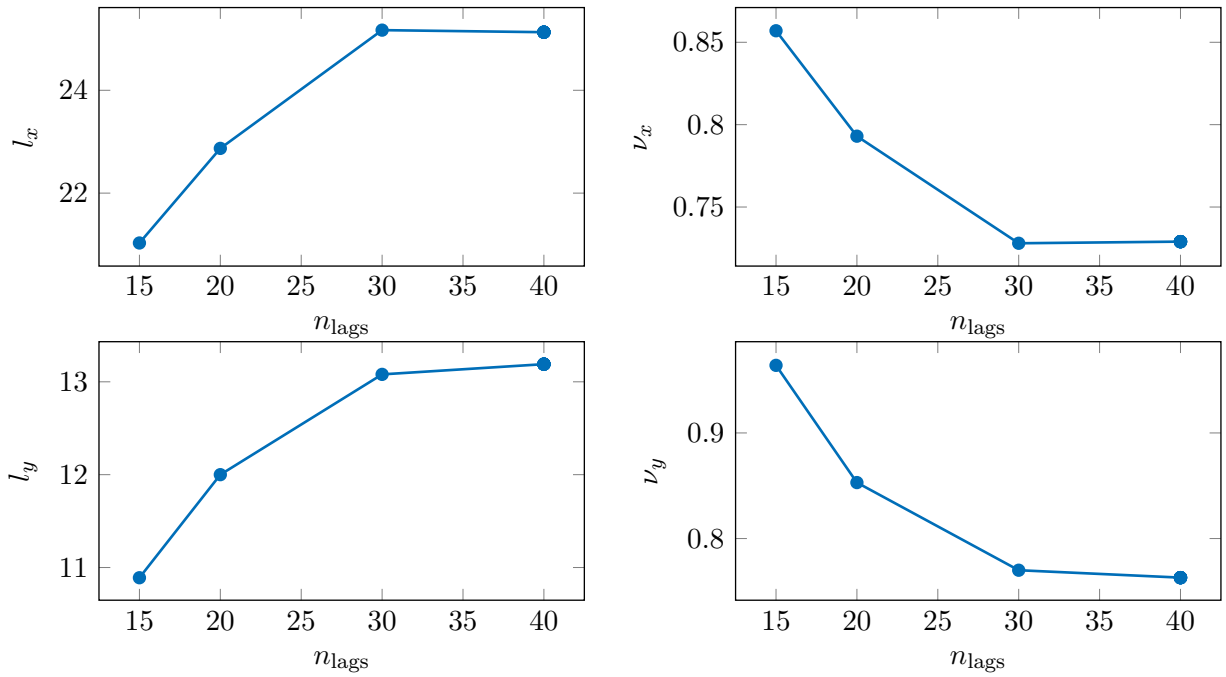

Figure 7.15: Convergence of the estimated correlation parameters in x and y direction [86].

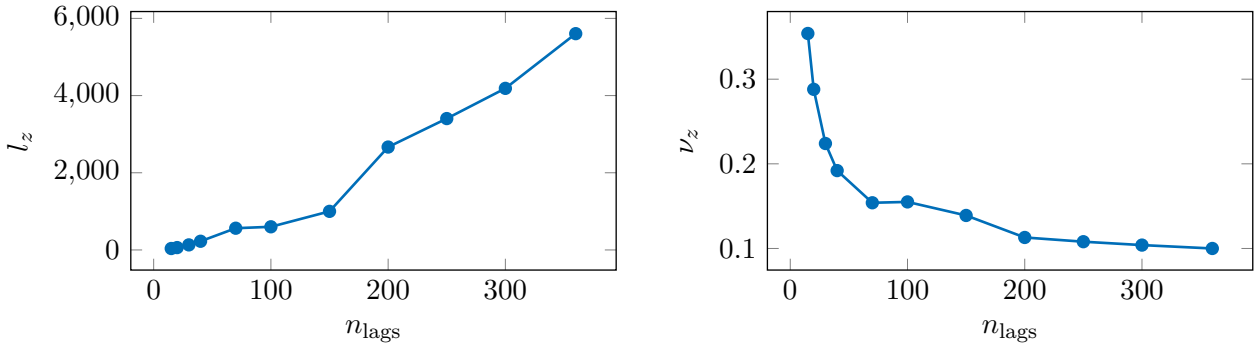

Figure 7.16: Convergence of the estimated correlation parameters in z direction [86].

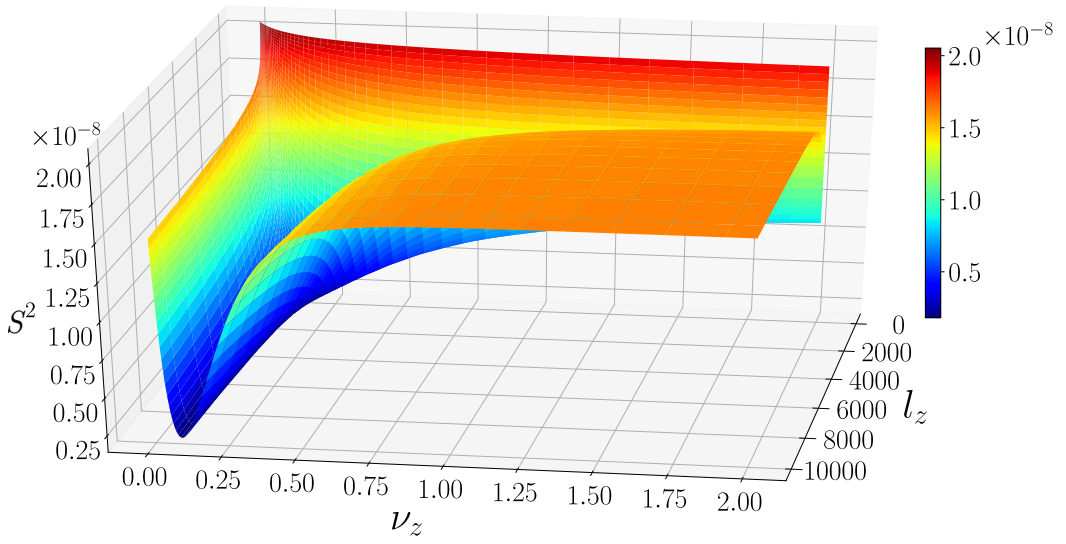

Figure 7.17: Behavior of the objective function for fitting the correlation function in z-direction with 300 lags [86].

The achieved fit of computed covariance and the considered model of Matérn covariance for 30 spatial lags in x and y direction and 300 lags in z direction is shown in Figure 7.18. Similar to the 2D case, the model qualitatively follows the trend of the binary covariance. Nevertheless, the model does not capture the spread in the correlation values but rather homogenizes the solution. The design correlation parameters are summarized in Table 7.3 together with their standard deviations.

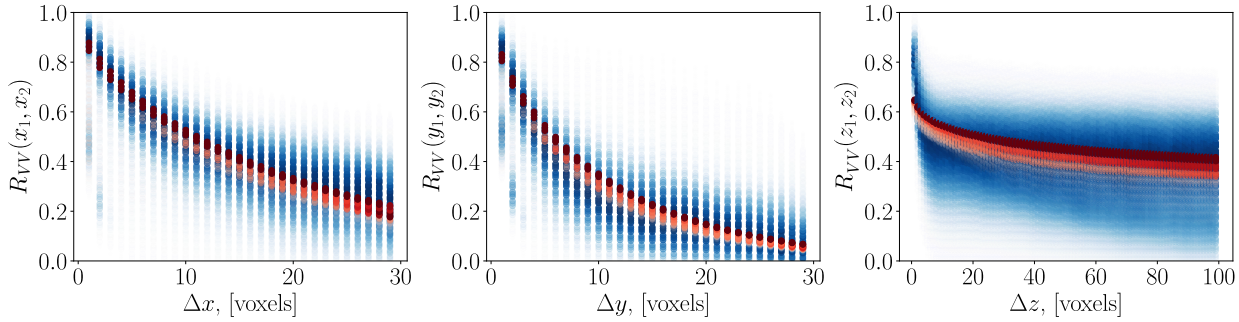

Figure 7.18: Fitted and computed auto-correlation of a 3D model (blue - sample correlation; red - Matérn model fit) [86].

$l_x, [voxels]$	$l_y, [voxels]$	$l_z, [voxels]$	$\nu_x, [-]$	$\nu_y, [-]$	$\nu_z, [-]$
25.17 ± 0.02	13.08 ± 0.01	4186.99 ± 10.31	0.728 ± 0.001	0.770 ± 0.001	0.104 ± 0.001

Table 7.3: Correlation parameter identification for a 3D structure using 300 lags [86].

Having determined the correlation parameters, the method described in section 7.3 is applied to generate realizations of the 3D random microstructure. The generation of every volume takes on average 6 seconds for the considered domain size. A representative realization is shown in Figures 7.19 and 7.20. The original sample together with one realization are depicted in Figure 7.21.

Visually, the overall geometry is similar to the original specimen. The underlying structure is well preserved, while the small features are varied. The distribution of the porosity computed with 5000 samples is shown in Figure 7.22. The porosity of the original specimen is $\phi = 0.7293$, which is close to the mean value computed with samples from the proposed model. The computed standard deviation again appears to be relatively small. However, the macroscopic porosity is not the only determining factor for the macroscopic mechanical behavior. The topological features, such as the strut connectivity, can have a significant influence on the response of the final product.

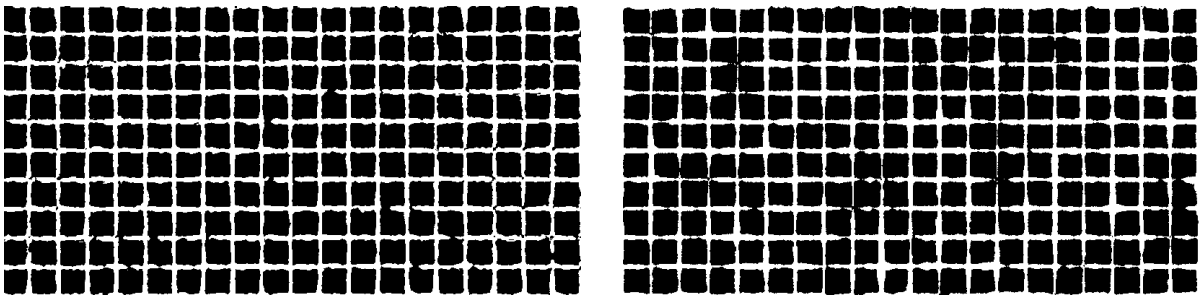

(a) Original sample (b) Realization

Figure 7.19: An example of a realization based on fitted correlation parameters: coronal slice 71 in the 3D volume [86].

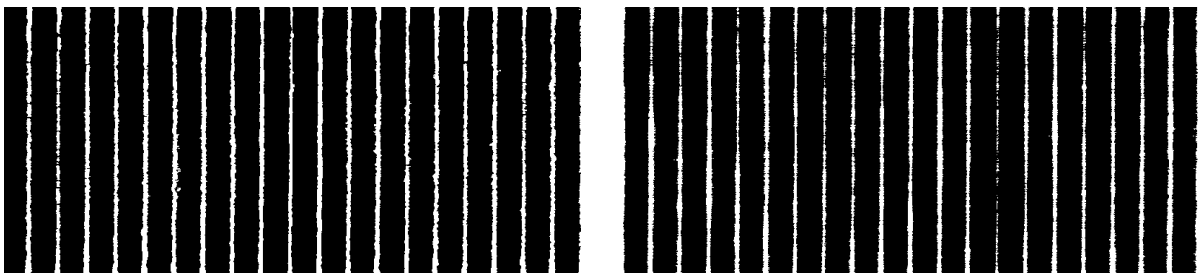

(a) Original sample (b) Realization

Figure 7.20: An example of a realization based on fitted correlation parameters: axial slice 213 in the 3D volume [86].

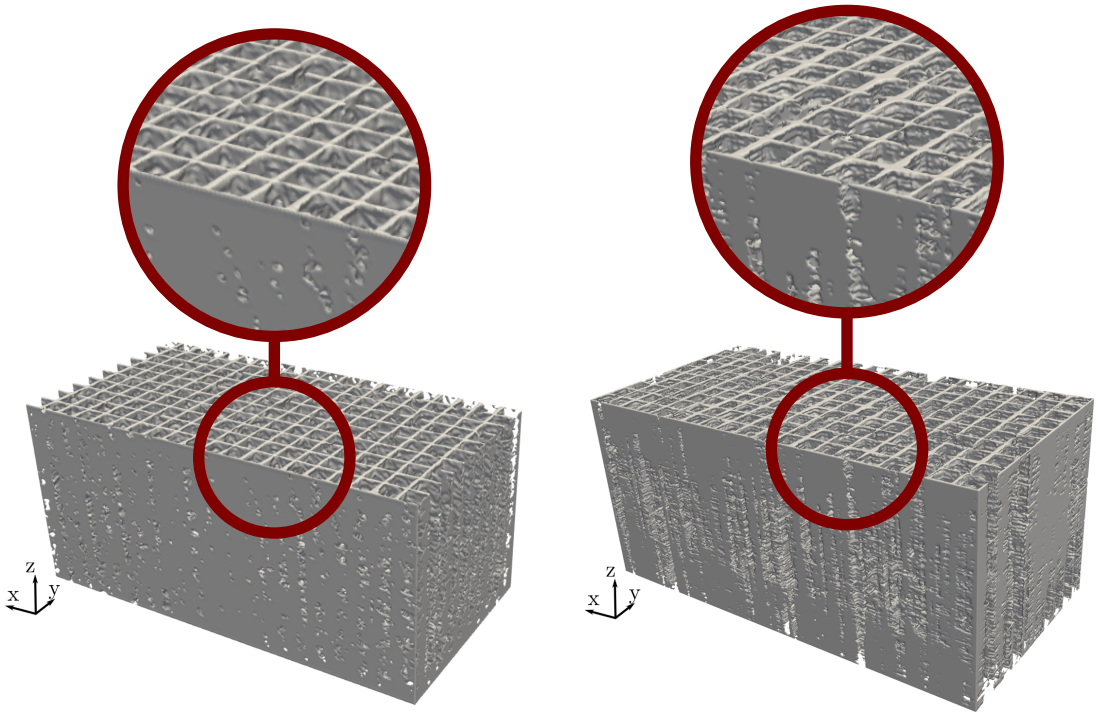

(a) Original sample (b) Realization

Figure 7.21: An example of a model realization based on fitted correlation parameters: full 3D model [86].

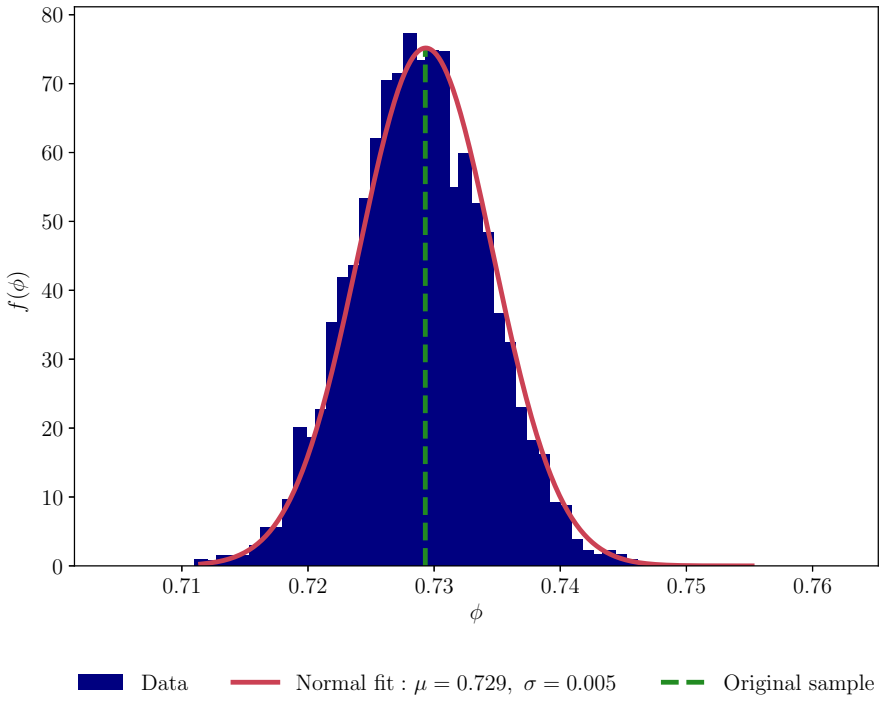

Figure 7.22: Porosity distribution for 3D square lattice realizations [86].

Multilevel Monte Carlo analysis of the homogenized mechanical behavior

In the following, the influence of the geometrical variability on the homogenized Young's modulus for this specimen is evaluated. The numerical analysis of the CT scan of the 600 L2 specimen was performed through applying the FCM directly on the provided image. The coarsest discretization level $\mathcal{L} = 0$ consists of $100 \times 46 \times 100$ finite cells with the polynomial degree $p = 1$. At the level $\mathcal{L} = 1$ the h-refinement is performed to obtain $200 \times 46 \times 100$ finite cells with polynomial degree $p = 1$. With every higher level, $\mathcal{L} > 2$, the finite cells' polynomial degree is raised from $p = 1$ to $p = 5$. These levels correspond to the numerical investigations discussed in section 6.2. Thus, the mechanical analysis of all 3D realizations with the correlation parameters determined above is performed using the same Finite Cell discretization levels as for the original CT image. As the constants c in Equation 7.28 are not known a priori for this problem, the screening procedure is held to evaluate the optimal hierarchy parameters.

For the screening procedure, a few samples on the levels $\overline{\mathcal{L}} = \{0, 1, 2, 3, 4, 5\}$ are evaluated. The fit of the constants for $\Delta_{\mathcal{L}} h_r, V_{\ell,r}$ and $\text{cost}(\mathcal{Q}_{M_\ell})$ are performed assuming an exponential dependence as in Equation 7.28 and then extrapolated to the higher levels. Using Equations 7.29 and 7.30 the optimal number of hierarchy levels together with the optimal number of samples at each level are estimated for different relative tolerances ε_r.

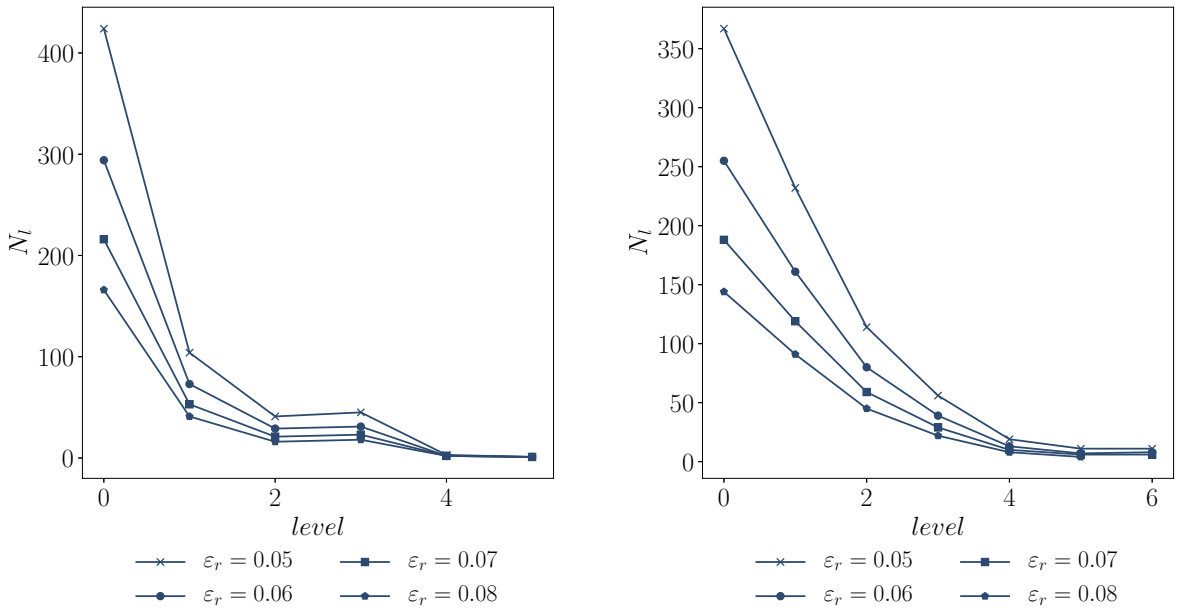

(a) Mean estimation

(b) Variance estimation

Figure 7.23: Results of MLMC screening procedure for the square lattice [86].

Figure 7.23 depicts the number of necessary samples for the mean and variance estimation of the homogenized Young's modulus. The mean value estimation requires a lower value of optimal levels than the variance estimation. The screening procedure shows that seven hierarchy levels with sample numbers larger than $N_\ell \geq (367, 232, 114, 56, 19, 11, 11)$ are required to achieve a relative error of 0.05 for the estimated variance. The mean value can be evaluated with the same achieved error with six levels and sample numbers

larger than $N_\ell \geq (424, 104, 41, 45, 3, 1)$. The final number of samples used to obtain the estimates of the moments is updated to achieve the target accuracy of $\varepsilon_r = 0.05$ giving $N_\ell = (621, 250, 146, 99, 38, 19, 15)$. Although the screening procedure is performed for the first two moments, the third and the fourth moments are evaluated with the provided number of samples to get an idea about the final distribution.

The results of the MLMC algorithm are summarized in Table 7.4.

μ, [MPa]	σ, [MPa]	γ, [-]	κ, [-]
20 625	1 619	−0.20	2.68

Table 7.4: The estimated moments from the MLMC procedure for the square grid lattice (γ is skewness, whereas κ is kurtosis) [86].

In Figure 7.24, a normal fit of the probability density function of the homogenized Young's modulus based on the estimated mean and variance together with the intervals that cover the 90%, 95%, 98%, and 99% of the probability mass. The determined skewness γ and kurtosis κ as in Table 7.4 are close to the one expected for the normal distribution (0 and 3 respectively). However, these estimates have significant uncertainty. Considering the sampling uncertainty related to the moment estimates, the plot shows a conservative visualization of the distribution and intervals.

The Young's modulus evaluated with the original sample falls into the 99% interval (shown as the dashed line in Figure 7.24). Overall, the performed MLMC procedure seems to capture the observed spread in the experimentally determined homogenized Young's modulus. Due to the additive manufacturing process's underlying complex physics, there are many geometrical and topological variations to be expected for such microscale lattices. Undoubtedly, these defects play a significant role in the final part's mechanical behavior, which is supported by this analysis.

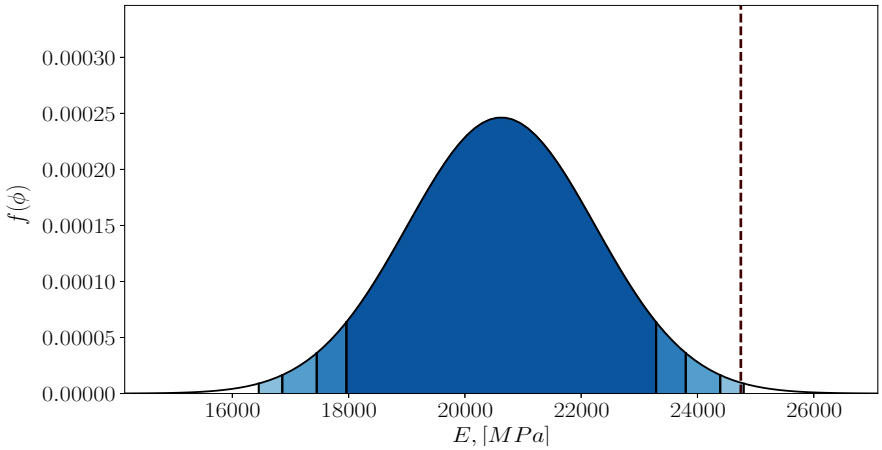

Figure 7.24: Results of MLMC on the homogenized Young's modulus for the square lattice. Normal fit based on the estimates of the first two moments. The shaded areas plot the intervals covering the 90%, 95%, 98%, and 99% of the probability mass [86].

Chapter 8

Concluding remarks

Additive manufacturing technology has undergone significant development in the past years. It allowed for the production of complex designs, especially lattices, which were impossible to produce traditionally. Alongside numerous advantages and improvements, this development has opened a wide range of unanswered questions and challenges. One of them is the analysis of process-induced defects. In fact, as-manufactured structures can exhibit significant variations from the design due to the manufacturing process. Undoubtedly, this change in the geometry influences AM products' quality and puts uncertainty on their applicability areas. To this extent, diverse questions have to be confronted. For example: what is the most suitable way to evaluate the process-induced defects? Can their effects be estimated numerically? Is there a connection between process parameters and arising deviations? The list of possible challenges can be extended much further. Thus, this thesis focused on addressing a few demands in additive manufacturing product analysis.

In this work, a numerical workflow to evaluate additively manufactured structures' structural behavior has been proposed. This research suggested several courses of action to enable easy and efficient analysis of the final parts. In particular, the following challenges have been explored:

- The acquisition of as-manufactured geometries via computed tomography (CT) provides all necessary information about process-induced defects up to a scan resolution. Nevertheless, these imperfections can be detected accurately only when the geometrical boundary is correctly deduced from CT images. Metal AM products can be complicated in this context. In the proposed framework, the standard single threshold technique is extended by a deep learning segmentation discussed in section 2.4. It was demonstrated that this technique provides reliable results when microarchitectured AM lattices with trapped powder are considered.
- The incorporation of CT-based geometrical models in the numerical analysis requires additional steps, which are commonly highly laborious. These steps can be avoided by using the Finite Cell Method, an immersed boundary approach. To this extent, a numerical integration scheme tuned explicitly for the CT-based analysis has been presented in section 4.2. Combining the FCM with the voxel-based pre-integration technique has shown a significant reduction of the necessary computational effort for CT-based numerical analysis.

- The Direct Numerical Simulation of a virtual experiment, especially on CT images, was mainly considered impossible. Thus, many investigations focused on smaller domain sizes or other simplifications. However, the parallel implementation of the FCM presented in section 4.3 allows pushing the computational boundaries further. It was demonstrated that with this approach, the full-scale simulation with microscopical geometrical defects is possible in a reasonable time. Furthermore, this opened possibilities to compare the as-designed and as-manufactured behavior at full scale.
- To allow further flexibility in choosing the numerical methods in this workflow, the computational homogenization technique has been introduced in chapter 5. As the imperfect AM products can demonstrate high irregularities, random internal porosity, and general high macroscopic porosity, the necessary modifications to the traditional homogenization approach have been investigated. It was shown that the proposed CT-based numerical homogenization technique provides an excellent agreement with both full-scale numerical simulation and experimental data, even for highly irregular structures.
- Another necessary computational advance built upon all previous points is the proposed use of strain gradient beam theories for numerical characterization of AM products. The methods introduced in sections 3.2 and 3.3 were for the first time used in the scope of as-manufactured AM product analysis and have been proved to provide more accurate results in comparison to the classical approaches. As the required input to these theories is a reliable homogenization procedure, the combination of these beam theories with the CT-based computational homogenization introduced in chapter 5 allowed for a more accurate and much quicker evaluation of the mechanical behavior of AM structures.
- All proposed tools and methods have been finalized with a novel approach to quantify the uncertainty introduced by the process-induced defects in chapter 7. It has been demonstrated that with the CT-based random field model, all geometrical defects up to the scan resolution can be incorporated and reproduced efficiently. The numerical results have indicated that with this approach, a certain spread of the mechanical quantities can be estimated without the need to manufacture many samples. Additionally, the obtained estimates indicate that the obtained spread corresponds to the experimentally determined data.

All in all, the proposed numerical workflow has been thoroughly investigated and validated on three printed metal lattices. However, the prospect for being able to fully understand, improve and evaluate the effects of the process-induced defects on the performance of AM products efficiently serves as a continuous stimulus to explore the following possible future directions in the context of the proposed numerical workflow:

- This thesis has focused on the evaluation and validation of the workflow in linear physics. Yet, the characterization of the AM products in non-linear regimes or other conditions such as, e.g., determination of yield stress, fatigue life, have to be investigated. To this end, the necessary extensions to the parallelization strategy of the FCM have to be looked at. In particular, the non-linear full-scale simulations would require storing a large amount of data about the internal variables. Thus, an

appropriate algorithm should be found to alleviate these memory-extensive computations.

- Another possible direction of research is an investigation of other computational homogenization techniques. In this work, mean-field homogenization has been used. However, the efficiency and applicability of other methods, such as FFT-based or asymptotic homogenization, in the scope of AM product simulations have to be addressed. In this context, the Periodic Boundary Conditions used in this thesis can be formulated in a weak form to facilitate their application for highly irregular structures further.
- The proposed binary random field model for uncertainty quantification of process-induced defects assumes the Matérn correlation model for the underlying Gaussian random field. A potential future direction would be to investigate alternative correlation models, e.g., models that introduce a periodic correlation structure. Additionally, a Bayesian approach could be applied for estimating the parameters of the correlation model. Thereby, a challenge that would need to be addressed is the increased computational cost for parameter fitting.
- Another essential direction is extending the proposed workflow to evaluate the intra-specimen variability induced by the manufacturing imperfections. The current random field model enables modeling such intra-specimen variability. An important future research step would be to incorporate multiple CT images of similar parts produced with different process parameters into the proposed model. This would allow evaluating the uncertainty introduced by a specific group of process parameters and provide necessary insights into the final parts' confidence levels. Furthermore, this direction would open up many possibilities in the optimization of process parameters.

List of Symbols

The notation used in this thesis is summarized in the following. Bold letters refer to tensor entities, while the medium ones to scalar values. The symbols and abbreviations are ordered by logical units in the order of appearence throughout this work.

Classical continuum mechanics

Ω	Volume or domain of the body
Γ	Domain boundary
χ	Deformation mapping
$\boldsymbol{u}$	Displacement vector
$\boldsymbol{x} = (x, y, z)$	Cartesian coordinate vector of a spatial point in the deformed configuration
$\boldsymbol{X} = (X, Y, Z)$	Cartesian coordinate vector of a spatial point in the initial configuration
$\boldsymbol{e}$	Unit vector in the deformed configuration
$\boldsymbol{E}$	Unit vector in the initial configuration
$\boldsymbol{F}$	Deformation gradient tensor
∇	Vector differential operator
$\boldsymbol{\varepsilon}$	Green-Lagrange strain tensor
$\boldsymbol{t}$	Cauchy traction vector
$\boldsymbol{b}$	Body load vector
$\mathcal{W}(\cdot)$	Classical strain energy density function
$\boldsymbol{C}$	Elasticity tensor
$\boldsymbol{\sigma}$	Cauchy stress tensor
$\boldsymbol{n}$	Outward unit normal vector
Γ_D	Dirichlet part of the domain boundary
Γ_N	Neumann part of the domain boundary
$\hat{\boldsymbol{t}}$	Prescribed Cauchy traction vector on Neumann boundary
$\hat{\boldsymbol{u}}$	Prescribed displacement vector on Dirichlet boundary

Finite Element Method

$\mathcal{B}(\cdot, \cdot)$	Bi-linear form
$\mathcal{F}(\cdot, \cdot)$	Linear form
$\boldsymbol{v}$	Test funciton
$\mathcal{V}$	Collection of test functions

$\mathcal{S}$	Collection of trial solutions functions
$H^1(\cdot)$	Sobolev space of degree one
$\mathcal{V}^h$	Finite element sub-space of $\mathcal{V}$
$\mathcal{S}^h$	Finite element sub-space of $\mathcal{S}$
$\boldsymbol{v}^h$	Finite-dimensiona trial functions
Ω_{el}	Domain of a finite element
(r, s, t)	Local coordinates of a finite element
p	Polynomial degree of element shape functions

Strain gradient continnum theory

Ω'	Micro-volume or micro-domain attached to every material point of the body
Γ'	Mciro-domain boundary
χ'	Micro-deformation mapping
$\boldsymbol{x}'$	Coordinate vector of a micro-spatial point in the deformed configuration
$\boldsymbol{X}'$	Coordinate vector of a micro-spatial point in the initial configuration
$\boldsymbol{u}'$	Micro-displacement vector
∇'	Vector differential operator defined in micro-coordinates
$\boldsymbol{\gamma}$	Micro-strain tensor
$\boldsymbol{\varkappa}$	Relative deformation, i.e., the difference between the macroscopic displacement gradient and micro-strain tensor
$\boldsymbol{\Theta}$	Micro-deformation gradient
$\mathcal{W}_{MM}(\cdot)$	Micromorphic strain energy density function
$\boldsymbol{\xi}$	Relative stress in micromorphic continuum
$\boldsymbol{\iota}$	Double stress in micromorphic continuum
$\mathcal{W}_{II}(\cdot)$	Strain energy density of Mindlin's Form II gradient elasticity
$\boldsymbol{A}$	Sixth-order gradient-elastic material tensor
$\boldsymbol{\Psi}^s$	Second-order strain-gradient length scale tensor
$\nabla_{surf} = \nabla - \boldsymbol{n} \otimes \boldsymbol{n} \cdot \nabla$	Surface gradient operator
$\hat{\boldsymbol{q}}$	Prescribed double stress traction vector
$d\hat{\boldsymbol{u}}_n$	Prescribed normal directional derivative of the displacement $\boldsymbol{u}$

Classical and strain gradient beam theories

F	Total applied force at the middle of the beam
w	Vertical deflection of a central axis of the beam
L	The distance between fixed and roller support in three-point bending test
M	Bending moment of the beam
Q	Shear force of the beam
E^*	Effective Young's Modulus
I	Effective moment of intertia
b	Width of the beam
h	Height of the beam

G^*	Effective shear Modulus
A	Effective cross-sectional area of a beam
D	Beam bending rigidity
D^{EB}	Classical Euler-Bernoulli bending rigidity
D^{T}	Classical Timoshenko bending rigidity
D_{gr}^{EB}	Strain gradient Euler-Bernoulli bending rigidity
D_{gr}^{T}	Strain gradient Timoshenko bending rigidity
$R(x)$	Generalized moment of the beam
g	High-order (directional) intrinsic length scale parameter

Finite Cell Method

Ω_e	Extended domain representing the union of the fictitious and physical domain in the Finite Cell Method
Ω_c	Volume/Domain of a finite cell
Ω_v	Volume/Domain of a voxel
$\mathcal{B}_e^{\alpha}(\cdot,\cdot)$	Extended bi-linear form in the Finite Cell method
$\mathcal{F}_e^{\alpha}(\cdot)$	Extended linear form in the Finite Cell method
$\alpha(\cdot)$	Indicator function
$\boldsymbol{B}$	Matrix of derivatives of shape functions
(s_x, s_y, s_z)	Voxel dimensions
(n_x, n_y, n_z)	Number of finite cells
(v_x, v_y, v_z)	Number of voxels in one finite cell
$\boldsymbol{K}_c$	Stiffness matrix of a finite cell
$\boldsymbol{J}$	Jacobian matrix
(k_r, k_s, k_t)	Local coordinate integration limits of every voxel in a finite cell

Computational homogenization

ϕ	Porosity
$()^*)$	Effective/homogenized quantity
ν	Poisson's ratio
E	Young's Modulus
$< \cdot >$	Volume averaging operator
$(\cdot)^M$	Macroscopic fields
l_w	Window size (frame width)
l_{RVE}	Size of the representative volume
k	Refinement depth

Uncertainty quantification

$V(\boldsymbol{x})$	Binary random field
$v(\boldsymbol{x})$	Outcome of the binary random field
$d(\boldsymbol{x})$	Threshold of the binary random field
$U(\boldsymbol{x})$	Gaussian random field
$u(\boldsymbol{x})$	Outcome of the Gaussian random field
μ	Mean value

σ	Standard deviation
$\rho(\boldsymbol{x}_1, \boldsymbol{x}_2)$	Auto-correllation coefficient function of a random field
$\mathbb{E}[\cdot]$	Mathematical expectation operator
$\boldsymbol{l} = (l_x, l_y, l_z)$	Vector of correlation length parameters
$\boldsymbol{\nu} = (\nu_x, \nu_y, \nu_z)$	Vector of smoothness parameters
$p(\cdot)$	Probability mass function
$\Phi(\cdot)$	Standard normal cumulative distribution function
$\Gamma(\cdot)$	Covariance of a random field
$\Phi_2(\cdot, \cdot, r)$	Joint cumulative distribution function of the bivariate standard normal distribution with correlation r
$F(\cdot;\cdot)$	Second-order cumulative distribution function
R	Auto-correllation function
$\Gamma(\cdot)$	Gamma function
$K_\nu(\cdot)$	Modified Bessel function of the second kind
$\boldsymbol{x}^l = (x^l, y^l, z^l)$	Cartesian coordinate vector of a spatial point in the local system of a periodic unit cell
$\boldsymbol{\mathcal{X}}^l = [\boldsymbol{x}_1^l; \ldots; \boldsymbol{x}_{n_l}^l]$	A set of local coordinates
N_{cells}	Total number of local periodic unit cells in the structure
$\hat{(\cdot)}$	Estimated quantities
$\boldsymbol{\mathcal{X}} = [\boldsymbol{x}_1; \ldots; \boldsymbol{x}_n]$	A set of global coordinates
$\boldsymbol{U}$	A vector of Gaussian random field
$\boldsymbol{R} = [\rho_{UU}(\boldsymbol{x}_i, \boldsymbol{x}_j)]_{n \times n}$	Correlation matrix of a Gaussian random field with correlation coefficient $\rho_{UU}(\boldsymbol{x}_1, \boldsymbol{x}_2)$
$\boldsymbol{L}$	Lower triangular matrix from Cholesky decomposition of the correlation matrix $\boldsymbol{R}$
$\boldsymbol{W}$	Vector of n-independent standard normal variables
$\mathcal{Q}$	Quantity of interest in Multilevel Monte Carlo method
$\mathcal{L}$	Total number of discretization levels in Multilevel Monte Carlo method
M_ℓ	Number of degrees of freedom at level ℓ
N_ℓ	Number of independent and identically distributed realizations at level ℓ
h_r	h-statistics for central moment r
γ	Skewness coefficient
κ	Kurtosis coefficient

List of abbreviations

AM	Additive manufacturing
LPBF	Laser Powder Bed Fusion
HU_{thres}	Hounsfield Units threshold value
CT	computed tomography
PBF	Powder Bed Fusion
CAD	computer-aided design
SLS	Selective Laser Sintering
EBM	Electron Beam Melting

SLM	Selective Laser Melting
HU	Hounsfield Units
ANN	Artificial Neural Network
CNN	Convolutional Neural Network
FEA	Finite Element Analysis
DNS	Direct Numerical Simulation
RVE	Representative Volume Element
FCM	Finite Cell Method
FEM	Finite Element Method
BC	Boundary Condition
NURBS	Non-Uniform Rational B-Splines
KUBC	Kinematic Uniform Boundary Conditions
PBC	Periodic Boundary Conditions
SUBC	Static Uniform Boundary Conditions
DOF	Degree of Freedom
MLMC	Multilevel Monte Carlo
QoI	Quantity of interest

Bibliography

[1] Abedian, A., Parvizian, J., Düster, A., Khademyzadeh, H., and Rank, E. (2013). Performance of Different Integration Schemes in Facing Discontinuities in the Finite Cell Method. *International Journal of Computational Methods*, 10(03):1350002.

[2] Aboudi, J. (1991). Chapter 2 - basic models in the mechanics of composites. In *Mechanics of Composite Materials*, volume 29 of *Studies in Applied Mechanics*, pages 14–34. Elsevier.

[3] Al-Saedi, D., Masood, S., Faizan-Ur-Rab, M., Alomarah, A., and Ponnusamy, P. (2018). Mechanical properties and energy absorption capability of functionally graded F2BCC lattice fabricated by SLM. *Materials & Design*, 144:32–44.

[4] Ansari, R., Faghih Shojaei, M., Mohammadi, V., Bazdid-Vahdati, M., and Rouhi, H. (2015). Triangular Mindlin microplate element. *Computer Methods in Applied Mechanics and Engineering*, 295:56–76.

[5] ASTM International (2017). *ASTM E 111-17: Standard Test Method for Young's Modulus, Tangent Modulus, and Chord Modulus*. West Conshohocken, PA: American Society for Testing and Materials.

[6] Babuska, I. (1973). The Finite Element Method with Penalty. *Mathematics of Computation*, 27(122):221–228. 00324.

[7] Bagheri, Z. S., Melancon, D., Liu, L., Johnston, R. B., and Pasini, D. (2017). Compensation strategy to reduce geometry and mechanics mismatches in porous biomaterials built with Selective Laser Melting. *Journal of the Mechanical Behavior of Biomedical Materials*, 70:17–27.

[8] Balobanov, V. (2018). *Computational structural mechanics within strain gradient elasticity: mathematical formulations and isogeometric analysis for metamaterial design*. PhD thesis, Aalto University.

[9] Balobanov, V. and Niiranen, J. (2018). Locking-free variational formulations and isogeometric analysis for the Timoshenko beam models of strain gradient and classical elasticity. *Computer Methods in Applied Mechanics and Engineering*, 339:137 – 159.

[10] Banhart, J. (2001). Manufacture, characterisation and application of cellular metals and metal foams. *Progress in Materials Science*, 46(6):559–632.

[11] Barba, D., Reed, R. C., and Alabort, E. (2020). Design of Metallic Lattices for Bone Implants by Additive Manufacturing. In *TMS 2020 149th Annual Meeting & Exhibition Supplemental Proceedings*, The Minerals, Metals & Materials Series, pages 745–759, Cham. Springer International Publishing.

[12] Bathe, K. J. (2007). *Finite Element Procedures*. Prentice Hall, New Jersey. 16197.

[13] Betz, W., Papaioannou, I., and Straub, D. (2014). Numerical methods for the discretization of random fields by means of the Karhunen–Loève expansion. *Computer Methods in Applied Mechanics and Engineering*, 271:109–129.

[14] Boas, F. E. and Fleischmann, D. (2011). Evaluation of two iterative techniques for reducing metal artifacts in computed tomography. *Radiology*, 259(3):894–902.

[15] Boas, F. E. and Fleischmann, D. (2012). CT artifacts: Causes and reduction techniques. *Imaging in Medicine*, 4(2):229–240.

[16] Bonet, J. and Wood, R. D. (1997). *Nonlinear Continuum Mechanics for Finite Element Analysis*. Cambridge University Press, Cambridge ; New York, NY, USA.

[17] Brown, J. A., Steck, D., Brown, J. A., and Long, K. N. (2017). Effect of Microstructure Constraints on the Homogenized Elastic Constants of Elastomeric Sylgard/GMB Syntactic Foam. Technical Report SAND–2017-8850R, 1376285.

[18] Buchanan, C. and Gardner, L. (2019). Metal 3D printing in construction: A review of methods, research, applications, opportunities and challenges. *Engineering Structures*, 180:332–348.

[19] Burstedde, C., Wilcox, L., and Ghattas, O. (2011). P4est: Scalable Algorithms for Parallel Adaptive Mesh Refinement on Forests of Octrees. *SIAM Journal on Scientific Computing*, 33(3):1103–1133.

[20] Campoli, G., Borleffs, M. S., Amin Yavari, S., Wauthle, R., Weinans, H., and Zadpoor, A. A. (2013). Mechanical properties of open-cell metallic biomaterials manufactured using additive manufacturing. *Materials & Design*, 49:957–965.

[21] Cao, X., Jiang, Y., Zhao, T., Wang, P., Wang, Y., Chen, Z., Li, Y., Xiao, D., and Fang, D. (2020). Compression experiment and numerical evaluation on mechanical responses of the lattice structures with stochastic geometric defects originated from additive-manufacturing. *Composites Part B: Engineering*, 194:108030.

[22] Chollet, F. et al. (2015). Keras. `https://github.com/fchollet/keras`.

[23] Christensen, J. and de Abajo, F. J. G. (2012). Anisotropic Metamaterials for Full Control of Acoustic Waves. *Physical Review Letters*, 108(12):124301.

[24] Clarke, D. (2011). *Tensor calculus: a primer*. Saint Mary's University, Halifax NS, Canada.

[25] Cliffe, K. A., Giles, M. B., Scheichl, R., and Teckentrup, A. L. (2011). Multilevel Monte Carlo methods and applications to elliptic PDEs with random coefficients. *Computing and Visualization in Science*, 14(1):3.

[26] Dallago, M., Winiarski, B., Zanini, F., Carmignato, S., and Benedetti, M. (2019). On the effect of geometrical imperfections and defects on the fatigue strength of cellular lattice structures additively manufactured via selective laser melting. *International Journal of Fatigue*, 124:348 – 360.

[27] D'Angella, D. (2021). *Reactions on trimmed locally-refined meshes*. PhD Thesis, Technische Universität München, Chair of Computational Modeling and Simulation. Chapter 7.

[28] De Oliveira, V. (2000). Bayesian prediction of clipped gaussian random fields. *Computational Statistics & Data Analysis*, 34(3):299–314.

[29] de Prenter, F., Verhoosel, C. V., van Zwieten, G. J., and van Brummelen, E. H. (2017). Condition Number Analysis and Preconditioning of the Finite Cell Method. *Computer Methods in Applied Mechanics and Engineering*, 316(Supplement C):297–327.

[30] DebRoy, T., Wei, H., Zuback, J., Mukherjee, T., Elmer, J., Milewski, J., Beese, A., Wilson-Heid, A., De, A., and Zhang, W. (2018). Additive manufacturing of metallic components – process, structure and properties. *Progress in Materials Science*, 92:112–224.

[31] Delgado, J., Ciurana, J., and Rodríguez, C. A. (2012). Influence of process parameters on part quality and mechanical properties for DMLS and SLM with iron-based materials. *The International Journal of Advanced Manufacturing Technology*, 60(5):601–610.

[32] Deshpande, V., Fleck, N., and Ashby, M. (2001). Effective properties of the octet-truss lattice material. *Journal of the Mechanics and Physics of Solids*, 49(8):1747 – 1769.

[33] Dirrenberger, J., Forest, S., and Jeulin, D. (2014). Towards gigantic RVE sizes for 3D stochastic fibrous networks. *International Journal of Solids and Structures*, 51(2):359–376.

[34] Dong, G., Tang, Y., and Zhao, Y. F. (2017). A survey of modeling of lattice structures fabricated by additive manufacturing. *Journal of Mechanical Design*, 139:32–38.

[35] Dong, Z., Liu, Y., Li, W., and Liang, J. (2019). Orientation dependency for microstructure, geometric accuracy and mechanical properties of selective laser melting AlSi10Mg lattices. *Journal of Alloys and Compounds*, 791:490–500.

[36] du Plessis, A., Sperling, P., Beerlink, A., Tshabalala, L., Hoosain, S., Mathe, N., and le Roux, S. G. (2018). Standard method for microct-based additive manufacturing quality control 2: Density measurement. *MethodsX*, 5:1117–1123.

[37] du Plessis, A., Yadroitsava, I., and Yadroitsev, I. (2020). Effects of defects on mechanical properties in metal additive manufacturing: A review focusing on X-ray tomography insights. *Materials & Design*, 187:108385.

[38] Düster, A., Parvizian, J., Yang, Z., and Rank, E. (2008). The Finite Cell Method for Three-Dimensional Problems of Solid Mechanics. *Computer Methods in Applied Mechanics and Engineering*, 197(45–48):3768–3782.

[39] Düster, A., Rank, E., and Szabó, B. A. (2017). The p-Version of the Finite Element Method and Finite Cell Methods. In Stein, E., Borst, R., and Hughes, T. J. R., editors, *Encyclopedia of Computational Mechanics*, volume 2, pages 1–35. John Wiley & Sons, Chichester, West Sussex.

[40] Echeta, I., Dutton, B., Feng, X., Leach, R., and Piano, S. (2020). Review of defects in lattice structures manufactured by powder bed fusion. *International Journal of Advanced Manufacturing Technology*, 106:2649–2668.

[41] El Elmi, A., Melancon, D., Asgari, M., Liu, L., and Pasini, D. (2020). Experimental and numerical investigation of selective laser melting–induced defects in Ti–6Al–4V octet truss lattice material: the role of material microstructure and morphological variations. *Journal of Materials Research*, 35(15):1900–1912.

[42] Elhaddad, M., Zander, N., Bog, T., Kudela, L., Kollmannsberger, S., Kirschke, J. S., Baum, T., Ruess, M., and Rank, E. (2018). Multi-Level hp-Finite Cell Method for Embedded Interface Problems with Application in Biomechanics. *International Journal for Numerical Methods in Biomedical Engineering*, 34(4):e2951.

[43] Elsevier (2021). Elsevier journal publishing agreement. `https://www.elsevier.com/about/policies/copyright`. Accessed: 2021-03-09.

[44] Fan, T. (2012). Concrete microstructure homogenization technique with application to model concrete serviceability. *Civil Engineering ETDs*.

[45] Fang, N., Xi, D., Xu, J., Ambati, M., Srituravanich, W., Sun, C., and Zhang, X. (2006). Ultrasonic metamaterials with negative modulus. *Nature Materials*, 5(6):452–456.

[46] Fenton, G. and Griffiths, D. (2008). Simulation. In *Risk Assessment in Geotechnical Engineering*, chapter 6, pages 203–238. John Wiley & Sons, Ltd.

[47] Fox, J. C., Moylan, S. P., and Lane, B. M. (2016). Effect of Process Parameters on the Surface Roughness of Overhanging Structures in Laser Powder Bed Fusion Additive Manufacturing. *Procedia CIRP*, 45:131–134.

[48] Fritzen, F., Forest, S., Kondo, D., and Böhlke, T. (2013). Computational homogenization of porous materials of Green type. *Computational Mechanics*, 52(1):121–134.

[49] Gao, X.-L. and Park, S. (2007). Variational formulation of a simplified strain gradient elasticity theory and its application to a pressurized thick-walled cylinder problem. *International Journal of Solids and Structures*, 44(22):7486–7499.

[50] Geng, L., Wu, W., Sun, L., and Fang, D. (2019). Damage characterizations and simulation of selective laser melting fabricated 3D re-entrant lattices based on in-situ CT testing and geometric reconstruction. *International Journal of Mechanical Sciences*, 157-158:231 – 242.

[51] Gibson, I., Rosen, D., Stucker, B., and Khorasani, M. (2021). *Powder Bed Fusion*, pages 125–170. Springer International Publishing, Cham.

[52] Gong, H., Rafi, K., Gu, H., Starr, T., and Stucker, B. (2014). Analysis of defect generation in Ti–6Al–4V parts made using powder bed fusion additive manufacturing processes. *Additive Manufacturing*, 1-4:87–98.

[53] Gould, P. L. (2013). *Material Behavior*, pages 71–89. Springer New York, New York, NY.

[54] Grasso, M. and Colosimo, B. M. (2017). Process defects and in situ monitoring methods in metal powder bed fusion: a review. *Measurement Science and Technology*, 28(4):044005.

[55] Gross, D. and Seelig, T. (2017). *Fracture Mechanics: With an Introduction to Micromechanics*. Mechanical Engineering Series. Springer International Publishing.

[56] Gümrük, R., Mines, R. A. W., and Karadeniz, S. (2013). Static mechanical behaviours of stainless steel micro-lattice structures under different loading conditions. *Materials Science and Engineering: A*, 586:392–406.

[57] Gusev, A. A. (1997). Representative volume element size for elastic composites: A numerical study. *Journal of the Mechanics and Physics of Solids*, 45(9):1449–1459.

[58] Hain, M. (2008). *Computational Homogenization of Micro-Structural Damage Due to Frost in Hardened Cement Paste*. PhD Thesis, Institut für Baumechanik und Numerische Mechanik, Leibniz-Universität Hannover.

[59] Handcock, M. S. and Wallis, J. R. (1994). An Approach to Statistical Spatial-Temporal Modeling of Meteorological Fields. *Journal of the American Statistical Association*, 89(426):368–378.

[60] Hansbo, P., Lovadina, C., Perugia, I., and Sangalli, G. (2005). A Lagrange multiplier method for the finite element solution of elliptic interface problems using non-matching meshes. *Numerische Mathematik*, 100(1):91–115.

[61] Hashin, Z. and Shtrikman, S. (1963). A variational approach to the theory of the elastic behaviour of multiphase materials. *Journal of the Mechanics and Physics of Solids*, 11(2):127 – 140.

[62] Haubrich, J., Gussone, J., Barriobero-Vila, P., Kürnsteiner, P., Jägle, E. A., Raabe, D., Schell, N., and Requena, G. (2019). The role of lattice defects, element partitioning and intrinsic heat effects on the microstructure in selective laser melted Ti-6Al-4V. *Acta Materialia*, 167:136 – 148.

[63] Hazanov, S. and Amieur, M. (1995). On overall properties of elastic heterogeneous bodies smaller than the representative volume. *International Journal of Engineering Science*, 33(9):1289 – 1301.

[64] Hazanov, S. and Huet, C. (1994). Order relationships for boundary conditions effect in heterogeneous bodies smaller than the representative volume. *Journal of the Mechanics and Physics of Solids*, 42(12):1995–2011.

[65] Heinze, S., Bleistein, T., Düster, A., Diebels, S., and Jung, A. (2017). Experimental and numerical investigation of single pores for identification of effective metal foams properties. *Journal of Applied Mathematics and Mechanics*, 98:682–695.

[66] Heinze, S., Joulaian, M., and Düster, A. (2015). Numerical Homogenization of Hybrid Metal Foams Using the Finite Cell Method. *Computers & Mathematics with Applications*, 70(7):1501–1517.

[67] Hill, R. (1952). The elastic behaviour of a crystalline aggregate. *Proceedings of the Physical Society A*, 65:349–354.

[68] Hill, R. (1963). Elastic properties of reinforced solids: Some theoretical principles. *Journal of the Mechanics and Physics of Solids*, 11(5):357–372.

[69] Holzapfel, G. A. (2000). *Nonlinear Solid Mechanics: A Continuum Approach for Engineering*. Wiley, Chichester, New York.

[70] Hua, Y., Timofeev, D., Giorgio, I., and Mueller, W. (2020). Effective strain gradient continuum model of metamaterials and size effects analysis. *Continuum Mechanics and Thermodynamics*.

[71] Hughes, T. J. R. (2000). *The Finite Element Method: Linear Static and Dynamic Finite Element Analysis*. Dover Publications, Mineola, NY.

[72] ISO/ASTM52900-15 (2015). *ASTM E 111-17: Standard Test Method for Young's Modulus, Tangent Modulus, and Chord Modulus*. West Conshohocken, PA: American Society for Testing and Materials.

[73] Joint Committee for Guides in Metrology (2008). *JCGM 100: Evaluation of Measurement Data - Guide to the Expression of Uncertainty in Measurement*.

[74] Jomo, J., Zander, N., Elhaddad, M., Özcan, A. I., Kollmannsberger, S., Mundani, R.-P., and Rank, E. (2017). Parallelization of the multi-level hp-adaptive finite cell method. *Computers and Mathematics with Applications*, 74(1):126–142.

[75] Jomo, J. N., de Prenter, F., Elhaddad, M., D'Angella, D., Verhoosel, C. V., Kollmannsberger, S., Kirschke, J. S., Nübel, V., van Brummelen, E. H., and Rank, E. (2019). Robust and parallel scalable iterative solutions for large-scale finite cell analyses. *Finite Elements in Analysis and Design*, 163:14–30.

[76] Kalender, W. A., Hebel, R., and Ebersberger, J. (1987). Reduction of CT artifacts caused by metallic implants. *Radiology*, 164(2):576–577.

[77] Kasperovich, G., Haubrich, J., Gussone, J., and Requena, G. (2016). Correlation between porosity and processing parameters in TiAl6V4 produced by selective laser melting. *Materials & Design*, 105:160–170.

[78] Kendall, M., Stuart, A., Ord, K., Forster, J., Arnold, S., and O'Hagan, A. (1994). *Kendall's Advanced Theory of Statistics, Classical Inference and the Linear Model*. A Hodder Arnold Publication. Wiley.

[79] Khakalo, S., Balobanov, V., and Niiranen, J. (2018). Modelling size-dependent bending, buckling and vibrations of 2D triangular lattices by strain gradient elasticity models: Applications to sandwich beams and auxetics. *International Journal of Engineering Science*, 127:33 – 52.

[80] Khakalo, S. and Niiranen, J. (2019). Lattice structures as thermoelastic strain gradient metamaterials: Evidence from full-field simulations and applications to functionally step-wise-graded beams. *Composites Part B: Engineering*, 177:107224.

[81] Khristenko, U., Constantinescu, A., Tallec, P. L., Oden, J. T., and Wohlmuth, B. (2020). A statistical framework for generating microstructures of two-phase random materials: application to fatigue analysis. *Multiscale Modeling & Simulation*, 18(1):21–43.

[82] Kingma, D. P. and Ba, J. (2014). Adam: A Method for Stochastic Optimization. *arXiv:1412.6980 [cs]*.

[83] Korshunova, N., Alaimo, G., Hosseini, S., Carraturo, M., Reali, A., Niiranen, J., Auricchio, F., Rank, E., and Kollmannsberger, S. (2021a). Bending behavior of octet-truss lattice structures: modelling options, numerical characterization and experimental validation. *Materials & Design*, page 109693.

[84] Korshunova, N., Alaimo, G., Hosseini, S., Carraturo, M., Reali, A., Niiranen, J., Auricchio, F., Rank, E., and Kollmannsberger, S. (2021b). Image-based numerical characterization and experimental validation of tensile behavior of octet-truss lattice structures. *Additive Manufacturing*, 41:101949.

[85] Korshunova, N., Jomo, J., Lékó, G., Reznik, D., Balázs, P., and Kollmannsberger, S. (2020). Image-based material characterization of complex microarchitectured additively manufactured structures. *Computers & Mathematics with Applications*, 80(11):2462 – 2480.

[86] Korshunova, N., Papaioannou, I., Kollmannsberger, S., Straub, D., and Rank, E. (2021c). Uncertainty quantification of microstructure variability and mechanical behaviour of additively manufactured lattice structures. *Preprint submitted to Computer Methods in Applied Mechanics and Engineering*, https://arxiv.org/abs/2103.09550.

[87] Koutsourelakis, P. S. and Deodatis, G. (2006). Simulation of multidimensional binary random fields with application to modeling of two-phase random media. *Journal of Engineering Mechanics*, 132(6):619–631.

[88] Krizhevsky, A., Sutskever, I., and Hinton, G. E. (2017). ImageNet classification with deep convolutional neural networks. *Communications of the ACM*, 60(6):84–90.

[89] Krumscheid, S., Nobile, F., and Pisaroni, M. (2020). Quantifying uncertain system outputs via the multilevel Monte Carlo method — Part I: Central moment estimation. *Journal of Computational Physics*, 414:109466.

[90] Kudela, L., Zander, N., Kollmannsberger, S., and Rank, E. (2016). Smart octrees: Accurately integrating discontinuous functions in 3D. *Computer Methods in Applied Mechanics and Engineering*, 306:406–426.

[91] Larsson, F., Runesson, K., Saroukhani, S., and Vafadari, R. (2011). Computational homogenization based on a weak format of micro-periodicity for RVE-problems. *Computer Methods in Applied Mechanics and Engineering*, 200(1):11–26.

[92] Latture, R. M., Begley, M. R., and Zok, F. W. (2018). Design and mechanical properties of elastically isotropic trusses. *Journal of Materials Research*, 33(3):249–263.

[93] Lazar, M. and Po, G. (2015a). The non-singular Green tensor of gradient anisotropic elasticity of Helmholtz type. *European Journal of Mechanics - A/Solids*, 50:152–162.

[94] Lazar, M. and Po, G. (2015b). The non-singular Green tensor of Mindlin's anisotropic gradient elasticity with separable weak non-locality. *Physics Letters A*, 379(24):1538–1543.

[95] Lei, H., Li, C., Meng, J., Zhou, H., Liu, Y., Zhang, X., Wang, P., and Fang, D. (2019). Evaluation of compressive properties of SLM-fabricated multi-layer lattice structures by experimental test and μ-CT-based finite element analysis. *Materials & Design*, 169:107685.

[96] Li, D.-Q., Xiao, T., Zhang, L.-M., and Cao, Z.-J. (2019). Stepwise covariance matrix decomposition for efficient simulation of multivariate large-scale three-dimensional random fields. *Applied Mathematical Modelling*, 68:169–181.

[97] Lin, P.-S. and Clayton, M. K. (2005). Properties of binary data generated from a truncated gaussian random field. *Communications in Statistics - Theory and Methods*, 34(3):537–544.

[98] Liu, L., Kamm, P., García-Moreno, F., Banhart, J., and Pasini, D. (2017). Elastic and failure response of imperfect three-dimensional metallic lattices: The role of geometric defects induced by Selective Laser Melting. *Journal of the Mechanics and Physics of Solids*, 107:160–184.

[99] Liu, Y., Li, J., Sun, S., and Yu, B. (2019). Advances in gaussian random field generation: a review. *Computational Geosciences*, 23(5):1011–1047.

[100] Love, A. (1944). *A Treatise on the Mathematical Theory of Elasticity*. Dover Books on Engineering Series. Dover Publications.

[101] Lozanovski, B., Leary, M., Tran, P., Shidid, D., Qian, M., Choong, P., and Brandt, M. (2019). Computational modelling of strut defects in SLM manufactured lattice structures. *Materials & Design*, 171:107671.

[102] Lu, Y., Wu, S., Gan, Y., Huang, T., Yang, C., Junjie, L., and Lin, J. (2015). Study on the microstructure, mechanical property and residual stress of SLM Inconel-718 alloy manufactured by differing island scanning strategy. *Optics & Laser Technology*, 75:197–206.

[103] Maconachie, T., Leary, M., Lozanovski, B., Zhang, X., Qian, M., Faruque, O., and Brandt, M. (2019). SLM lattice structures: Properties, performance, applications and challenges. *Materials & Design*, 183:108137.

[104] Malvern, L. E. (1977). *Introduction to the Mechanics of a Continuous Medium*. Prentice Hall, Englewood Cliffs.

[105] Man, B. D., Nuyts, J., Dupont, P., Marchal, G., and Suetens, P. (1998). Metal streak artifacts in X-ray computed tomography: A simulation study. In *1998 IEEE Nuclear Science Symposium Conference Record. 1998 IEEE Nuclear Science Symposium and Medical Imaging Conference (Cat. No.98CH36255)*, volume 3, pages 1860–1865 vol.3.

[106] Mazur, M., Leary, M., McMillan, M., Sun, S., Shidid, D., and Brandt, M. (2017). 5 - mechanical properties of Ti6Al4V and AlSi12Mg lattice structures manufactured by selective laser melting (SLM). In Brandt, M., editor, *Laser Additive Manufacturing*, Woodhead Publishing Series in Electronic and Optical Materials, pages 119–161. Woodhead Publishing.

[107] Melancon, D., Bagheri, Z., Johnston, R., Liu, L., Tanzer, M., and Pasini, D. (2017). Mechanical characterization of structurally porous biomaterials built via additive manufacturing: experiments, predictive models, and design maps for load-bearing bone replacement implants. *Acta Biomaterialia*, 63:350–368.

[108] Michel, J. C., Moulinec, H., and Suquet, P. (1999). Effective properties of composite materials with periodic microstructure: A computational approach. *Computer Methods in Applied Mechanics and Engineering*, 172(1):109–143.

[109] Mikla, V. I. and Mikla, V. V. (2014). 2 - computed tomography. In Mikla, V. I. and Mikla, V. V., editors, *Medical Imaging Technology*, pages 23–38. Elsevier, Oxford.

[110] Mindlin, R. (1964). Microstructure in linear elasticity. *Archive for Rational Mechanics and Analysis*, 16:51–78.

[111] Mishnaevsky, L. (2007). *Microstructure–Strength Relationships of Composites: Concepts and Methods of Analysis*, chapter 4, pages 65–113. John Wiley & Sons, Ltd.

[112] Mura, T. (1987). *Micromechanics of Defects in Solids*. Mechanics of Elastic and Inelastic Solids. Springer Netherlands.

[113] Nemat-Nasser, S., Hori, M., and Achenbach, J. (2013). *Micromechanics: Overall Properties of Heterogeneous Materials*. North-Holland Series in Applied Mathematics and Mechanics. Elsevier Science.

[114] Ngo, T. D., Kashani, A., Imbalzano, G., Nguyen, K. T. Q., and Hui, D. (2018). Additive manufacturing (3D printing): A review of materials, methods, applications and challenges. *Composites Part B: Engineering*, 143:172–196.

[115] Nguyen, V.-D., Béchet, E., Geuzaine, C., and Noels, L. (2012). Imposing periodic boundary condition on arbitrary meshes by polynomial interpolation. *Computational Materials Science*, 55:390–406.

[116] Nguyen, V.-D. and Noels, L. (2014). Computational homogenization of cellular materials. *International Journal of Solids and Structures*, 51(11):2183–2203.

[117] Nguyen, V. P., Kerfriden, P., and Bordas, S. P. A. (2014). Two- and three-dimensional isogeometric cohesive elements for composite delamination analysis. *Composites Part B: Engineering*, 60:193–212. 00010.

[118] Nguyen, V. P., Stroven, M., and Sluys, L. J. (2011). Multiscale continuous and discontinuous modeling of heterogeneous materials: A review on recent developments. *Journal of Multiscale Modelling*, 03(04):229–270.

[119] Niiranen, J., Balobanov, V., Kiendl, J., and Hosseini, S. (2019). Variational formulations, model comparisons and numerical methods for Euler-Bernoulli micro- and nano-beam models. *Mathematics and Mechanics of Solids*, 24(1):312–335.

[120] Niiranen, J., Khakalo, S., Balobanov, V., and Niemi, A. H. (2016). Variational formulation and isogeometric analysis for fourth-order boundary value problems of gradient-elastic bar and plane strain/stress problems. *Computer Methods in Applied Mechanics and Engineering*, 308:182–211.

[121] Nitsche, J. (1971). Über ein Variationsprinzip zur Lösung von Dirichlet-Problemen bei Verwendung von Teilräumen, die keinen Randbedingungen unterworfen sind. *Abhandlungen aus dem Mathematischen Seminar der Universität Hamburg*, 36(1):9–15.

[122] Norouzi, A., Rahim, M. S. M., Altameem, A., Saba, T., Rad, A. E., Rehman, A., and Uddin, M. (2014). Medical image segmentation methods, algorithms, and applications. *IETE Technical Review*, 31(3):199–213.

[123] Ogorodnikov, V. A., Kablukova, E. G., and Prigarin, S. M. (2018). Stochastic models of atmospheric clouds structure. *Statistical Papers*, 59(4):1521–1532.

[124] O'Masta, M., Dong, L., St-Pierre, L., Wadley, H., and Deshpande, V. (2017). The fracture toughness of octet-truss lattices. *Journal of the Mechanics and Physics of Solids*, 98:271 – 289.

[125] Onck, P., Andrews, E., and Gibson, L. (2001). Size effects in ductile cellular solids. part i: modeling. *International Journal of Mechanical Sciences*, 43(3):681 – 699.

[126] Owen, D. B. (1956). Tables for computing bivariate normal probabilities. *The Annals of Mathematical Statistics*, 27(4):1075–1090.

[127] Pahr, D. H. (2003). *Experimental and Numerical Investigations of Perforated FRP-Laminates*. VDI-Verlag.

[128] Pahr, D. H. and Zysset, P. K. (2008). Influence of boundary conditions on computed apparent elastic properties of cancellous bone. *Biomechanics and Modeling in Mechanobiology*, 7(6):463–476.

[129] Parvizian, J., Düster, A., and Rank, E. (2007). Finite Cell Method. *Computational Mechanics*, 41(1):121–133.

[130] Pasini, D. and Guest, J. K. (2019). Imperfect architected materials: Mechanics and topology optimization. *MRS Bulletin*, 44(10):766–772.

[131] Pattanayak, D. K., Fukuda, A., Matsushita, T., Takemoto, M., Fujibayashi, S., Sasaki, K., Nishida, N., Nakamura, T., and Kokubo, T. (2011). Bioactive Ti metal analogous to human cancellous bone: Fabrication by selective laser melting and chemical treatments. *Acta Biomaterialia*, 7(3):1398–1406.

[132] Portela, C. M., Greer, J. R., and Kochmann, D. M. (2018). Impact of node geometry on the effective stiffness of non-slender three-dimensional truss lattice architectures. *Extreme Mechanics Letters*, 22:138 – 148.

[133] Prashanth, K. G., Scudino, S., Chaubey, A. K., Löber, L., Wang, P., Attar, H., Schimansky, F. P., Pyczak, F., and Eckert, J. (2016). Processing of Al–12Si–TNM composites by selective laser melting and evaluation of compressive and wear properties. *Journal of Materials Research*, 31(1):55–65.

[134] Prell, D., Kyriakou, Y., Kachelrie, M., and Kalender, W. A. (2010). Reducing metal artifacts in computed tomography caused by hip endoprostheses using a physics-based approach. *Investigative Radiology*, 45(11):747–754.

[135] Prigarin, S., Martin, A., and Winkler, G. (2004). Numerical models of binary random fields on the basis of thresholds of gaussian functions. *Sib. Zh. Vychisl. Mat.*, 7:165–175.

[136] Pyka, G., Kerckhofs, G., Papantoniou, I., Speirs, M., Schrooten, J., and Wevers, M. (2013). Surface Roughness and Morphology Customization of Additive Manufactured Open Porous Ti6Al4V Structures. *Materials*, 6(10):4737–4757.

[137] Płatek, P., Sienkiewicz, J., Janiszewski, J., and Jiang, F. (2020). Investigations on Mechanical Properties of Lattice Structures with Different Values of Relative Density Made from 316L by Selective Laser Melting (SLM). page 2204.

[138] Rahman Rashid, R. A., Mallavarapu, J., Palanisamy, S., and Masood, S. H. (2017). A comparative study of flexural properties of additively manufactured aluminium lattice structures. *Materials Today: Proceedings*, 4(8):8597–8604.

[139] Rashed, M., Ashraf, M., Mines, R., and Hazell, P. J. (2016). Metallic microlattice materials: A current state of the art on manufacturing, mechanical properties and applications. *Materials & Design*, 95:518 – 533.

[140] Reißner, H. (1931). Eigenspannungen und Eigenspannungsquellen. *ZAMM - Journal of Applied Mathematics and Mechanics / Zeitschrift für Angewandte Mathematik und Mechanik*, 11(1):1–8.

[141] Renishaw-PLC (2020). *Data sheet: SS 316L-0407 powder for additive manufacturing*. Renishaw-PLC.

[142] Reuss, A. (1929). Berechnung der Fließgrenze von Mischkristallen auf Grund der Plastizitätsbedingung für Einkristalle. *ZAMM - Journal of Applied Mathematics and Mechanics / Zeitschrift für Angewandte Mathematik und Mechanik*, 9(1):49–58.

[143] Ronneberger, O., Fischer, P., and Brox, T. (2015). U-Net: Convolutional Networks for Biomedical Image Segmentation. *arXiv:1505.04597 [cs]*.

[144] Sab, K. (1992). On the homogenization and the simulation of random materials. *Eur. J. Mech, A/Solids*, (5):585–607.

[145] Sacks, J., Welch, W. J., Mitchell, T. J., and Wynn, H. P. (1989). Design and Analysis of Computer Experiments. *Statistical Science*, 4(4):409–423.

[146] Sanaei, N., Fatemi, A., and Phan, N. (2019). Defect characteristics and analysis of their variability in metal L-PBF additive manufacturing. *Materials & Design*, 182:108091.

[147] Sanchez-Palencia, E. and Zaoui, A., editors (1987). *Homogenization Techniques for Composite Media: Lectures Delivered at the CISM International Center for Mechanical Sciences, Udine, Italy, July 1-5, 1985*. Lecture Notes in Physics. Springer-Verlag, Berlin Heidelberg.

[148] Sarker, A., Tran, N., Rifai, A., Elambasseril, J., Brandt, M., Williams, R., Leary, M., and Fox, K. (2018). Angle defines attachment: Switching the biological response to titanium interfaces by modifying the inclination angle during selective laser melting. *Materials & Design*, 154:326–339.

[149] Schillinger, D. (2012). *The P- and B-Spline Versions of the Geometrically Nonlinear Finite Cell Method and Hierarchical Refinement Strategies for Adaptive Isogeometric and Embedded Domain Analysis*. PhD thesis, Technische Universität München, Munich.

[150] Sehlhorst, H.-G. (2011). *Numerical Homogenization Strategies for Cellular Materials with Applications in Structural Mechanics*. PhD Thesis, Technische Universität Hamburg.

[151] Seifi, M., Gorelik, M., Waller, J., Hrabe, N., Shamsaei, N., Daniewicz, S., and Lewandowski, J. J. (2017). Progress towards metal additive manufacturing standardization to support qualification and certification. *JOM*, 69(3):439–455.

[152] Sha, Y., Jiani, L., Haoyu, C., Ritchie, R. O., and Jun, X. (2018). Design and strengthening mechanisms in hierarchical architected materials processed using additive manufacturing. *International Journal of Mechanical Sciences*, 149:150 – 163.

[153] Shidid, D., Leary, M., Choong, P., and Brandt, M. (2016). Just-in-time design and additive manufacture of patient-specific medical implants. *Physics Procedia*, 83:4 – 14.

[154] Shinozuka, M. and Deodatis, G. (1996). Simulation of Multi-Dimensional Gaussian Stochastic Fields by Spectral Representation. *Applied Mechanics Reviews*, 49(1):29–53.

[155] Sing, S. L., Wiria, F. E., and Yeong, W. Y. (2018). Selective laser melting of lattice structures: A statistical approach to manufacturability and mechanical behavior. *Robotics and Computer-Integrated Manufacturing*, 49:170 – 180.

[156] Spiegel, M., Lipschutz, S., and Spellman, D. (2009). *Vector Analysis. Schaum's Outlines (2nd ed.)*. USA: McGraw Hill.

[157] Suquet, P. (1985). *Elements of Homogenization for Inelastic Solid Mechanics*.

[158] Svenning, E., Fagerström, M., and Larsson, F. (2016). Computational homogenization of microfractured continua using weakly periodic boundary conditions. *Computer Methods in Applied Mechanics and Engineering*, 299:1 – 21.

[159] Szabó, B. A. and Babuška, I. (1991). *Finite Element Analysis*. John Wiley & Sons, New York.

[160] Szabó, B. A., Düster, A., and Rank, E. (2004). The p-version of the finite element method. In Stein, E., editor, *Encyclopedia of Computational Mechanics*. John Wiley & Sons, Chichester, West Sussex.

[161] Tahaei Yaghoubi, S., Balobanov, V., Mousavi, S. M., and Niiranen, J. (2018). Variational formulations and isogeometric analysis for the dynamics of anisotropic gradient-elastic Euler-Bernoulli and shear-deformable beams. *European Journal of Mechanics - A/Solids*, 69:113–123.

[162] Tancogne-Dejean, T. and Mohr, D. (2018). Elastically-isotropic truss lattice materials of reduced plastic anisotropy. *International Journal of Solids and Structures*, 138:24 – 39.

[163] Tancogne-Dejean, T., Spierings, A. B., and Mohr, D. (2016). Additively-manufactured metallic micro-lattice materials for high specific energy absorption under static and dynamic loading. *Acta Materialia*, 116:14–28.

[164] Teckentrup, A. L., Scheichl, R., Giles, M. B., and Ullmann, E. (2013). Further analysis of multilevel Monte Carlo methods for elliptic PDEs with random coefficients. *Numerische Mathematik*, 125(3):569–600.

[165] Temizer, İ., Wu, T., and Wriggers, P. (2013). On the optimality of the window method in computational homogenization. *International Journal of Engineering Science*, 64:66–73.

[166] Temizer, I. and Zohdi, T. I. (2007). A numerical method for homogenization in non-linear elasticity. *Computational Mechanics*, 40(2):281–298.

[167] Teubner, M. (1991). Level surfaces of gaussian random fields and microemulsions. *EPL (Europhysics Letters)*, 14(5):403.

[168] Torabi, J., Ansari, R., and Darvizeh, M. (2018). A C1 continuous hexahedral element for nonlinear vibration analysis of nano-plates with circular cutout based on 3D strain gradient theory. *Composite Structures*, 205:69–85.

[169] Torabi, J., Ansari, R., and Darvizeh, M. (2019). Application of a non-conforming tetrahedral element in the context of the three-dimensional strain gradient elasticity. *Computer Methods in Applied Mechanics and Engineering*, 344:1124–1143.

[170] Tyrus, J., Gosz, M., and DeSantiago, E. (2007). A local finite element implementation for imposing periodic boundary conditions on composite micromechanical models. *International Journal of Solids and Structures*, 44(9):2972–2989.

[171] Van Bael, S., Kerckhofs, G., Moesen, M., Pyka, G., Schrooten, J., and Kruth, J. (2011). Micro-CT-based improvement of geometrical and mechanical controllability of selective laser melted Ti6Al4V porous structures. *Materials Science and Engineering: A*, 528(24):7423–7431.

[172] Vanmarcke, E. H. (2007). Random field modeling of the void phase of soils. *Georisk: Assessment and Management of Risk for Engineered Systems and Geohazards*, 1(1):57–68.

[173] Voigt, W. (1889). Über die Beziehung zwischen den beiden Elastizitätskonstanten isotroper Körper. *Annalen der Physik*, 38:573 – 587.

[174] Wang, C., Reddy, J., and Lee, K. (2000). Chapter 2 - bending of beams. In Wang, C., Reddy, J., and Lee, K., editors, *Shear Deformable Beams and Plates*, pages 11–38. Elsevier Science Ltd, Oxford.

[175] Wang, P., Lei, H., Zhu, X., Chen, H., and Fang, D. (2019). Influence of manufacturing geometric defects on the mechanical properties of AlSi10Mg alloy fabricated by selective laser melting. *Journal of Alloys and Compounds*, 789:852 – 859.

[176] Wauthle, R., Vrancken, B., Beynaerts, B., Jorissen, K., Schrooten, J., Kruth, J.-P., and Van Humbeeck, J. (2015). Effects of build orientation and heat treatment on the microstructure and mechanical properties of selective laser melted Ti6Al4V lattice structures. *Additive Manufacturing*, 5:77–84.

[177] Wood, A. T. A. and Chan, G. (1994). Simulation of Stationary Gaussian Processes in $[0,1]^d$. *Journal of Computational and Graphical Statistics*, 3(4):409–432.

[178] Xu, W., Lui, E. W., Pateras, A., Qian, M., and Brandt, M. (2017). In situ tailoring microstructure in additively manufactured Ti-6Al-4V for superior mechanical performance. *Acta Materialia*, 125:390–400.

[179] Yan, C., Hao, L., Hussein, A., and Raymont, D. (2012). Evaluations of cellular lattice structures manufactured using selective laser melting. *International Journal of Machine Tools and Manufacture*, 62:32 – 38.

[180] Yang, Z., Ruess, M., Kollmannsberger, S., Düster, A., and Rank, E. (2012). An Efficient Integration Technique for the Voxel-Based Finite Cell Method. *International Journal for Numerical Methods in Engineering*, 91(5):457–471.

[181] Yoder, M., Thompson, L., and Summers, J. (2018). Size effects in lattice structures and a comparison to micropolar elasticity. *International Journal of Solids and Structures*, 143:245 – 261.

[182] Yuan, L., Ding, S., and Wen, C. (2019). Additive manufacturing technology for porous metal implant applications and triple minimal surface structures: A review. *Bioactive Materials*, 4:56–70.

[183] Yuan, Z. and Fish, J. (2007). Toward realization of computational homogenization in practice. *International Journal for Numerical Methods in Engineering*, 73(3):361–380.

[184] Zander, N. (2017). *Multi-Level hp-FEM: Dynamically Changing High-Order Mesh Refinement with Arbitrary Hanging Nodes.* PhD Thesis, Technische Universität München, München.

[185] Zervos, A. (2008). Finite elements for elasticity with microstructure and gradient elasticity. *International Journal for Numerical Methods in Engineering*, 73(4):564–595.

[186] Zhang, B., Li, Y., and Bai, Q. (2017). Defect Formation Mechanisms in Selective Laser Melting: A Review. *Chinese Journal of Mechanical Engineering*, 30(3):515–527.

[187] Zheng, X., Lee, H., Weisgraber, T. H., Shusteff, M., DeOtte, J., Duoss, E. B., Kuntz, J. D., Biener, M. M., Ge, Q., Jackson, J. A., Kucheyev, S. O., Fang, N. X., and Spadaccini, C. M. (2014). Ultralight, ultrastiff mechanical metamaterials. *Science*, 344(6190):1373–1377.

[188] Zhou, H., Zhang, X., Zeng, H., Yang, H., Lei, H., Li, X., and Wang, Y. (2019). Lightweight structure of a phase-change thermal controller based on lattice cells manufactured by slm. *Chinese Journal of Aeronautics*, 32(7):1727 – 1732.

[189] Zohdi, T. I. and Wriggers, P. (2005). *An Introduction to Computational Micromechanics.* Lecture Notes in Applied and Computational Mechanics. Springer-Verlag Berlin Heidelberg.